MOLECULAR MODELING OF ADSORPTION OF SIMPLE AND COMPLEX FLUIDS ON NANOPOROUS MATERIALS FOR CHARACTERIZATION

by

RICHARD T. CIMINO

A dissertation submitted to the

Graduate School-New Brunswick

Rutgers, The State University of New Jersey

In partial fulfillment of the requirements

For the degree of

Doctor of Philosophy

Graduate Program in Chemical and Biochemical Engineering

Written under the direction of

Alexander V. Neimark

And approved by

_____

_____

_____

_____

_____

New Brunswick, New Jersey

OCTOBER, 2016

ABSTRACT OF THE DISSERTATION

Molecular Modeling of Adsorption of Simple and Complex Fluids on Nanoporous Materials for Characterization

By RICHARD T. CIMINO

Dissertation Director:

Alexander V. Neimark

The process of adsorption – in particular physisorption – occurs when the molecules of a fluid accumulate upon a solid surface. Adsorption is influenced by temperature, pressure, and adsorbate composition – as well as the adsorbate-adsorbent interactions, which are dependent on the chemistry and topology of the adsorbent. The influence of these factors is reflected in the adsorption behavior – the quantitative and qualitative interactions between the adsorbed species and the adsorbent. The unique features of adsorption have led to its widespread use for the characterization of porous materials. Of particular interest is the class of materials with pores which have a characteristic dimension on the order of nanometers, termed *nanoporous materials*. This dissertation focuses on the accurate modeling of adsorption through analytical, computational and simulation techniques and the application of adsorption modeling to characterization of nanoporous materials. Analytical and computational models were developed to predict the specific behavior of simple fluids (N_2, Ar, Kr, CO_2) and complex fluids (polymers) interacting with nanoporous materials and transferrable tools were created to facilitate adsorbent characterization based upon adsorption behavior. The tools and models presented in this dissertation aid one to understand the peculiarities of adsorption behavior, in particular the phenomena of capillary hysteresis, scanning hysteresis, and the so-called “critical conditions” of adsorption and to exploit these peculiarities to

derive useful information about nanoporous materials. In particular: a suite of analytical models was developed for the analysis of scanning isotherms, suitable for any simple nonpolar fluid, from which pore size distributions and pore domain correlation/connectivity may be derived. A set of adsorption isotherm kernels was developed using Quenched Solid density functional theory to analyze adsorption isotherms of Ar and CO_2 on micro-mesoporous carbons, capable of distinguishing slit, cylindrical, and spherical pore geometries. A new criterion for the critical conditions of polymer adsorption on surfaces – the incremental chemical potential – has been demonstrated and applied to the case of liquid polymer chromatography. An expression for the overall partition coefficient was developed which takes into account adsorbent geometry and column porosity. It was shown that the adsorption and elution behavior of polymers can be predicted for nonporous and porous column substrates using this partition coefficient, with minimal parameterization.

Dedication

To my loving husband and our shared future

ACKNOWLEDGEMENTS

The work of this thesis would have been impossible without the help, support, encouragement, questioning, editing, and nitpicking of a great many individuals. I would like to thank first and foremost my dissertation advisor Dr. Alexander V. Neimark, who has taken me from the state of knowing nothing, to knowing I know nothing. I am eternally indebted to him for his constant support, kindness and guidance throughout my doctoral studies. I am also grateful for the technical advice and support I have received from Dr. Aleksey Vishnyakov, who as always regarded me with much more respect than I deserve. I thank and acknowledge the guidance I received from the former doctoral students and postdoctoral researchers in Dr. Neimark's group – Drs. Peter Ravikovitch, Gennady Gor, Yangzheng Lin, Christopher Rasmussen, John Landers, and Ming-Tsung Lee, with whom I have become lifelong friends and colleagues. I also would like to acknowledge my PhD "mentee" Silvio Dantas, who has taught me so much about being a mentor. From Rutgers University, I wish to thank the many educators and staff members who have watched me grow over the past nine (yes nine!) years, including Deans Bernath, Rankin, and Prendergast for accepting me into the Engineering school all those years ago. From the Chemical Engineering Department, Drs.Yee Chiew, Nina Shapley and Marianthi Ierapetritou and Dr. David Axelrod from the Molecular Biology and Biochemistry Department for continually inspiring to become an educator, and Lynn DiCaprio and Debbie Moon for their administrative help and friendship. Outside of Rutgers, I would like to thank our industrial collaborators Drs. Matthias Thommes, Katie Cychosz, and Yefim Brun who have contributed so much to this thesis and have taught me so much about experimental reality vs. my theoretical research. For my work in Chapter 2, I would like to thank Dr. Mark Newman (U. Mich.) for useful discussions of percolation theory and simulation. Financially, this dissertation would be impossible without the funding I have received from the Bevier Fellowship, the School of Engineering Fellowship and the Chemical and Biochemical Engineering Fellowship, as well as NSF GOALI grants "Multiscale Modeling of Adsorption

Equilibrium and Dynamics in Polymer Chromatography" and 'Theoretical Foundations of Interaction Nanoparticle Chromatography".

For their emotional and moral support, I would like to thank my entire family, especially my husband Cory Pinto, my parents Wendy and Joseph Talik and grandparents Phyllis and Bruce Taistra. Your unflagging encouragement has made this whole process possible. I would also like to thank Rabbi Hannah Orden and the friends I have made at Congregation Beth Hatikvah for providing me with just the right amount of menucha every Shabbos to prevent me from going insane. Finally, I wish to thank and acknowledge Marc Gunn, Dr. Patrick Lane, Liz Rodriguez & Nicole Keating, Heather Teysko, Stephen West, Ross Blotcher & Carie Poppy, the McElroy and Smirl families, Tybee Diskin and Andie Bolt for providing endless humor and cathartic release from the stresses of my commute and the tedious work of my PhD.

ער איז אַ מבֿין ווי אַ באָק אויף אַ כּלי-זמר

Er iz a meyvn vi a bok oif a klezmer!

He's an expert like a goat is a musician!

- *Yiddish Saying*

TABLE OF CONTENTS

ABSTRACT ii

DEDICATION iv

ACKNOWLEDGEMENTS v

TABLE OF CONTENTS vii

LIST OF TABLES ix

LIST OF ILLUSTRATIONS x

CHAPTER 1. Introduction 1

PART I: ADSORPTION OF SIMPLE FLUIDS

CHAPTER 2. Experimental and Theoretical Studies of Scanning Adsorption-Desorption Isotherms ……24

CHAPTER 3. Characterization of Micro-Mesoporous Carbons by High Pressure CO_2 Adsorption ……59

PART II: ADSORPTION OF COMPLEX FLUIDS

CHAPTER 4. Thermodynamic analysis of critical conditions of polymer adsorption 78

CHAPTER 5. Critical conditions of polymer adsorption and chromatography on non-porous substrates ……88

CHAPTER 6. Mechanisms of Chain Adsorption on Porous Substrates and Critical Conditions of Polymer Chromatography ……....112

Appendix A: Supplementary Information for Chapter 2 142

Appendix B. Supplementary Information for Chapter 3 152

Appendix C. Supplementary Information for Chapter 4 161

Appendix D: Supplementary Information for Chapter 5 167

Appendix E: Supplemental Information for Chapter 6 175

ACKNOWLEDGEMENT OF PREVIOUS PUBLICATIONS 180

LIST OF PUBLICATIONS AND PRESENTATIONS 182

GENERAL CONCLUSIONS AND OUTLOOK 185

BIBLIOGRAPHY 189

LIST OF TABLES

Table 2.1 Coordination number z and percolation threshold q_c determined in the Bethe model from scanning isotherms ……48

Table 3.1 Cumulative pore volume calculations by the DFT and Gurvich methods 73

LIST OF ILLUSTRATIONS

Fig. 1.1. IUPAC classification of adsorption isotherms 5

Fig. 1.2 IUPAC classification of hysteresis loops 7

Fig. 1.3 Schematic of an ideal Gaussian chain 13

Fig. 1.4. Schematic of a SAW chains 15

Fig. 1.5 Real chain model used in this dissertation 16

Fig. 2.1. Characteristic types of hysteresis behavior H1 and H2 25

Fig. 2.2. N_2 (77 K) isotherms on SBA-15 and KIT-6 29

Fig. 2.3 Ar (87 K) on four 3DOm carbons 31

Fig. 2.4. Xe (151 K) adsorption and desorption scanning isotherms on Vycor glass 32

Fig. 2.5. N_2 (77 K) primary and scanning adsorption and desorption isotherms on Vycor glass 33

Fig. 2.6. Main hysteresis loop for the nitrogen adsorption-desorption cycle on SBA-15 37

Fig. 2.7. Comparison of PCM with experiments for N_2 adsorption on SBA-15 and KIT-6 40

Fig. 2.8. Comparison of the PCM with experiments for Xe adsorption on Vycor glass 41

Fig. 2.9. Figure illustrating two pathways for capillary evaporation 43

Fig. 2.10. The fraction $Q_{-}(q, Q_{+})$ of unfilled pores; Bethe approximation and MC simulation 46

Fig. 2.11. Scanning isotherms for Xe on Vycor glass; Bethe approximation 49

Fig. 2.12. The main adsorption and desorption isotherms of 3DOm carbons 50

Fig. 2.13. $q(\chi)$ for Vycor glass; Bethe approximation and MC simulation 52

Fig. 2.14. $q(\chi)$ for 3DOm Carbons 53

Fig. 2.15. Integral and differential distributions for Vycor 54

Fig. 2.16. Differential PSDs for 3DOm carbons 55

Fig. 3.1 Experimental isotherms of Ar, N_2 and CO_2 adsorption for CMK-3 samples a, b and c 70

Fig. 3.2. Pore size distributions for CMK-3 a, b and c 72

Fig. 3.3. Cumulative pore volume V(D) as a function of pore width *D* for CMK-3 a and b 73

Fig. 4.1. Characteristic conformations of tethered chains 78

Fig. 4.2. $\mu_{incr}(U,N)$for thethered chains 82

Fig. 4.3. Scaling of R_g and μ_{incr} 85

Fig. 5.1. Schematics of different conformations of chains near a surface 98

Fig. 5.2. $\mu_{incr}(U,N)$for different anchoring distances, z 101

Fig. 5.3. Henry coefficient $K_H(N)$ 102

Fig. 5.4. Retention volumes for polystyrenes on a nonporous substrate 104

Fig. 5.5 *K(U)* chains of length *N* between 2 and 200 105

Fig. 5.6. Correlation between U' and X' 106

Fig. 5.7. Effect of stagnant zone in the interstitial volume on retention 109

Fig. 6.1. Characteristic conformations of polymer chain interacting with nanoporous substrate 117

Fig. 6.2. $\Delta\mu(z,U)$ 120

Fig. 6.3. Henry coefficient $K_H(N)$ 122

Fig. 6.4. $\mu_{incr}(U,N)$ for chains confined to pores 125

Fig. 6.5. ΔF and K_P for the chains completely confined to a pore 126

Fig. 6.6. Partially confined chains in two cis/trans conformations 128

Fig. 6.7 $\mu_{incr}(U,N)$ & ΔF for partially confined chains 130

Fig. 6.8. Model porous substrate 133

Fig 6.9. Retention volumes for polystyrenes on a porous substrate 134

Fig. 6.10. Contributions of adsorption mechanisms in SEC, LCCC, and LAC regimes 138

CHAPTER 1

Introduction

1.1 Motivation

The process of adsorption – in particular physisorption – occurs when the molecules of a fluid accumulate on a solid surface, or within the pores of a porous solid. Adsorption is influenced by temperature, pressure, and adsorbate composition as well as the adsorbate-adsorbent interactions, which are dependent on the chemistry and topology of the adsorbent. The influence of these factors is reflected in the adsorption behavior – the quantitative and qualitative interactions between the adsorbed species and the adsorbent. The unique features of adsorption have led to its widespread use for the characterization of porous materials. Of particular interest is the class of materials with pores which have characteristic dimension of nanometers, termed *nanoporous materials*. This dissertation focuses on the accurate modeling of adsorption through analytical, computational and simulation techniques and the application of adsorption modeling to the characterization of nanoporous materials. Analytical and computational models were developed to predict the adsorption behavior of simple fluids, such as N_2, Ar, Kr, CO_2 and complex fluids (in particular, polymers) interacting with nanoporous materials and tools were created to facilitate adsorbent characterization based upon adsorption behavior. The tools and models presented in this dissertation aid our understanding of the peculiarities of adsorption behavior, in particular the phenomena of capillary hysteresis, scanning hysteresis, and the so-called “critical conditions” of adsorption. This knowledge enables us to exploit these peculiarities to derive useful information about the adsorbent.

This dissertation is divided into two parts. In PART 1 a suite of analytical models and computational tools is developed for the analysis of adsorption isotherms of simple fluids interacting with silica and carbons. These tools enable one to determine the textural properties of

a material, including the pore size distribution, surface area, volume and pore domain correlation/connectivity. In **Chapter 2**, the phenomena of capillary and scanning hysteresis are described in detail, and three models are presented that distinguish the characteristics of the porous domains within a material, based solely on information derived from adsorption isotherms. These methods are applied to nanoporous materials which exhibit several characteristic pore topologies, including parallel cylindrical pores, inkbottle pores, and disordered networks. In **Chapter 3** a set of eight high-resolution adsorption isotherm kernels was developed using Quenched Solid density functional theory [1, 2] to analyze adsorption isotherms of CO_2 and Ar on micro-mesoporous carbons. These kernels are tailored to specific pore geometries including: slit, cylindrical, and spherical pores, and take into account the atomistically rough surface of amorphous carbons. PART 2 of this dissertation applies the fundamentals of adsorption to the description of polymer interactions with porous materials. In **Chapter 4** a new criterion for the critical conditions of polymer adsorption on surfaces – the equality of incremental chemical potentials – is demonstrated and the scaling of the incremental chemical potential and chain radii of gyration with the adsorption potential is investigated. This criterion is then applied to the case of liquid polymer chromatography in **Chapters 5-6**. In **Chapter 5**, it is illustrated for the first time that critical conditions (as well as the size exclusion and interaction chromatography regimes) are observable for experimental liquid polymer chromatography on nonporous substrates. A simple model of chain retention is developed based upon the *overall partition coefficient* for chains interacting with nonporous surfaces, and Monte Carlo simulations are performed to estimate the partition coefficient, which is a function of the incremental chemical potential. This model is extended in **Chapter 6** to the case of porous substrates, where three mechanisms of chain adsorption are distinguished: adsorption on the external surface, confinement to pores and partial confinement to pores. Lastly, it is argued that the critical conditions of polymer adsorption are identical for porous and nonporous substrates, provided that these three mechanisms of adsorption are taken into account.

1.2 Background

1.2.1 Adsorption Isotherms

An adsorption isotherm is a graph of the amount of adsorbate present on an adsorbent as a function of external pressure *p*, at constant temperature, *T*. The shape and quantity of an adsorption isotherm can tell one much about the properties of both the adsorbent and adsorbate, and acts as a "fingerprint" of the porous material. These features have led to adsorption's widespread use for the characterization of porous media, since the pioneering works of van Bemmelen published in 1897 [3] and of Zsigmondy [4] in 1911.

There are several common methods of measuring adsorption isotherms; the two most prominent methods being the gravimetric and manometric techniques. A gravimetric experiment consists of repeated weighing a sample adsorbent exposed to ambient pressure of the adsorbate. The gravimetric method is very useful for isotherms which may be assessed at or near room temperature, such as water vapor adsorption. However, the gravimetric technique becomes impractical for other analysis gasses such as Ar and N_2, which are typically measured near their boiling temperatures (87 and 77 K, respectively). For such systems, it is common to use the manometric adsorption technique, in which the sample adsorbent is closed in a cell and repeatedly exposed to the adsorbate at increasing external pressure, while submerged in an appropriate temperature bath. Adsorption of these vapors (N_2, Ar, Kr etc…) is normally measured at discrete intervals below the saturation pressure (p_0), and thus isotherms are often plotted in terms of relative pressure – p/p_0.

The mechanism of adsorption and its reverse process – desorption – varies greatly and depends on the properties of the adsorbent and adsorbate. One major factor which influences the adsorption process is the pore size. The pores of an adsorbent are classified based upon their characteristic dimension (typically, the width of the pore mouth): micropores (< 2nm), mesopores

(2 - 50 nm) and macropores (> 50 nm). Due to their small size, adsorption in micropores is controlled mainly by the interactions of the adsorbate molecules with the pore walls. Molecules pack into micropores at low relative pressures, and may make up a significant amount of the adsorbed volume. In contrast, adsorption in meso- and macropores is a function of both the adsorbate-adsorbent and adsorbate-adsorbate interactions. As pores become larger than a few molecular diameters, it is possible for films of adsorbate to form along the pore walls. As the external pressure increases, adsorbate molecules will continue to layer on top of the primary film, until the pores eventually fill completely with adsorbate. One feature distinguishing mesopores is that pore filling occurs at pressures less than the saturation pressure (p_0) of the vapor. This effect, called capillary condensation, occurs due to enhanced attraction caused by the fluid-wall interactions (the attractive potential and curvature) and fluid-fluid interactions (surface tension). Adsorption and condensation in macropores occur at or near the saturation pressure, as the adsorbate properties approach those of a bulk fluid. The analysis of adsorption behavior in macropores is beyond the scope of this work, which deals primarily with micro-mesoporous phenomena.

Adsorption isotherms are classified based upon their shapes, which in general are indicative of the presence of micro, meso, and macropores. **Fig. 1.1** below is a reproduction of the IUPAC classification of adsorption isotherms [5].

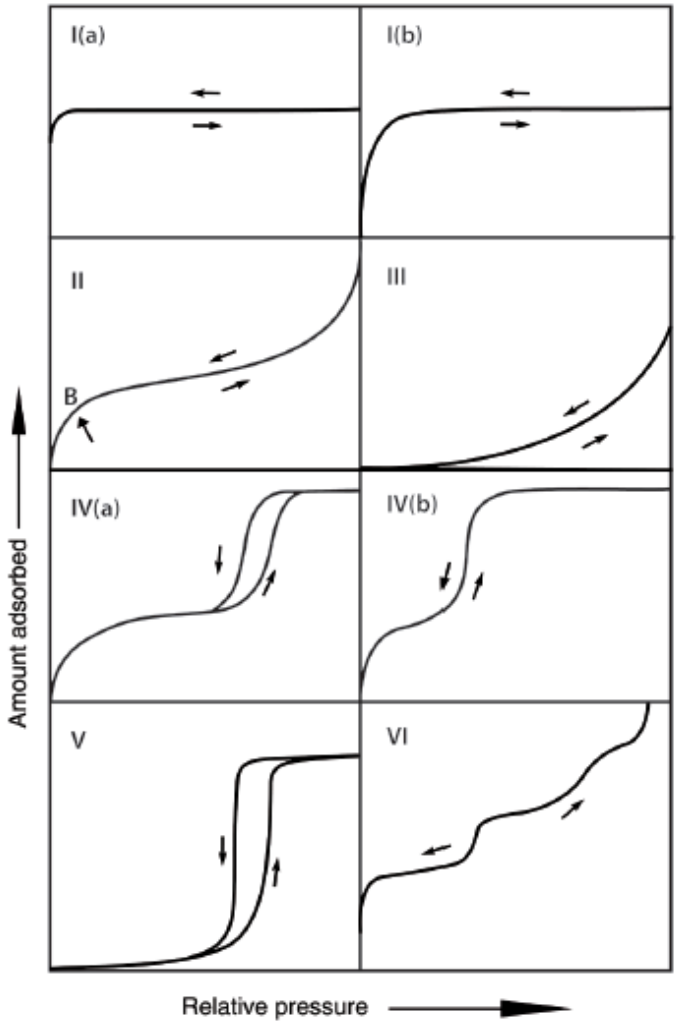

Fig. 1.1 IUPAC classification of adsorption isotherms.

Isotherms of type I are typical of adsorbents comprised primarily of micropores. Depending on the pore size range and distribution, the filling transition (plateau) of the isotherm occurs at different relative pressures. Type I(a) isotherms occur when the material has a narrow range of micropores, no larger than a few the molecular diameters. Pores fill at low relative pressures, due to the strong adsorbate-adsorbent interactions present in small micropores. Type I(b) isotherms are the product of microporous adsorbents with a wider distribution of micropores and additionally, may contain some small mesopores (~ 2nm). Type IV isotherms are typical of mesoporous adsorbents and relatively strong adsorbent-adsorbate interactions. Type IV isotherms are distinguished by their

concave shape and plateau region at low relative pressures due to monolayer formation on the pore walls and a distinctive capillary condensation transition at high relative pressure. Type IV isotherms often exhibit capillary hysteresis, which is discussed below. Isotherms of types III and V are indicative of weak adsorbent-adsorbate interactions. Type III/V isotherms do not exhibit monolayer formation; rather, adsorption is mediated by the presence of beneficial adsorption sites from which adsorption nucleation events occur. Type II and type VI isotherms are commonly displayed by nonporous or macroporous adsorbents, where the surface area is comparably low relative to micro-mesoporous materials. One (II) or more (VI) distinctive layering transitions may occur in these isotherms related to the ordering of adsorbate molecules in layers on the surface of the adsorbent. These materials do not exhibit plateau regions near the saturation pressure, due to the lack of mesopores and only partial filling of macropores.

1.2.2. Capillary Hysteresis in Mesopores

As mentioned above, an important aspect of the adsorption-desorption process in mesoporous materials is that the amount adsorbed along the path of increasing pressure is not necessarily the same as the amount adsorbed while pressure decreases. It was recognized early on that this phenomenon, called hysteresis, could provide valuable information about the adsorbent[6-9]. There are several general types of hysteresis, given common labels under IUPAC classification [5], reproduced here in **Fig. 1.2**.

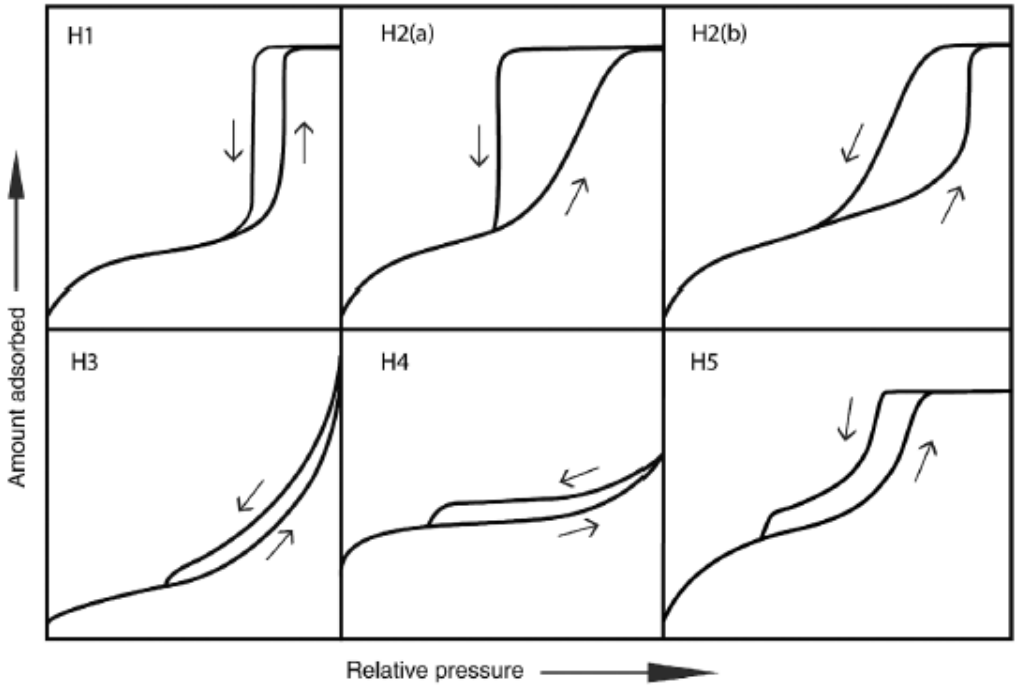

Fig. 1.2 IUPAC classification of adsorption hysteresis.

Hysteresis loops of Type H1 indicate an array of narrow uniform mesopores, and are common for mesoporous silica and other "designer" materials such as templated carbons for which the fluid in the pores acts independently of its neighboring pores (more below). Type H2 loops arise due to more complex, connected pore structures. Type H2(a) hysteresis is characterized by a sharp desorption "knee" which arises due to the pore blocking effect – a phenomenon by which evaporation of fluid in large pores is delayed, and relies on the evaporation of smaller, connected pores. The more gradual slope of H2(b) hysteresis occurs when the distribution of the connector pores is broader than in H2(a), and is also controlled by pore-blocking. Hysteresis behavior of Type H3 is typical for non-rigid aggregates comprised of flakes or sheets such as ash, and certain geological materials (clays etc…) which may reorient themselves upon increasing pressure, and then collapse upon decreasing pressure. Type H3 is also indicative of partially filled macropores which may also be present in the same materials. Hysteresis of type H4 is found in many aggregated crystals of zeolites, some mesoporous zeolites, and micro-mesoporous carbons. Type

H5 hysteresis is common in mesoporous materials with very narrow "necks" or windows between pores. Hysteresis of types H3-H5 are further characterized by a distinctive step on the desorption branch, which is caused by the stretching and snapping of the liquid film and formation of vapor bubbles in large pores which are blocked by small neighboring pores during desorption. This phenomenon is known as *cavitation*. Cavitation occurs at a characteristic range of relative pressures per adsorbate. For N_2 @ 77K, this occurs between $p/p_0 = 0.4 – 0.5$. A detailed discussion of cavitation is beyond the scope of this dissertation. For an excellent introduction to the subject, the reader is referred to the Doctoral Dissertation of Dr. Christopher Rasmussen (published online)[3]. Two of these primary types of hysteresis (H1 and H2) are further discussed in **Chapter 2**. These types are observed for the rigidly-structured materials that I studied, which have limited internal flexibility, such as SBA-15, KIT-6, Vycor porous glass, and various carbons.

1.2.3. Adsorption and Pore Size

The adsorption of specific adsorbents in porous materials has been investigated heavily and a voluminous literature exists on the topic. It is beyond the scope of this short introduction to survey even a fraction of the extant literature on gas adsorption. Instead, the reader is referred to several important books on the topic [10-12]. It is however pertinent to mention briefly the most common analytical and simulation-based methods to describe the relationship between adsorption behavior of these adsorbates and the properties of the porous adsorbent, as well as the common pore models that are assumed. These models and methodologies are central to our current understanding of the phenomenon of adsorption in porous media and form the basis upon which this dissertation is founded.

1.2.3.1. Pore Models

A discussion of the topic of pore models must begin with mentioning the concept of *independent domains*, as discussed in Everett [10]. Essentially, the assumption of *independent*

domains states that an adsorbent can be described as a collection of many individual 'domains' or pore bodies, none of which interacts directly with another. In the context of an adsorption/desorption experiment, this means that the filling and emptying of one pore body does not affect the filling/emptying of another – i.e. these pore bodies behave independently. This assumption has important consequences for the application of the analytical and simulation based methods described below; virtually every model in widespread use assumes independent domains when determining adsorbent properties such as pore size distributions (PSDs).

The most common adsorption models are based upon the behavior of fluid in single pores or on surfaces of specific geometry: planar surfaces, cylinders, slit pores, and spheroids. Assuming independent domains, the adsorption and desorption from any one of these pores is dependent only upon the individual pore geometry and adsorbate properties. Using the methods below, adsorption from such simple pores can be aggregated to produce a coherent picture of the total porosity in an adsorbent.

At the next level of complexity are pore models that include the interaction between the fluid in adjacent pores, or pores of different sizes. The simplest of these models is the inkbottle pore, which has two or more principle radii of different widths. The filling and emptying of such a pore is determined in conjunction with a correlative equation, such as the Kelvin-Laplace-Cohan theory, which captures the physical-chemical relationship between a pore's principle diameter and the pressure at which the pore fills or empties (more below). Beyond inkbottle pores are the fractal and network models, which seek to describe the adsorption/desorption process based on a collection of pores and their connectivity. In particular, the percolation theory has proved effective in describing the degree of connectivity and disorder in a porous material. (See **Chapter 2**).

1.2.3.2. Methods for Simple Fluids in Single Pores

The simplest equation describing the relationship between adsorption and pore size in a single pore is the Kelvin-Laplace-Cohan Equation: $RT\ln\left(\frac{p}{p_0}\right) = \frac{-\gamma V_m}{(r-h)}$. This equation states the equality of the chemical potentials of the vapor phase (LHS) and liquid phase (RHS) adsorbate during pore filling. Here, the relative pressure p/p_0 is inversely related to the effective pore diameter r-h, where r is the pore diameter and h is the fluid film thickness along the pore wall. The fluid properties are defined by the surface tension γ and molar volume of the vapor V_m and the temperature of the system T. During desorption, equilibrium between the condensed vapor and external pressure alters the relationship slightly: $RT\ln\left(\frac{p}{p_0}\right) = \frac{-2\gamma V_m}{(r-h)}$; the factor of 2 arising from the assumption of a vapor-liquid interface at both ends of the pore. Thus, for a pore of any size, it is possible to determine the relative pressure at which that pore will fill with condensed vapor and the corresponding pressure at which it will evaporate. Applying the K-L-C equation to an experimental isotherm, it is possible to approximate the mesoporous PSD of the material by identifying the relative pressure at which the vapor condenses in the adsorbent. This method was first discussed by Barrett, Joyner and Halenda (BJH) [13]. A further development of this theory came with the work of Derjaguin [14], and Broekhoff & de Boer[15], who modified the K-L-C equations to include an additional contribution from the so-called disjoining pressure: $RT\ln\left(\frac{p}{p_0}\right) = \frac{-\gamma V_m}{(r-h)} + \Pi(h)V_m$. The disjoining pressure $\Pi(h)$ represents a force exerted on the walls of the adsorbent by the adsorbate, which may act to constrict or dilate the pore. For many simple fluids such as nitrogen and argon, there exist explicit equations for the disjoining pressure which utilize reference isotherms such as that of Frenkel, Halsey, and Hill given in ref. [11]

Analytical methods, such as the ones described above work reasonably well for model systems consisting of regular structures in the range of mesopores. However, as pores become smaller or the geometry becomes more complex, we must rely on simulation and computation to

determine the relationship between pore size and adsorption. The simulation of adsorption for simple molecules had been explored for many geometries and adsorbent/adsorbate combinations. Fluid models have varied vastly, from hard-spheres to multi-centered Lennard-jones molecules, to sophisticated models including dipole interactions. One prominent group of computational methods is that of Density Functional Theory (DFT), which has proven an incredibly powerful tool for predicting the pattern of adsorption in a wide range of pore sizes. Several recent papers [16-24] utilized the combination of experimental N_2 and Ar adsorption and DFT to calculate pore properties for various materials, including various silicas[22], activated [20], 3DOm[21], and CMK[24] carbons. In each of these cases there is a regular, ordered (hierarchical) mesoporous domain consisting of spherical, cylindrical or slit shaped pores. Additionally, these materials all exhibit a significant contribution to adsorption from micropores, necessitating such a broadly accurate predictive method. The DFT method hinges on the determination of the most-likely density profile of a fluid within an adsorbing pore. This is accomplished by minimization of the grand potential $\Omega[\rho(\mathbf{r})]$, which is a functional of the fluid density $\rho(\mathbf{r})$:

$$\Omega[\rho(\mathbf{r})] = F[\rho(\mathbf{r})] + f[\rho(\mathbf{r}), \Phi_{attr}(|\mathbf{r} - \mathbf{r}'|)]$$

Here, $F[\rho(\mathbf{r})]$ is the Helmholtz free energy of adsorbate confined to the adsorbing pore, and f is a function of the intermolecular potentials between adsorbate atoms (and the adsorbent atoms, in more modern versions of DFT[16]). The minimization of $\Omega[\rho(\mathbf{r})]$ furnishes the equilibrium adsorption at a single pressure. This calculation is then repeated at many pressures to produce an adsorption isotherm. These isotherms may then be grouped together to produce an isotherm 'kernel', from which PSDs may be calculated. In **Chapter 3**, a formulation of the Nonlocal and Quenched Solid density functional theories are described in detail, as they are applied to the adsorption of Ar and CO_2 in micro-mesoporous carbons.

1.2.4. Polymer adsorption

Liquid polymer adsorption is a ubiquitous phenomenon, occurring in myriad natural and man-made processes involving interactions between polymers and solid phases. Polymer adsorption plays an important role in biological [25] as well as industrial and consumer applications; in particular, polymers are crucial components of many separation processes [26]. For more than half a century, researchers have sought to model the complex behavior of polymers near surfaces using first theoretical and later, simulation based techniques, with the goal of predicting adsorption behavior as it applies to these aforementioned applications. What follows is a very brief overview of several important polymer models used both historically and at the present, as well as a summary of the concepts in polymer adsorption germane to this dissertation. These concepts are further developed and discussed at length in PART II of this dissertation.

1.2.4.1. Chain Models

The course of the past eighty years has witnessed an evolution in the popularity and prevalence of polymer chain models beginning from the most simplistic representation - namely random-walks or 'flights' to the most complex representations, which take into account various inter- and intra- chain interactions. Broadly, chain models can be classified as either *ideal* 'statistical' models or *real* models - i.e. models which account for excluded volume. The theoretical underpinnings of both ideal and real chain models and their application to adsorption were developed between the 1930's and 1950's. The brief discussion below is meant as a cursory introduction to chain models as they pertain to Monte Carlo simulations of adsorption. Detailed descriptions of these models can be found elsewhere [27, 28].

Ideal Chains

The earliest model polymer is the 'random coil' model, which was first conceived as an application of the random walk. A random coil consists of a series of segments, described as points

$\boldsymbol{r_1, r_2 \ldots, r_N}$ each separated by a discreet distance *b*, known as the Kuhn length. Chain conformations $\vec{\boldsymbol{r}}(\boldsymbol{N})$ are determined by random configurations of these points, with an average end-to-end distance $\boldsymbol{r_{1,N}}$ obeying the Gaussian distribution (see **Fig. 1.3** below).

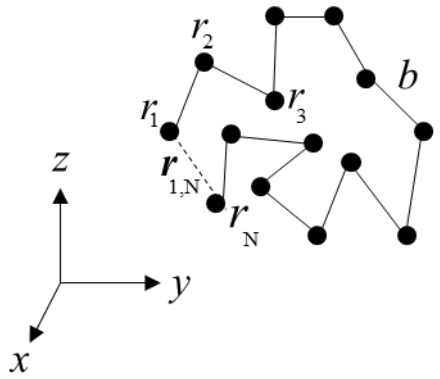

Fig. 1.3 Schematic of an ideal Gaussian chain

In the 1950s Simha, Frisch and Eirich [29] expanded upon the early attempt of Broda and Mark [30] to describe adsorption of polymers. In this case, the adsorbent surface was defined as a planar "reflecting" surface, meaning that chains were confined to one side of the interface. They developed the adsorption probability *P(N)* - the probability that *N* chain segments will be adsorbed to the surface - as a function of the Gaussian distribution and were the first to describe the thermodynamic properties of chain monolayer formation. The adsorption of ideal chains was investigated heavily in the 1960s, with key contributions from Silberberg [31], Forsman and Hughes [32] and Rubin [33]. These works were mainly concerned with the adsorption behavior of ideal chains in the "dilute solution limit" – i.e. single chains with no chain-chain interactions.

The first Monte Carlo simulations of ideal chains were undertaken by Di Marzio and McCrackin [34]. The primary goal of this and subsequent works prior to the 1980's was to revisit the theoretical results of the Gaussian chain model – mainly single chain behavior near surfaces

and the physics of monolayer formation – in order to understand the limits and applicability of ideal chains. Further simulation studies and theoretical models describing ideal chain adsorption were proposed in the next two decades, most notably the grand canonical formulation of Birshtein [35] in 1979 and the scaling formulation of Eisenriegler, Kremer and Binder [36] in 1982, who coupled Monte Carlo simulations of ideal chains with his scaling theory (discussed further below).

Real Chains

Simple Models of Excluded Volume

At the next level of complexity beyond ideal chain models are the models which introduce the concept of *excluded volume*. Excluded volume models all share in common the property that two chain segments cannot occupy the same physical space at the same time. This distinguishes excluded volume chains from ideal chains, in which chain segments are allowed to overlap completely. Perhaps the earliest mention of excluded volume effects in the context of polymers can be attributed to Kuhn [37]. Building on this and other early attempts[38, 39], Flory, was the first to describe in detail excluded volume chains by statistical methods[40]. Flory was followed by Montroll [41], Debye & Rubin [42] , and Zimm et. al [43] who described the statistics of real chains in terms of Markov Processes.

The simplest implementation of excluded volume is the self-avoiding walk (SAW). In the SAW model, segments are "grown" in any direction with equal probability, however two segments cannot share the same coordinates. As such, SAW chains behave differently than ideal chains in the same volume. SAW chains are often confined to a (cubic) lattice for ease of computation, with chain segments corresponding to the vertices of the lattice. In the absence of special growth techniques such as Configurational Bias MC [44] simulations of SAWs are confined to short chains or dilute solutions, due to the frequency with which the end of the chain will grow into itself. A schematic of several SAW chains on a cubic lattice is illustrated in **Fig. 1.4** below.

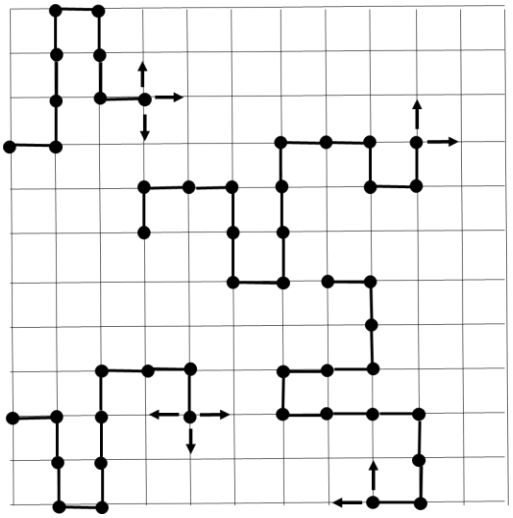

Fig. 1.4. Schematic of a SAW chains. Arrows indicate possible directions for placement of subsequent segments.

Off lattice real chains

With the emergence of high-speed computing in the late 1990s and early 2000s, the simulation of off-lattice chains with complex self-interaction potentials became feasible. These chains, known as "real chains" were studied extensively and in particular the adsorption behavior of end-tethered real chains was compared with earlier results for ideal chains, with general agreement [45-47] (more below). Real chain models encompass a wide range of complexities, from atomistic models to coarse-grained representations. Monte Carlo chain models are typically coarse, consisting of a "pearl necklace" of spherical chain segments connected variously by hard bonds or harmonic potentials. Non-neighbor segments likewise vary in interaction, ranging from hard-sphere to Lennard-Jones type interactions. Real, off lattice coarse-grained representations of polymer chains (such as in **Fig. 1.5** below) are used throughout PART II of this dissertation.

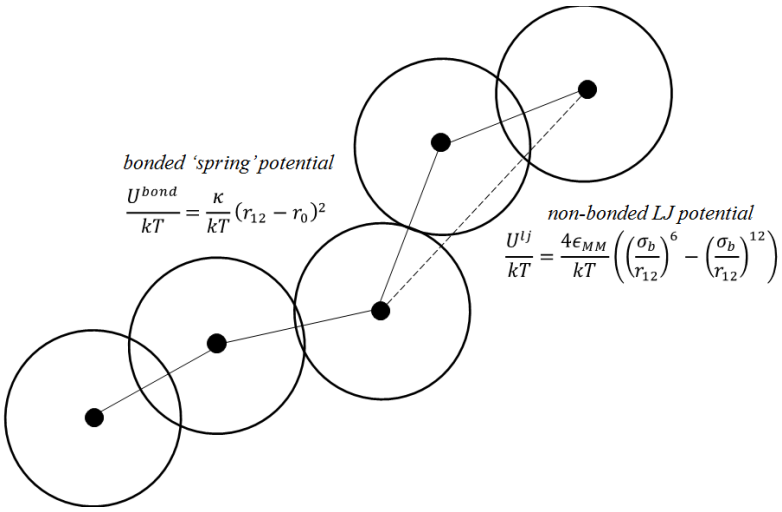

Fig. 1.5 Real chain model used in this dissertation. Spherical chain segments (beads) are connected by harmonic bonds and interact with non-nearest neighbor beads via the Lennard-Jones potential.

1.2.4.2. The adsorption transition and critical adsorption

Broadly, the one of the main challenges in polymer adsorption is to accurately describe the qualitative behavior of chains near plane surfaces. Over the past several decades, prime importance was given to the determination of the *adsorption transition* and *critical adsorption* of polymer chains. It was observed as early as Silberberg[31], Rubin [33] and DeGennes [48], that there exists a "critical" transition point ε_c of the attractive surface potential ε for which the number of adsorbed monomers scales with the molecular weight of the chain. At this point, the chain transitions from having most segments free, to having most segments adsorbed. The behavior of chains near this transition point is often characterized in the language of a first order *phase transition*, and obeys the scaling law $M = N^{\phi} f\left(\tau N^{\phi}\right)$ in the limit of long chains (see **Chapter 4** and **Appendix C** for details). The so-called crossover exponent ϕ was first predicted theoretically as equal to 0.5, following the mean-field approximation. This number has been confirmed by simulations, within a certain degree of accuracy (see **Chapter 4**).

Identical to the critical transition (above) is the critical point of adsorption or CPA, defined here as the point at which entropic (confinement) and enthalpic (adsorption) forces on a chain are perfectly balanced. The CPA for ideal chains has been studied rigorously using simulations. In general, these studies have focused on the behavior of chains tethered to plane surfaces, since the CPA for tethered chains is associated with a geometrical transition from a three-dimensional coil (weak adsorption) to a two-dimensional coil (strong adsorption) which coats the adsorbent surface. The position of this transition was shown to be chain length independent by Eisenriegler, Kremer and Binder [36] and later by Meirovitch and Livne [49], who formulated the behavior of end-tethered polymers using theory borrowed from analogous phenomenon found in electromagnetic materials. The geometrical transition has been used extensively since these formative works as a litmus test of the critical adsorption potential. However, recently new criteria have been developed for determining the CPA using a thermodynamic instead of geometrical criterion. Two such criteria are the chain length independence of the chain free energy used by Wang[50] and the equality of incremental chemical potentials, developed in this dissertation (see **Chapter 4** and applications in **Chs. 5-6**.)

1.2.4.3. The Partition Coefficient

Apart from the problem of monolayer formation and the adsorption transition, another typical quantifier of polymer adsorption is the *partition coefficient, K*. The partition coefficient is the ratio between the concentrations of adsorbed and non-adsorbed polymer chains, and it is heavily dependent on chain chemistry/topology, the chain-solution and chain-surface interactions. Exact equations for the partition coefficient for ideal chains were developed by Casassa and coworkers in the 1960s for a broad range of adsorbent geometries, from plane surfaces to slit, cylindrical or square channels, and also to spherical confinements both in the presence and absence of attractive interactions [51, 52]. In these equations, the partition coefficient is a function of the aspect ratio λ between the polymer radius of gyration in free solution, Rg, and the characteristic dimension of the

confinement – i.e. slit width or cylindrical diameter, etc. It was shown that there are significant effects on the partition coefficient depending on the effective adsorption potential and polymer concentration [53]. By the 1980s and early 1990s, these theoretical results for ideal chains were tested against experimental observations and illustrated using Monte Carlo simulations, reviewed in [54]. Of particular importance are the results of Davidson, Suter and Deen [55], who were some of the first to simulate chains in three-dimensional confinement *and* calculate the associated partition coefficient. Davidson et. al calculated the partition coefficient for freely jointed ideal chains confined to a cylindrical pore using a primitive form of chain insertion. One random walk at a time was generated using Monte Carlo (random point generation) and then the center of mass (COM) was placed at various positions within the cylindrical pore. If the entire chain fell within the pore, then a success was recorded. The fractional success rate as a function of the chain COM position $p(\mathbf{r})$ was calculated by integrating along the radial position $\mathbf{r} = 0$ to R, the pore radius. They defined the partition coefficient K as:

$$K = \int_0^R p(\mathbf{r})\mathbf{r}d\mathbf{r} \Big/ \int_0^R \mathbf{r}d\mathbf{r}$$

This procedure was repeated for different pore-to-chain length ratios for pores with purely steric walls and also pores with a square well potential of width $b \sim$ segment length. Chain configurations existing within the attractive well were Boltzmann weighted to calculate $p(\mathbf{r})$ in order to correctly account for energetic interactions.The partition coefficient as a function of pore size for different chain lengths was fitted to an empirical relationship and compared with earlier scaling and theoretical results from Casassa [51]. The partition coefficient was found to be very sensitive to ε, the potential energy of the well. This effect is most dramatic at large values of the molecule-to-pore size aspect ratio, λ. For example, at λ =1.0 the partition coefficient for a 50-mass-point chain in a pore with $\varepsilon = 0.2$ is 18 times larger than when there is no attractive interaction. Thus, they showed that chemically different polymers of similar size can be separated based on their relative attraction for the porous medium. This principle is exploited experimentally in

separation processes such as interaction liquid polymer chromatography and ion exchange chromatography.

Later, Cifra, Bleha and coworkers[53, 56, 57] as well as Yethiraj & Hall[58] and Wang & coworkers [50] to name the most seminal, investigated the equilibrium partitioning of NRRW and SAW chains in pores with adsorption potentials. Of particular import are the results of Gong & Wang [50], who, building on the work of Cifra and Bleha [57] , proved that the partition coefficient for SAW chains confined to pores cannot become chain length independent, while the partition coefficients for NRRWs can. This discovery was controversial, due to the fact that the critical conditions of polymer adsorption had been observed experimentally for porous materials in the context of polymer chromatography[59-63]. In contrast to SAW and NRRW, the partition behavior of real chains in pores remained an open question, most studies being performed exclusively on SAW lattice chains [64]. Indeed, most of the work done in the past decade on real chains has focused on special cases of polymer adsorption, with large strides being made in the topics of polymer translocation [65] and adsorption of copolymers and branched/brush polymers on surfaces of variable adsorption potential [66-69].

Partial Confinement/Flower Conformations

In all of the work mentioned above, adsorption in pores is limited to the case of *complete confinement*, i.e. all segments of the chain confined to the pore. This approach was justified by experimental observation, that the vast majority of surface area – and therefore the available space for polymer adsorption – was provided by the pores themselves. As such, adsorption in pores and the associated partition coefficient could be treated ignoring the effect of the outer surface of porous materials. It was shown [50] that critical conditions do not exist for excluded volume polymers confined to pores. This finding is in direct conflict with the general experimental observation that critical conditions are found on porous materials. The explanation given for this contradiction was

the following – that the observation of critical conditions in experiments is only an apparent one, the product of the limits of experimental resolution [50].

However, there is an alternate explanation for this contradiction, which requires the relaxation of our assumption of complete confinement. Instead, chains must be allowed to explore not only the pore volume, but also the external surface area of the adsorbent. The addition of adsorption to the external surface greatly increases the overall conformational entropy of adsorbed chains, especially when the aspect ratio λ is ≤ 1. The relationship between the adsorption potential on the external surface and in confinement, as well as the relative importance of each mechanism of adsorption remain open questions. In several landmark works, the groups of Hermsen [70, 71]and Neimark[72, 73] explored the partitioning of chains between pores and the external surface of adsorbents. Hermsen was the first to calculate the free energy of chains as a function of an order parameter – the center of mass position – along the axis of a cylindrical pore perforating a plane surface. Using the bond-fluctuation model (a type of SAW), Hermsen measured the free-energy as a function of this order parameter for chains of finite length, and found that there is a significant barrier to chain insertion within pores, relative to the external surface [70, 71]. In the work of Neimark et. al [72], this free energy barrier was explored for the case of real chains adsorbed partially within in a spherical pore and partially on the external surface in what are called *flower conformations*. In this work (ibid.) it was assumed that the adsorption potential was only present within the pore. They found that there is a critical value of the free energy (as a function of the number of chain segments within the pore) for which the free energy is a minimum. They calculated the *translocation probability* or, likelihood that the entire chain would enter the pore, based upon this free energy as a function of the adsorption potential. In [73], the concept of flower conformations (partial confinement) was extended using the self-consistent field theory of DeGennes [48] to explore the contributions to adsorption and partitioning of chains by three adsorption mechanisms – adsorption on the external surface, complete confinement, and partial

confinement. A combined partition coefficient was developed, which includes contributions from each mechanism. Importantly, it was illustrated that critical conditions (i.e. the chain length independence of the partition coefficient exist for ideal and excluded volume chains adsorbed on the external surface, and that critical conditions do not exist for real chains when confined completely to pores. Furthermore, the relative contribution of adsorption from partial and complete confinement was measured for pores of different sizes, and it was shown that as pore size decreases, the relative importance of partial confinement increases dramatically. In PART II of this dissertation the work of [72, 73] is revisited, and it is shown using a real chain model and Monte Carlo simulations, that the critical conditions of polymer adsorption exist when all three modes of adsorption are taken into account.

1.3 Brief Summary of Tasks and Outcomes

The work of this dissertation is divided into research tasks with the following outcomes.

Task 1: *Development of a comprehensive methodology to distinguish and characterize the topology of porous materials utilizing scanning adsorption/desorption isotherms.*

Outcomes for Task 1: A methodology was developed for the analysis of adsorption isotherms of simple fluids interacting with micro-mesoporous materials. This methodology enables one to distinguish three general mesopore topologies: uncorrelated pores, partially correlated pores, and disordered networks of pores, derived entirely from information provided by scanning adsorption isotherms. In addition, these tools enable one to determine the pore and neck size distributions and the pore network connectivity.

Task 2: *Development of DFT adsorption isotherm kernels for argon and carbon dioxide adsorption on micro-mesoporous carbons.*

Outcomes for Task 2: A set of eight high-resolution adsorption isotherm kernels was developed using quenched solid density functional theory [1, 2] to analyze adsorption isotherms of CO_2 and Ar on micro-mesoporous carbons. These kernels take into account the atomistically rough surface of amorphous carbons and are tailored to specific pore geometries, including slit, cylindrical, and spherical pores. For the first time, hybrid NLDFT and QSDFT CO_2 kernels have been developed which enable the distinction of both micro- and mesopores by using high pressure adsorption. Ar kernels have been and CO2 kernel will be implemented into gas adsorption analysis software developed by Quantachrome Instruments, Boynton Beach, FL.

Task 3: *Development of a Monte Carlo simulation model for the description of adsorption and chromatography of polymers on porous surfaces.*

Outcomes for Task 3: As part of this task, a new criterion for the critical conditions of polymer adsorption on surfaces – the equality of incremental chemical potentials – was demonstrated and was proven using scaling arguments and a simple Monte Carlo model. This methodology was next applied to the case of polymers interacting with nonporous surfaces. It was found for the first time that critical conditions (as well as the size exclusion and interaction chromatography regimes) are observable for experimental liquid polymer chromatography on nonporous substrates. The *overall partition coefficient*, which describes the chain retention, was derived for chains interacting with nonporous surfaces. Later, this model was extended to the case of porous substrates, where three mechanisms of chain adsorption were distinguished: adsorption on the external surface, confinement to pores and partial confinement to pores. Using real-life examples and Monte Carlo simulations, it was shown that the critical conditions of polymer adsorption are identical for porous and nonporous substrates. The results of modeling are in agreement with the experiments performed at DuPont Experimental Station.

CHAPTER 2

Experimental and Theoretical Studies of Scanning Adsorption-Desorption Isotherms

2.1 Introduction

Capillary condensation hysteresis is one of the longest-studied and still enigmatic phenomena in adsorption science [74-77]. It is well documented, both experimentally and theoretically, that during the adsorption-desorption cycle, capillary condensation in mesopores (larger than ~4 nm in diameter) occurs generally at a higher pressure of adsorbing gas then evaporation. As such, adsorption and desorption isotherms form a pronounced hysteresis loop that is repeatable in subsequent cycles. A better understanding of the specifics of hysteretic behavior of adsorption and desorption isotherms is important for practical problems of pore structure characterization. The shape of the hysteresis loop contains information about the pore structure. The adsorption and desorption isotherms provide primary information about porosity, surface area, and pore size distribution, which are calculated from the experimental data using various empirical and theoretical methods [78, 79].

Starting from the seminal work of Zsigmondy [4] published in 1913 and elaborated by Kraemer [80], McBain [6], Cohan [7, 9], Schofield [81], de Boer [82], Dubinin [83] and Everett [74] among other prominent physico-chemists, capillary condensation hysteresis has been studied based on the classical Kelvin-Laplace theory of capillarity using model cylindrical and ink-bottle pores. The main hysteresis mechanisms were recognized: *delayed condensation* due to the formation of metastable adsorption films, *initiation of capillary condensation* upon condensation in neighboring smaller pores, *pore blocking* resulting in the delay of evaporation from the pores blocked by smaller ones, and *cavitation* in metastable condensed fluid at the tensile stress limit.

The theory of capillary hysteresis in individual pores culminated in the independent domain theory (IDT) developed by Everett and coauthors in the 1950s and discussed in detail in his seminal review[74] . This review can be considered as a watershed between what we will call the classical

period of capillary hysteresis theory, which was based on the interfacial thermodynamics and simple geometrical models of pores, and the modern period of investigations related to the applications of methods of statistical physics of random networks and Monte Carlo simulations.

Arising from interplay of geometrical, topological, and thermodynamic factors, the characteristic features of capillary condensation hysteresis are quite distinct for different types of porous materials. Experimentally, these distinct features of adsorption hysteresis are prominently displayed in the behavior of scanning isotherms, which provide additional information about the pore network geometry, including its connectivity and pore size distribution that cannot be revealed from the main adsorption and desorption branches. Scanning isotherms are measured by reversing the direction of the gas pressure variation in the adsorption or desorption process. Scanning behavior has been studied extensively starting from the truly exceptional work of van Bemmelen published in 1897 [3] throughout the mid-20th century, furnishing an abundance of experimental data [74, 84]. Theoretically, it has been well understood since the seminal works of Everett that the description of scanning isotherms cannot be achieved based on the models of adsorption in individual pores [74]; it is necessary to take into account a cooperative nature of capillary condensation and desorption processes in three dimensional pore networks with distributed geometrical parameters of individual pores.

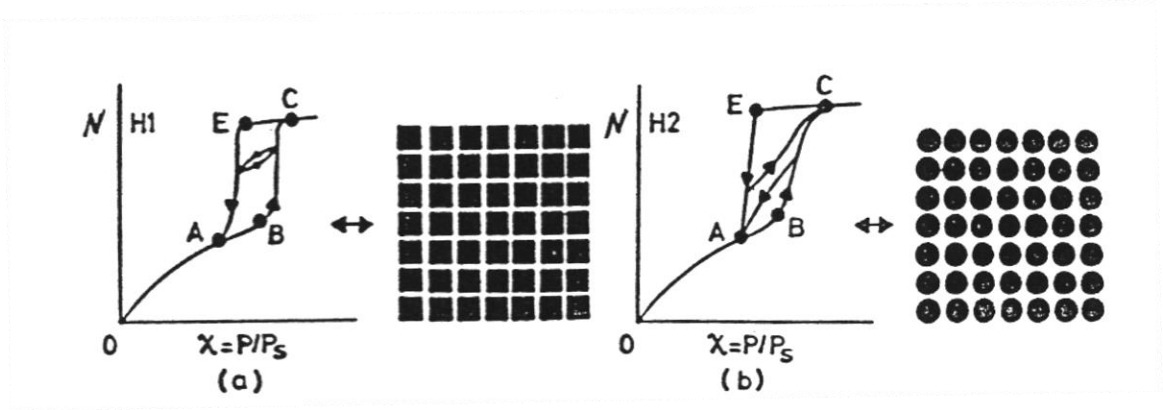

Fig. 2.1. Characteristic types of hysteresis behavior, H1 (left) and H2 (right). A and C are the lower and upper points of closure of the hysteresis loop; B and E correspond to the onsets of capillary condensation and evaporation, respectively. Figure taken from Neimark [85].

Two characteristic types of hysteresis behavior are distinguished in hysteresis loops of type H1 and H2 by IUPAC classification [78] (**Fig. 2.1**). In materials with pore networks formed by channels with unimodal pore size distributions, the scanning isotherms form closed loops crossing the main hysteresis loop of type H1. This behavior is observed in ordered structures like MCM-41, SBA-15, and controlled porous glasses (CPG). In materials consisting of pore channels with alternating enlargements (voids) and constrictions (necks), the scanning isotherms approach the upper and lower points of closure of the main hysteresis loop of type H2. This behavior is observed in disordered structures like Vycor and silica gel. The IUPAC classification reflects ideal structures, yet it is useful for revealing the main mechanisms of capillary phenomena in pore networks.

Application of the percolation theory to capillary condensation hysteresis in pore networks originates from the pioneering works of Wall and Brown [86] Neimark [87, 88] and Neimark and Kheifets [89] and Mason [90, 91]. Wall and Brown[86] performed Monte Carlo simulations to account for the pore blocking effects during desorption. Neimark et al. [87, 89] considered the pore blocking effects during desorption, as well as for initiated capillary condensation during adsorption, in pore networks with an uncorrelated distribution of pore sizes using the bond percolation model in the Bethe approximation. The Bethe network model of pores connected by necks was employed by Mason [90, 91] and Neimark [92] to describe the capillary hysteresis of xenon (Xe) on Vycor glass to improve the independent domain theory model of Everett[74]. Neimark [92] and later Mason [93] and Parlar and Yortsos [94] suggested very similar theories of scanning adsorption and desorption isotherms utilizing the Bethe network model with different coordination numbers. The cavitation mechanism of desorption was incorporated in the percolation model by Parlar and Yortsos [95].

Wilkinson and Willemsen [96] introduced the model of invasion percolation to describe the propagation of the interface between wetting and non-wetting phases into the pore network in the process of wetting. However, the invasion percolation model does not account for the volatility of wetting liquid and is not directly applicable to vapor adsorption. It should be noted that starting

from the initial papers [86, 89]it was understood the percolation model offers a unified description of the desorption of condensed wetting fluid and the intrusion of non-wetting fluid. The percolation theory of scanning mercury intrusion-extrusion cycles was developed by Neimark [97, 98].

Modeling of adsorption and desorption processes in three-dimensional (3D) pore networks was performed in many further works by using various computational algorithms [99-103]. One of the most advanced is the dual pore-site network model suggested Mayagoitia, Rojas, and Kornhauser [104]. This model implies direct simulation of the capillary condensation and desorption processes in 3D networks with randomly distributed pore and neck sizes, which determine the conditions of pore filling and emptying. Within the dual pore-site model, Cordero et al [105] and Rojas et al [106] simulated both scanning adsorption and desorption isotherms for various 3D networks. Although the primary goal of the percolation models was the development of improved methods for pore size analysis [99, 100, 107], there were no successful attempts to incorporate into the characterization methods the information contained in the scanning isotherms.

This Chapter of the dissertation aims to lay the groundwork for developing a practical methodology for calculating the network connectivity and pore size distributions from the scanning isotherms. This aim is especially topical now due to the recent advances in high-precision automated measurements of scanning isotherms [108] and the necessity to characterize the pore structure of novel designer porous materials, the list of which has been increasing exponentially during last two decades [75, 109-111]. In **Section 2.2**, we present a series of scanning isotherms measured on selected samples of SBA-15 silica, KIT-6 silica, and 3DOm carbon materials. SBA-15 example and the literature data on Xe adsorption on Vycor [74] represent case-study systems for evaluation of the limits of applicability of the independent pore models, which are discussed in **Section 2.3**. After analysis of the conventional deterministic and uncorrelated models, we suggest a partial correlation model (PCM) and show that this model provides a quantitative test for networking effects. We show that while the PCM provides a reasonable quantitative description of scanning adsorption isotherms for all systems considered, the deviation between theoretical and

experimental scanning desorption isotherms points toward the importance of accounting for the pore blocking effects in 3D networks of Vycor, KIT-6, and 3DOm structures. The percolation models of scanning hysteresis loops are discussed in **Section 2.4**. Here, we first elaborate on the earlier work of Neimark [92] and formulate the theory of scanning isotherms using the Bethe approximation. Then, we perform direct modeling of scanning desorption isotherms using Monte Carlo simulation on the 3D cubic lattice. We compare the theoretical and experimental results for selected systems. **Section 2.5** is devoted to the formulation of the practical methodology for calculating the *network connectivity* defined as an effective coordination number linked to the percolation threshold and the *neck size distribution* from the main and scanning desorption isotherms. Thus the determined neck size distribution complements the pore size distribution calculated from the main adsorption isotherm. This methodology is verified on Vycor and applied to 3DOm samples. The main conclusions are summarized in **Section 2.6**, where we justify and suggest the proposed methodology for advanced characterization of mesoporous materials.

2.2 Experimental studies.

2.2.1 SBA-15 and KIT-6 silicas

As typical examples of H1 hysteresis behavior, we have chosen SBA-15 and KIT-6 silicas. SBA-15 is a silica material with a hexagonally ordered 2D array (*p6m* symmetry) of cylindrical channels [112]. SBA-15 samples are often used for reference measurements due to their simple pore geometry in order to validate the theoretical models [113] [114]. It is commonly assumed that adsorption and desorption processes occur in the SBA-15 channels independently providing a case-study system for the IDT model (See **Fig. 2.1** in **Appendix A** for DFT pore analysis of SBA-15). The pore network in KIT-6 silica represents 3D gyroidal structure of cubic (*Ia3d*) symmetry [115, 116] exhibiting network effects [117]. Adsorption-desorption isotherms on both samples, **Fig. 2.2**, form a prominent H1 hysteresis loop. Scanning isotherms cross the main hysteresis loop as expected in the schematics of **Fig. 2.1**(left).

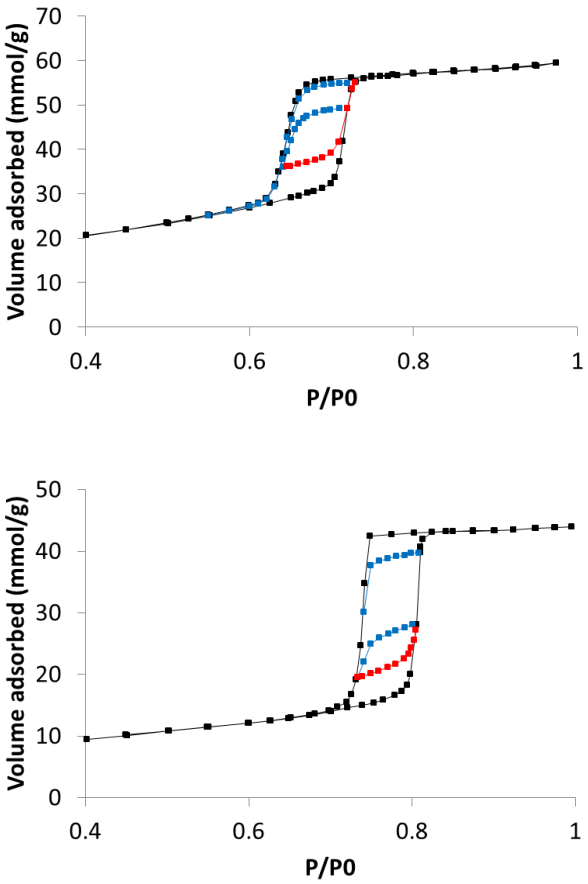

Fig. 2.2. Nitrogen (77 K) primary (black) and scanning adsorption (red) and desorption (blue) isotherms on SBA-15 (left) and KIT-6 (right) samples. Note the closed loop structure, associated with H1 type materials.

2.2.2 3DOm carbon

Recently discovered 3D ordered mesoporous carbons (3DOm) are obtained by hard templating of silica spherical nanoparticle colloidal crystals [118]. The pore network geometry in 3DOm carbons is composed of spherical voids, or cages formed in place of silica nanoparticles, which are connected by narrow windows, or necks. Four samples produced from nanoparticles of different size, 10, 20, 30, and 40 nm, were studied. For the cage-like pore network geometry, one would expect to get an H2 hysteresis loop, as in **Fig. 2.1**(right). However, as shown in **Fig. 2.3**, the adsorption-desorption isotherms presented are of H1 type, and the behavior of scanning isotherms, especially for samples with smaller pores, is similar to that on SBA-15 and KIT-6. As the pore size

progresses up to 40 nm, the hysteretic behavior becomes more complex and reflects the existence of some secondary pore structure. Also, it was shown that the isotherms on the 40 nm sample are affected by a secondary pore structure displayed by a prominent inflexion of the main adsorption branch at P/Po~0.85 (**Fig. 2.3** bottom right). In earlier work [108], 3DOm carbons were analyzed by N_2 and Ar gas adsorption, and it has been suggested that the pore blocking mechanism plays an important role in the desorption process.

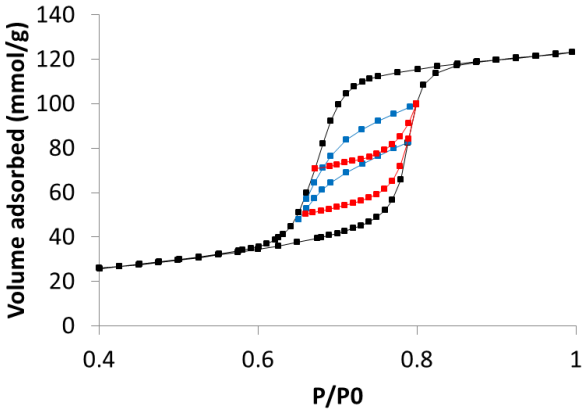

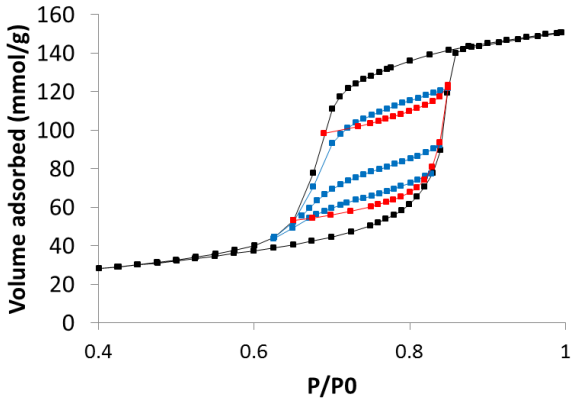

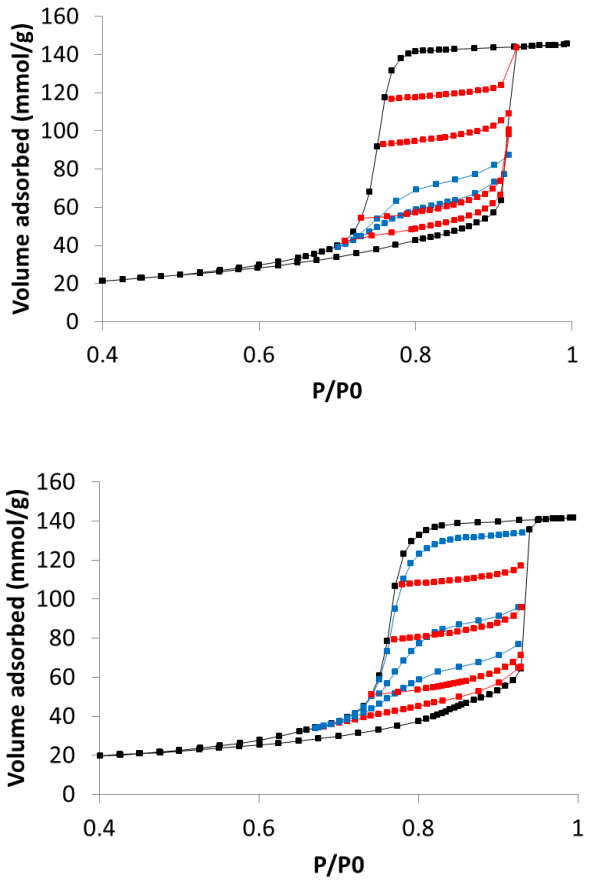

Fig. 2.3 Argon (87 K) primary (black) and scanning adsorption (red) and desorption (blue) isotherms on four 3DOm carbons templated on colloidal crystals of 10 , 20 , 30 and 40 nm silica nanoparticles (top to bottom). Note the following characteristic features: the boundary hysteresis loop for all samples is of type H1; while the scanning isotherms on the10 nm sample are qualitatively similar to those on SBA-15 and KIT-6 (**Fig. 2.2**), as the pore size increases the desorption scanning isotherms tend to bend; the isotherms on the 40 nm sample are affected by a secondary pore structure displayed by a prominent inflexion of the main adsorption branch at P/Po~0.85.

2.2.3. Vycor glass

Vycor glass is siliceous compound, which is formed by the thermal spinodal decomposition of a two-phase alkali-borosilicate – silica solution upon cooling. During the decomposition, the phases separate and the borosilicate is dissolved away, leaving a highly disordered silica matrix that possesses a network of pores with alternating enlargements and constrictions [119]. Detailed simulation of the pore structure formation during spinodal decomposition was performed using

molecular simulations by Gelb and Gubbins [120]. Vycor glass has been playing an extremely important role in the theory of adsorption as a case-study example of disordered pore networks due to availability of high-resolution experimental data and a consensus among the researchers about the specifics of its pore system geometry. The experimental data on xenon (151 K) adsorption and desorption scanning on Vycor collected by Brown in 1963 and presented in the review of Everett [74, 84], served as a benchmark for many theories of capillary condensation, starting from the IDT of Everett to percolation models of Mason [91, 93] Neimark [88, 92], Parlar and Yortsos [94] and Seaton et. al [100] to lattice DFT models of Monson, Kierlik, and Rosinberg [121] , among the others. This data re-plotted in **Fig. 2.4** represents a typical H2 hysteresis behavior in compliance with the schematic of **Fig. 2.1**(right). The main hysteresis loop has a prominent triangular shape. The scanning isotherms converge at the closure points of the hysteresis loop rather that crossing the loop as in the case of H1 hysteresis.

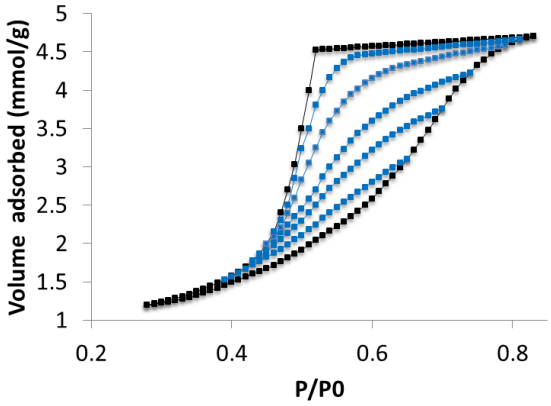

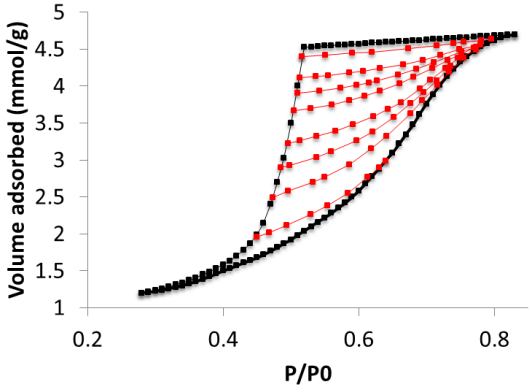

Fig. 2.4. Xenon (151 K) adsorption (left) and desorption (right) scanning isotherms on Vycor glass. Note typical H2 type hysteresis behavior; the scanning isotherms converge at the closure points of the hysteresis loop. Data reprinted and units converted from Everett [74].

The hysteresis behavior shown in **Fig. 2.4** for xenon adsorption is typical for other adsorbates on Vycor. In **Fig. 2.5**, experimental data for N_2 (77 K) adsorption is presented that have the same features.

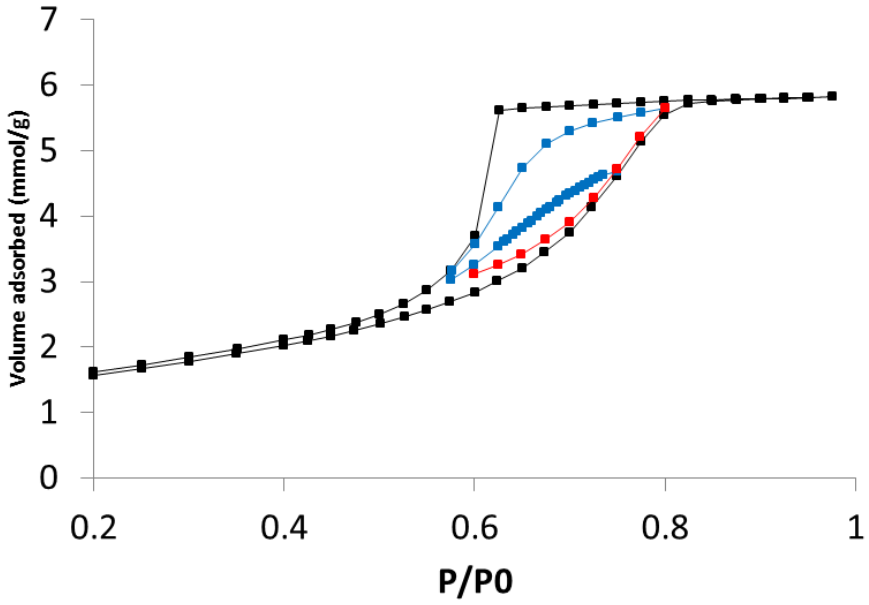

Fig. 2.5. N_2 (77 K) primary (black) and scanning adsorption (blue) and desorption (red) isotherms on Vycor glass. Note the typical scanning behavior for H2 type hysteresis similar to that of xenon shown in **Fig. 2.4**.

2.3. Models of independent pores

The IDT model of adsorption proposed by Everett [74, 122, 123] is based on an assumption that the pore space may be subdivided into individual regions or 'domains', which are non-interacting and adsorb and desorb independently of one another. This assumption of pore independence is explicitly or implicitly used in all conventional methods of pore structure characterization from BJH to DFT methods, which ignore the cooperative mechanisms of capillary condensation and desorption due to pore networking effects. At the same time, DFT based independent pore models can correctly determine the underlying mechanism of condensation, i.e.

the existence of metastable pore fluid associated with condensation, and when applicable, provide the most straightforward methods for practical applications.

Following Everett [74], each pore treated as an independent domain is characterized by two parameters, the relative pressures of condensation χ_+ and desorption χ_-. These pressures depend on the pore size and shape. Standard methods of calculating pore size distributions often assume that pores are cylindrical and the pore diameter d_p determines the pressures of condensation and desorption, $\chi_+(d_p)$ and $\chi_-(d_p)$. As such, there exists a one-to-one correspondence between adsorption and desorption pressures for a particular pore: for every relative pressure point $\chi_a = \chi_+(d_p)$ along the adsorption boundary curve there exists a companion point on the desorption boundary curve, $\chi_d = \chi_-(d_p)$. We will call a model, which is based on this assumption, a *deterministic model*. The alternative approach within the independent pore models, which also dates back to Everett [74] and was accepted in earlier works on percolation models [85, 86, 90-93, 107], is to assume that the pressures of condensation χ_+ and desorption χ_- in a given pore are not correlated: the former is determined by the pore size d_p as $\chi_+(d_p)$ and the latter is determined by the neck size d_n as $\chi_-(d_n)$. In case of multiple necks, d_n represents the size of the largest neck. This assumption is equivalent to the assumption of the absence of correlation between the pore and neck sizes, and is called an *uncorrelated model*.

Below, we propose a *partial correlation model* within the independent domain theory, as a compromise between the deterministic and uncorrelated models, and suggest a method for assessing the significance of networking effects. However, first, we have to introduce a method how to convert the experimentally measured adsorption isotherms, which represent the adsorbed amount measured in experiments, into the fractions of filled and unfilled pores, which are required for modeling the adsorption process in a network of pores.

2.3.1 Reference isotherms and fractions of filled and unfilled pores.

In the process of gas adsorption, an individual pore may exist in two states, *unfilled*, when the pore walls are covered by adsorption films and the pore center is occupied by vapor-like adsorbate, and *filled*, when the whole pore volume is occupied by liquid-like, condensed adsorbate. The transitions between these states are associated with the capillary condensation and capillary evaporation (desorption) transitions. Consequently, one calls the adsorbate state in unfilled pores *vapor-like* and the adsorbate state in filled pores *liquid-like*. In order to relate the processes of pore filling and emptying to measured adsorption and desorption isotherms, it is necessary to separate the adsorption in unfilled and filled pores. To this end, we introduce the reference isotherms in unfilled and filled pores, $V_s(\chi)$ and $V_c(\chi)$. The former represents an interpolation of the reversible adsorption isotherm to the hysteresis region and reflects the build-up of the adsorption film. The film isotherm $V_s(\chi)$ is modeled as

$$V_s(\chi) = S \cdot h(\chi) \tag{2.1}$$

where S is the surface area of the adsorbent and $h(\chi)$ is the effective thickness of the adsorbed layer that is proportional the reference adsorption isotherm on a non-porous surface of the same origin. Eq. 2.1 is a standard approximation that does not take into account the pore wall curvature. The film reference isotherm is commonly modeled with the Frenkel-Halsey-Hill (FHH) equation with specific adsorbent-adsorbate parameters K and m:

$$h(\chi) = \left(\frac{K}{-\ln \chi}\right)^{\frac{1}{m}} \tag{2.2}$$

Parameters K and m are chosen such that the effective thickness is in Ångstroms. Below, we employ the recommended parameters used for validation of the NLDFT models [124]: for nitrogen-silica adsorption, $K = 44.54$ and $m = 2.241$; for argon-silica adsorption, $K = 73.17$ and $m = 2.665$. The specific surface area, S, can be determined in several ways. In the examples considered below, S was found by aligning the boundary adsorption isotherm with the reference isotherm, using S as a fitting parameter. The BET surface area may serve as a starting point for

such fitting. We found that in general, the BET and fitted surface areas differed by 15 % or less for all sample materials. (See **Appendix A** for details)

The reference desorption isotherm $V_c(\chi)$ reflects compressibility of condensed fluid in filled pores and related effects. $V_c(\chi)$ should be determined by extrapolation of the reversible part (upper plateau) of the desorption isotherm starting from the upper closure point *C* of the main hysteresis loop. In the first approximation, it can be modeled by a tangent to the desorption isotherm at the capillary condensation pressure, χ_c, as

$$V_c(\chi) = \left(\frac{dV}{d\chi}\right)|_{\chi_c}(\chi - \chi_c) + V(\chi_c) \tag{2.3}$$

Using the reference isotherms $V_s(\chi)$ and $V_c(\chi)$, the experimental isotherm $V(\chi)$ may be presented through the fraction of unfilled pores at the relative pressure χ, $Q(\chi)$, as

$$V(\chi) = V_s(\chi) \cdot Q(\chi) + (1 - Q(\chi)) \cdot V_c(\chi) \tag{2.4}$$

From this equation, the fraction of unfilled pores $Q(\chi)$ is estimated in the region of hysteresis as

$$Q(\chi) = \frac{V_c(\chi) - V(\chi)}{V_c(\chi) - V_s(\chi)} \tag{2.5}$$

Beyond the hysteresis region, $Q(\chi) = 0,\ \chi < \chi_A\ ;\ 1,\ \chi > \chi_C$

The fractions of unfilled pores on the main adsorption or desorption isotherms are determined from Eq. 2.5, as

$$Q_+(\chi) = \frac{V_c(\chi) - V_+(\chi)}{V_c(\chi) - V_s(\chi)} \qquad Q_-(\chi) = \frac{V_c(\chi) - V_-(\chi)}{V_c(\chi) - V_s(\chi)} \tag{2.6}$$

The transition from the hysteresis loop formed by the experimental adsorption-desorption isotherms to the hysteresis loop formed by the fractions of unfilled pores is illustrated in **Fig. 2.6** with the example of the SBA-15 isotherm given in **Fig. 2.2**(left). The positions of points A, B, C, and E were determined by expert choice with accuracy of ~2% with respect to the deviations between the corresponding isotherms. (See **Appendix A** for details.)

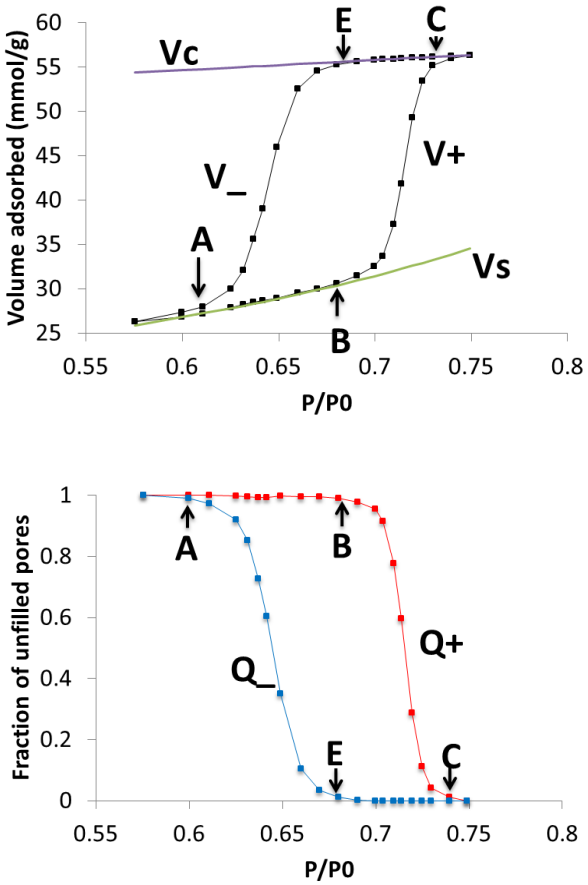

Fig. 2.6. Top - Main hysteresis loop for the nitrogen adsorption-desorption cycle on SBA-15. Bottom – The main hysteresis loop recalculated via Eq.6 in terms of the fractions of unfilled pores along the adsorption and desorption isotherms, Q_+ and Q_-.

Eq. 2.4 is applicable for any isotherm. For the scanning adsorption $V_+(\chi, \chi_d)$ and desorption isotherms $V_-(\chi, \chi_a)$ it reads:

$$V_+(\chi, \chi_d) = V_s(\chi) \cdot Q_+(\chi, \chi_d) + (1 - Q_+(\chi, \chi_d)) \cdot V_c(\chi) \tag{2.7}$$

$$V_-(\chi, \chi_a) = V_s(\chi) \cdot Q_-(\chi, \chi_a) + (1 - Q_-(\chi, \chi_a)) \cdot V_c(\chi) \tag{2.8}$$

Here and below, we use the denotations $(\chi, \chi_{a/d})$ to define the scanning isotherms that originate from points $\chi_{a/d}$ on main adsorption or desorption isotherms.

The uncorrelated model implies that the fraction of unfilled pores during scanning adsorption, $Q_+(\chi, \chi_d)$, decreases from its initial value $Q_-(\chi_d)$, as

$$Q_+(\chi, \chi_d) = Q_-(\chi_d) \cdot (1 - Q_+(\chi)) \tag{2.9}$$

This equation states that the probability of a pore that was unfilled at $\chi = \chi_d$ to be filled at the current relative pressure χ is equal to the fraction of filled pores, $1 - Q_+(\chi)$, on the main adsorption isotherm at χ. Similarly, the fraction of unfilled pores during scanning desorption, $Q_-(\chi, \chi_a)$, increases from its initial value $Q_+(\chi_a)$ as the pressure decreases, as

$$Q_-(\chi, \chi_a) = Q_+(\chi_a) + (1 - Q_+(\chi_a))Q_-(\chi) \quad (2.10)$$

This equation states that the probability of a pore that was filled at $\chi = \chi_a$ to be unfilled at the current relative pressure χ is equal to the fraction of unfilled pores, $Q_-(\chi)$ on the main desorption isotherm at χ. The scanning isotherms are determined by Eq. 2.8 with the fractions of unfilled pores calculated with Eq. 2.9 and 2.10. The theoretical scanning isotherms in the uncorrelated model implies that the scanning isotherms approach the closure points of the main hysteresis loop, as for the H2 type hysteresis in **Fig. 2.1** (right). It was shown [88, 92] that the *uncorrelated model* describes with Eqs. 7, 8 and 9 almost quantitatively the scanning adsorption isotherms on Vycor glass, but it fails to predict the shape of scanning desorption isotherms shown in **Fig. 2.4**. This inconsistency was interpreted by the importance of pore blocking percolation effects, which make desorption a cooperative process in a sense that the evaporation events in different pores occur in a correlated manner.

2.3.2. Partial correlation model

The uncorrelated model implies that the scanning isotherms converge at the points of closure of the main hysteresis loop. In order to extend the independent pore model to more general situations, when the scanning adsorption-desorption isotherms form closed loops intersecting the main hysteresis loop, we introduce a partial correlation model (PCM). The PCM is based on experimental observation that in the absence of networking effects the shape of the scanning isotherm resembles the shape of the main isotherm. As such, the PCM implies that the fraction of unfilled pores $Q_-(\chi, \chi_a)$ along the scanning desorption isotherm is a linear function of the fraction of unfilled

pores $Q_{-}(\chi)$ along the main desorption isotherm. For scanning desorption starting at $\chi = \chi_a$ and approaching the boundary desorption branch at $\chi = \chi_d$,

$$Q_{-}(\chi, \chi_a) = Q_{+}(\chi_a) + \big(Q_{-}(\chi_d) - Q_{+}(\chi_a)\big)\big(Q_{-}(\chi)/Q_{-}(\chi_d)\big) \tag{2.11}$$

Similarly, the fraction of unfilled pores $Q_{+}(\chi, \chi_d)$ along the scanning adsorption isotherm is assumed to be a linear function of the fraction of unfilled pores $Q_{+}(\chi)$ along the main adsorption isotherm. For scanning adsorption starting at $\chi = \chi_d$ and approaching the boundary adsorption branch at $\chi = \chi_a$,

$$Q_{+}(\chi, \chi_d) = Q_{-}(\chi_d) - \big(Q_{-}(\chi_d) - Q_{+}(\chi_a)\big)\Big(\big(1 - Q_{+}(\chi)\big)/\big(1 - Q_{+}(\chi_a)\big)\Big) \tag{2.12}$$

Note that Eq. (2.11) is reduced to Eq. 2.9 of the uncorrelated model at $\chi_d \to \chi_A$ and, respectively, Eq. (2.12) is reduced to Eq. 2.10 of the uncorrelated model at $\chi_a \to \chi_C$.

As shown in **Fig. 2.7**, the PCM, Eqs. (11) and (12), is in reasonable agreement with experimental scanning isotherms, both adsorption and desorption, on SBA-15 and KIT-6 samples with the characteristic H1 hysteresis loops. In the case of H2 hysteresis, the PCM predictions agree with the scanning adsorption data and strongly deviate from the scanning desorption, **Fig. 2.10**. Deviations from the predictions of the independent pore model point towards the importance of the networking effects, which are more pronounced during desorption due to the pore blocking effect. In this way, the PCM serves as a test of the pore blocking effects, which in particular are pronounced in disordered pore networks like that of Vycor glass during desorption.

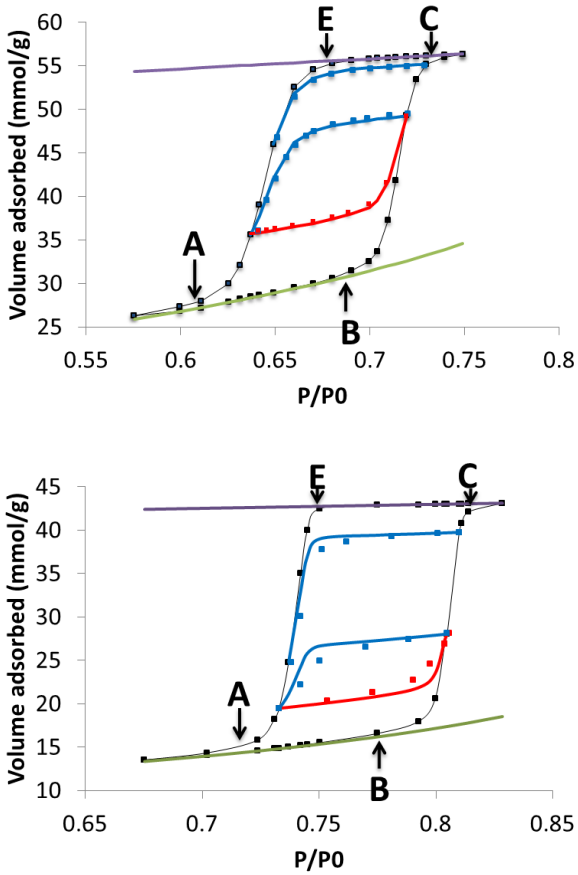

Fig. 2.7: Comparison of PCM with experiments for N_2 adsorption on SBA-15 (top) and KIT-6 (bottom).

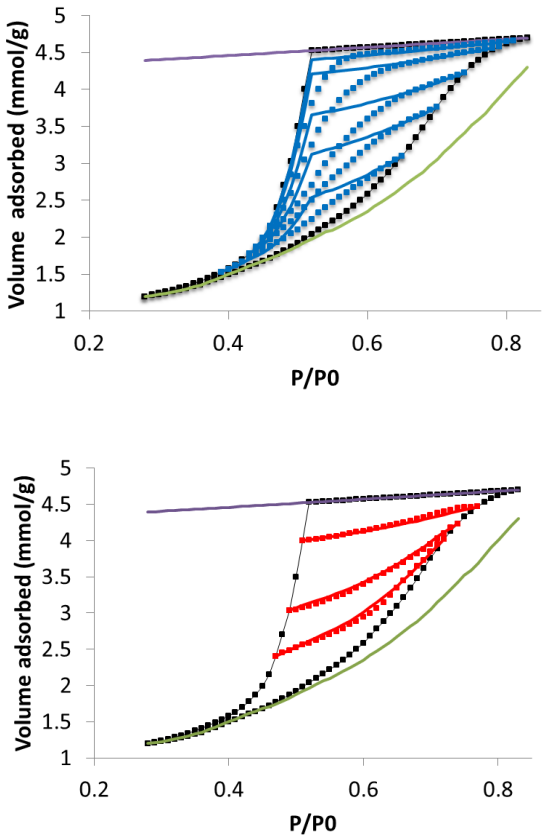

Fig. 2.8: Comparison of the PCM with experiments for Xe adsorption on Vycor glass; scanning desorption (top), scanning adsorption (bottom). Experimental data taken from Everett [74].

The PCM has the following interpretation in the ink-bottle pore model: within the assumption of independent pores, the pressure of condensation χ_+ in a given pore is determined by the size d_p of the pore and the pressure of desorption χ_- is determined by the size d_n of the largest neck. Let us suppose that larger pores have a higher probability to have larger necks, particularly, that the pores larger than d_p have at least one neck larger than $d_n = g(d_p)$, where g is a certain monotonic function. In this case, the scanning desorption isotherm, $V_-(\chi, \chi_a)$, that originates at $\chi = \chi_a = \chi_+(d_p)$ must merge with the main desorption isotherm at $\chi = \chi_d = \chi_-(d_n)$. The fraction $Q_+\left(\chi_a(d_p)\right)$ of unfilled pores in the beginning of scanning desorption at $\chi_a = \chi_+(d_p)$ represents the fraction of pores larger than d_p and these pores have necks larger than d_n. Along the main desorption isotherm at $\chi = \chi_d = \chi_-(d_n)$, the fraction of unfilled pores

$Q_{-}(\chi_d(d_n))$ includes the fraction of pores larger than d_p, $Q_{+}\left(\chi_a(d_p)\right)$, plus the fraction of pores that are smaller than d_p but have necks larger than d_n. The fraction of this latter group of pores equals $Q_{-}(\chi_d) - Q_{+}(\chi_a)$. These are the pores from which the condensed adsorbate evaporates along the scanning desorption path $V_{-}(\chi, \chi_a)$ initiated at $\chi_a = \chi_{+}(d_p)$, so that the scanning and the main desorption isotherms should meet at $\chi = \chi_d = \chi_{-}(d_n)$, and $V_{-}(\chi, \chi_a)|_{\chi = \chi_d = \chi_{-}(d_n)} = V_{-}(\chi)|_{\chi = \chi_d = \chi_{-}(d_n)}$. Respectively, the scanning adsorption isotherm that originates at $\chi_d = \chi_{-}(d_n)$ should merge with the boundary adsorption isotherm at $\chi_a = \chi_{+}(d_p)$, forming a closed scanning hysteresis loop.

2.4. Percolation models

The networking effects are most prominently displayed during the desorption process, which occurs in a cooperative fashion as the condition of evaporation from a given pore depends on the neighboring pores. When the pore is not blocked and condensed fluid has an interface with the vapor phase, evaporation occurs at the equilibrium relative pressure χ_e which is determined by the pore size. If the pore is blocked by narrower pores, the condensed fluid cannot evaporate at $\chi = \chi_e$and becomes metastable at $\chi < \chi_e$. These pores we call metastable at given χ. Evaporation may occur only when the pore is connected to the vapor phase by a series of metastable pores. Only when this condition is met, the vapor-liquid interface, or meniscus, may percolate through the network and initiate evaporation of the metastable fluid at a relative pressure that is smaller than the equilibrium one. This mechanism is called in the literature the pore-blocking or percolation mechanism.

When the size of blocking pores is so small that the condensed fluid approaches the limit of metastability and evaporates spontaneously even so the neighboring pores are still filled, one deals with the cavitation mechanism. Cavitation, as was recently shown [125, 126], takes place in the range of relative pressures 0.50-0.42 for nitrogen adsorption at 77.4K and is characterized by the abrupt step on the desorption isotherm. In the following percolation model, we do not consider

the cavitation mechanism, since it is not relevant for the systems considered in this work. It is worth noting that the cavitation mechanism was introduced in the percolation model of Parlar and Yortsos [95].

2.4.1. Desorption from a pore network as a percolation process.

The following discussion is based the ideas put forward in earlier works of Neimark [88, 92]. Let us consider the desorption process in a network comprised of pores connected by narrower necks, **Fig. 2.1** (right). In this model, the pores represent the network sites and the necks represent the network bonds. We assume that desorption is controlled by the size of necks, and the condensed fluid is "ready" to evaporate from any pore at given relative pressure χ provided that the condition of the vapor-liquid interface formation is met. This condition along the scanning desorption isotherm $V_{-}(\chi, \chi_a)$ is met in two cases schematically illustrated in **Fig. 2.9**. The pore must be connected by a continuous chain of metastable necks either with the external surface of the sample, or with an initially unfilled pore, in which the interface existed in the beginning of desorption at $\chi = \chi_a$. In other words, in order to trigger desorption, the meniscus must percolate to the pore either from the external surface, or from an initially unfilled pore.

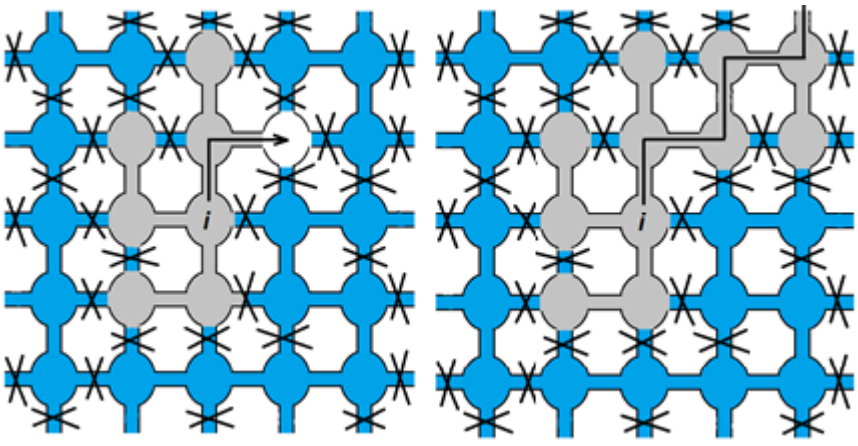

Fig. 2.9. Two pathways for evaporation: pore *i* is connected with the external surface by metastable necks (left) and pore *i* is connected with an initially unfilled pore (colored white) by metastable necks. Stable necks are crossed, filled pores are blue, unfilled pores are gray.

To account for this condition, we introduce a probability factor $\alpha(q(\chi), Q_+(\chi_a))$ which depends upon the fraction of metastable necks $q(\chi)$ and the fraction of unfilled pores in the beginning of scanning, $Q_+(\chi_a)$. This factor has the interpretation of a probability of finding a path of metastable necks by which a randomly chosen pore is connected to the vapor-liquid interface. As such, the fraction of unfilled pores along the scanning isotherm is the sum of the fraction of initially unfilled pores and the fraction of initially filled pores multiplied by the probability of the existence of a metastable pathway:

$$Q_-(\chi, \chi_a) = Q_+(\chi_a) + \left(1 - Q_+(\chi_a)\right) \cdot \alpha(q(\chi), Q_+(\chi_a)) \tag{2.13}$$

For the main desorption branch ($Q_+ = 0$), meniscus percolation originates from the external surface only, and the probability of desorption $\alpha(q, 0)$ reduces to the percolation probability $Q_p(q)$ in the classical bond percolation problem[88], $\alpha(q, 0) = Q_p(q)$, and

$$Q_-(\chi) = Q_p(q(\chi)) \,. \tag{2.14}$$

The percolation probability for a macroscopically large network is a step-wise function. Below the percolation threshold q_c, $Q_p(q) = 0$ at $q < q_c$. This means that until the fraction of metastable pores is below the percolation threshold, evaporation may occur only from the pores located near the external surface of the porous body, since the probability that the pore in the bulk of the body is connected with the external surface by a chain of metastable necks is zero. The percolation probability rapidly increases above the percolation threshold, as $Q_p(q) \propto (q - q_c)^\beta$. For 3D networks, $\beta \approx 0.46$ [127]. As such, in the framework of the percolation theory, the onset of desorption from a fully saturated network indicated as point E in **Figs. 2.1-10** corresponds to the percolation threshold,

$$q(\chi_E) = q_c. \tag{2.15}$$

The process of evaporation of condensed fluid along the scanning desorption isotherm begins at $\chi > \chi_E$ provided that $q(\chi) > 0$. The probability factor $\alpha(q, Q_+)$ monotonically increases with q at given $Q_+ > 0$. A general analytical expression for $\alpha(q, Q_+)$ for three-dimensional

networks does not exist. It depends on the pore connectivity, or the network coordination number z, and also on the network topology. Below, we use two approaches to determine $\alpha(q, Q_+)$.

2.4.1.1 Bethe approximation

The Bethe approximation was employed in early works on percolation models of capillary phenomena [87-91] and it was shown to provide a qualitatively correct description of the percolation process. The Bethe approximation neglects the topological correlations of the distribution of network elements caused by the existence of cycles in real networks that makes possible the ability to obtain an analytical solution. The percolation probability $Q_p(q)$ in the Bethe network with the coordination number z is defined from the following system of algebraic equations,

$$Q_p(q) = 1 - y^z\,, \quad y = (1-q) + qy^{z-1} \tag{2.16}$$

where y is the probability that the desired path through the metastable necks does not exist provided that the first step is taken towards one of z neighboring sites . The percolation probability $Q_p(q)$ vanishes below the percolation threshold

$$q_c = 1/(z-1)\,. \tag{2.17}$$

The problem of desorption from a partially saturated pore network is a bond-site percolation problem [92] since the probability α of desorption from an initially filled site depends on both the fraction q of the metastable bonds and the fraction Q_+ of the initially unfilled sites. The probability factor $\alpha(q, Q_+)$ fulfills the system of algebraic equations, similar to (2.16),

$$\alpha(q, Q_+) = 1 - y^z \quad , \quad y = (1-q) + q(1-Q_+)\cdot y^{z-1} \tag{2.18}$$

Eq. (2.18) considers that the probability y is equal to the sum of probabilities of the following events: 1) the chosen neck is stable (probability 1-q) and 2) the chosen neck is metastable (probability q) and leads to an initially filled site (probability $1 - Q_+$) but all z-1 paths from this

site fail to connect it with an initially unfilled site (probability y^{z-1}). The function $\alpha(q, Q_+)$ for the Bethe network with the coordination number z=6 is presented in **Fig. 2.12** together with the respective fraction $Q_-(q, Q_+)$ of unfilled pores along the primary and scanning desorption isotherms determined by Eq. 2.13 .

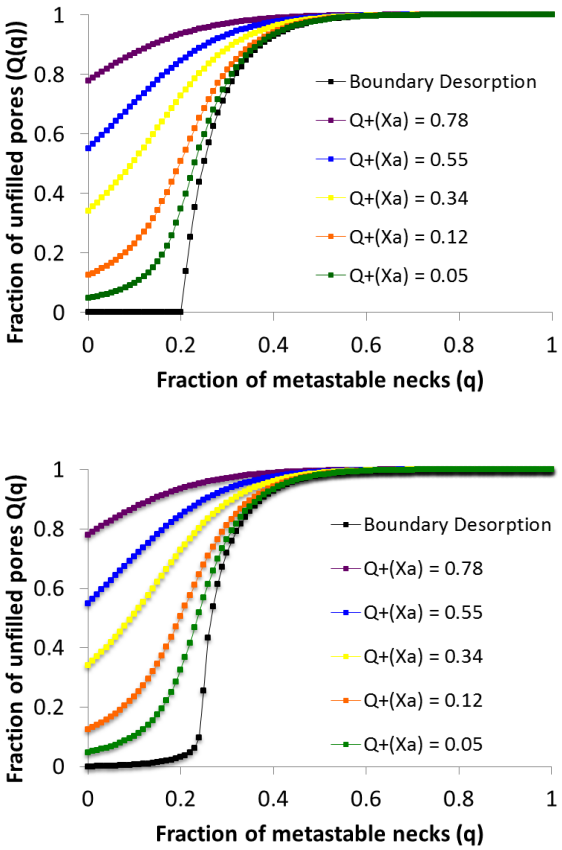

Fig. 2.10. The fraction $Q_-(q, Q_+)$ of unfilled pores (right) along the main ($Q_+ = 0$) and scanning desorption isotherms; values of $Q_+ = 0.05, 0.12, 0.34, 0.55, 0.78$ correspond to the desorption isotherms of Xe on Vycor glass shown in **Fig.2.4** (top). Coordination number z=6. Bethe approximation (top), percolation threshold $q_c = 0.2$. MC simulation on the cubic lattice of 200x200x200 sites (bottom) percolation threshold $q_c \approx 0.25$. The rounding of the percolation probability at the threshold is caused by the boundary effects.

2.4.1.2. 3D lattice simulation

The bond-site percolation process can be directly simulated on a 3D network to determine the fraction of unfilled pores $Q_-(q, Q_+)$ along primary and scanning desorption curves as a

function of the fractions of metastable necks q and of initially unfilled pores Q_+. The implemented algorithm draws heavily from the one Newman and Ziff [128] suggested for modeling classical bond or site percolation problems. We considered a 3D cubic lattice of *L*x*L*x*L* sites with the outer bonds connected to vapor phase, mimicking the external surface of the porous body. The details of the algorithm can be found in **Appendix A**. The calculations were performed for the lattice size L=200. This size was chosen as a compromise between the speed of calculations and the inaccuracy caused by the boundary effects. As shown in **Appendix A**, the results with L=200 and L=275 are barely distinguishable, **Fig. A.2**. The simulation results are shown in **Fig. 2.10** (bottom). The rounding of the percolation probability ($Q_+ = 0$) at the threshold, $q_c \approx 0.25$, is caused by the boundary effects. It is worth noting that the simulation data for the percolation threshold q_c of 3D networks decreases with the coordination number z in accord with the following approximate relationship,

$$q_c \approx 1.5/z \tag{2.19}$$

Although the percolation threshold predicted by the Bethe approximation, Eq. 2.17, is smaller than that for the real 3D network with same coordination number, the qualitative behavior of the calculated dependencies is quite similar except for the vicinity of the percolation threshold.

2.5. Use of scanning isotherms for pore structure characterization

Scanning isotherms contain additional information about the specifics of pore structure compared with the primary adsorption and desorption isotherms. As suggested above, the PCM may be used to distinguish the materials for which networking effects are present and, as in the example with Vycor glass (**Fig. 2.8**), to call for the application of percolation models.

2.5.1. Network connectivity

The network connectivity is characterized by its coordination number *z*, which determines the percolation threshold q_c according to the Eqs. 2.17 or 2.19, depending on the type of the

network model. The percolation concept implies that the onset of desorption along the primary desorption isotherm (point E) corresponds to the percolation threshold, however the value of the percolation threshold cannot be determined without additional information. We suggest to determine the coordination number using the scanning desorption isotherm. Indeed, the network connectivity can be estimated from equality of the theoretical fraction of unfilled pores at $\chi = \chi_E$ along the scanning isotherm,

$$Q_{-}(\chi_E, \chi_a) = Q_{+}(\chi_a) + \left(1 - Q_{+}(\chi_a)\right) \cdot \alpha\left(q_c, Q_{+}(\chi_a)\right) \tag{2.20}$$

The fractions of unfilled pores $Q_{+}(\chi_a)$ and $Q_{-}(\chi_E, \chi_a)$ are defined from Eq. 2.9 and 2.10, as

$$Q_{+}(\chi_a) = \frac{V_c(\chi_a) - V_{+}(\chi_a)}{V_c(\chi_a) - V_s(\chi_a)} \quad \text{and} \quad Q_{-}(\chi_E, \chi_a) = \frac{V_c(\chi_E) - V_{-}(\chi_E|\chi_a)}{V_c(\chi_E) - V_s(\chi_E)} \tag{21}$$

Solution of the algebraic equation (20) with respect to q_c for given scanning desorption isotherm $V_{-}(\chi|\chi_a)$ is straightforward in the Bethe approximation, when the function $\alpha(q_c, Q_{+})$is defined by Eqs. 2.17 and 2.18.

Sample	Vycor	Vycor	3DOm, 10 nm	3DOm, 20 nm	3DOm, 30 nm	3DOm, 40 nm
z	6.6	7.2	6.6	6.6	5.2	5.2
q_c	0.18	0.16	0.18	0.18	0.24	0.24
$Q_{+}(\chi_A)$	0.34	0.12	0.24	0.27	0.68	0.09

Table 2.1. Coordination number z and percolation threshold q_c determined in the Bethe model from scanning isotherms. The fraction of unfilled pores $Q_{+}(\chi_a)$ at the onset of scanning at $\chi = \chi_a$ is shown in the 3rd column. For Vycor glass, two scanning isotherms were used to show the difference between the results obtained with different scanning isotherms.

Using the Bethe model, we calculated the percolation threshold and the coordination number for the samples of Vycor glass and 3DOm carbons from the scanning isotherms given in **Figs. 2.3** and **2.4**. This data are presented in **Table 2.1**.

For Vycor glass, we used two scanning isotherms originating from χ_a= 0.34 and 0.12 to determine the connectivity that produced comparable results. For 3DOm carbons, the scanning isotherm with the largest $Q_{+}(\chi_a)$ was used for each sample. Due to the imprecise definition of the

percolation threshold (no sharp knee is present) for these materials, the point E positions were determined by "squaring up" the edges of the primary desorption isotherms. The obtained values of coordination numbers for all the samples are around $z = 6$, which points towards the possibility to employ a simple cubic network as a reasonable 3D model of the pore networks in these samples.

The predictions of the scanning desorption isotherms using the probability factors $\alpha(q, Q_+)$ determined with the chosen value of the coordination number z =6.6 for Vycor glass are presented in **Fig. 2.11**. In stark contrast to **Fig. 2.8**, the theoretical desorption scanning isotherms agree well with the experimental data with exception of the lowest scanning isotherm, confirming the consistency of the proposed percolation model.

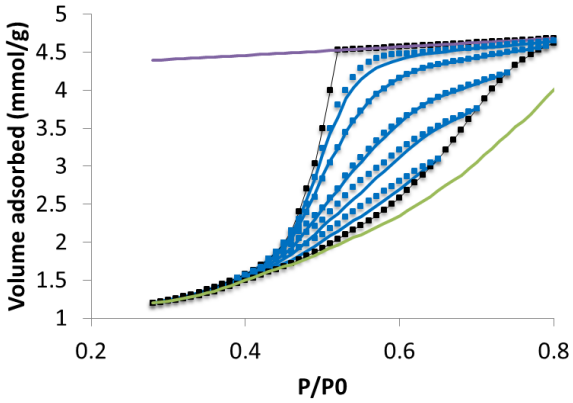

Fig. 2.11. Experimental and predicted scanning isotherms for Xe adsorption on Vycor glass, using the Bethe approximation and fitted the coordination number z=6.6. Experimental data from Everett [74]

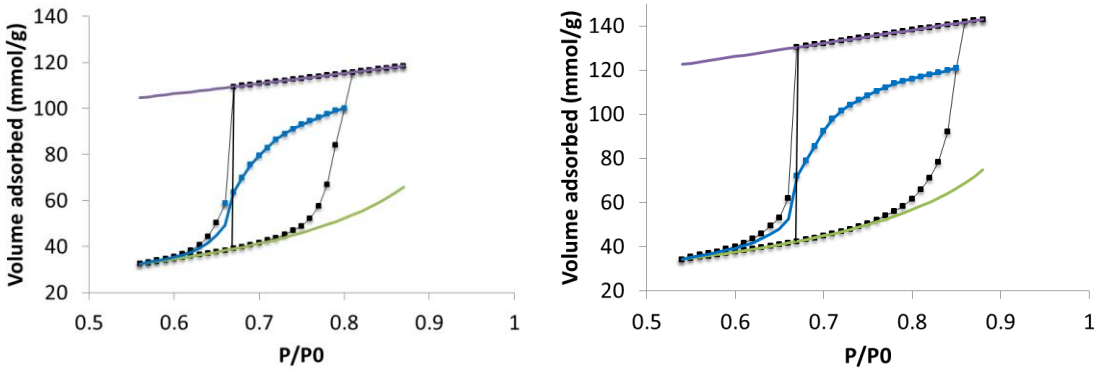

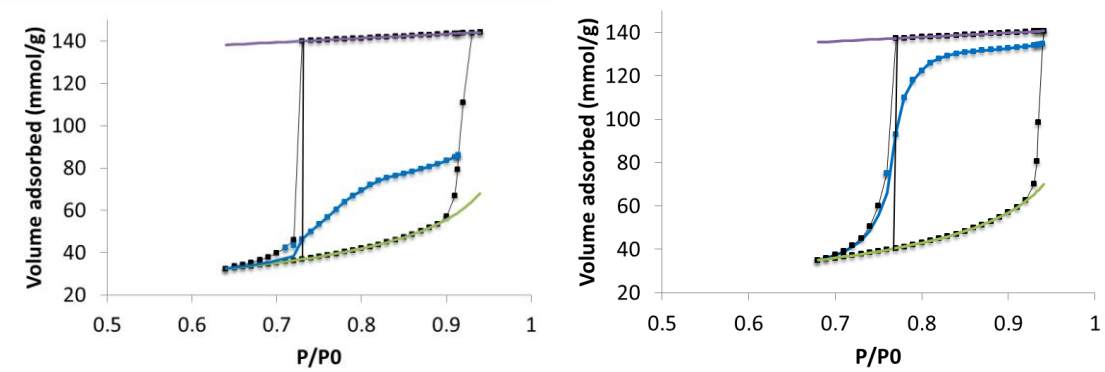

Fig. 2.12. The main adsorption and desorption isotherms and the scanning isotherm used for determining the network connectivity and neck size distribution calculations of 3DOm carbons. Vertical lines are drawn at at $\chi = \chi_E$; intersection with the scanning isotherm represents the point at which Eq. 20 is solved to determine the coordination number. Coordination numbers determined in the Bethe approximation are listed in **Table 2.1**. Upper raw: 10 nm, 20 nm, Bottom raw: 30 nm, 40 nm.

The main adsorption and desorption isotherms together with the scanning isotherm that was used for calculations of connectivity of 3ODm carbons are shown in **Fig. 2.12**. The scanning isotherm calculated with the determined coordination number z determined from the experimental value at $\chi = \chi_E$ agrees with the experimental data points in the range: $\chi_E \leq \chi < \chi_C$.

2.5.2. Pore neck size distribution

Once the coordination number of the pore network is determined, one can determine the dependence of the fraction of metastable necks on the relative pressure, $q(\chi)$, as follows. The fraction of metastable necks at $\chi = \chi_E$ equals the percolation threshold, $q(\chi_E) = q_c$. Above the threshold, for $\chi_A < \chi < \chi_E$, the fraction of metastable necks $q(\chi)$ is determined by the primary desorption isotherm via the percolation probability function $Q_p(q)$ by solving Eq. 2.16. with respect to q,

$$q(\chi) = Q_p^{-1}\left(\frac{V_c(\chi) - V_-(\chi)}{V_c(\chi) - V_s(\chi)}\right) \text{ at } \chi_A < \chi < \chi_E \tag{2.22}$$

where Q_p^{-1} is the inverse function to $Q_p(q)$, which depends on the coordination number. Below the threshold, for $\chi_E \leq \chi < \chi_C$, the fraction of metastable necks $q(\chi)$ is determined from

the scanning desorption isotherm via the probability factor $\alpha(q, Q_+(\chi_a))$ by solving Eq. 2.18 with respect to q.

$$q(\chi) = \alpha^{-1}\left(\frac{Q_-(\chi,\chi_a)-Q_+(\chi_a)}{1-Q_+(\chi_a)}, Q_+(\chi_a)\right) \text{ at } \chi_E \le \chi < \chi_C \tag{2.23}$$

where α^{-1} is the inverse function to $\alpha(q, Q_+(\chi_a)$, the fraction of unfilled pores $Q_+(\chi_a)$ and $Q_-(\chi, \chi_a)$ are defined respectively by (6) and from (10), as

$$Q_-(\chi, \chi_a) = \frac{V_c(\chi)-V_-(\chi,\chi_a)}{V_c(\chi)-V_s(\chi)} \tag{2.24}$$

The fraction of the metastable necks as a function of the relative pressure, $q(\chi)$, determined according to the above scheme for Vycor glass is presented in **Fig. 2.13** for two percolation models, the Bethe approximation on the left panel, and 3D cubic lattice simulation on the right panel. It the former case, the two parts of the $q(\chi)$ function determined from the main desorption isotherm at $\chi_A < \chi < \chi_E$ and from the scanning isotherm at $\chi_E \le \chi < \chi_C$ merge at $\chi = \chi_E$, since the condition $q(\chi_E) = q_c$ is fulfilled for both Eqs. 2.22 and 2.23 due to the choice of the coordination number *z* from Eq. 2.19. For the cubic lattice model with the predetermined coordination number z=6 and percolation threshold of 0.25, there is a step at $\chi = \chi_E$, due to a mismatch of data derived from the main and the scanning isotherms. However, this step is minor, and it does not affect the neck size distribution derived from the $q(\chi)$ function significantly, as shown below. The same approach for determining the fractions of metastable necks $q(\chi)$ was applied for 3DOm carbons. The isotherms used for calculations are shown in **Fig. 2.12**. The calculated PSDs are presented in **Fig. 2.16** in the same style used for Vycor glass in **Fig. 2.15**. In all cases, the difference between the results obtained from the Bethe approximation and from the 3D cubic lattice simulation is insignificant for practical applications.

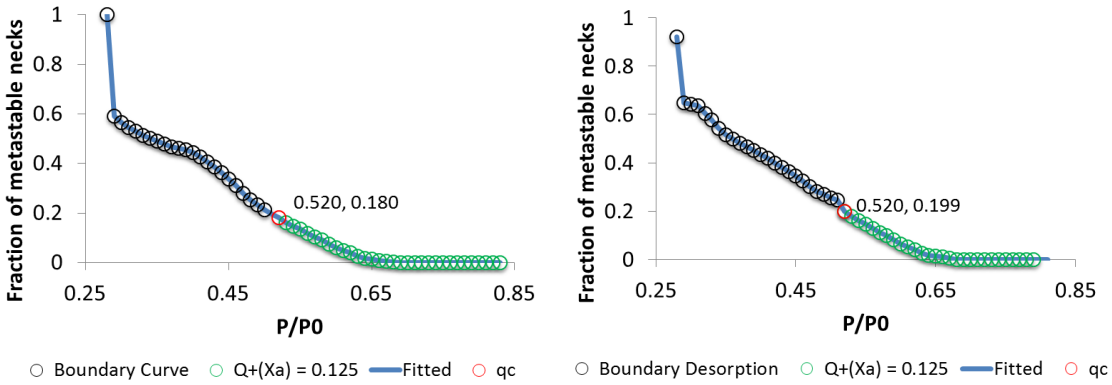

Fig. 2.13. The fraction of the metastable necks as a function of the relative pressure, $q(\chi)$, for Vycor glass [74], calculated using the scanning isotherm with $Q_+(\chi_a) = 0.125$. Bethe approximation (left) and 3D cubic lattice MC simulation (right).

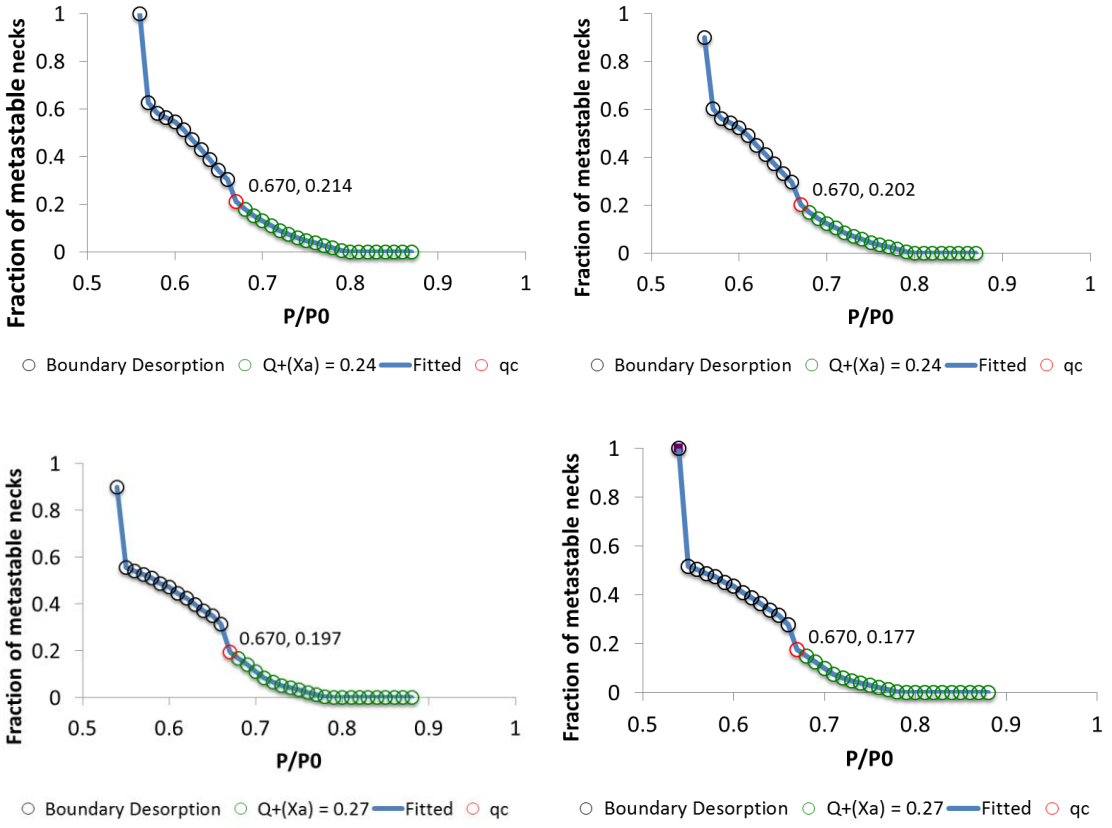

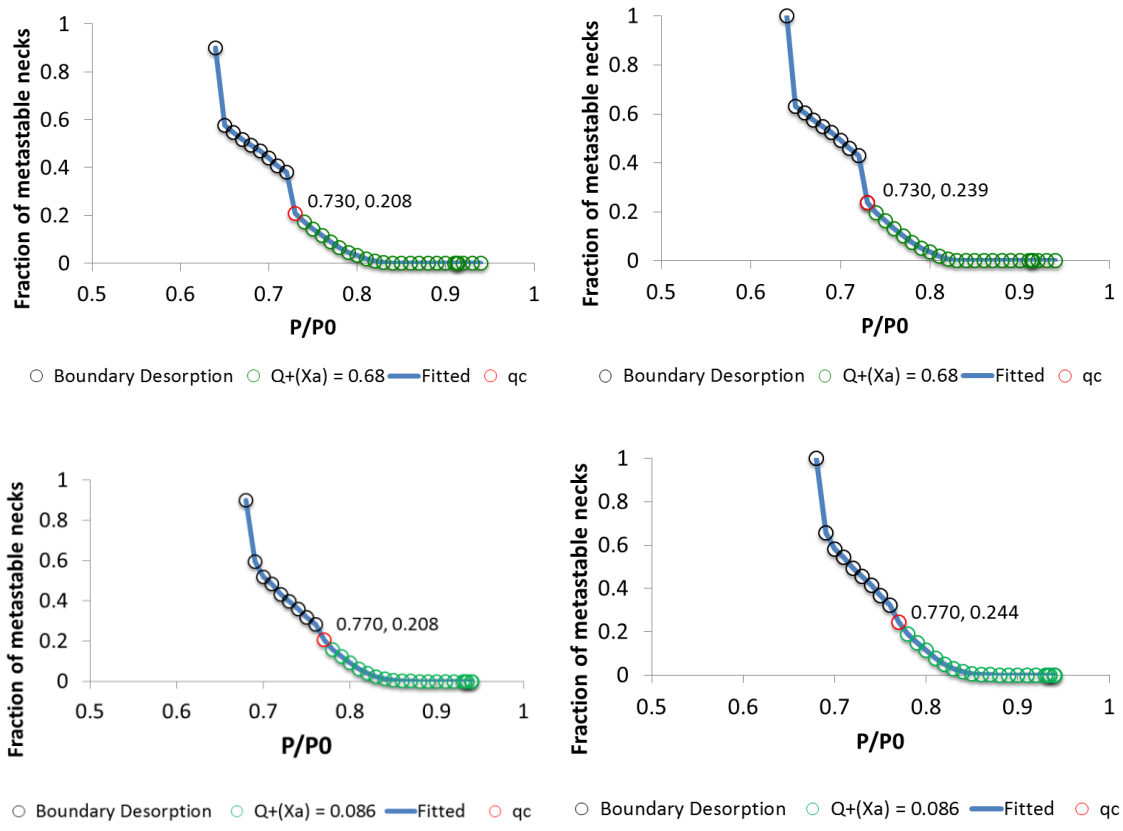

Fig. 2.14. The fraction of the metastable necks, $q(\chi)$, as a function of the relative pressure for 3DOm Carbons. using the 3D cubic lattice MC simulation (left) and Bethe approximation with fitted coordination number (right). From top to bottom: 10 nm, $Q_+(\chi_a) = 0.24$; 20 nm, $Q_+(\chi_a) = 0.27$; 30 nm, $Q_+(\chi_a) = 0.68$; 40 nm, $Q_+(\chi_a) = 0.09$.

The pore neck distribution is obtained by using a certain correlation between the neck size d_n and the relative pressure $\chi_-(\mathrm{d}_n)$, at which fluid in this pore becomes metastable. The function $q(\chi)$ determines the integral number distribution function, $\phi_n(\mathrm{d}_n)$, which represents the fraction of necks smaller than d_n, as

$$\phi_n(\mathrm{d}_n) = 1 - q\big(\chi_-(\mathrm{d}_n)\big) \tag{2.25}$$

Let us introduce another distribution function, which has a more direct relevance to the evaporation process. Indeed, the condition of evaporation from an individual pore is mainly determined by the size of the largest neck. As such, the probability, $\phi_m(\mathrm{d}_n)$, that the largest neck is smaller than d_n, and the number distribution, $\phi_n(\mathrm{d}_n)$, are related via the balance of probabilities,

$$\phi_m(\mathrm{d}_n) = \left(\phi_n(\mathrm{d}_n)\right)^z \tag{2.26}$$

The second term in the RHS of Eq. 2.26 equals the probability that all z necks of the pore are smaller than d_n. The neck size distributions $\phi_n(\mathrm{d}_n)$ and the pore distribution by the largest neck, $\phi_m(\mathrm{d}_n)$ complement the pore size distribution, $\phi_p(\mathrm{d}_p)$. The latter is determined from the main adsorption isotherm, assuming that the fraction of unfilled pores $Q_+(\chi)$ gives the fraction of pores larger than d_p, condensation in which does not occur at the relative pressure $\chi = \chi_+(d_p)$,

$$\phi_p(\mathrm{d}_p) = 1 - Q_+\left(\chi_+(d_p)\right). \tag{2.27}$$

Note that thus defined $\phi_p(\mathrm{d}_p)$ is the integral number distribution function.

The integral and differential distribution functions for pore and neck diameters for Vycor glass are presented in **Fig. 2.15**. In this case, we used the Kelvin equation for Xenon at 225K to correlate the pore and neck size and the relative pressures of condensation and desorption, $\chi_+(d_p)$ and $\chi_-(\mathrm{d}_n)$. Although the Kelvin equation underestimates the pore size at the nanoscale [129] this choice is dictated by unavailability of more advanced methods for Xe adsorption.

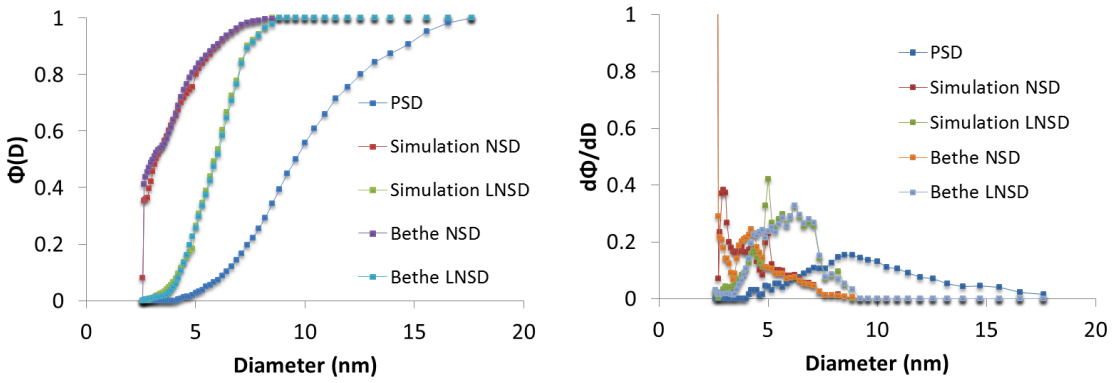

Fig. 2.15. Integral (left) and differential (right) distributions for Vycor [74]. Pore size distribution (PSD), $\phi_p(\mathrm{d}_p)$, calculated from Eq.27 (blue curves). Neck size distribution (NSD), $\phi_n(\mathrm{d}_n)$, and largest neck size distribution (LNSD), $\phi_m(\mathrm{d}_n)$, were calculated using the Bethe model, (purple curves) and using the 3D cubic lattice simulation (red curves). Note the striking similarity in the neck size distributions obtained with the two methods.

For calculations of PSDs in 3DOm carbons, we used the QSDFT relationships for spherical (pore) and cylindrical (neck) pore geometries for argon on carbon derived in Ref.[108] to correlate the pore and neck size and the relative pressures of condensation and desorption, $\chi_+(d_p)$ and $\chi_-(\mathrm{d}_n)$. The neck side distributions were calculated using the proposed percolation models, the Bethe approximation and the 3D cubic lattice MC simulation. The pore size distribution was calculated from the adsorption isotherm by the QSDFT method [108], rather than via Eq. 2.27. The results of thus calculated differential pore and neck size distributions are presented in **Fig. 2.16**; the same style and denotations are used as in **Fig. 2.15** (right).

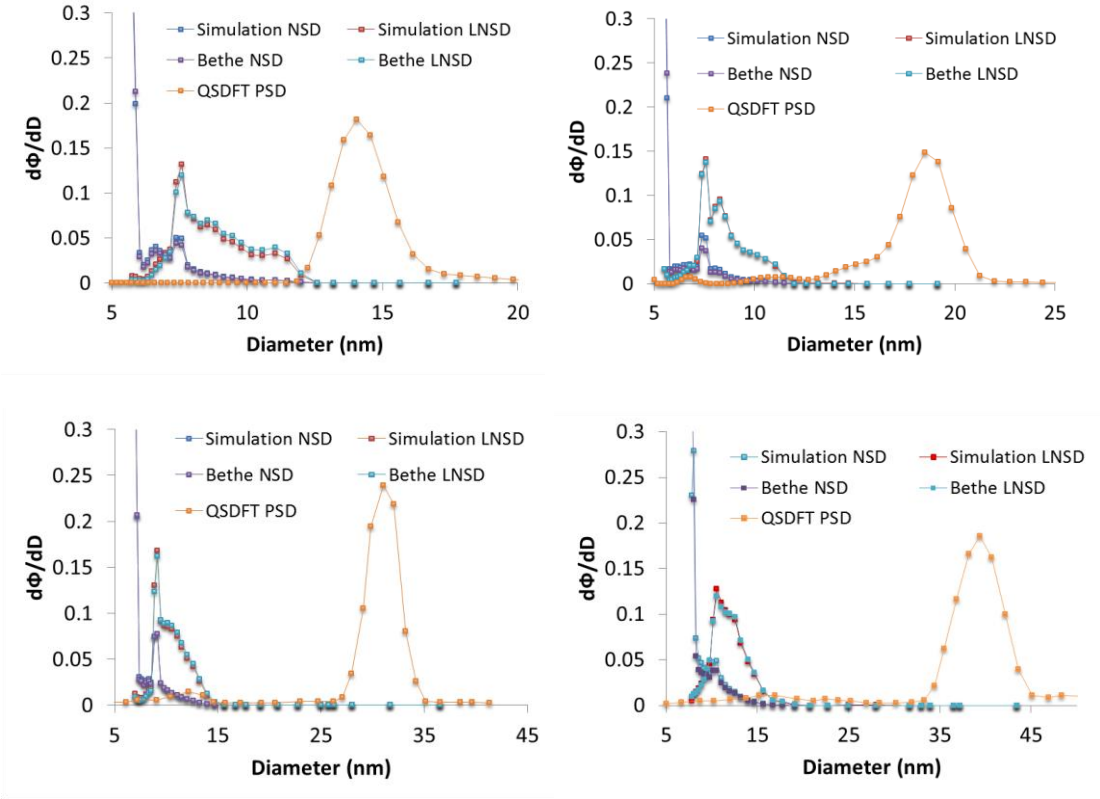

Fig. 2.16. Differential PSDs for 3DOm carbons; (top left to bottom right) 10 nm, 20 nm, 30 nm, and 40 nm carbons. Pore size distribution (PSD), $\phi_p(\mathrm{d}_p)$ (orange curves), calculated by the QSDFT method from the main adsorption isotherm [108]. Neck size distribution (NSD), $\phi_n(\mathrm{d}_n)$, and largest neck size distribution (LNSD), $\phi_m(\mathrm{d}_n)$, were calculated from the main and scanning desorption isotherms shown in **Fig. 2.14** using the percolation method; the Bethe model (purple curves) and the 3D cubic lattice MC simulation (red curves). Note the striking similarity in the neck size distributions obtained with the two methods for all the samples.

Two conclusions can be drawn from **Figs. 2.15** and **2.16**. First, the neck size distributions, $\phi_n(\mathrm{d}_n)$, and largest neck size distributions, $\phi_m(\mathrm{d}_n)$, calculated using the Bethe model and the 3D cubic lattice simulation are very similar, almost indistinguishable for any practical application. As such, one can use the Bethe approximation for practical calculations of the network connectivity and the neck size distribution using experimental data on the main and scanning desorption isotherms. Secondly, the distribution of the pores by the largest neck size better reflects the structural features of pore networks than the distribution of neck sizes, and can be recommended as a complement to the pore size distribution to be used in establishing the structure-property relations.

2.6. Summary

Although the phenomenon of adsorption hysteresis has been attracting a lot of attention among both experimental and theoretical communities for several generations of researchers, its adequate description, despite major progress achieved in recent years, is still lacking for complex porous systems. Indeed, the interplay between the thermodynamic and geometrical factors gives rise to distinct features of hysteresis in different materials. Experimentally, these distinct features are prominently displayed in the behavior of scanning isotherms, which provide additional information about the pore network geometry, including its connectivity and pore size distribution, which cannot be revealed from the main adsorption and desorption branches. Theoretically, it has been well understood since the seminal works of Everett [74] that the description of scanning isotherms cannot be achieved based on the models of adsorption in individual pores; it is necessary to take into account a cooperative nature of capillary condensation and desorption processes in three dimensional pore networks with distributed geometrical parameters of individual pores.

In this chapter of the dissertation, we analyze adsorption and desorption scanning isotherms on porous materials of different yet well characterized structure: regular hexagonal array of pore channels in SBA-15 silica, cubically ordered three dimensional gyroid structure in KIT-6 silica,

ordered three dimensional network of spheroidal cages in 3DOm carbons. The classical system of Xenon adsorption on disordered pore network of Vycor porous glass [84] is served as a reference system.

Firstly, we analyze the limitations of the models of individual pores and suggest an original partial correlation model (PCM) to distinguish the importance of the pore blocking effects. We show that while the PCM satisfactory describes the behavior of scanning isotherms on SBA-15 silica with independent pore channels, the deviation between the experimental and theoretical scanning desorption isotherms found for other samples and especially for Vycor glass point towards the necessity to account for the pore blocking effects. As such, the PCM applied to scanning desorption isotherms is suggested as a test for the pore blocking effects.

Secondly, we revisit and advance the percolation model of adsorption hysteresis put forward earlier by Neimark [92] for simulation the scanning desorption process in the pore and neck networks. Two percolation models were implemented: an analytical Bethe approximation and a Monte Carlo simulation on 3D cubic lattice. We show that both models reasonably describe the behavior of scanning desorption isotherms. We formulate a method for determining the effective pore network coordination number z from the consistency condition of the Bethe approximation applied to the main desorption and scanning desorption isotherms. The network coordination number characterizes the connectivity of the pore structure. Interestingly, the coordination numbers for Vycor glass and four different samples of 3DOm carbons were found in the range between 5 and 7 that justifies the use of the 3D cubic lattice with z=6 as a structural model of pore structures in these materials.

Thirdly, we suggest a percolation method for calculating the distributions of pore neck sizes using experimental data on the main adsorption and desorption isotherms and one scanning desorption isotherm. The proposed method is illustrated on the Vycor glass and 3ODm samples.

As such, we attempted to lay groundwork for developing a practical methodology for calculating the network connectivity and pore size distributions from the scanning isotherms. With

the current accuracy of high-resolution adsorption measurements, which provides an opportunity of measuring scanning isotherms in automated regimes of commercial instruments, this desired methodology becomes feasible. It may provide new useful information about the geometrical specifics of pore networks in novel designer nanomaterials.

CHAPTER 3

Characterization of Micro-Mesoporous Carbons by High Pressure CO_2 Adsorption

3.1 Introduction

Porous carbon materials are ubiquitous in both industrial and consumer applications. Prized for their large surface area, porous carbons are excellent candidates for applications such as CO_2 capture and sequestration[130], filtration processes[131] and as templates for catalyst growth[132, 133]. More recently, advanced templating procedures have been developed that enable one to tailor the porosity of carbons to exhibit hierarchical structures composed of micro-, meso-, and macropores [118, 134, 135]. The pore structure of these carbons is determined by the precursor (template) material, such as bare silica spheres[118], SBA- [112]and MCM-type silica[136].

Knowledge of the textural properties of carbon materials [137] (the geometry and topology of the pore structure) is integral to understanding their behavior in applications. Traditionally, adsorption of N_2 vapor at its boiling point (77K) has been used as a molecular probe for porous materials characterization. However, the strong interaction of N_2 with carbon surfaces makes N_2 diffusion into the smallest carbon micropores difficult[138], and necessitates the use of turbomolecular pumps capable of rarefying gas to a high extent ($p/p_0 \sim O(10^{-7})$). More recently, Argon gas is increasingly being used to supplement N_2 adsorption measurements. Argon gas (Ar) is capable of resolving smaller micropores (0.7-1 nm) at higher relative pressures than N_2 due to Ar's minimal interaction with carbon surfaces. However, the pore volume of carbon materials often contains significant contributions from ultramicropores (<0.7nm), and access to these micropores by Ar is restricted by diffusion limitations. To better access these pores, CO_2 at 273K was proposed as a probe molecule [138-140]. Due to the linear shape of CO_2 molecules and the high temperature adsorption, diffusion of CO_2 @ 273K is much faster than N_2 or Ar at their respective boiling points

(77K and 87K); thus CO_2 adsorption @ 273K enables the resolution of ultramicropores at elevated pressures ($p/p_0 \sim O(10^{-3})$) relative to N_2 or Ar [141].

Conventional adsorption analyzers utilized for nanoporous materials characterization are limited to pressures below 1 atm which corresponds to a maximum relative pressure for measurements with CO_2 at 273 K of $p/p_0 \sim 3 \times 10^{-2}$ (ambient pressure). At these conditions, only pores < 1 nm can be explored and thus CO_2 adsorption could only be used for accessing the micropores of nanoporous carbons. Until recently, low pressure CO_2 adsorption had to be coupled with N_2 and Ar adsorption [138, 142] in order to obtain the complete micro-mesopore size distribution of the carbon material. However, recent improvements in adsorption instrumentation and technology have led to the development of commercially available high pressure adsorption analyzers capable of pressures that exceed the saturation pressure of CO_2 at 273K. In the present work, we have investigated the possibility of utilizing CO_2 high pressure adsorption at 273 K up to the saturation pressure of CO_2 (ca.35 bar) for assessing both micro and mesopores in a single adsorption experiment.

Several data reduction methods are available for porous materials characterization that use as their primary input adsorption isotherms[143]. Of these, density functional theory methods [144] are particularly useful for their ability to provide pore size, surface area, and volume distributions for a material in both micro- and mesopores based on adsorption data from a single isotherm. Many formulations of density functional theory exist, tailored to specific applications. One of the most common formulations is Non-Local Density Functional Theory (NLDFT), which has been used extensively for the characterization of porous carbons[145, 146]. While NLDFT is well-suited to description of carbon mesopores where surface roughness is less significant, it is less suited to carbon micropores due to the presence of distinctive layering transitions which are a consequence of the smooth pore-wall model. In recent years, DFT methods which account for surface roughness have been introduced that overcome this limitation[147, 148].

One such method is Quenched Solid Density Functional Theory (QSDFT), which was developed by one of the authors[2]. QSDFT accounts for surface roughness by introducing a tunable roughness parameter [149]. QSDFT has been used extensively for the analysis of N_2 and Ar adsorption on carbon materials [150]. Isotherm analysis by QSDFT or indeed any DFT method works by fitting an "adsorption kernel" of theoretical isotherms to an experimental isotherm. As mentioned above, until recently, the range of CO_2 adsorption was limited to micropores (< 2nm) and pressures $p/p_0 < 0.03$ (~1 bar). As such, pre-existing DFT kernels for CO_2 adsorption were also limited to micropores, where adsorption is described well by NLDFT. With the introduction of high pressure CO_2 adsorption experiments, the need arose for kernels that extend into the mesopore range to be used for adsorption isotherm analysis up to CO_2 saturation pressure (34.85 bar). These kernels must take into account micropores as well as the expanded range of pore structures and surface roughness that arise in mesoporous templated carbons. To this end, a new hybrid set of DFT kernels was calculated that includes both NL- and QSDFT isotherms, in the full range of relative pressures $p/p_0 \leq 1$. These kernels are shown to produce pore size distributions and pore volume estimates that are comparable with N_2 [151] and Ar kernels, and may provide a faster and more efficient means of characterizing the porosity of micro- and mesoporous carbons which can supplement traditional measurements.

The remainder of this chapter is structured as follows. In **Section 3.2**, the experimental methodology for measuring CO_2 adsorption at 273K is described along with the new adsorption measurement equipment capable of performing these measurements. **Section 3.3** describes the computational DFT methodology needed to generate adsorption isotherm kernels for characterization of high pressure CO_2 isotherms. **Section 3.4** presents three novel hybrid adsorption kernels which may be used to analyze high pressure CO_2 isotherms, along with recommendations for their appropriate usage. **Section 3.5** presents the high-pressure CO_2 adsorption results on several characteristic porous carbons, along with complimentary N_2 and Ar

adsorption isotherms. **Section 3.6** illustrates the application of the kernels from **Section 3.4** to the experimental isotherms from **Section 3.5**. In **Section 3.7**, the unique features of CO_2 adsorption measurements and the application of the adsorption kernels are discussed, and it is proposed that CO_2 adsorption offers a complimentary measurement technique that can be used in conjunction with N_2 or Ar adsorption for studying porous carbons. Conclusions are drawn in **Section 3.8**.

3.2 Experimental Methodology – High Pressure CO_2 adsorption at 273K

Measurements of Ar adsorption at 87K and N_2 adsorption at 77K were performed using a high resolution low pressure manometric adsorption analyzer (Autosorb IQ-MP, Quantachrome Instruments, Boynton Beach, USA). CO_2 adsorption at 273K was measured using a manometric high pressure adsorption instrument (iSorb, Quantachrome Instruments, Boynton Beach, USA). Both instruments were coupled with Quantachrome's cryo-cooler to maintain constant temperature in the sample cell. Adsorption isotherms for all three analysis gases were measured on three micro-mesoporous carbons, synthesized according to the methods given by Ryoo et al,[152] and Froeba et al.[153] and hereafter referred to as CMK-3 *a*, *b*, and *c*. Prior to the adsorption experiments, the carbon samples were outgassed at 423 K overnight under turbomolecular pump vacuum.

3.3 Computational Methodology – NL and QSDFT kernels

Until the present, DFT kernels for CO_2 adsorption were tailored to analysis of the micropores (< 2nm) of nanoporous carbons [145, 154] reflecting the experimental limitation to low pressures (p/p_0 < 0.03, 1 bar). In this chapter of the dissertation, we extend the experimental and analytical pressure range to $p/p_0 = 1$, necessitating the creation of a new model which can describe CO_2 adsorption in pores much larger than 2nm. This model must include information about the assumed pore geometry and surface heterogeneity present at the mesoscale, while still incorporating the existing micropore information. This was accomplished by hybridizing the

QSDFT for mesopores with an extant NLDFT model [145, 154] for micropores which has been readily applied to carbon-CO_2 systems[149, 155], to create hybrid kernels termed NL/QSDFT.

The development of the NL/QSDFT kernels requires a set of theoretical isotherms for a wide range of pore sizes and relative pressures. This set (kernel) of isotherms, which takes into account the pore geometry, CO_2-CO_2 and CO_2-carbon interactions may then be used to analyze experimental adsorption isotherms. The methodology for calculating the theoretical isotherms is described in detail below.

DFT Approach

The adsorption process is considered here within the Grand Canonical ensemble at a given temperature *T* and chemical potential μ. The conditions of adsorption equilibrium are determined by the grand potential of the system, which is a *functional* of the solid and fluid density. In NLDFT the grand potential Ω_f is only applied to the fluid[146, 156], while the solid interactions are represented by an external potential U_{ext}:

$$\Omega_f\left[\rho_f(\mathbf{r})\right] = F_f\left[\rho_f(\mathbf{r})\right] - \int \mathrm{d}\mathbf{r}\rho_f(\mathbf{r})[\mu_f - U_{ext}(\mathbf{r})] \tag{3.1}$$

In Eq. 3.1, **r** is the n-dimensional position vector describing distance from the pore center. The fluid density profile across the pore is $\rho_f(\mathbf{r})$ and μ_f is the fluid chemical potential. F_f is the intrinsic Helmholtz free energy of the fluid, expressed as a sum of ideal F_{id} and excess hard sphere F_{ex}^{HS} terms, as well as an attractive term which is calculated via the mean-field approximation:

$$F_f\left[\rho_f(\mathbf{r})\right] = F_{id}\left[\rho_f(\mathbf{r})\right] + F_{ex}^{HS}\left[\rho_f(\mathbf{r})\right] + \frac{1}{2}\int\int \mathrm{d}\mathbf{r}\mathrm{d}\mathbf{r}'\rho_f(\mathbf{r})\rho_f(\mathbf{r}')u_{ff}(|\mathbf{r}-\mathbf{r}'|) \tag{3.2}$$

Here, u_{ff} is the fluid-fluid interaction potential. The optimal density profile occurs when the grand thermodynamic potential Eq. 3.1 is at a minimum.

The adsorption predictions of NLDFT are well-suited for micro- and ultramicropores (pore openings ≤ 2nm), where the continuum approximation breaks down and the assumption of molecularly smooth surfaces is reasonable. At this level, pores are no more than a few CO_2 molecules wide and the layering transitions which are inherent in both experimental isotherms and NLDFT can be understood to correspond to the packing of adsorbate molecules within small confinements. However, as amorphous or semi-crystalline carbon pores approach the mesopore range, there are no longer pronounced adsorption layering steps displayed by the experimental adsorption isotherms [147, 154, 157]. This indicates a significant level of surface roughness (heterogeneity), which must be accounted for by the model. The QSDFT model has been shown to accurately account for surface heterogeneity by introducing molecular roughness and is utilized here for carbon mesopores.

Within the QSDFT method, the grand thermodynamic potential is a function of both the solid and the fluid. As such, Ω in QSDFT is represented as a functional of fluid *and* solid densities $\rho_f(\mathbf{r})$ and $\rho_s(\mathbf{r})$ respectively. The solid is composed of hardcore spheres, which interact with the fluid molecules via a pairwise, attractive potential. The grand potential Ω_{sf} for QSDFT is analogous to Eq. 3.1 and is given by:

$$\Omega_{sf}\left[\rho_f(\mathbf{r}), \rho_s(\mathbf{r})\right] = F_{sf}\left[\rho_f(\mathbf{r}), \rho_s(\mathbf{r})\right] - \mu_f \int \mathrm{d}\mathbf{r}\rho_f(\mathbf{r}) - \mu_s \int \mathrm{d}\mathbf{r}\rho_s(\mathbf{r}) \tag{3.3}$$

Here, μ_s is the chemical potential of the solid molecules, and F_{sf} is the Helmholtz free energy containing ideal, excess hard sphere and attractive terms for both the solid and fluid:

$$F_{sf}\left[\rho_f(\mathbf{r}), \rho_s(\mathbf{r})\right] = F_{id}\left[\rho_f(\mathbf{r})\right] + F_{id}[\rho_s(\mathbf{r})] + F_{ex}\left[\rho_f(\mathbf{r}), \rho_S(\mathbf{r})\right] +$$
$$\frac{1}{2}\int\int \mathrm{d}\mathbf{r}\mathrm{d}\mathbf{r}'\rho_f(\mathbf{r})\rho_f(\mathbf{r}')u_{ff}(|\mathbf{r}-\mathbf{r}'|) + \frac{1}{2}\int\int \mathrm{d}\mathbf{r}\mathrm{d}\mathbf{r}'\rho_s(\mathbf{r})\rho_s(\mathbf{r}')u_{ss}(|\mathbf{r}-\mathbf{r}'|) +$$
$$\int\int \mathrm{d}\mathbf{r}\mathrm{d}\mathbf{r}'\rho_s(\mathbf{r})\rho_f(\mathbf{r}')u_{sf}(|\mathbf{r}-\mathbf{r}'|) \tag{3.4}$$

In Eq. 3.4, u_{ss} and u_{sf} represent the pairwise attractive potentials of the solid-solid and solid-fluid interactions, respectively. The key term in Eq. 3.4 is the excess Helmholtz free energy$F_{ex}[\rho_f(\mathbf{r}), \rho_S(\mathbf{r})]$. To calculate this term, we employ Rosenfeld's Fundamental Measure Theory (FMT) [149, 158, 159], which is consistent with the Percus-Yevick equation of state for a bulk hard sphere fluid[149].

The term "quenched" in QSDFT is related to the quality of the solid density by which it is considered constant throughout the optimization of the grand potential Ω_{sf}. This simplification greatly reduces the computational intensity of the QSDFT calculations, wherein only the fluid density is allowed to vary. The optimal density profile in QSDFT is found by taking the derivative of Ω_{sf} in fluid density and setting it equal to zero:

$$\left(\frac{\partial \Omega_{sf}[\rho_f(\mathbf{r}),\rho_s(\mathbf{r})]}{\partial \rho_f(\mathbf{r})}\right)_{\rho_s(\mathbf{r})} = 0 \tag{3.5}$$

the solution of Eq. 3.5 leads to the Euler-Lagrange equation for fluid density:

$$\rho_f(\mathbf{r}) = \Lambda_f^{-3} \exp\left\{c^{(1)}\left(\mathbf{r}, [\rho_f, \rho_s]\right) - \beta \int d\mathbf{r}' \rho_f(\mathbf{r}) u_{ff}(|\mathbf{r} - \mathbf{r}'|) + \beta\mu_f - \beta \int d\mathbf{r}' \rho_s(\mathbf{r}) u_{sf}(|\mathbf{r} - \mathbf{r}'|)\right\} \tag{3.6}$$

where $c^{(1)}$ is the direct correlation function : $c^{(1)}\left(\mathbf{r}, [\rho_f, \rho_s]\right) = -\beta\partial F_{ex}[\rho_f(\mathbf{r}), \rho_s(\mathbf{r})]/d\rho_f(\mathbf{r})$ and depends on both the fluid and solid densities. Here and throughout, $\beta = (k_B T)^{-1}$, where k_B is Boltzmann's constant, T is the absolute temperature and $\Lambda_f^{-3} = h/(2\pi mkT)^{\frac{1}{2}}$ is the thermal de Broglie wavelength of the fluid, h is Planck's constant, and m is the mass of the fluid molecule.

Parameters of the model

Fluid-fluid interaction parameters

The CO_2-CO_2 molecular interaction parameters are presented as Lennard-Jones potentials of single spheres, with the following parameters: fluid-fluid interaction energy $\epsilon_{ff} = 239.94\ k_B$ [K], fluid molecule radius $\sigma_{ff} = 0.3454$ nm and hard sphere diameter d_{HS} = 0.3495 nm. It is well-known that CO_2 is not a spherical molecule, and as such, the LJ model is limited in its ability to reproduce the thermodynamic properties of CO_2. For the current parameterization, the bulk vapor and liquid densities and surface tension of the liquid-vapor interface in CO_2 @ 273K are accurately reproduced [160-162] (*see* **Appendix B part A**. *for details*). However, the saturation pressure of CO_2 at high temperature (experimentally 34.85 bar @ 273K) using a one-center LJ fluid is not sufficiently accurate(p_0^{DFT} = 38.9 bar) [145]. In previous works, the parameterization was valid for the low relative pressure range (< 0.03 p/p_0), where the fluid is primarily confined to micropores and solid-fluid interactions dominate. However, in larger mesopores, the fluid-fluid interactions supersede the solid-fluid, and the exact value of the saturation pressure becomes more important – most notably for the correct determination of the pressures of capillary condensation and evaporation. As such, in this work the saturation pressure was taken as an additional parameter. The value of p_0 by which isotherms were normalized was chosen to generate the best agreement with pore size predictions for the selected carbons in **Section 3.3**, as derived from conventional analysis gases (Ar and N_2) and validated by XRD analysis [152] [153] (*See* **Appendix B part B**. *for details of model saturation pressure*).

Solid-fluid interaction parameters

The parameters for the solid-fluid interactions are the same as those previously used for CO_2-carbon interactions in both NLDFT[145, 154] and QSDFT [155], and are tailored to the DFT methods used. For the NLDFT isotherms which are of exclusively slit geometry, the external potential U_{ext} takes the form of the 1-dimensional Steele potential [163]

$$U_{Steele} = 2\pi\rho_s^0 \Delta\sigma_{sf}^2\epsilon_{sf}\left[\left(\frac{2}{15}\right)\left(\frac{\sigma_{sf}}{\mathbf{z}}\right)^{10} - \left(\frac{\sigma_{sf}}{\mathbf{z}}\right)^{4} - \frac{\sigma_{sf}^4}{3\Delta(0.61\Delta+\mathbf{z})^3}\right] \quad (3.7)$$

which is a sum of the interactions of CO_2 fluid molecules with two parallel, attractive walls:

$$U_{ext}(\mathrm{z}) = U_{Steele}(\mathrm{z}) + U_{Steele}(D - \mathrm{z}) \tag{3.8}$$

Here, *z* is the dimensionless distance from the edge of the pore and *D* is the pore width, measured as internal width. The interlayer distance Δ is 0.335 nm, the bulk density of carbon is ρ_s^0 is 114 nm^{-3}, σ_{sf}= 0.343 nm, and $\epsilon_{sf} = 81.5\ k_B$.

For the QSDFT isotherms, the CO_2-carbon interactions u_{sf} are presented as a 9-3 Lennard-Jones potential, with the same σ_{sf} and ϵ_{sf} as for the NLDFT Steele potential:

$$u_{sf} = \frac{2\pi}{3}\epsilon_{sf}\rho_s\sigma_{sf}^3\left[\left(\frac{2}{15}\right)\left(\frac{\sigma_{sf}}{\mathrm{z}}\right)^9 - \left(\frac{\sigma_{sf}}{\mathrm{z}}\right)^3\right] \tag{3.9}$$

However, the solid density ρ_s is no longer constant. Instead, the solid density $\rho_s(z)$ is a function of the distance along the pore width axis *z*. The solid density profile is represented by a linear ramp:

$$\rho_s(z) = \begin{cases} \rho_s^0 & 0 \le z < h_0 \\ 0.75\rho_s^0\left(1 - \frac{z-h_0}{2\delta}\right) & h_0 \le z < h_0 + 2\delta \\ 0 & h_0 + 2\delta < z \end{cases} \tag{3.10}$$

where h_0 = 2x0.34 nm is the thickness of the solid wall and $\delta = 0.13$ nm is the roughness parameter [2, 149]. This density profile (3.10) is applied in pores of both slit and cylindrical geometry (discussed below in **Section 3.4**) whenever the computational method is QSDFT. The increased complexity of this hybrid NL/QSDFT surface model (containing micropores with smooth walls, and mesopores with rough walls) represents an improvement over the simple pore structures previously used for characterizing adsorbents by DFT. It is a more realistic representation of the surface roughness as a whole, which may vary depending on pore size.

Recovery of the PSD by DFT

The pore size distribution (PSD) *f*(*D*) is calculated using an experimental isotherm $N_{exp}(p/p_0)$ by solving the integral adsorption equation (Eq. 3.11). The experimental isotherm is

represented as the convolution of the DFT kernel $N_{DFT}(p/p_0, D)$, which consists of a set of theoretical isotherms in a series of pores within a range of pore sizes $D=D_{min} \ldots D_{max}$

$$N_{exp}(p/p_0) = \int_{D_{min}}^{D_{max}} N_{DFT}(p/p_0, D) f(D) dD \quad (3.11)$$

where D_{min} and D_{max} are the minimum and maximum pore sizes provided by the kernel. Inversion and solution of Eq. 3.10 is obtained using the quick non-negative least square method [164]. In this method Eq. 3.10 is represented as a matrix equation, solved using the discrete Tikhonov regularization method and combined with the non-negative least square algorithm [165].

3.4. High Pressure NL/QSDFT CO_2 Kernels for Micro-Mesoporous Carbons

Theoretical isotherms of CO_2 adsorption were calculated for slit and cylindrical carbon pores within the complete range of micro and mesopore sizes (0.36 to 50.2 nm) that can be probed experimentally with high-resolution CO_2 adsorption measurements. The adsorption of CO_2 in micropores of carbon is assumed to be completely reversible, and as such only equilibrium isotherms are calculated in the micropore range (<2nm). In contrast to argon and nitrogen adsorption at 77 and 87 K, CO_2 adsorption and desorption isotherms at 273 K are fully reversible (see discussion) Here, it is suitable to calculate only the equilibrium isotherms for CO_2 at this temperature and range of pressures. The relative pressure range of the kernels extends over a wide range $p/p_0 = 1x10^{-9}$ to 1, and is divided into a logarithmic grid of 600 pressure points. Details of the developed kernels, which reflect a variety of possible adsorbent morphologies in micro-mesoporous carbon coupled with various degrees of surface roughness/heterogeneity are outlined below:

(K1) Hybrid kernel of NLDFT and QSDFT equilibrium isotherms in slit pores ranging from 0.356 to 50.232 nm, referred to as the slit pore kernel. NLDFT is used to calculate adsorption in pores < 2.0 nm and QSDFT is used for the remainder of the kernel.

(K2) Hybrid kernel of QSDFT equilibrium isotherms in cylindrical pores ranging from 0.356 to 50.232 nm, referred to as the cylindrical pore kernel. Isotherms for the smallest micropores < 0.5175 nm are slit NLDFT isotherms with the remainder (0.5175-50.232 nm) being cylindrical equilibrium isotherms.

(K3) Hybrid kernel of NLDFT and QSDFT equilibrium isotherms in slit and cylindrical pores ranging from 0.356 to 50.232 nm, called the slit-cylindrical kernel. Pores of width < 2 nm are of slit geometry and pores > 2nm are of cylindrical geometry. NLDFT is used to calculate adsorption in pores < 2 nm and QSDFT is used for the remainder of the kernel.

The choice of isotherm kernels for characterizing micro-mesoporous carbons and calculating the PSD should be made based on the first principles knowledge of the adsorbent material and the pore geometries for micro-and mesopores. For the examples discussed in this work, the templating or synthesis procedure used to manufacture the adsorbent sample determines the shape of the mesopores (slit-like or cylindrical structures) and activation determines the model best-suited for micropores. An important but alone not sufficient criterion is the degree of fitting of the PSD to the experimental isotherm. Improper choice of pore geometry generally leads to poorly fitted isotherms and can serve as a good indication of the applicability of a different model geometry. (*See* **Appendix B part C** *for fitting example*).

3.5. Experimental Results

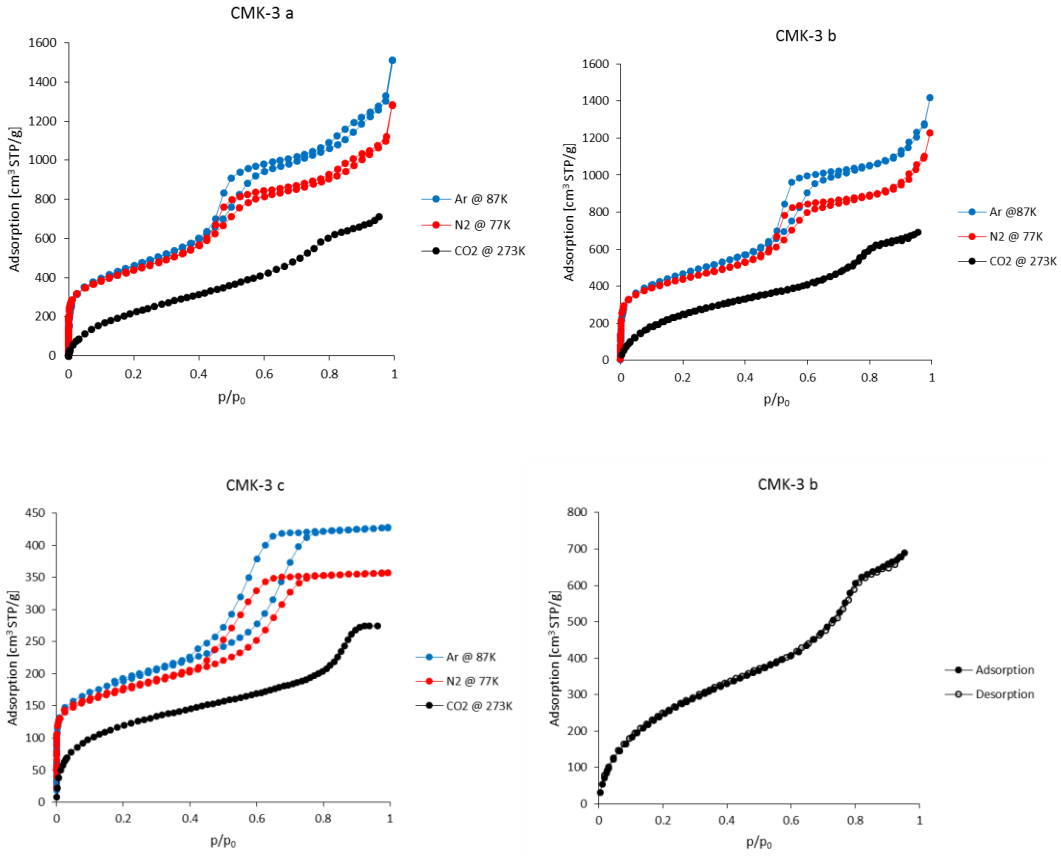

Fig. 3.1 Experimental isotherms of Ar (blue), N_2(red) and CO_2 (black) adsorption at 87, 77, and 273K respectively for CMK-3 samples *a*, *b* and *c*. Plotted values of Ar and N_2 are in terms of excess adsorption, CO_2 – absolute adsorption. Bottom right – adsorption (filled) and desorption (open) branches of CO_2 isotherm on CMK-3 *b*.

Figure 3.1 illustrates the adsorption of the three adsorbates – Ar @ 87K, N_2 @ 77K, and CO_2 @ 273K on the CMK-3 carbons labeled *a*, *b*, and *c*, respectively. The adsorption isotherms were measured using the methods and techniques described above in **Section 3.2**. The adsorption data in **Fig. 3.1** are presented in terms of the adsorbed amount. The absolute adsorbed amount is not always straightforward; indeed, it is necessary to take into account both information about the analysis gas and the behavior of the experimental isotherm. In **Section 3.7** we discuss the necessary conversion of the high surface excess data into adsorbed amount.

The CMK-3 *a* and *b* isotherms (**Fig. 3.1**) clearly indicate the presence of three distinct pore domains across all analysis gases. Characteristic of N_2 and Ar adsorption at 77 and 87 K, respectively, there is a steep micropore filling transition present in both samples below $p/p_0 = 0.1$. For CO_2 (273 K) the micropore filling region is shifted to higher relative pressures , as to be expected due to the closer vicinity to the bulk critical temperature T_C = 304K of CO_2 (T/T_C, N_2 = 0.61, T/T_C, Ar = 0.58 T/T_C CO_2 = 0.9). Analogous to micropore filling, capillary condensation into the primary mesopores occurs for CO_2 at higher relative pressures (i.e. around $p/p_0 = 0.75$) as compared to nitrogen and argon (around $p/p_0 = 0.5$). Additionally, both samples exhibit a secondary mesopore domain as evidenced by capillary condensation of N_2 and Ar in the relative pressure range from 0.75 – 0.9, which again is shifted to even higher relative pressures for CO_2 adsorption - i.e very close to the saturation pressure Interestingly, while nitrogen and argon capillary condensation are accompanied by hysteresis, mesopore filling with CO_2 is in all cases reversible as clearly illustrated in **Fig. 3.1** (bottom, right). This figure shows the complete adsorption-desorption loop for CMK-3 *b*, in which the adsorption branch (filled circles) totally coincides with the desorption branch (open circles). This feature is present in the isotherms of all three carbons (not shown, for clarity), indicating that CO_2 at these conditions behaves as a near-critical fluid. In a manner similar to CMK-3 *a* and *b*, the Ar/N_2 isotherms of CMK-3 *c* indicate significant microporosity, as well as well-defined mesopores as indicated by type H1 hysteresis loop. Similar as in case of CMK-3 a and b, pore filling of both the mico-and mesopores is shifted to higher relative pressures for CO_2.

3.6. Application of Hybrid Kernels to Experimental Adsorption Isotherms

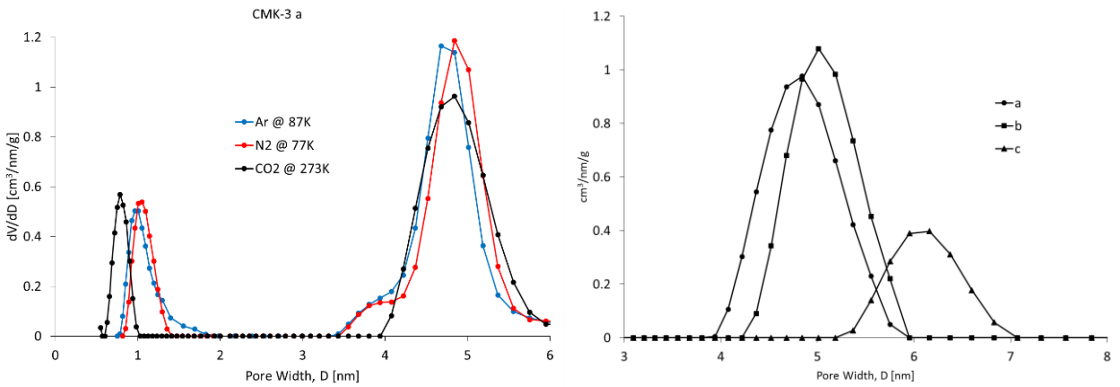

Fig. 3.2. (Left) Differential pore size distributions for CMK-3 *a* generated from experimental Ar @87K, N_2 @ 77K, and CO_2 @273K isotherms using slit-cylindrical equilibrium kernels. (Right) Primary mesopore size distributions for all three CMK-3 samples.

As shown before, CMK-3 [21] consists of ordered mesopores, but also exhibits some disordered microporosity giving rise a characteristic bimodal distribution of micropores ~ 1nm and mesopores ~ 5nm. The differential pore size distributions of CMK-3 *a*, *b* and *c* were calculated for CO_2 @ 273K using the hybrid slit-cylindrical kernel (K3) described in detail above. Using this kernel, the PSD of CO_2 can be directly compared with the results derived from that of Ar or N_2 adsorption, for which comparable adsorbent models exist (see [151] for N_2 and **Appendix B part E.** *for Ar kernels*). The micro-mesopore CO_2 pore size predictions for CMK-3 *a* are in reasonably good agreement with the Ar/N_2 results, illustrated in **Fig. 3.2** (left). CO_2 adsorption correctly captures the bimodal pore size distribution of the CMK-3 materials *and* **Fig. 3.2** (right) illustrates the ability of the CO_2 kernel to differentiate between the primary mesopore sizes of these three samples. The cumulative pore volumes of the two smaller-pore CMK-3s (*a* & *b*) show striking similarity across all three analysis gases, plots of which are shown below in **Fig. 3.3.**

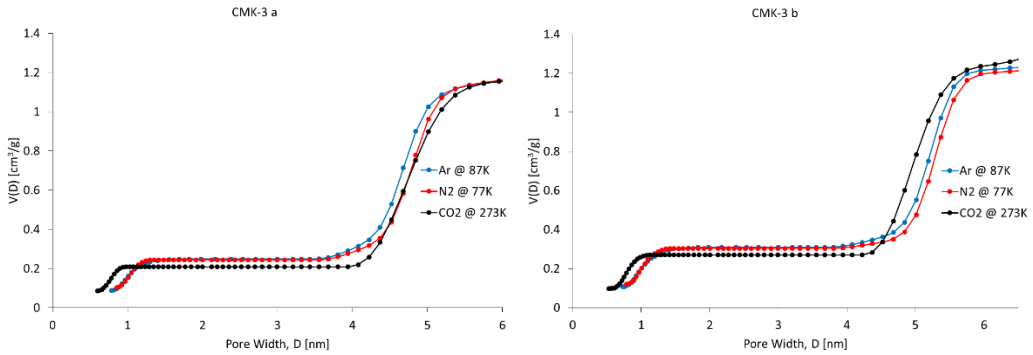

Fig 3.3. Cumulative pore volume V(D) as a function of pore width *D* for CMK-3 *a* and *b*. Measurements for Ar @ 87K – blue, N_2 at 77K – red and CO_2 @273K – black (absolute adsorption).

Fig. 3.3 compares the DFT cumulative pore volume plots as obtained from N_2, Ar and CO_2 adsorption and demonstrates reasonably good agreement between of N_2, Ar and the cumulative CO_2 pore volumes obtained from the high pressure adsorption isotherms coupled with the application of the novel hybrid CO_2 DFT kernel. Furthermore, the pore volume (referring to micro- and primary mesopores) are in good agreement with the pore volumes which can be obtained by applying the classical Gurvich rule as shown in **Table 3.1**.

Sample	DFT [cm3/g]	Gurvich Rule [cm3/g]
CMK-3 a	1.15	1.3
CMK-3 b	1.25	1.34
CMK-3 c	0.54	0.58

Table 3.1. Comparison of cumulative pore volume estimates from DFT and the Gurvich Rule, as measured by CO_2. For samples with secondary mesoporosity (*a*,*b*) Gurvich volume is assessed from the plateau of the primary mesopore (p/p_0 ~ 0.85)

3.7. Discussion

The ability of CO_2 to accurately capture the pore size and volume of the CMK-3 samples described indicates that CO_2 offers an efficient alternative method for the assessment of porosity

in carbons. At the present, standard adsorption techniques [138, 143, 166] rely on N_2 and increasingly, Ar adsorption at cryogenic temperatures. While these methods are extremely accurate, adsorption below 100K requires relatively long equilibration times [138], and consequently very long measurement times (1-2 days). CO_2 adsorption at high temperature (273K) increases the speed of gas diffusion in the pores of the sample, allowing CO_2 to reach and fill ultramicropores at relative pressures much larger than cryogenic adsorbates ($p/p_0 = 1x10^{-3}$ as opposed to $1x10^{-7}$), shortening total measurement times to several hours.

The high temperature and pressures involved in CO_2 adsorption experiments also lead to unusual adsorbate behavior, particularly in mesopores. As mentioned above, hysteresis – the quality of non-reversibility in an adsorption-desorption isotherm, is not observed for CO_2 at this temperature. According to standard theory[167], hysteresis should arise in fluid confined to mesopores due to the differing states of equilibrium that occur on the adsorption and desorption branches of an isotherm. Upon adsorption, vapor-phase adsorbate adheres reversibly to the surface of pores, forming a "liquid like" phase on the surface which is in equilibrium with the vapor. As external pressure p increases, this adsorbed layer becomes a film of increasing thickness, which grows until coming into contact with the liquid film from the opposite pore wall. At this point, the fluid condenses and forms a meniscus which is in equilibrium with the bulk vapor phase outside the pores. Upon desorption, this meniscus recedes into the pore until the fluid "snaps" apart, becoming again a film on the pore walls. In the case of conventional adsorbates, this produces two distinct branches on the adsorption isotherm corresponding to 1.) the film growth and condensation (adsorption branch) and 2.) the receding meniscus and fluid evaporation (desorption branch). It is hypothesized that the absence of hysteresis in CO_2 is indicative of the fact that the fluid is very near the critical point (304K, 75bar). In this case, the pore fluid does not behave as distinct vapor and liquid phases, but as a semi-critical fluid. This behavior is most pronounced in moderately sized (4-6nm) mesopores, where the condensation pressure is depressed significantly relative to the bulk.

The semi-criticality of the fluid in these mesopores may lead to large density fluctuations, which cannot be captured by conventional DFT based on mean-field approximations. More sophisticated 3-center fluid models [168, 169] of CO_2, in concert with a Monte Carlo approach may yield isotherms which are more characteristic in the mid-mesopore range.

As mentioned above, it is important to remember that adsorption characterization methods such as DFT for high-pressure CO_2 adsorption must utilize the absolute amount adsorbed. Several methods exist for approximating the absolute adsorption amount, based on the fluid properties and assumptions about the pore volume. A general expression for the absolute amount adsorbed n^a is given by:

$$n^a = n^s \left(1 - \frac{\rho_v}{\rho_l}\right)^{-1} \left[1 + \left(\frac{\rho_v}{\rho_l}\right)\left(\frac{V_\Sigma}{V_{filled}} - 1\right)\right] \tag{3.12}$$

where n^s is the excess amount adsorbed, ρ_v and ρ_l are the bulk liquid and vapor densities of the adsorbate, V_Σ is the total pore volume of the sample, and V_{filled} is the volume of those pores which are entirely filled with adsorbate. For cryogenic gases Ar & N_2, it is straightforward to determine the pressure at which micropores and mesopores fill completely – both transitions being marked by well-defined points along the experimental isotherm. As such, the volume of filled pores at any pressure between these points (or after capillary condensation) can be approximated by either the micropore or mesopore volume. However, the pressure of micropore filling in CO_2 adsorption isotherms on micro-mesoporous materials is often indistinguishable, as shown in **Fig. 3.1**. Here, the only clearly defined pressure for CO_2 isotherms is the capillary condensation point. After this pressure, it is suitable to assume that $V_{filled} = V_\Sigma$, thereby reducing Eq. (3.12) to

$$n^a = n^s \left(1 - \frac{\rho_v}{\rho_l}\right)^{-1} \tag{3.13}$$

Here, we utilize a definition Eq. (3.13) to estimate the absolute amount adsorbed. This equation, which relies solely on the bulk fluid properties, has been shown (**Fig. 3.3**) to provide an accurate

estimate of the absolute amount adsorbed for micro- and mesoporous carbons when the pore domains are relatively small. Using this value of the absolute adsorption, CO_2 pore volume measurements agree with measurements from other adsorbates and with the estimates ascertained from the Gurvich rule.

3.8. Summary

In this chapter of the dissertation, we propose a new tool for characterization of porous materials – namely high pressure CO_2 adsorption at 273K, which may be used in concert with traditional adsorbents N_2 and Ar to obtain a more complete picture of the structure of porous carbons in a single measurement. The adsorption of CO_2 at high temperature allows for fast diffusion to micropores, meaning quicker and more efficient measurements and equilibration times than are present for N_2 or Ar adsorption, or CO_2 at cryogenic temperatures. To accurately measure CO_2 adsorption @ 273K, new adsorption equipment capable of withstanding the high pressures and temperatures of CO_2 at saturation (34.85+ bar) has been developed and tested on several characteristic carbon adsorbents. It was found that the adsorption of CO_2 at high temperature produces reversible isotherms, which in general extend from $p/p_0 = 1x10^{-3}$ to 1, with pore filling occurring over a wider range of relative pressures than are present in adsorption at cryogenic conditions.

To analyze these adsorption isotherms, novel high-pressure hybrid NL/QSDFT kernels of absolute adsorption isotherms for several pore geometries were developed with pore sizes ranging from the ultramicropores (0.36nm, or one CO_2 molecule wide) to the limit of experimental CO_2 pore size measurements ~ 50nm. These kernels were tested on two standard hierarchical CMK-3 carbons as well as one larger-mesopore CMK-3 carbon with a disordered pore structure. The CO_2 pore size distributions were compared to the results from N_2 and Ar adsorption using analogous kernels. It was found that CO_2 measurements of pore size and pore volume are in general agreement

with N_2 or Ar. In some cases, CO_2 adsorption has been shown to be more sensitive to the presence of ultramicropores than N_2 or Ar, leading to a more complete picture of the total pore volume.

CHAPTER 4

Thermodynamic analysis of critical conditions of polymer adsorption

4.1 Introduction

Polymer adsorption to solid surfaces is a ubiquitous phenomenon with a wide range of technological and healthcare applications. Behavior of chain molecules at a surface is determined by competition between attraction due to adsorption and repulsion due to entropic penalty of the impermeable surface. Depending on the adsorption energy and temperature, the polymer assumes qualitatively different conformations: from a 3d solvated coil with one or few adsorbed monomers at weak adsorption and high temperature to a 2d chain with most monomers attached to the surface at strong adsorption and low temperature, as illustrated in **Fig. 4.1**. The transition between the regimes of weak and strong adsorption is quite sharp, and in the limit of "infinite" chain length, can be treated as a critical phenomenon[170]. The respective value of the adsorption energy U_c at given temperature T is called the critical point of adsorption (CPA). Alternatively, the critical condition of adsorption is characterized by the critical temperature T_c at given adsorption energy U.

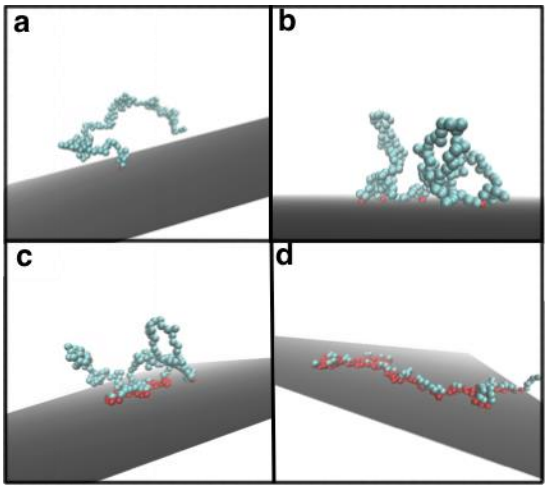

Fig. 4.1. Characteristic conformations of tethered chains. Adsorbed monomers are marked in red, solvated – in blue. Snapshots from MC simulations of freely-jointed chains composed of 200 Lennard-Jones particles. (a) reduced adsorption energy, $U = 0$ (fully solvated coil at non-adsorbing wall), (b) -5.4 (CPA), (c) -7 (moderate adsorption), (d) -10 (strong adsorption).

The phenomenon of polymer adsorption attracted close attention of theoreticians starting from the 1930s when Broda and Mark[171] suggested the first statistical mechanical description of polymer adsorption. In the 1950s, Simha, Frisch and Eirich[29] modified the ideal Gaussian chain model for polymers to describe adsorption at a planar interface. The problem was then investigated heavily in the 1960's[31, 33, 34, 172-175]. One of the earliest discussions of the transition between solvated and adsorbed chains may be found in the work of Higuchi[172], and Rubin[33] may be credited with introducing the term 'critical energy' with respect to ideal and excluded volume chains. DeGennes in his landmark review[170] showed the existence of the CPA using the self-consistent field theory[173]. Later on, there was much research to quantify the CPA using enumerative and self-consistent field theories, scaling theory and Monte Carlo simulations [35, 36, 49, 176-179] the results of which were reviewed in [52, 180-182]. Due to the relative ease of simulation and reduced number of configurations possible, these methods were most often applied to lattice models of single chains end-tethered to a flat adsorbing surface, with notable exceptions [46, 183]. The CPA for tethered chains has been defined using geometrical and thermodynamic criteria. The geometrical approach is based on the scaling relationships for the fraction of adsorbed monomers and the chain gyration radii in normal and longitudinal directions [36]. The thermodynamic approach is based on the definition of the CPA from chromatographic experiments as the condition at which the partition coefficient between free and adsorbed chains is independent of the degree of polymerization. The earliest proponents of this method were Skvortsov and Gorbunov[184] and much recent work using this method has been published by Gong and Wang[50] and others [64].

4.2 Definition of the Critical Point of Adsorption (CPA)

In this chapter of the dissertation, we present a new thermodynamic method for determining the CPA that provides a link between the thermodynamic and geometrical approaches

for characterizing polymer adsorption. We propose to define the CPA from the equality of the incremental chemical potentials of adsorbed (tethered) and free chains,

$$\mu_{incr}^{ad} = \mu_{incr}^{free} \tag{4.1}$$

The incremental chemical potential $\mu_{\text{incr}}(N)$ is defined as the difference in the excess free energies of chains composed of N and N+1 monomers, $\mu_{\text{incr}}(N) = F_{\text{ex}}(N+1) - F_{\text{ex}}(N)$. As such, the free energy $F_{\text{ex}}(N)$ is determined by the summation of the incremental chemical potentials for each degree of polymerization from 0 (monomer) to N-1, $F_{ex}(N) = \sum_{i=0}^{N-1} \mu_{incr}(i)$. Noteworthy here is the principal difference between the definition of CPA from the condition of equality of incremental chemical potentials, $\mu_{\text{incr}}(N)$, that we use in Eq. 4.1, and the condition of equality of the chain chemical potentials or the excess chain free energy, $F_{\text{ex}}(N)$, used in the previously published papers[184]-[64]. The proposed thermodynamic method is based on the experimental definition of the CPA in polymer chromatography, where the CPA separates the regimes of so-called size exclusion chromatography (SEC) and liquid adsorption chromatography (LAC) [185-187].

The elution time at the CPA is chain length independent. This property is utilized in the so-called liquid chromatography at critical conditions (LCCC) for separation of polymers by their functionalities and morphology rather than by the molecular weight. To fulfill this requirement, the partition coefficient, which is determined by the difference of the chain free energies in adsorbed and free states, $K(N) \propto \exp\left(-\beta\left(F_{ex}^{ad}(N) - F_{ex}^{free}(N)\right)\right)$, must be chain length independent [184]. Thus, the condition (Eq. 4.1) of the equality of the incremental chemical potentials is equivalent to the condition, $\partial K/\partial N = 0$.

Moreover, the "chain increment *ansatz*"[188] implies that the incremental chemical potential $\mu_{\text{inc}}(N)$ for sufficiently long chains is constant and does not depend on the chain length N. This *ansatz* holds for ideal chains. However, its extension to real chains has been a subject of

intense discussions [188, 189]. One recent detailed MC study[189] confirmed that the chain increment *ansatz* holds for free chains (N>>10) with Lennard-Jones non-bonded monomer-monomer interactions at good solvent conditions, which are considered here. Below, we show that this *ansatz* holds also for tethered chains, and the proposed CPA definition (Eq. 4.1) can be read as the equality of two length independent constants. The critical value of adsorption energy U_c can be determined by calculating the incremental chemical potential μ_{incr}^{ad} for different values of N and U and utilizing the fact that the plots μ_{incr}^{ad} versus U at different N should intersect at $U = U_{c,}$ as shown in **Fig. 4.2** (a).

4.3 Simulation Methodology

The proposed thermodynamic method of definition of the CPA from the equality of incremental chemical potentials (Eq. 4.1) is illustrated drawing on the classical case study example of polymer chains tethered at the adsorbing plane surface. We performed MC simulations of freely joined chains of Lennard-Jones (LJ) particles of LJ diameter σ_{ff} bound by harmonic bonds. Non-bonded interactions were modeled with LJ potential with the cutoff distance of $r_c = 10\sigma_{ff}$ and no shift or tail correction added to the potential. The monomers interacted with the surface via the square well potential of width σ_{ff} and depth $-U$ measured in the units of the LJ interaction energy ϵ_{ff}. The chain terminal bead was tethered at the surface at the distance of $0.5\sigma_{ff}$, in the center of the adsorption well. The simulation box dimensions are of sufficient size, such that it is impossible for the polymer chain to "wrap around" the box and interfere with itself. In this way, we ensure we are examining the dilute solution limit, with no influence from neighboring polymers. Equilibration of the system included displacement, configurational bias regrowth [190], and particle insertion/deletion moves.

The free energies were calculated with the incremental gauge cell method (IGCM) proposed by our group recently.[188] The IGCM is based on the Gauge Cell methodology,[191,

192] and assumes that a simulation cell of volume V_P and a polymer of length N_P is in thermodynamic equilibrium with a finite-volume 'gauge cell' V_G of N_G monomers which behave as ideal gas. Gauge cell monomers may be added to/removed incrementally from the free end of the polymer, and the composite system ($V_P + V_G = V$, and $N_P+N_G = N$) is immersed in a constant temperature bath, T. The free energy for the polymer is given by the Helmholtz free energy, $F_P(N) = -kT\ln\big(Q(N,V,T)\big)$ and the incremental chemical potential $\mu_{incr}(N)$ is defined as the difference in free energy of a polymer of N_P and N_P+1 monomers $\mu_{incr}(N_P) = F_P(N_P+1) - F_P(N_P)$. Making use of the equilibrium between the gauge and simulation cells, the incremental chemical potential is determined from the average number of monomers in the gauge cell, and the ratio $P(N)$ of the probabilities to observe N_G and N_G-1 monomers in the gauge cell over the course of a simulation:[188] $\mu_{incr}(N_P) = kT\ln(\frac{P_{N_G}}{P_{N_G-1}}) - kT\ln(\frac{V_G}{\Lambda^3 N_G})$.

4.4 Results

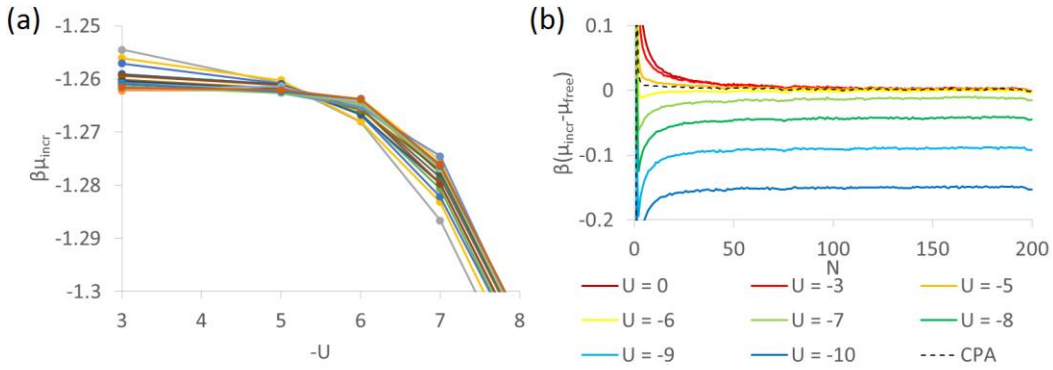

Fig. 4.2. (a) Dependence of the incremental chemical potential on the adsorption energy U for tethered chains of different length N from 25 to 200. The intersection point corresponds to the CPA at Uc=-5.4 +/- 0.05 for the free jointed LJ chain model. Calculations performed with the IGCM. (b) Chain length dependence of the incremental chemical potential. Calculations support the chain increment ansatz: for sufficiently large N the incremental chemical potential is constant

Figure 4.2 (a) shows the IGGC incremental chemical potential obtained in simulations for the chains of different lengths for N varying from 30 to 200 in multiples of 10. The CPA of Uc = -5.4 +/- 0.05 is determined from the point of intersection, which is clearly defined.

Noteworthy, we define here the CPA not from the condition of intersection of the free energies $F_{ex}(N)$, as was done in earlier works [184]-[64], but from the condition of intersection of the incremental chemical potentials $\mu_{\text{incr}}(N)$ in accord with Eq. 4.1. Additional calculation data is presented in the **Appendix C**. The chain length dependence of the incremental chemical potential (reduced by the respective free chain incremental chemical potential) is shown in **Fig. 4.2** (b). In the repulsion and weak adsorption regime, $U>U_c$, the chains are extended and the difference $\mu_{incr}^{ad} - \mu_{incr}^{free}$ vanishes for large N (> 100). At the CPA, $U = U_c$=-5.4, the equality (1) holds starting from the chain length of N=25. In the adsorption regime, the asymptotic value of the incremental chemical potential is constant in conjunction with chain increment *ansatz*, but it depends progressively on U. The linearity of the length dependence of the chain free energy is also demonstrated, and the reader is directed to the supplementary material for details.

4.5 Scaling Analysis of Tethered Chains near the CPA

The proposed thermodynamic definition of the CPA complies with the geometrical definitions employed in earlier works. DeGennes defined the CPA from the criterion that below the CPA, the probability P_a of adsorption for a monomer distanced from the tethered end by n monomers decreases to 0 as n increases. Above the CPA, this probability approaches a finite limit as $n \to \infty$. Furthermore, it was suggested and confirmed in lattice and off-lattice simulations [36, 183] that the chain adsorption behavior near the CPA is determined by a scaling relationship between the number of adsorbed monomers M, chain length N, and dimensionless deviation of the adsorption energy U from the CPA energy U_c, $\tau = \frac{U-U_c}{U_c}$ in the form

$$M = N^{\phi} f\left(\tau N^{\phi}\right) \tag{4.2}$$

Most of the published values of the crossover exponent ϕ fall into the interval between 0.52 and 0.48 [36, 47, 49, 50, 183, 193, 194]. As determined in MC simulations of self-avoiding chains [183], the crossover exponent ϕ = 0.5 +/- 0.02 that coincides with its mean field value of

0.5 [181, 183]. In the following scaling analysis, we adopt the value of ϕ = 0.5 that is sufficient with respect of the statistical accuracy of our simulation data. To secure that the fraction of adsorbed monomers *M/N* does not depend on *N* in the limit of large *N*, the scaling equation (4.2) implies that in the limit of $x = \tau N^{\phi} \to -\infty$, the scaling function $f(x) \propto |x|^{\frac{1}{\phi}-1}$. As such, assuming ϕ = 0.5, $M/N \propto |\tau|^{\frac{1}{\phi}-1} = |\tau|$, provided that $N \gg |\tau|^{-2}$. At the CPA in the limit of $|\tau| \ll N^{-1/2}$, the fraction of adsorbed monomers decreases with the chain length as $\frac{M}{N} \propto N^{\phi-1} = N^{-1/2}$. Based on this scaling *ansatz* (4.2), the CPA and crossover exponent can be evaluated from simulations by counting the fraction of adsorbed monomers and fitting the results to equation (4.2). Extrapolation of the linear asymptote in the adsorption regime gives the CPA of U_c = -5.4 +/- 0.05 in compliance with the proposed thermodynamic method. DeGennes' method and that of equation (4.2) are illustrated for chains of length *N*=200 in the supplementary material, and show clear correspondence with the IGCM value of the CPA.

The scaling ansatz implies also that the chain gyration radii in the normal $R_{\perp}$ and parallel $R_{\parallel}$ directions to the surface scale as[36]

$$R_{\perp} = N^{\nu_3} h_{\perp}\left(\tau N^{\phi}\right) \text{ and } R_{\parallel} = N^{\nu_3} h_{\parallel}\left(\tau N^{\phi}\right) \tag{4.3}$$

Here and below, ν_3 = 0.588 and ν_2 = ¾ are the 3d and 2d Flory exponents for polymer chains[183] and $x = \tau N^{\phi}$. The scaling functions $h_{\perp}$ and $h_{\parallel}$ fulfill the following asymptotes. In the adsorption limit at $x = \tau N^{\phi} \to -\infty$, $R_{\perp}$ does not depend on *N* while $R_{\parallel}$ scales as N^{ν_2}. These conditions require that $h_{\perp} \propto |x|^{-\frac{\nu_3}{\phi}}$ and $h_{\parallel} \propto |x|^{\frac{\nu_2-\nu_3}{\phi}}$, and respectively,

$$R_{\perp} \propto |x|^{-\frac{\nu_3}{\phi}} N^{\nu_3} = |\tau|^{-\frac{\nu_3}{\phi}},\ R_{\parallel} \propto |x|^{\frac{\nu_2-\nu_3}{\phi}} N^{\nu} = |\tau|^{\frac{\nu_2-\nu_3}{\phi}} N^{\nu_2}, \text{ at } x \to -\infty \tag{4.4}$$

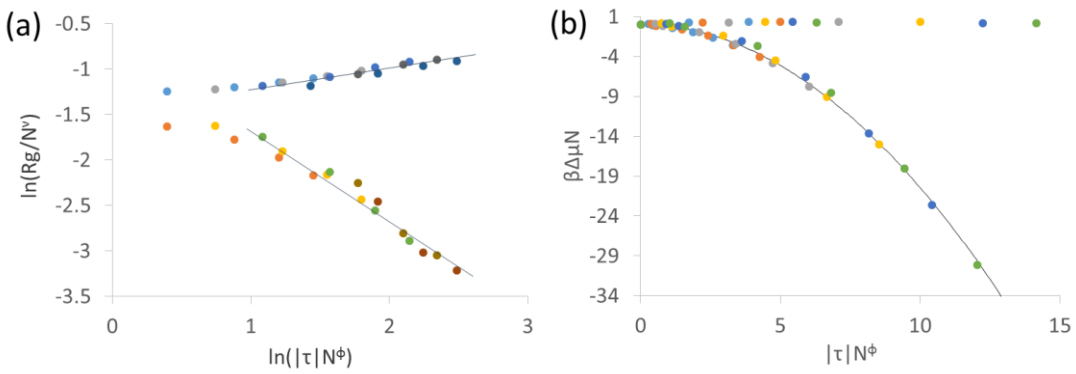

Fig. 4.3. (a) Scaling of the gyration radii in the adsorption regime. Linear asymptotes correspond to the theoretical slopes of $-\frac{\nu_3}{\phi} \approx -1.176$ = for $R_\perp$ (descending upper branch) and $\frac{\nu_2-\nu_3}{\phi} \approx 0.324$ for $R_\parallel$ (ascending branch). The plot is based on the CPA of U_c = -5.4 determined by the thermodynamic method. (b) Parabolic scaling of the incremental chemical potential, multiplied by N.

The geometrical scaling is illustrated in **Fig. 4.3** (a), where the gyration radii $R_\perp$ and $R_\parallel$ calculated for chains of different lengths and surfaces of different adsorption energy are presented using the scaling coordinates of (3). The slopes of linear asymptotes in the adsorption regime correspond to the predicted values of of $-\frac{\nu_3}{\phi} \approx -1.176$ = for $R_\perp$ and $\frac{\nu_2-\nu_3}{\phi} \approx 0.324$ for $R_\parallel$.

In the repulsion limit at $x = \tau N^\phi \to \infty$, both $R_\perp$ and $R_\parallel$ scale as N^{ν_3}, and respectively $R_\perp/R_\parallel \sim 1$. At the very CPA in the limit of $|\tau| \ll N^{-1/2}$, $h_\perp$ and $h_\parallel$ approach certain constants, $h_\perp(0)$ and $h_\parallel(0)$. Thus, this scaling *ansatz* (4) implies that $R_\perp/R_\parallel$ is independent of N at $\tau \to 0$. This conclusion was used[36, 49, 183] for the practical calculation of the CPA from the point of intersection of $R_\perp/R_\parallel$ versus U plots for the chains of different length N. However, since the scaling *ansatz* holds only with the provision of large N, such a geometrical method applied for finite length chains may overestimate the critical point, as shown in the supplementary material.

Finally, the geometrical scaling can be extended to the scaling of the chain free energy found by Gong and Wang [50]: For sufficiently long chains, the difference in free energy (approximated by the difference in incremental chemical potential times the degree of

polymerization, $\beta\mu \cdot N$) between the chain at one value of the incremental chemical potential and the corresponding value at the CPA may be described as a scalable function,

$$\beta\Delta\mu \cdot N = \beta\left(\mu_{incr} - \mu_{incr}^{CPA}\right) \cdot N \sim f(|\tau|N^{\phi}) \tag{4.5}$$

Where the function $f(|\tau|N^{\phi})$ in the limit of strong adsorption fulfills a power law with an exponent α, $f\left(|\tau|N^{\phi}\right) = A\left(|\tau|N^{\phi}\right)^{\alpha}$, so that $\beta\Delta\mu \sim |\tau|^{\alpha}N^{\alpha\phi-1}$. As the degree of polymerization approaches infinity, we assume as above, that the difference in chemical potential becomes negligible and independent of the degree of polymerization, i.e. $N^{\alpha\phi-1} = 1$. For the mean-field crossover exponent, $\phi = \frac{1}{2}$ this implies $\alpha = 2$. As such, we conclude that for large *N*, the difference in chemical potential scales with the deviation from the critical point quadratically, as $\Delta\mu \sim |\tau|^2$, $N \to \infty$. **Figure 4.3** (b) illustrates the collapse of the incremental chemical potential data onto a master curve. For the case of strong adsorption, the curve is given by the parabola $\beta\Delta\mu N = A(|\tau|N^{0.5})^2$, which follows from Eq. (4.5) above. The degree with which this scaling law applies to finite size chains, such as those considered here, gives credence to the mean field value of ϕ = 0.5, and corroborates the similar findings for the scaling of free energy by others[50] despite the disparity in computational approaches.

4.6 Summary

In conclusion, we have proposed a new thermodynamic method for determining the CPA of polymer chains from the equality of the incremental chemical potentials of adsorbed and free chains and demonstrated its abilities with off-lattice MC simulations of a freely jointed chain of LJ particles. For the chemical potential calculations we employed the incremental gauge cell method suggested earlier [188]. We found that the proposed method provides a consistent description of the critical behavior in line with the classical scaling approach with the crossover exponent of ϕ = 0.5. The established scaling relationships for the density of adsorbed monomers, chain radii of gyration, and most interestingly, the chain incremental chemical potential provide a detailed

description of the transition from the 3d conformations at weak adsorption to the 2d conformations at strong adsorption. The proposed method can be extended from the surface-tethered chains considered here to polymer adsorption in more complex geometries, including porous substrates, and with various types of adsorption interactions. The proposed method is directly related to the experimental definition of the CPA in chromatographic experiments from the chain length independence of the partition coefficient [52]. As such, this thermodynamic method is expected to provide a rationale for modeling the polymer partitioning, especially in the regime of liquid chromatography at critical conditions [185-187].

CHAPTER 5

Critical conditions of polymer adsorption and chromatography on non-porous substrates

5.1 Introduction

Polymer adsorption is the key phenomenon occurring in numerous practical applications such as colloidal stabilization, adhesion, painting, coating, and liquid chromatography, among others. From the theoretical point of view, this phenomenon is a special case of interfacial phase transitions in polymer chains interacting with heterogeneous systems[195]. Polymer adsorption is governed by a competition between enthalpic attraction and entropic repulsion. At weak adsorption energy and high temperature, entropy penalty is prohibitive and chains are effectively repelled from the surface. The free energy of adsorbed chains increases with the chain length and the partition coefficient, which determines the concentration of adsorbed molecules, decreases. At stronger adsorption energy and low temperature, enthalpy gain exceeds entropy loss and chains are predominantly adsorbed. The free energy of adsorbed chains decreases with the chain length and the partition coefficient increases. The transition from weak to strong adsorption regimes upon variation of adsorption strength or temperature is quite sharp. Following the seminal work of DeGennes[48], it is treated as a critical phenomenon occurring at the so-called critical point of adsorption (CPA).

The aforementioned regimes of adsorption are realized in three modes of liquid chromatography of polymers: weak or ideally no adsorption – in size exclusion chromatography (SEC), strong adsorption – in liquid adsorption chromatography (LAC), and an intermediate regime corresponding to the CPA – in liquid chromatography at critical conditions (LCCC)[60]. Critical conditions (i.e. CPA) are experimentally found for a large number of polymers, and LCCC has become a very popular technique for polymer characterization, complimentary to SEC and LAC[26]. It is noteworthy that LCCC is used as a first step (first dimension) in the majority of reported 2-dimentional chromatographic separations of copolymers and other complex

polymers[60]. The key advantage of LCCC is that the partition coefficient at the CPA is chain length-independent and the separation occurs with respect to the chemical (composition, end-groups, microstructure, and topology) differences in polymer chains, rather than to their size or molecular weight.

As with any mode of polymer chromatography, LCCC is usually performed on columns packed with porous particles[26, 60]. However, the presence of pores is the main factor in the shortcomings of LCCC such as low mass recovery, peak splitting and distortion, and reduced efficiency due to dynamic effects caused by a substantial increase of chain equilibration time especially in a case of narrow pores[26, 196]. In SEC and LAC modes, the presence of pores is presumed to be essential: in SEC separation occurs as a result of partition of polymer chains between the pores and interstitial volume outside the particles; in LAC the internal (pore) surface increases column loading capacity. However, for LCCC the necessity of porous substrates is not obvious, assuming that the CPA exists also in the case of non-porous substrate. Here, we demonstrate for the first time both experimentally and theoretically all three modes of polymer chromatography on non-porous substrates, including the existence of the CPA. The ability to perform LCCC on non-porous columns may improve efficiency and mass recovery of the separations without any of the shortcomings of the porous substrates.

The phenomenon of critical adsorption on planar non-porous surfaces has been extensively studied in the literature by using various theoretical and simulation methods (see reviews[34, 48, 180, 181]). Some of the most notable advances were the grand canonical formulation of Birshtein[35] and the scaling formulation of Eisenriegler, Kremer and Binder[36]. With the emergence of high speed computing, there was renewed interest in studies of polymer adsorption. Off-lattice, real chains (i.e. chains with excluded volume effects) were studied extensively and compared with earlier scaling results for ideal (Gaussian) chains, with general agreement[45-47, 49]. However, these studies were mainly concerned with the geometrical transformations of chains

at critical conditions and the respective scaling relationships and did not focus directly on the adsorption thermodynamics that determines the chromatographic separation. The authors interested in chromatographic separation, e.g.[50] among the others, established the CPA from the condition of length independence of the excess free energy *F(N)* of the tethered chains (bound to the surface by one end) of *N* monomer units, which was calculated directly using various random walk or Monte Carlo simulation models. In our recent work[197] (**Chapter 4** of this dissertation), we suggested a thermodynamic definition of CPA based on the notion of the *incremental chemical potential (ICP)*, which represents the difference of excess free energy of chains of size *N* and *N*+1 monomer units, respectively[198]. Drawing on an example of real chains tethered to planar surfaces, it was shown that the CPA condition may be derived from the condition of equality of the incremental chemical potentials of chains in the adsorbed and free (non-adsorbed) states[197]. The respective calculations of the free energies of adsorbed chains were performed with the original incremental gauge cell Monte Carlo simulation technique[198]. However, these results cannot be directly applied to the calculation of partition coefficients, which govern polymer separation, since tethered chains do not represent all possible conformations of adsorbed chains. Here, we extend this methodology to the case of untethered chains allowing us to determine the partition coefficient between adsorbed (retained) and free (unretained) chains following a rigorous adsorption theory. The partition coefficient is controlled in simulations by an effective adsorption interaction potential *U* between the chain segments and the surface. We show that at a specific value of this potential, $U=U_{CPA}$, the incremental chemical potential of the retained chains happens to be equal to that of unretained chains, and this condition corresponds to the chain length-independent separation at the CPA observed in the chromatographic experiments. The calculated partition coefficient is further used to predict the elution of a series of linear polystyrenes upon chromatographic separation on a column packed with nonporous particles to match the respective experiments. In the experiments, the partition coefficient is controlled by varying the solvent composition at constant temperature, which corresponds to varying the model adsorption potential *U*. Without invoking any adjustable

parameters related to the column structure, we are able to describe quantitatively the observed transition from SEC to LAC regimes of separation upon the variation of solvent composition, with the intermediate LCCC mode occurring at a well-defined CPA. Therewith, we establish a relationship between the experimental solvent composition and the effective adsorption potential used in simulations.

The rest of this chapter of the dissertation is structured as follows. In **Section 5.2**, we discuss the link between the Gibbs adsorption theory and the definitions of the retention volume and partition coefficient adopted in the chromatographic literature. We suggest to define the retained analyte through the Gibbs excess adsorption quantified by the respective Henry constant and show the relevance of the Henry constant to the retention volume and partition coefficient. In **Section 5.3**, we establish the CPA condition as the equality of the incremental chemical potentials of retained and unretained macromolecules. We also discuss the incremental gauge cell MC simulation for calculating the chain free energy and Henry constant. The simulation model and details of the simulation technique are given in **Section 5.4**. The results of calculations of the incremental chemical potentials and Henry coefficients for the chains of varying length at different adsorption potentials are presented in **Section 5.5**. The experimental data on separation of linear polystyrenes on a column packed with non-porous particles is given in **Section 5.6**, and the correlation between the experimental and modeling results is presented in **Section 5.7**. **Section 5.8** discusses possible hydrodynamics effects during polymer separation on non-porous columns. Brief conclusions are summarized in **Section 5.9**.

5.2. Retention volume, partition coefficient, and Henry constant

In liquid chromatography, two chromatographic phases are introduced to differentiate between the two states of the solute (analyte): retained and unretained. The phase with retained analyte is called the stationary phase and the phase with unretained analyte – mobile phase. The experimentally measured quantity is retention time t_R (time required for a chromatographic peak

to elute from the column following sample injection) or retention volume $V_R = \dot{v}_0 \cdot t_R$ where $\dot{v}_0$ is volumetric flow rate, so that V_R is a volume of liquid passing with the analyte. The molecules of the solvent (liquid) used to carry the analyte along the column are unretained by definition and occupy the entire mobile phase, while their concentration in the stationary phase is assumed to be zero. As such, the volume of mobile phase V_M is set equal to the retention volume of the solvent, which with a good approximation equals to the liquid volume of the column V_L. The retention of the analyte is considered relative to the carrying solvent, so that in the case of retained analyte, $V_R > V_L$. In order to eliminate the effect of column geometry, the so-called retention factor[199-201] $k' = V_R / V_L - 1$ is introduced as a parameter characterizing the retention of the analyte on a column packed with particles with specific surface chemistry at selected chromatographic conditions.

In liquid chromatography, retention is usually considered as a result of distribution (partition) of the analyte between its retained and unretained states,[199-201] and the retention volume is related to the volumes of mobile and stationary phases, V_M and V_{ST} ,

$$V_R = V_M + K V_{ST} \tag{5.1}$$

This equation assumes thermodynamic equilibrium between the mobile and stationary phases, respectively. The partition (distribution) coefficient, K, is defined as the ratio of equilibrium concentrations of the analyte in the retained (stationary) and unretained (mobile) phases. Note that equation (5.1) is applicable to various mechanisms of interaction between the analyte and the stationary state, including adsorption and the chromatographic partition. In case of polymer chromatography, the adsorption mechanism is more common due to a significant size of the polymer analyte compared to the size of the bonded phase, and this mechanism of retention will be assumed in the rest of this chapter of the dissertation.

The use of Eq.5.1 requires the definition of the volume of the stationary phase, which is a subject of the long-lasting discussions in the chromatographic literature[202, 203]·[204] As related to liquid chromatography of polymers, which, as liquid chromatography of any analytes, is commonly performed on porous substrates, the size of macromolecules could be comparable with the pore dimensions. For this reason, the volume of stationary phase is typically associated with the volume of pores, and the volume of mobile phase – with the interstitial volume outside the porous substrate.[26, 47, 52, 60] In this case, the partition coefficient K_{pore} describes the equilibrium distribution between the free macromolecules in the bulk solution within the interstitial volume and the macromolecules confined within the pores. This approach was first introduced by Casassa[205] to analyze the elution in SEC, where the polymer partition between the pores and the interstitial volume is due to steric interaction inside pores, and then extended to the adsorbing macromolecules in LAC and LCCC [26, 60, 201, 206]. The partition coefficient between the pores and the interstitial volume depends on the strength of adsorption interaction and sizes of the analyte and pores. For the non-adsorbing solvent, $K_{pore} = 1$, for non-adsorbing macromolecules in SEC regime $K_{pore} < 1$, for strongly adsorbing macromolecules in LAC regime, $K_{pore} > 1$. Therewith, the critical condition of adsorption was assumed to correspond to $K_{pore,CPA}=1$, so that retention time of polymer analytes in LCCC does not depend on their molar mass and equals to that of solvent. Such definition of LCCC was theoretically justified for ideal chains and it was experimentally verified in various applications (See **Chapter 1** of this dissertation for a detailed discussion).

However, the representation of the stationary phase as comprised of the pore volume, accepted in the liquid chromatography of polymers, ignores the possibility of partitioning within the interstitial volume due to interaction of the analyte with the external surface of the substrate. This deficiency becomes especially obvious in case of the columns packed with non-porous particles considered in this work. To remedy this situation, we will use the fundamental concepts

of adsorption theory[207] to describe partitioning of polymer analytes between the bulk solution and the adsorbent surface.

We present the retention volume through the Henry constant K_H defined according to the Gibbs adsorption theory as the ratio of the *excess adsorption* of the analyte per unit surface area of packed particles to its bulk concentration c_0 in the solvent. A similar thermodynamic approach was used earlier for the theoretical description of the chromatographic separation of low-molecular weight analytes, for example by F. Riedo and E. Kovats[208]**,** Kazakevich[200, 202, 206], and Yun et al.[209], yet it has not been applied systematically to polymer adsorption in liquid chromatography.

The excess adsorption is defined as the difference between the equilibrium amount of analyte in the adsorption system and the amount of analyte in the system of comparison. The latter represents the homogeneous analyte solution of concentration c_0 in the volume equaled to the volume of the mobile phase, i.e. the volume of liquid V_L. As such, the total amount of analyte N_{tot} in the column is presented as the amount of analyte in the bulk solution of volume V_L plus the excess adsorption that is proportional to the surface area S of the solid phase, $N_{tot} = c_0 V_L + K_H c_0 S$. Here, K_H is the Henry constant defined according to the Gibbs adsorption theory as the ratio of the *excess adsorption* of the analyte per unit surface area of the stationary phase and its bulk concentration c_0 in the solvent. Assuming that the amount of the retained analyte equals the excess adsorption, the retention volume can be presented as

$$V_R = V_L + K_H S \tag{5.2}$$

This thermodynamic approach naturally relates the experimentally measurable retention volume with the Henry constant and the geometrical characteristics of the column. For the packing of non-porous spherical particles of effective radius R_P, the adsorbent surface area per unit volume of liquid is $S/V_L = (3/R_P)(1-\epsilon)/\epsilon$. Here, $\epsilon = V_L/V_{col}$ is the column porosity, defined as the ratio of the

liquid volume V_L to the total column volume, V_{col}. Hence, Eq. 5.2 can be re-written in terms of the capacity factor k' as

$$V_R = (1+ k')V_L, \quad k' = K_H (3/R_P) (1-\epsilon)/\epsilon \tag{5.3}$$

Alternatively, one can use the partition coefficient K defined in the spirit of adsorption practice[207] through the excess adsorption expressed per unit volume of the solid phase V_S (adsorbent) rather than per its unit area. In this case, Eq. 5.2 can be re-written as

$$V_R = V_L + K_H S = V_L + KV_S, \text{ where } K = K_H (S/V_S) = K_H (3/R_P) \tag{5.3'}$$

Note that the above equation is equivalent to the traditional Eq. 5.1, if the volume of solid phase V_S is formally considered as the volume of a stationary phase. The volume of solid phase V_S does not correspond to the definition of the stationary phase traditionally used in the chromatographic literature as a volume in which the retained analyte is located. The advantage of Eq. 5.3' with V_S playing a role of the stationary phase volume is that, this volume, $V_S = V_{col} - V_L$, is clearly defined and can be used in practice for predictions of the retention volume. In the following discussion, we will use the notion of the partition coefficient K implied by Eq. 5.3', to describe the thermodynamic equilibrium between the retained and unretained analyte.

The thermodynamic definition of excess adsorption naturally includes the situation of analyte repulsion from the adsorbent surface, e.g. by entropy-driven steric interaction responsible for size-exclusion effects in SEC. In the case of repulsion, the analyte is excluded from the mobile phase. This effect takes place even in the case of non-porous columns, but only in the interstitial volume between the particles, which usually is ignored in conventional models of SEC. The excess adsorption of non-adsorbing or weakly-adsorbing macromolecules and respective Henry constant are negative, so that the retention volume of the analyte is smaller than that of the solvent. In this case, the analyte excess adsorption is negative and, respectively, k' and $K < 0$.

It should be emphasized that utilization of Henry constant K_H in Eqs. 5.3 and 5.3' to describe the adsorption mechanism of chromatographic retention is more practical as compared to the traditional description of stationary phase in Eq. (5.1), employed in liquid chromatography[203]. It does not require the introduction of the adsorption layer or any stationary phase volume and uses easily measurable the total liquid volume of the column V_L as the reference for comparison. Below, we show that by using the Henry constant as the thermodynamic parameter describing the partition of macromolecules through Eqs. 5.3 and 5.3', it is possible to describe in a unified fashion the chromatographic separation on non-porous substrates in both LAC and SEC regimes as well as in LCCC mode.

5.3. Critical conditions of polymer adsorption and Henry constant

We employ the thermodynamic definition of the critical conditions of polymer adsorption, which is directly related to the chromatographic measurements: at CPA, the partition coefficient K between the retained and unretained analyte is chain length (i.e. molecular weight) independent provided that the chain length N is not too short, i.e. beyond a certain small number[73] of chain segments N^*

$$at\ CPA \rightarrow dK/dN = 0 \quad for\ N > N^* \tag{5.4}$$

The molecular weight independence of the partition coefficient for chains $N > N^*$ implies that all such chains have the same probability to be in the mobile or stationary phases and thus cannot be separated based solely on their molecular weight. This definition implies that at CPA, the partition coefficients for chains of different length must converge to the same constant value $K=K_{CPA}$. Noteworthy, the magnitude of K_{CPA} is not pre-defined. Let us remind that in our approach, the amount of retained analyte is defined through the Gibbs excess adsorption and the partition coefficient K is proportional to the Henry constant K_H via Eq. 5.3'. Qualitatively, K_{CPA} is expected

to be around 0, since it separates the SEC and LAC regimes characterized, respectively, by negative and positive K_H. This differs from the common assumption of $K_{pore,CPA}$=1 used in previous works, which considered the chain partition between the interstitial and pore volumes [50, 52].

Assuming a thermodynamic equilibrium during the chromatographic process, the partition coefficient for the chain of length N, $K(N)$, is determined by the difference between the excess Helmholtz free energy of the retained (adsorbed) and free macromolecules respectively, $\underline{\Delta F} = F^{ads}(N) - F^0(N)$, and is proportional to the Boltzmann factor of $\underline{\Delta F}$: $K \sim \exp[-\Delta F/k_BT]$, were k_B and T are Boltzmann constant and temperature, respectively. From here on, all energy terms are given in k_BT units. To formulate a thermodynamically consistent criterion of the CPA, we invoke the definition of the chain incremental chemical potential $\mu_{incr}(i)$ as the difference between the excess free energy of chains of length $N+1$ and N: $\mu_{incr}(N) = F(N+1) - F(N) = dF/dN$ [198]. The chain excess free energy is determined by the summation of the incremental chemical potentials of its constituent segments $F(N) = \sum_{i=0}^{N-1} \mu_{incr}(i)$. Note that $\mu_{incr}(0)$ represents the excess chemical potential of a monomer (single segment). According to the chain increment ansatz[210], the incremental chemical potential of free unconfined chains is independent of the chain length, $\mu_{incr}^0(i) = \mu_{incr}^0 = const$, provided that the chain is sufficiently long, $i > N^*$. Respectively, the free energy of unconfined chains is a linear function of the chain length, $F^0(N) = F^0(N^*) + (N - N^*)\mu_{incr}^0$. The CPA condition (5.4) implies that $d\Delta F/dN=0$ and respectively, the incremental chemical potential of adsorbed chains at the CPA must be chain length independent and equal to the incremental chemical potential of free chains,

$$\mu_{incr} = \mu_{incr}^0 \tag{5.5}$$

As such, the thermodynamic condition of the equality of incremental chemical potentials is equivalent to the chromatographic definition of the CPA as the condition of chain length

independent elution. Note that this CPA condition is different from the condition of equality of the chain excess free energy, $F^{ads} = F^0$, used in the earlier works.[64, 211]

In **Section 4** of this dissertation[197], we verified the CPA condition (5.5) for adsorbing chains tethered to a non-porous surface and showed that this thermodynamic condition is consistent with classical scaling relationships which exist at the CPA for the fraction of adsorbed monomer segments, chain radii of gyration and chain free energy[36, 48]. Here, we consider a general case of chains which are not tethered, yet interact with the surface through an adsorption potential. Characteristic conformations of chains interacting with the surface are shown in **Figure 5.1**.

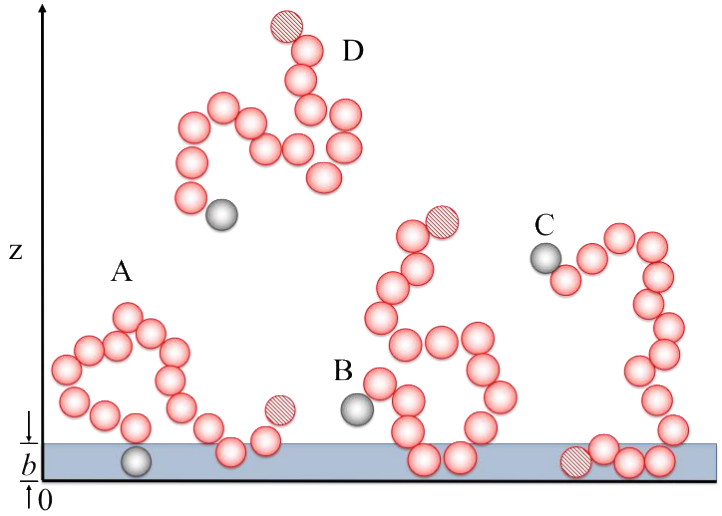

Fig. 5.1. Schematics of different conformations of chains near the surface used for Monte Carlo calculation of the chain free energies. The polymer molecules are modeled as freely jointed chains of beads, representing Kuhn segments of size *b*. The dark strip represents a square-well adsorption potential of width *b*. To account for the entropic restrictions of allowed conformations, the chains are distinguished by the position *z* of the end segment (gray beads). Adsorbed conformations include (A) the chains end-anchored at the surface (tethered chains) and (B, C) the chains anchored beyond the adsorption well with at least one segment located inside the well. The free chain reference (D) is anchored at sufficient distance $z > N$ to exclude possible interactions with the surface.

As defined above in Eq. (5.3'), the partition coefficient is directly proportional to the adsorption Henry constant, $K_H(N)$, that is the ratio of the excess adsorption per unit surface area

and the bulk concentration of the chains with *N* segments. The Henry constant $K_H(N)$ at a plane surface can be presented as the integral along the z-direction perpendicular to the adsorbing surface of the ratio of the Boltzmann factors of the chains located at distance z from the surface and free chains[73].

$$K_H(N) = \int_{z=0}^{\infty} \left[\exp\left(-\left(F(N,z) - F^0(N)\right)\right) - 1\right] dz \tag{5.6}$$

Here, $F(N,z)$ is the excess free energy of chains anchored by the end segment at the distance z to the surface. For sufficiently large z, $F(N,z) \to F^0(N)$. The ratio of Boltzmann factors $\exp\left(-F(N,z)\right) / \exp\left(-F^0(N)\right)$ represents the ratio of concentrations of chains anchored at distance z and free chains. A detailed derivation of Eq. (5.6) is given in **Appendix D**. In order to calculate the Henry constant, $K_H(N)$, one has to compute the excess free energy, $F(N,z)$, as a function of the anchoring distance z. This is done below using the incremental chemical potential representation of the free chain energy $F(N,z) = \sum_{i=0}^{N-1} \mu_{incr}(i,z)$ and employing the incremental gauge cell MC method[198]. A respective schematic of this procedure is shown in **Appendix D Figure 1**.

5.4. Chain model and simulation methodology

To compute the chain free energy and analyze its dependence on the chain length and adsorption potential, we employ the methodology developed in our previous works[72, 197, 198]. The simulation set-up is the same as before[197], so that the results obtained there for tethered chains are used as references. The polymer molecules are modeled as freely jointed chains of beads connected by harmonic springs. In this simplistic model, the beads represent Kuhn segments of length *b*, and there is no chain stiffness or limitations on bond angles or torsions. Exclusion volume effects are introduced via Lennard-Jones (LJ) interactions between non-bonded beads. Simulations were performed at dimensionless temperature T^* = 8 to ensure "good" solvent conditions in the bulk[212]. Adsorption at the solid surface is modeled by a square-well interaction between beads

and the adsorbing surface of width equal to the bead diameter *b*. The magnitude of this potential, *U*, is varied from 0 to -1 to capture the whole range adsorption, exclusion, and critical conditions.

Independent simulations were performed for chains anchored at discrete distances z, measured in units *b*, by varying the chain lengths from $N = 1$ to $N = 200$ as illustrated in **Appendix D Fig. D1**. Free energy minimization is accomplished by the Metropolis method and the incremental chemical potentials $\mu_{incr}(i,z)$ are measured via the incremental gauge cell method[198]. Each simulation consisted of 400 million MC moves per chain (displacement, insertion/deletion and configurational bias regrowth[44]) to equilibrate chain conformations, followed by 500 million moves to sample the conformational space and to compute the incremental chemical potential $\mu_{incr}(i,z)$. The incremental chemical potentials $\mu_{incr}(i,z)$ of chains of length *i* from 1 to *N* are summed to compute the chain excess free energy $F(N,z) = \sum_{i=0}^{N-1} \mu_{incr}(i,z)$. The free chain excess free energy $F^0(N)$ is computed by anchoring the chain at z=N to exclude a possibility of its interaction with the surface. Our calculations showed that $F(N,z)$ converges to $F^0(N)$ at distances z exceeding the calculated radius of gyration $R_G(N)$ of the free chain of length *N*. The Henry constant $K_H(N)$ was then computed with Eq. 5.6.

5.5. Determination of the critical point of adsorption in Monte Carlo simulations

In Figure 5.2, the incremental chemical potentials μ_{incr} of the chains anchored at different distances *z* are plotted as a function of the chain length *N* at the adsorption potential $U = U_{CPA} = -0.725$. As shown above in **Section 4** of this dissertation, this value corresponds to the CPA in the case of tethered chains. At this value of the adsorption potential, the two key features of the incremental chemical potential are apparent. First, for all chains of $N > 10$ and any *z*, the incremental chemical potential is practically constant, i.e. chain length-independent. Second, the incremental chemical potential approaches that of the free chain, fulfilling the CPA condition (5.5): $\mu_{incr} = \mu^0_{incr}$. We also have demonstrated (not shown) that at $z > R_G$, the incremental chemical potential is

constant and equals to μ_{incr}^{0} for any *N*, which is a logical result for the short-range square well adsorption potential utilized, i.e. as the anchoring distance increases, the number of configurations affected by the surface decreases. Notably, CPA in the general case of adsorbing yet untethered chains is the same as for the tethered chains.

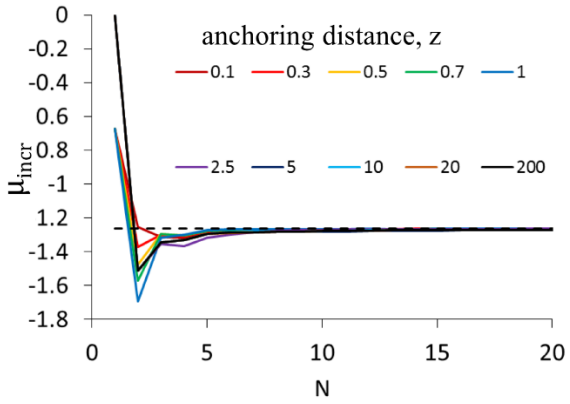

Fig. 5.2. Incremental chemical potential as a function of *N* for different anchoring distances z at the critical value of the adsorption potential U_{CPA} = -0.725. All lines converge to the dotted line $\mu_{incr} = \mu_{incr}^{0}$ as *N* becomes sufficiently large.

After summation of the incremental chemical potentials and calculation of the free energies, the Henry constant was obtained using Eq. (5.6), and plotted as a function of adsorption potential (**Fig. 5.3**, left) for a series of characteristic chain lengths *N*, and as a function of *N* for various adsorption potentials (**Fig. 5.3**, right).

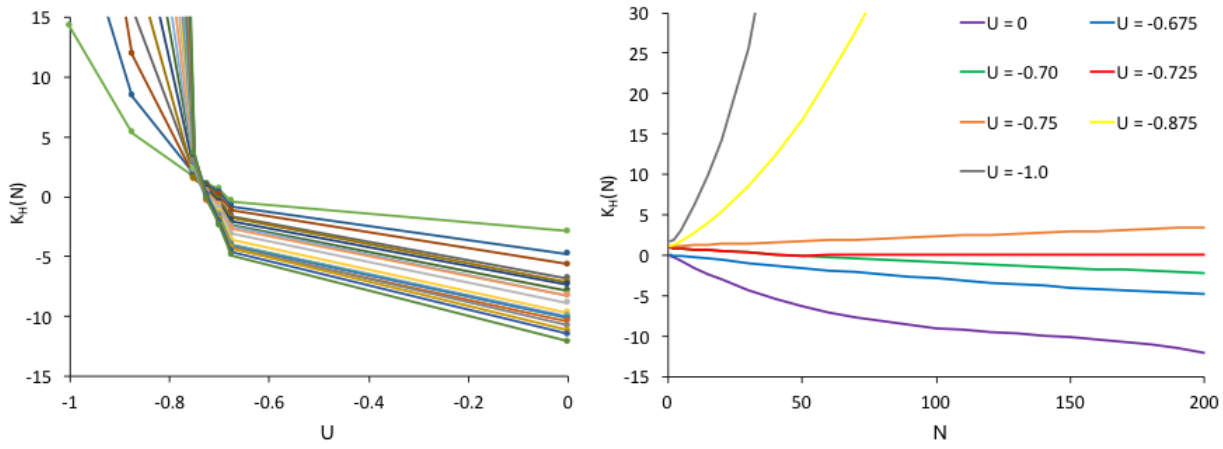

Fig. 5.3. (Left) Henry constant $K_H(N)$ computed for a series of characteristic chain lengths *(N = 20-200)* as a function of the adsorption potential *U*. The intersection point corresponds to the CPA at $U = U_{CPA}$ = -0.725. (Right) Henry constant as a function of *N* for different values of *U*. At U_{CPA} = -0.725, $K_H(N)$ is constant (LCCC mode), decreasing $K_H(N)$ values correspond to SEC mode at $U > U_{CPA}$, increasing $K_H(N)$ values correspond to LAC mode at $U < U_{CPA}$

The Henry constant is given naturally in the units of length (*b*). For the adsorption potentials weaker than the critical potential, the Henry constant is negative, indicating negative excess adsorption and depletion from the surface (**Fig. 5.3**, left). There is a significant spread of the Henry constants at zero adsorption potential, indicating increased selectivity of separation in SEC mode. Then, the spread of K_H becomes narrower as the critical potential is approached. At the CPA, the Henry constant is the same for all chain lengths (intersection point in **Fig. 5.3**, left) – a consequence of its relation to chain excess free energy. The Henry constant at the CPA is close to 0 yet is slightly positive $K_H(N)_{CPA}$ = 1.25 +/- 0.45; its magnitude rapidly increases as the strength of the adsorption potential deviates from the CPA value. Above the critical potential, the Henry constant (and excess adsorption) is positive and chains are separated in the reverse order to that of the weak potentials.

Likewise, the behavior of the Henry constant as a function of the chain length (**Fig. 5.3**, right) at various values of adsorption potential *U* confirms the existence of critical conditions at

U_{CPA} = -0.725 as predicted by the incremental chemical potential. Here, it is shown that for $U > U_{CPA}$, $K_H(N)$ is a decreasing function of N, implying shorter chains are more likely to be adsorbed than longer ones. At the other end of the spectrum, when $U < U_{CPA}$, $K_H(N)$ increases with N, indicating longer chains have a higher probability to be adsorbed. At $U=U_{CPA}$, the Henry constant is constant for chains with $N > 10$, which is consistent with the definition of critical conditions in Eq. (5.4).

In the chromatographic experiments, the retention factor k' or the partition coefficient $K = k'V_S/V_L$ can be estimated from the directly measurable retention volume V_R. In order to directly compare the experiments to the theoretical predictions, it is necessary to convert the thermodynamically derived Henry constant $K_H(N)$ into the partition coefficient K from Eq. (5.3'). To accomplish this conversion, one needs to know the following parameters of the chromatographic column: the column porosity ϵ, total liquid volume V_L and effective particle radius R_P. The comparison between the experimental data and the theoretical prediction is illustrated below.

5.6. Experimental confirmation of the existence of CPA in chromatographic separation on a non-porous column

A series of isocratic chromatographic experiments was performed using a column packed with non-porous particles. Separation was completed using Waters Corporation (Milford, MA, USA) Alliance® 2695 chromatography system coupled with Waters 2489 UV/Vis dual-wavelength absorbance on-line detector. Imtakt (Portland, OR) 4.6mm ID x 150 mm Presto® FF-C_{18} column packed with 2 micron diameter non-porous C_{18}-bonded silica particles was used for separation. The mobile phase was comprised of mixtures of two HPLC-grade solvents, tetrahydrofuran (THF) and acetonitrile (ACN), both obtained from J.T. Baker (Phillipsburg, NJ) and used without further purification. The percentage of ACN ranged from 0% to 56% by volume to cover the full range of elution modes as shown previously for a similar porous substrate[213]. Column temperature was kept constant at 35℃ and mobile phase flow rate v_0 was 0.25 ml/min. The series of narrow

polydispersity linear polystyrenes (PS) ranging in peak molar mass M from 1350 to 186,000 g/mol was purchased from Waters. Retention time t_R was measured using the UV/Vis detector. Toluene was used to measure unretained liquid volume. Retention volume V_R for each individual polystyrene at each solvent composition characterized by the vol% ACN, X, was assessed using the standard formula $V_R = \dot{v}_0 \cdot t_R$ and is presented in **Fig. 5.4** (left) as a function of Log M. The data clearly demonstrates the transition from the SEC mode of separation at lower ACN concentrations (X<54%) to the LAC mode at higher concentrations (X>54%). The LCCC mode is observed at X= 54%, when the retention volume is chain length independent within the experimental error.

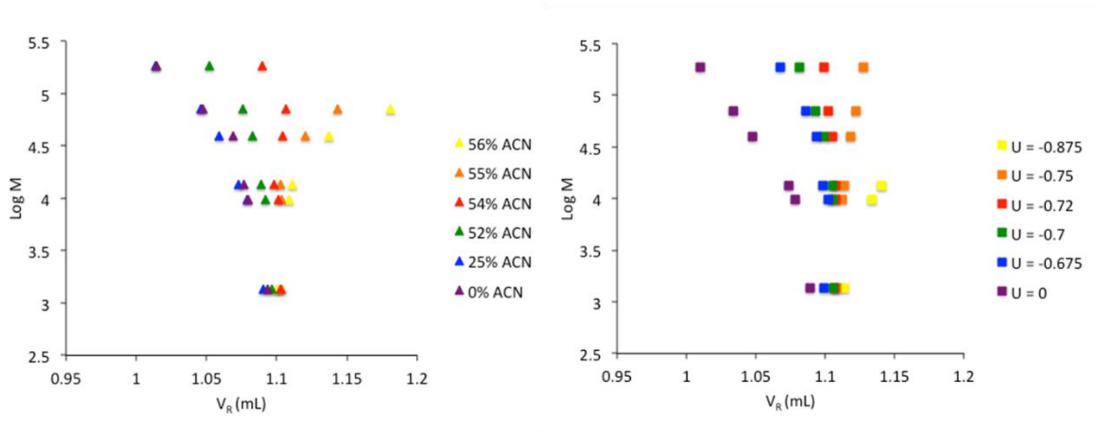

Fig. 5.4. (Left, triangle symbols) experimental and (right, square symbols) theoretical retention volumes for a series of polystyrenes as a function of vol % ACN, X=0 to 56%, in the eluent (left) and the adsorption potential, U=0 to -0.875 in k_BT units (right). CPA corresponds to X=54% and U=-0.725, respectively.

5.7. Correlation between the experimental and modeling results

For the column employed in experiments, R_P (the average particle radius) is ~1 micron, as reported by the vendor. It is assumed that the retention volume measured by UV detector of a tracer molecule (toluene), V_R = 1.088 ml, is an approximation of the total liquid volume V_L. Taking into account the total column volume V_{col} = 2.49 ml, the column porosity is estimated as $\epsilon = \frac{V_L}{V_{col}} =$ 0.44. Using these parameters in Eq. 5.3', we calculated the partition coefficients for several chains of different lengths N (**Fig. 5.5**). These chain lengths correspond directly to the molecular weights

of the experimental polystyrene chains described in **Fig. 5.4** (left), using the scaling b = 2nm, corresponding to the Kuhn segment length for polystyrene in a thermodynamically good solvent[62].

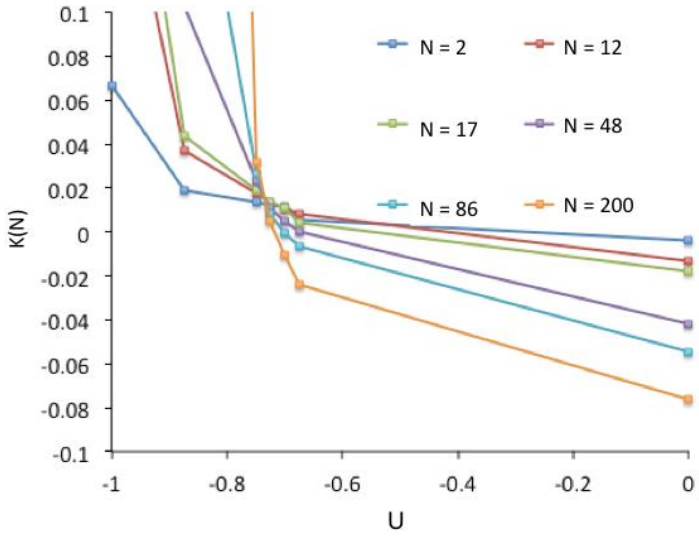

Fig. 5.5 Partition coefficient K as a function of the adsorption potential U for chains of length N between 2 and 200.

The partition coefficient K in **Fig. 5.5** clearly illustrates the transition from SEC to LAC modes with the decrease of the adsorption potential. For weak potentials $U > -0.725$, the partition coefficient is negative indicating effective 'repulsion' from the stationary phase. Here, the shorter chains have smaller partition coefficients than larger chains, constituting the size-exclusion mode. Conversely, at stronger negative adsorption potentials $U < -0.725$, K is positive and the order of partitioning with respect to chain length is reversed. Finally, in the vicinity of $U_{CPA} = -0.725$, the K-values for all chains intersect, indicating the position of the critical adsorption potential.

The calculated values of partition coefficients K were next used to calculate directly the retention volume of the chains from equation (5.3') to compare the experimental retention volumes with those predicted by simulations. The results of these calculations are presented in **Fig. 5.4**

(right) alongside the experimental retention volumes in **Fig. 5.4**, (left). There is a striking quantitative similarity between the theoretical and experimental data that allows us to conclude that the effective adsorption potential *U* used in the simulations depends on the solvent composition *X* with the respective CPA values of X_{CPA}=54% and U_{CPA}=-0.725. Using the theoretical and experimental values of the retention volumes, one can construct a correlation between *U* and *X* using an interpolation scheme. At **Fig. 5.6**, such a relationship is shown in the corresponding dimensional units. This correlation may then be used to predict the retention behavior at an arbitrary solvent composition, or for gradient elution separation in a similar system[213].

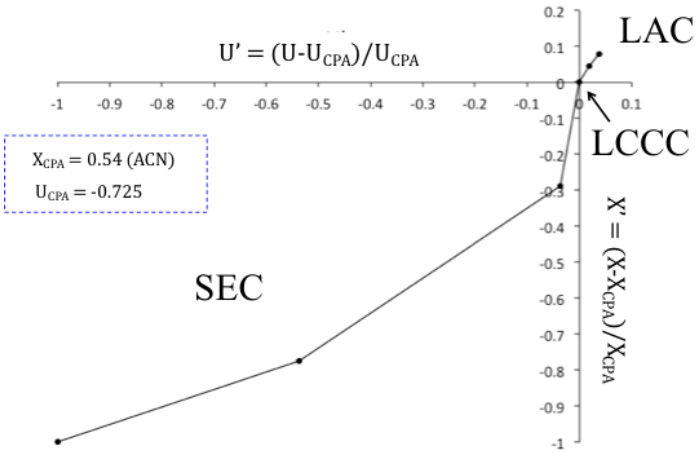

Fig. 5.6. Correlation between the reduced adsorption potential $U' = (U-U_{CPA})/U_{CPA}$ and reduced solvent composition $X' = (X-X_{CPA})/X_{CPA}$. The respective CPA values are X_{CPA}=54% and U_{CPA}=-0.725.

The reduced adsorption potential $U' = (U-U_{CPA})/U_{CPA}$ and reduced solvent composition $X' = (X-X_{CPA})/X_{CPA}$ presented in **Fig. 5.6** are normalized by the critical values $U_{CPA} = -0.725$ and $X_{CPA} = 0.54$, respectively. In these coordinates, the size-exclusion order of elution corresponds to negative values of *U'* and *X'*, and the adsorption mode - to positive. At the critical conditions, $U' = X' = 0$. The transition from SEC to LAC modes occurs within a very narrow range of mobile phase compositions, which is also found to be true for the adsorption potential. The correlation

shown in **Fig. 5.6** may serve as a justification for various solvent strength models discussed in the HPLC literature[199] [202, 203].

The experimental retention diagram shown in **Fig. 5.4** (left) illustrates for the first time all three modes of polymer chromatography on a non-porous column, including the existence of critical conditions, i.e. molecular weight independent elution at eluent composition close to 54% ACN. Such a conclusion was possible because of including into consideration both size-exclusion (entropy-driven) and adsorption (enthalpy-induced) interactions occurring in the interstitial volume between particles, which are commonly ignored in both size-exclusion and interaction chromatography[60]. The SEC-type behavior of the chromatographic system is observed at lower concentration of ACN (below 54%) (**Fig. 5.4**, left). Thus, in pure THF (purple triangles), the difference in retention volumes for the large and low molecular weight chains differs by more than 10%, and the largest chains elute well before an injected flow marker (toluene, V_R = 1.088 ml). As the column used is non-porous, only interstitial volume can contribute to such size-exclusion type of elution. For large chains, the transition from SEC to LAC is very sharp, so that at 55% ACN and higher the retention of large chains far exceeds those of the smallest molecular weight.

The correspondence of the experimental data to the results of simulation shown in **Fig. 5.4** is remarkable: almost quantitative agreement is found without invoking any adjustable parameters related to the column geometry. The thermodynamic model proposed for the partition coefficient involves known geometrical parameters of the experimental column and its packing particles. The effective adsorption potential then is mapped to the experimental solvent composition.

5.8. Effect of hydrodynamic separation

In the theoretical consideration above, we took into account only the thermodynamic mechanism of separation of macromolecules as it is related to the interplay between steric (entropic) and adsorption (enthalpic) interaction. Such an approach is well accepted for the analysis

of chromatographic separation of macromolecules inside pores, but never was used for description of the separation outside pores. It is a general consensus[60] to ignore both adsorption and steric interactions in interstitial volume and to consider the latter as a source of possible hydrodynamic (flow-induced) separation in hydrodynamic chromatography (HDC)[214]. Inhomogeneity of the flow field as a potential mechanism of separation by size in the chromatographic column packed with porous particles has been introduced by DiMarzio and Gutman[215] at the same time as Cassasa offered his thermodynamic, entropy-driven mechanism[51, 205]. The commonly accepted theory currently is that the thermodynamic mechanism of separation is dominant only inside pores, while the separation (if any) outside pores occurs by flow-induced forces[201]. This theory is based on the assumption that liquid inside pores represents so-called stagnant mobile phase, where mass transfer occurs predominately by molecular diffusion, while the mass transfer in the interstitial volume is described by the laminar flow convection accompanied by diffusion. Usually, this laminar flow is described by a parabolic (Poiseuille) flow velocity profile using the analog of an open tube channel[214] (see also **Appendix D**). The separation occurs due to a distribution of the residence time of chains of difference size as a function of their distance from the wall. The parabolic flow velocity profile allows for a small solute to be close to the walls where the flow is stagnant, while the larger molecules remain nearer the center of the tube where flow is fastest. Qualitatively, the result of such flow-induced separation is the same as of the steric effect in SEC: the larger analytes elute earlier than the smaller ones. Quantitatively, the standard HDC model for polymers in a packed bed[214] only superficially underestimates the spread of the retention times for the system considered in this work, as shown in the **Appendix D** where the results of separation in the aforementioned experimental system (polystyrenes in THF) are modeled using both the hydrodynamic and thermodynamic theories.

It is hypothesized that a discrepancy between the HDC model and experimental results described here can be attributed to the non-Poiseuille nature of the packed bed flow profile, which

is characterized by a pronounced stagnant (boundary layer with zero or low flow velocity) zone in the mobile phase near the surface of the particles, and a plug-flow velocity profile within the channels between particles, outside the stagnant zone[216]. Which mechanism really controls the separation in the interstitial volume depends on the size of the stagnant zone, which is affected by eluent viscosity, particle geometry, flow rate and diffusion coefficient of the analyte. If the stagnant zone is narrower than the size (radius of gyration R_G) of a polymer chain, then the hydrodynamic (flow) effects prevail (**Fig. 5.7**, left). In the opposite case of a wide stagnant zone (**Fig. 5.7**, right), all chains that interact with the surface are located within the stagnant zone and are effectively shielded from the "moving" part of the mobile phase flow. In this case, the separation is controlled by the thermodynamic effects with competing steric and adsorption interactions, and the hydrodynamic effects have less impact. As shown in **Appendix D**, the estimation of the width of the stagnant layer in the aforementioned experimental system[217], leads to a value far exceeding 10 Kuhn segments (radius of gyration of the largest chain considered), which justifies the use of the thermodynamic approach in simulation.

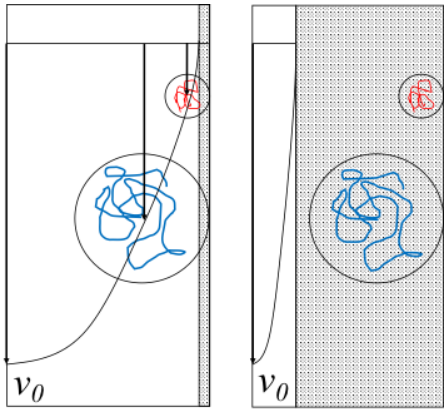

Fig. 5.7. Effect of stagnant zone in the interstitial volume on retention. (Left) Stagnant zone (width denoted by black arrow) is smaller than chain's radius of gyration, hydrodynamic effects prevail. (Right) Stagnant zone is larger than radius of gyration, thermodynamic effects govern the separation.

5.8. Summary

This chapter of the dissertation presents a novel thermodynamic method to describe the macromolecule adsorption on nonporous surfaces and to examine the critical conditions of adsorption using the incremental gauge cell MC method. The developed theoretical approach is applied to chromatographic separation of polymer analytes on non-porous column. The proposed approach implies the thermodynamic equilibrium between unretained and retained analyte treated in terms of the Gibbs adsorption theory. The amount of retained analyte is defined through the Gibbs excess adsorption that is quantified by the respective Henry constant K_H. Therewith, the partition coefficient K between retained and unretained analyte is introduced through the Henry constant K_H. Such definition implies that (i) at weak or no adsorption characterized by negative K_H (partition coefficient $K(N)<0$ and progressively decreases with N), the chains are effectively repelled from the surface and the chain elution proceeds in the SEC mode with larger chains eluted first; (ii) at strong adsorption characterized by positive K_H ($K(N)>0$ and progressively increases with N), the chains are adsorbed at the surface and the chain elution proceeds in the LAC mode with smaller chains eluted first; (iii) the critical point of adsorption (CPA), which separates SEC and LAC modes, is experimentally defined by the simultaneous elution of chains regardless of their length, and corresponds to the conditions of chain length independence of K_H ($K(N)$=const=K_{CPA} ~ 0).

From the thermodynamic standpoint, the CPA is defined by the equality of the incremental chemical potentials of adsorbed (retained) and free (unretained) chains. Using the incremental gauge cell MC method, we calculated the free energies and the respective Henry constants and partition coefficients of the adsorbing chains of different lengths at given adsorption potential. Upon the increase of the adsorption potential, we traced the transition from the SEC to LAC modes of separation with clearly defined intermediate mode corresponding to CPA. The theoretical results were compared with the specially designed chromatographic experiments with linear polystyrenes separated on a column packed with nonporous particles. For the first time, all three modes of elution

were demonstrated on a non-porous column, both experimentally and theoretically. We found that by choosing the appropriate conversion factors derived entirely from the column parameters, it is possible to qualitatively reproduce the retention behavior of a series of linear polystyrenes across a broad range of solvent compositions, encompassing the SEC, LAC, and LCCC conditions. The comparison of the experimental and calculated retention volumes allowed establishing the relationship between the solvent concentration and the effective adsorption potential used in simulations.

The simulation model employed here is one of the most simplistic models of the polymer chains with excluded volume. However, it captures the main competing mechanisms of polymer separation: entropic repulsion leading to size-exclusion mode of separation and enthalpic attraction due to adsorption. The advantage of this model is the absence of adjustable parameters except for the effective adsorption potential that allowed for a direct mapping of the theoretical results to the experimental data. This model can be further elaborated to take into account more complex chain topologies and microstructures, like specifics of end groups, star polymers, block- and statistical copolymers, etc. One of the important issues is the effect of inhomogeneous flow patterns in the packed beds that may lead to the hydrodynamic separation coupled with the thermodynamic separation was also considered.

CHAPTER 6

Mechanisms of Chain Adsorption on Porous Substrates and Critical Conditions of Polymer Chromatography

6.1. Introduction

Adsorption of polymer chains on porous substrates is a complex physico-chemical phenomenon relevant to a broad range of applications such as drug delivery, filtration, and adhesion, as well as various separation methods including liquid chromatography of macromolecules. Adsorption of polymeric chains is governed by the competing mechanisms of enthalpic attraction and entropic repulsion[61]. At strong adsorption conditions, the enthalpy gained due to adsorption interaction exceeds the entropy loss due to restrictions imposed by confining pore geometry on chain conformations, and chains are predominantly adsorbed. The free energy of adsorbed chains decreases with the chain length and the partition coefficient that determines the concentration of adsorbed chains increases. At weak adsorption conditions, the entropy penalty is prohibitive and chains are effectively repelled from pores. The free energy of adsorbed chains increases with the chain length and the partition coefficient decreases. The transition between strong and weak adsorption is quite sharp, and following the seminal work of de Gennes[48] and others[33, 35, 36] who studied *chain adsorption on plain surfaces*, it is treated as a critical phenomenon, occurring at what is termed the critical point of adsorption (CPA). Skvortsov and Gorbunov (S-G)[211] demonstrated the CPA conditions during adsorption in pores using the *ideal chain* model without the effect of excluded volume. However, the subsequent molecular simulation studies with more elaborate models of *real chains with excluded volume*[50, 57] questioned the existence of CPA for polymer adsorption on porous substrates despite the fact that the experimental manifestation of this phenomenon is widespread in polymer chromatography[61, 213, 218, 219]. Here, we investigate this controversy by using Monte Carlo simulations and posit that the critical conditions in polymer chromatography are related to the

specific mechanism of partial confinement of chains in so-called flower conformations[73], when only a part of the chain is located inside the pore.

As noted above, the phenomenon of critical adsorption is widely exploited in polymer chromatography. Separation of macromolecules is typically performed on porous substrates. When adsorption is weak (ideally, negligibly small), steric (size exclusion) interactions between the polymer chains and porous substrate provides separation by molecular size. This separation regime is known as size exclusion chromatography (SEC) that is widely used to measure molar mass distribution of polymers. In SEC mode, larger chains are excluded from the pore volume and elute earlier than their smaller counterparts. When adsorption is strong, in the regime of liquid adsorption chromatography (LAC), adsorption prevails and retention increases with the molecular weight; the order of elution is opposite to that in SEC with larger chains retained more strongly than shorter chains. The intermediate regime of mutual compensation between the attractive adsorption and repulsive steric interactions is called liquid chromatography at critical conditions (LCCC)[218, 219]. In LCCC, elution of polymer chains is molecular weight-independent, enabling the separation of polymer fractions by other structural and/or chemical factors, e.g. by the type and number of various functional groups in telechelic polymers[220]. The respective experimental conditions that correspond to the CPA for a given class of polymers can be achieved by variation of either solvent composition or temperature of the polymer solution[63]. Although LCCC is widely used for separation of complex polymers and biopolymers by difference in chemical structure, and the critical adsorption conditions are well documented for many systems, the mechanisms of chain adsorption on porous substrates are still poorly understood and the conclusions derived from different theoretical models are controversial.

Detailed analyses of critical adsorption on non-porous surfaces were performed by using various theoretical and computational models[29-36, 73, 211, 221]. The underlying theory of LCCC on porous substrates was suggested by Skvortsov and Gorbunov (S-G)[211], who

considered adsorption of *ideal* chains confined in slit-shaped pores. In modeling studies, the adsorption strength is controlled by the magnitude of the effective interaction energy, U. S-G defined the CPA as the value of $U = U_C$, at which the difference in free energies between adsorbed and unconfined chains vanishes. This condition was interpreted as a complete mutual compensation of the effects of enthalpic and entropic interactions so that the concentration of chains confined in pores equals to the concentration of unconfined chains in bulk solution. They showed that the CPA exists for ideal chains and corresponds to the conditions of molecular weight-independent elution in LCCC.

However, further modeling studies showed that the existence of CPA for chains adsorbed in pores is limited to the ideal chains. In Monte Carlo simulations of real chains with excluded volume, Cifra & Bleha[57] and Gong & Wang[50] found that the equilibrium partition between the free unconfined chains in the solution and chains confined within pore channels of several shapes always depends on the chain length regardless of the adsorption potential. These authors suggested to redefine the CPA as the magnitude of adsorption potential, $U = U_C$, at which the partition coefficient varies the least with the chain length. This definition may explain the apparent observation of critical conditions in chromatographic experiments, assuming that the deviations in the partition coefficient are smaller than the limits of experimental accuracy. This conclusion was confirmed by Yang and Neimark[73] who used self-consistent field theory (SCFT) to simulate adsorption of real chains inside spherical cavities.

Another mechanism that may explain the experimental evidence of critical conditions for chain adsorption on porous substrates is the presence of partially confined or 'flower' chain conformations[73, 222, 223]. Specifically, it has been shown[73] that when the characteristic chain size exceeds the pore size, the portion of chains completely confined within pores diminishes, as the adsorption potential reduces to its critical value ($U \rightarrow U_C$), and the flower conformations outweigh completely confined states. This effect is accompanied by the adsorption of chains on

the external surface of the substrate[221], where the chain entropy is significantly increased relative to the pore[70].

In the previous chapter of this dissertation, the critical conditions of chain adsorption were studied with a MC simulation model of real (excluded volume) chains interacting with non-porous substrates, in particular, in chromatographic columns packed with non-porous particles[197, 221]. In that case, adsorption occurs *exclusively* on the particle external surface. In this chapter, we re-examine the phenomenon of polymer adsorption on porous substrates and its application to polymer chromatography using the same MC simulation model that was used. We explore chain adsorption taking into account three general mechanisms[73] : adsorption on the external surface, complete adsorption inside pores, and partial adsorption in pores in flower conformations, see **Fig. 6.1**. We determine the critical conditions for this model and show that while the CPA does not exist for completely confined chains, it does exist for the chains which are allowed to be adsorbed partially within the pores and on the external surface. Moreover, in the vicinity of CPA, these two adsorption mechanisms (external adsorption and partial confinement) dominate and the fraction of completely confined chains diminishes.

The remainder of this chapter is structured as follows. In **Section 6.2**, we re-visit the thermodynamic definition of the critical condition of adsorption and show that the CPA implies the equality of the incremental chemical potentials of adsorbed and free chains, rather that the equality of the respective free energies as was assumed in earlier literature. **Section 6.3** details our MC simulation set-up employed for modeling adsorption of real chains. In **Section 6.4**, we study chain adsorption at the plain surface, and show the existence of CPA at a certain value of the effective adsorption potential $U = U_{C.}$ This value is then used as a benchmark to probe the existence of critical conditions for chains completely confined to pores in **Section 6.5**. It is shown that, in contrast to ideal chains, the CPA does not exist for real chains completely confined to pores and the partition coefficient of completely confined chains progressively decreases with the chain length. In **Section**

6.6, we study the mechanism of partial confinement in flower conformations and calculate the respective partition coefficient, which turns out to be chain length independent at the same critical adsorption potential $U = U_C$, as determined for the external surface. In **Section 6.7**, these partition coefficients are combined into an apparent partition coefficient, which is calculated and used to predict the retention volumes of chain molecules on porous adsorbents. Using a simplistic model of a surface corrugated with an array of ink-bottle spherical pores, we calculate the retention volumes for a series of linear polystyrenes separated on a chromatographic column packed with porous particles. The model involves two column parameters, the packing porosity and surface area, which are adjusted to get a quantitative agreement with the experiment. The relative weights of different mechanisms of adsorption are discussed, and it is shown that adsorption on the external surface and in flower conformations are dominant. As the magnitude of the adsorption potential increases to its critical value, the chains are expelled from the pores to the external surface, helping to explain the existence of the CPA for porous substrates. The results are summarized in **Section 6.8**.

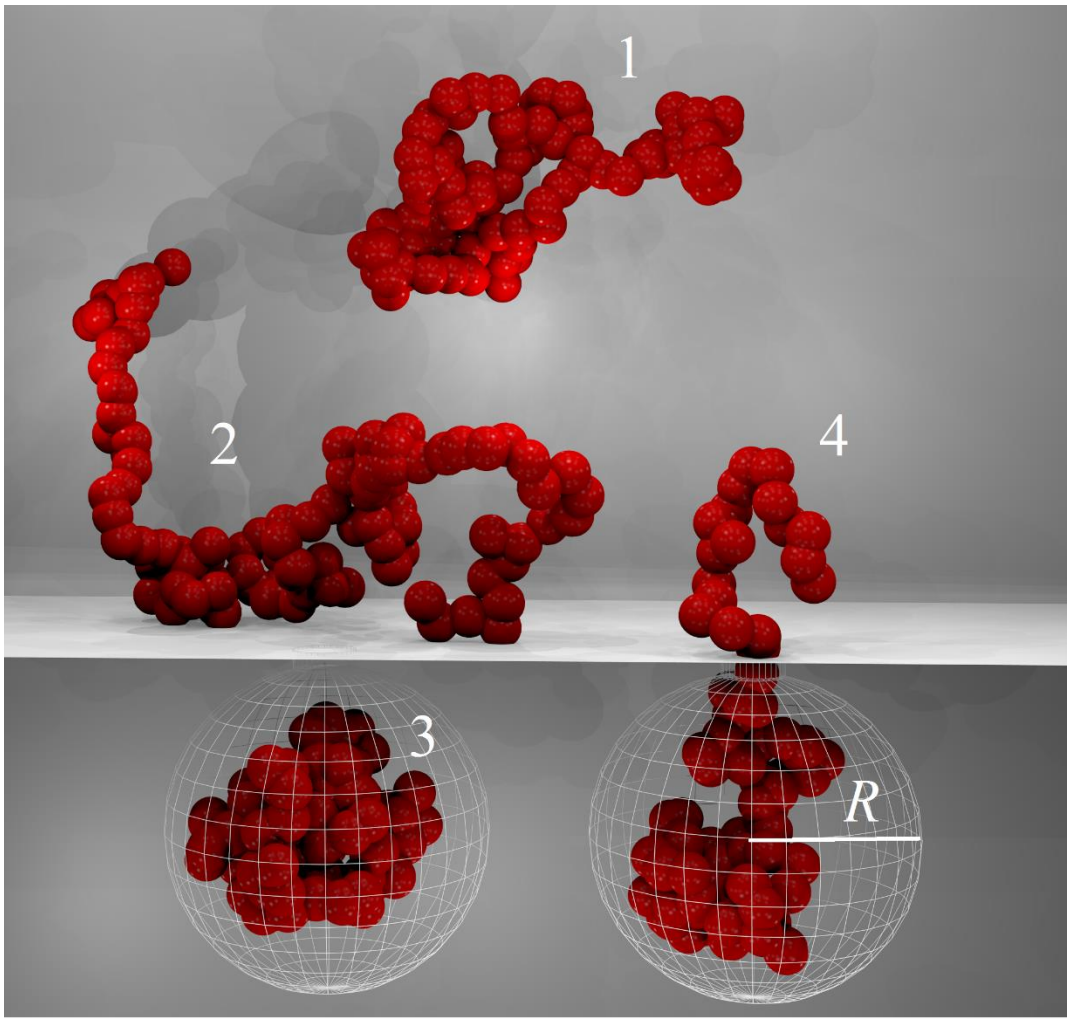

Fig. 6.1. Characteristic conformations of polymer chain interacting with nanoporous substrate: 1 – unconfined chain in bulk solution, 2 – chain adsorbed at the external surface, 3 – chain completely confined within the pore, 4 – partially confined flower conformation.

6.2. Critical conditions of polymer adsorption

There are several definitions for the critical conditions of adsorption for polymer chains based on various chain properties, i.e. number of adsorbed monomers[33], radius of gyration[36], and chain free energy[211]. The latter definition implies the equality of the excess free energies of adsorbed and free chains, $F(N) = F^0(N)$. This condition is correct for the models of ideal chains, however, for real chains with excluded volume, it holds only in the limit of infinitely long chains. As shown in[73, 197] in the general case of real chains with exclusion volume, the CPA condition

of chain length independent separation requires the equality of the incremental chemical potentials of adsorbed and free chains:

$$\mu_{incr}(N) = \mu^0_{incr} \quad \text{at CPA for} \quad N > N^* \tag{6.1}$$

This condition is held provided that the chain length N is sufficiently long, $N > N^*$, (N^* is a certain small number (~10) of chain segments[198]).

The incremental chemical potential defined as the difference between free energies of chains of length N+1 and N, $\mu_{incr}(N) = F(N+1) - F(N)$, is a measure of the work necessary to add or remove a segment at the end of a chain[210]. As such, the free energy of a chain is the sum of the incremental chemical potentials of its constituent segments $F(N) = \sum_{i=0}^{N-1} \mu_{incr}(i)$. For a free unconfined chain, it has been shown previously that the free energy F^0 is a linear function of the incremental chemical potential: $F^0(N) = \sum_{i=0}^{N^*-1} \mu^0_{incr}(i) + (i - N^*)\mu^0_{incr}$ [210]. Similar linear dependence holds also for the chains tethered or adsorbed to a nonporous surface[73, 197].

The CPA condition (6.1) follows from the fact that the chain partition coefficient depends on the difference of the excess free energies of adsorbed and free chains, $F(N) - F^0(N) = \Delta F(N)$, which must be chain length independent, but not necessarily null, at the CPA. The latter implies that

$$d\,\Delta F(N)/dN = 0 \ \text{ at CPA} \tag{6.2}$$

and therefore, $\mu_{incr} = \frac{dF(N)}{dN} = \mu^0_{incr} = \frac{dF^0(N)}{dN}$, confirming Eq. (6.1). A general derivation of the critical condition (6.1) is given the **Appendix E**.

In order to demonstrate the existence of critical conditions on porous substrates, MC simulations were undertaken to calculate the incremental chemical potential of chains of different length at various adsorption states shown in **Fig. 6.1**. The incremental chemical potentials were summed to calculate the chain free energies, which were utilized to determine the respective

partition coefficients for the three different mechanisms of chain adsorption. The details of the simulation procedure are outlined below.

6.3. Chain model and simulation methodology

6.3.1 *Chain and Adsorbent Models*

The polymer molecules are modeled as freely jointed chains of spherical beads of diameter b. Adjacent beads are connected by a harmonic potential $U_b=k(r_{12} - b)^2$ where k is the harmonic spring constant, equal to 50 k_BT/b^2 and r_{12} is the center-center distance between the beads. In this model, there is no stiffness or limitation on bond angles or torsions and non-neighbor beads interact via the standard Lennard Jones potential $U_{LJ} = \varepsilon((b/r_{12})^{12}-(b/r_{12})^6)$, where ε is the bead-bead interaction energy, equal to $0.125k_BT$. The number of beads in the chain varies from $N = 1$ to $N = 200$ as in our previous studies[197, 221]. These chains have corresponding gyration radii of $R_G = 1$ to $10b$ in free solution, calculated during simulation by ensemble average. The free chains approach thermodynamically good solvent conditions, i.e. random-coil conformation with excluded volume interaction, by setting reduced temperature $T^*=k_BT/\varepsilon = 8$, near the athermal limit[212]. The adsorption interaction between the beads and the surface is modeled by a square-well potential of width b. The same adsorption potential is applied to both the plain surface and the spherical pore walls. The magnitude of the adsorption potential, U, is varied from 0 to $-1k_BT$ to capture the full range of adsorption and exclusion conditions[221]. All energies mentioned below are in k_BT units.

6.3.2 Simulation Methodology

The chains were equilibrated by a series of 400 million MC displacement, insertion, removal, and configurational bias regrowth[44] moves using the standard Metropolis algorithm. The incremental chemical potential of the chains was determined via the incremental gauge cell method[198] and averaged over 500 million MC production moves. Free chain radii of gyration were likewise averaged over 500 million MC production moves, after equilibration. Simulation

details and the method for determining the critical conditions for different adsorption mechanisms (external surface, complete confinement, and partial confinement) are given below.

6.4. Determination of the critical point of adsorption on a nonporous surface

The simulation method for determining the CPA follows the procedure outlined in **Chapter 5** of this dissertation [221]. Chains are anchored by their terminal monomers at distance z = 0... L from the surface of the planar adsorbent measured in b units, where L is sufficiently far from the surface to approximate a free chain. For every z, the incremental chemical potential is measured for each chain length N = 1-200 (corresponding to gyration radii $R_G \sim 1 \ldots 10b$ in free solution) using the incremental gauge cell method[198]. The difference between the incremental chemical potential of the adsorbed chain and a free chain, $\Delta\mu = \mu_{incr} - \mu^0_{incr}$ acts as an indicator of the regime of adsorption.

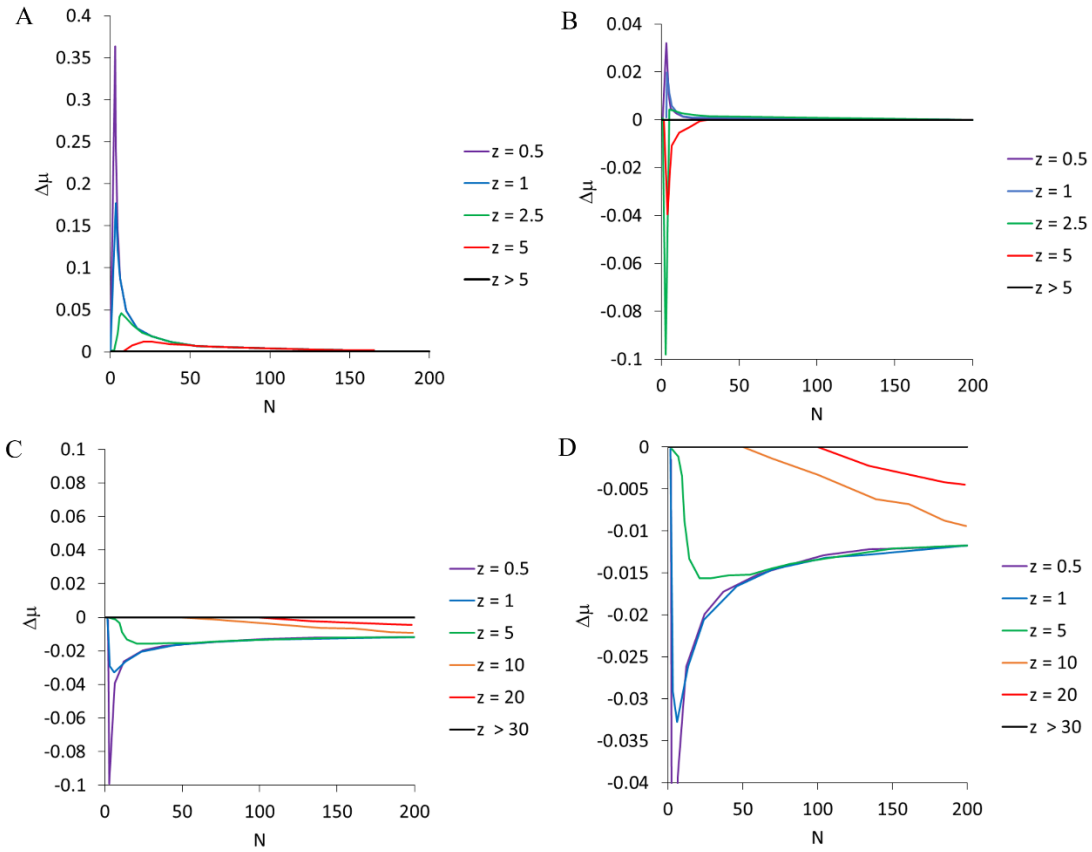

Fig. 6.2. Chain length dependence of the incremental chemical potential difference $\Delta\mu(z,U)$ of anchored chains at several *U*. A) $U = 0$. B) $U = -0.725$ (CPA), C) $U = -1$. D) Zoom of case C for large *N*. The range of anchoring distances z varies from 0.5 to 200.

The plots in **Fig. 6.2** show the incremental chemical potential difference $\Delta\mu$ as a function of chain length *N* for chains anchored at different distances *z* from the surface. For the case of zero adsorption potential ($U = 0$, **Fig. 6.2**. A), $\Delta\mu$ is positive reflecting effective repulsion from the surface due to entropic restrictions. As chains become longer or are anchored farther away from the surface, the surface effect diminishes and the incremental chemical potential tends to that of a free chain. The critical conditions are found for $U = -0.725$ (**Fig. 6.2**. B). At the CPA, the difference in chemical potentials $\Delta\mu = 0$ for all anchoring distances *z* for chains longer than a certain length $N^* = 20$. The chemical potential for chains close to the surface is either slightly positive (for very short chains, which are unlikely adsorbed) or negative (for longer chains, for which the probability of adsorption in higher). Beyond the critical point (**Figs. 6.2**. C, D), the incremental chemical potential of the adsorbed chains is negative, since the majority of chains are strongly adsorbed. Interestingly, long chains (N > 100) tethered at distances $z = 10\text{-}20b$ do come into contact with the adsorption well (see **Fig. 6.2**.D), indicating the existence of "stretched" states with chain gyration radii exceeding the maximum gyration radius $R_G(N=200) \sim 10b$ of free chains. These "stretched" states (**Fig. 6.1.2**) are entropically less favorable than free chains (**Fig. 6.1.1**), but their free energy is partially compensated for by the strong adsorption interaction. Notably, the CPA determined by this method is identical to that found by the geometrical method whereby chains tethered directly to the surface are exposed to an increasing potential field[197].

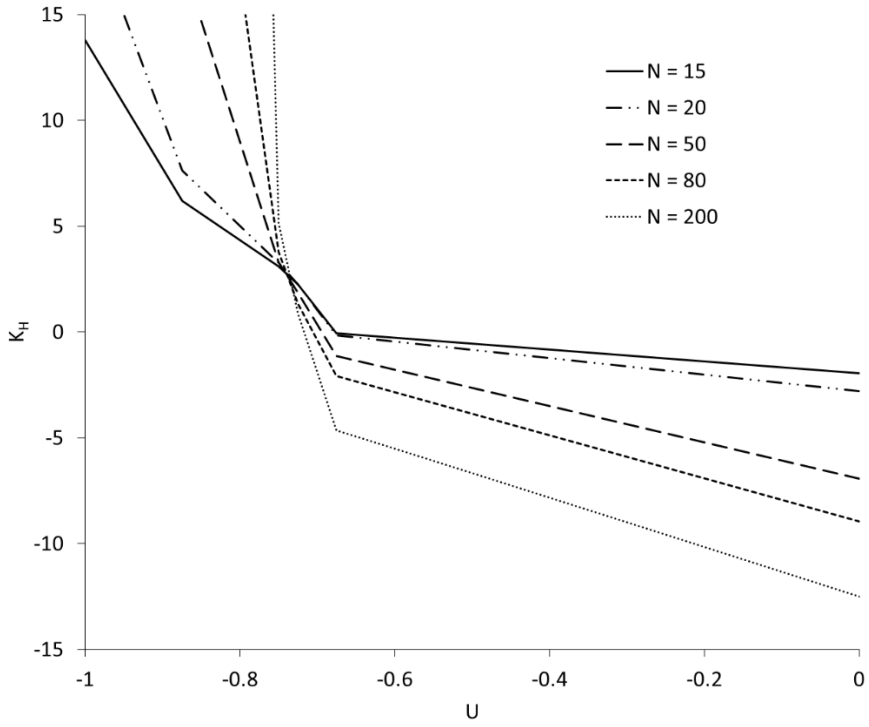

Fig. 6.3. The Henry coefficient $K_H(N)$ computed for a series of characteristic chain lengths *(N = 15-200)* as a function of the adsorption potential *U*. The intersection point corresponds to the CPA at $U = U_C = -0.725$. Here, K_H is given in units of *b*.

The transition from weak to strong adsorption conditions and the existence of a well-defined CPA are reflected in the dependence of the Henry adsorption coefficient[73, 221] on the adsorption potential (see **Fig. 6.3**). The Henry coefficient, which represents the ratio of the surface excess concentration of chains c_s to their bulk concentration c_0, $K_H = c_s/c_0$, is calculated using the following equation[73]:

$$K_H(N) = \int_{z=0}^{L} [\exp\left[-\left(F(N,z) - F^0(N)\right)\right] - 1]\ dz \qquad (6.3)$$

Notably, the Henry coefficient K_H has the dimension of length, presented in Eq. (6.3) and below in terms of Kuhn segments, *b*, since *z* is also measured in *b*. Equation (6.3) states that the Henry coefficient is the integral of the Boltzmann weighted difference in the free energy of anchored $F(N,z)$ and free $F^0(N)$ chains. The plot of the Henry coefficient K_H as a function of the adsorption potential illustrates several key features of adsorbed chains. For weak potentials, $|U| <$

$|U_C|$, the Henry coefficient is negative, reflecting effective entropic repulsion and respectively, negative excess adsorption. As a consequence, weak potentials produce a significant spread of the Henry coefficient values across different chain lengths. The chains are mostly repelled from the surface in proportion to their size and K_H decreases with chain length. As the adsorption potential approaches the critical condition, $U \sim U_C$=0.725, the Henry coefficients for all chain lengths intersect at the critical value $K_H \sim 1.25$. At these conditions, which are identical to the case of a tethered chain[197, 221], all chains are equally likely to adsorb or to remain free, so the Henry coefficient is chain length-independent. Noteworthy, the critical value of K_H is not zero reflecting the CPA condition of the equality of the incremental chemical potentials rather than chain free energies. Above the critical potential $|U| > |U_C|$ there is a sharp transition wherein the chains become strongly adsorbed to the surface. Smaller chains are less likely to adsorb than larger ones, and so the Henry coefficient increases with chain length.

6.5. Probing the existence of critical conditions for completely confined chains

The value U_C of the critical potential on the nonporous surface acts as a benchmark to probe the critical point on porous surfaces. In this and the following section, the existence of critical conditions is investigated using simple model pores under two different geometric constraints: complete or partial confinements. It will be shown that, under specific circumstances, critical conditions exist on porous surfaces and the critical adsorption potential on a porous surface is equal to the critical potential on a nonporous surface.

Adsorption in pores is modeled by confining chains to spherical pores of various sizes. We explore the range of pore radii $R_{pore} = 1.5\text{-}6b$ that corresponds to the conditions of strong $R_G/R_{pore} \sim 10$ to moderate $R_G/R_{pore} \sim 2$ confinement for the largest (N = 200) chains considered. The adsorption potential at the internal surface of pores is assumed to have the same square-well form as the potential at the external surface.

To demonstrate the effect of pore size on adsorption behavior, we present in **Fig. 6.4** the results of two computational experiments. In the first experiment, chains of lengths N =1-200 were completely confined within pores of a range of pore sizes R_{pore} = 2, 3, 4, 5 and 6b at $U = U_C$, and the chains were allowed to equilibrate. The incremental chemical potential of these chains was measured and plotted as a function of the chain length (see **Fig. 6.4**.A). It is clear from **Fig. 6.4**.A that the incremental chemical potential of confined chains is a monotonically increasing function of chain length due to the increasingly prohibitive entropic penalty to insertion of additional beads in a pore volume. The incremental chemical potential intersects the unconfined (free) chain value for some chain length $N = N^*$, (equivalently, gyration radius $R_G = R_G^*$), referred to here as the *critical chain length* and *critical gyration radius*, respectively. At N^* (R_G^*), the enthalpic and entropic interactions are exactly balanced. The values of the critical chain length/gyration radius are dependent on the pore size R_{pore} and decrease progressively as R_{pore} gets smaller. The dependence of N^* and R_G^* on R_{pore} is plotted below in **Fig. 6.4**.B.

The critical chain length N^* is quadratic in R_{pore} ($N^* \sim R_{pore}^2$) (equivalently, $R_G \sim N^{0.5}$) indicating that chains of length $N < N^*$ behave as *free chains* in the pore when the adsorption potential is at its critical value, U = -0.725. However, any chain larger than N^* will not hold to this scaling, due to the penalty imposed by the positive incremental chemical potential. The dependence of the critical gyration radius R_G^* on the pore size approaches a linear asymptote ($R_G^* \sim R_{pore}$) (**Fig. 6.4**.B, solid line) for large pores ($R_{pore} \geq 4$), indicating that as pore size increases, it is possible to directly predict the maximum chain size that will adsorb in the pore. There is deviation from the asymptote for small pores $R_{pore} \leq 4$, which is explained by the increasing effect of entropic confinement.

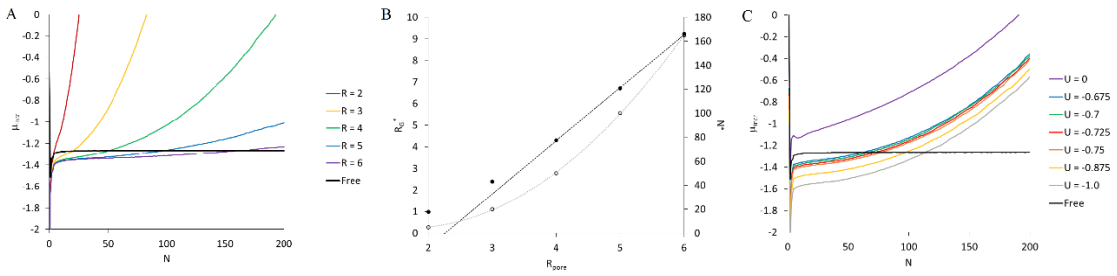

Fig. 6.4. Incremental chemical potential as a function of N for chains of length N = 1-200. A - chains confined to pores of size R_{pore} = 2, 3, 4, 5 and 6b at U = -0.725. Black line represents the incremental chemical potential of unconfined ('free') chain. B – Chain length N* (open circles) and gyration radii R_G* (closed circles) for which $\mu_{incr} = \mu_{incr}^{0}$, both as a function of R_{pore} for U = -0.725. Solid black line – asymptotic dependence of R_G* vs R_{pore} for larger pores. Dashed line – parabolic dependence of N* on R_{pore}. C - Chains confined to a pore of size R_{pore} = 4b for various adsorption potentials U spanning from 0 to -1. Black line represents the incremental chemical potential of unconfined chains.

In the second experiment, the incremental chemical potential of the chains was measured as a function of the adsorption potential U, for a single pore size, R_P = 4b *(*see **Fig. 6.4**.C*)*. At this pore size, chains of N < 50 beads ($R_G \leq 4$ in free solution) fit comfortably within the pore when exposed to adsorption potential U corresponding to critical conditions on a plain surface U = -0.725 (as per **Fig. 6.4**.B). However, beyond N = 50, the incremental chemical potential increases rapidly with N for all adsorption potentials considered. In the limit of an extremely strong potential, it is conceivable that any chain consisting of N < 200 beads could adsorb within the pore. However, the monotonically increasing chemical potential indicates that longer chains (N >> 200) would be totally excluded from this pore.

Fig. 6.4.C clearly demonstrates the absence of the critical adsorption conditions for this pore. This situation is applied in general case: critical conditions (Eq. 6.1) do not exist for real chains confined to pores of comparable or smaller size than that of the free chain. The results illustrated in **Fig. 6.4** confirm the earlier findings for excluded volume chains, which were reported for various pore geometries[50, 64]. To further illustrate this point, the difference in free energy $\Delta F = F(N) - F^0(N)$ and the partition coefficient $K_P = \exp[-\Delta F]$ for chains confined to pores of sizes R_{pore} = 1.5b and 4b are plotted as functions of N in **Fig. 6.5** below.

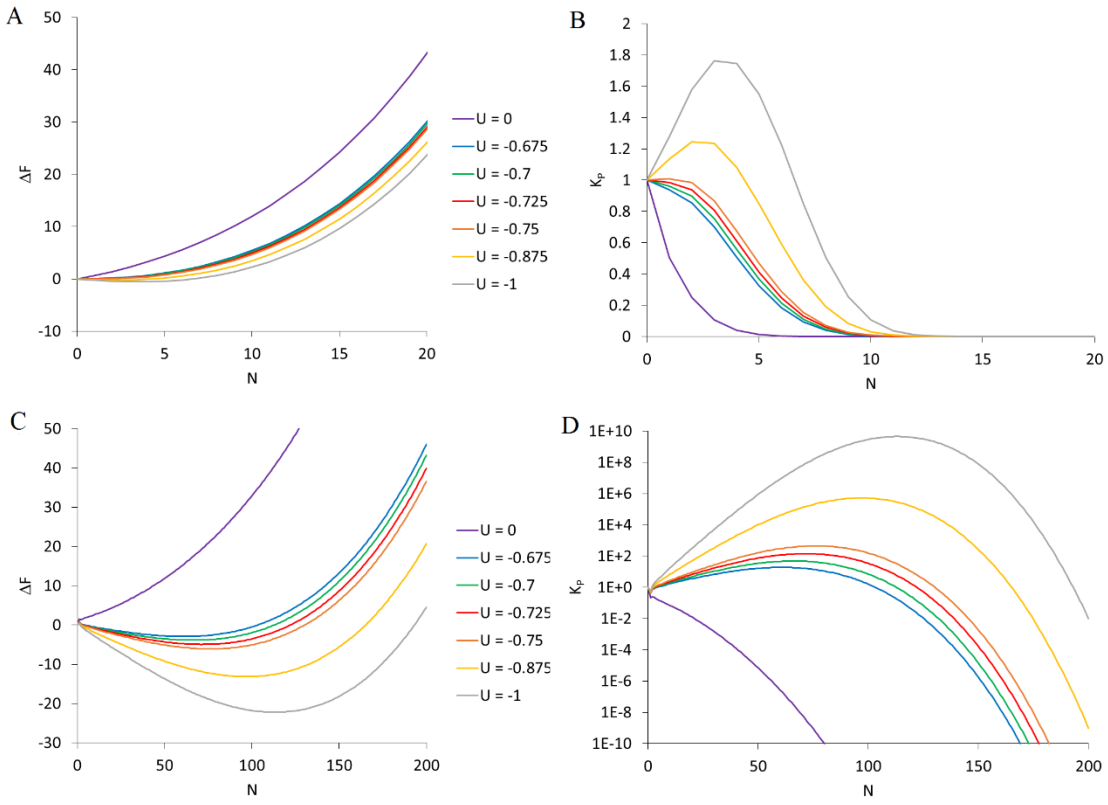

Fig. 6.5. The chain length dependences of the free energy difference $\Delta F = F(N) - F^0(N)$ (A,C) and the respective partition coefficient K_P (B,D) for the chains completely confined to a pore of $R_{pore} = 1.5b$ (top) and $4b$ (bottom) for a series of adsorption potentials $U = 0$ to -1.

The difference in free energy ΔF of confined chains plotted in **Fig. 6.5**.A,C shows several interesting features. First, in the absence of adsorption ($U = 0$), the free energy is monotonically increasing with N *regardless of the pore size*. This is consistent with the effect of a pore being gradually filled up with the chain of beads – as the pore fills, the work required to add another bead to the chain increases due to strictly entropic forces. In the presence of an adsorption potential, the shape of the free energy dependence changes dramatically. Instead of being monotonically increasing, the free energy experiences a minimum[72], after which the free energy becomes progressively positive as N increases. This minimum is more pronounced for the larger ($4b$) pore (**Fig. 6.5**.C) than the smaller pore (**Fig. 6.5**.A), and the chain length N_M at the point of minimum varies with U and R_{pore}.

The partition coefficient K_P for chains completely confined to pores is defined in terms of the exponent of the difference in free energy of confined and unconfined chains $K_P = \exp[-\Delta F]$. The plots of K_P as a function of chain length (**Fig. 6.5**, B,D) further illustrate the absence of critical conditions for finite length chains, regardless of pore size. At zero adsorption potential, the partition coefficient monotonically decreases as chain length increases, reflecting the increasing difficulty to force larger excluded volume chains into the pores. In the presence of adsorption potential, the partition coefficient is non-monotonic in a manner similar to the free energy. The partition coefficient increases with chain length for chains, which can fit in the pore with minimal restriction ($N < N_M$). The length N_M of the chains "most likely" residing inside the pore shifts to slightly larger values as adsorption potential increases. However, for $N > N_M$, the partition coefficient rapidly decreases with the chain length for all adsorption potentials due to severe entropic limitations, with the smaller ($1.5b$) pore (**Fig. 6.5**.B) accommodating roughly 10 beads ($R_G = 1.6b$ in free solution), and the larger ($4b$) pore (**Fig. 6.5**.D) up to 40 beads ($R_G = 4b$ in free solution) . The non-monotonic behavior of the partition coefficient reinforces the conclusion that critical conditions do not exist for the real chains completely confined to pores, when pore size R_{pore} is comparable to chain size R_G. This effect would not be observed for ideal chains, for which the CPA does exist [52]. Below, we show that the critical behavior observed in experiments is due to the adsorption mechanisms involving the external surface of the substrate.

6.6. Partially confined chains

The characteristic chain length N_M mentioned above is of special interest. Provided the pore has an opening, chains of length $N > N_M$ tend to escape from the pore, at least partially, forming so-called flower conformations[73]. Depending on the pore size, these partially confined states have been shown to make up a significant portion of chain's conformations[73]. A flower conformation consists of a "root" or *trans* section of the chain residing inside the pore and a "stem" or *cis* section hanging out of the pore. The stem of the flower conformation may either be adsorbed, if the

adsorption potential U is strong, or protrude into the bulk solution, if U is weak, (see **Fig. 6.6.** A, B). Partially confined flower chains help us to explain the presence of critical conditions on porous substrates where the pores are of smaller size than the polymer chains in free solution $R_{pore} < R_G$.

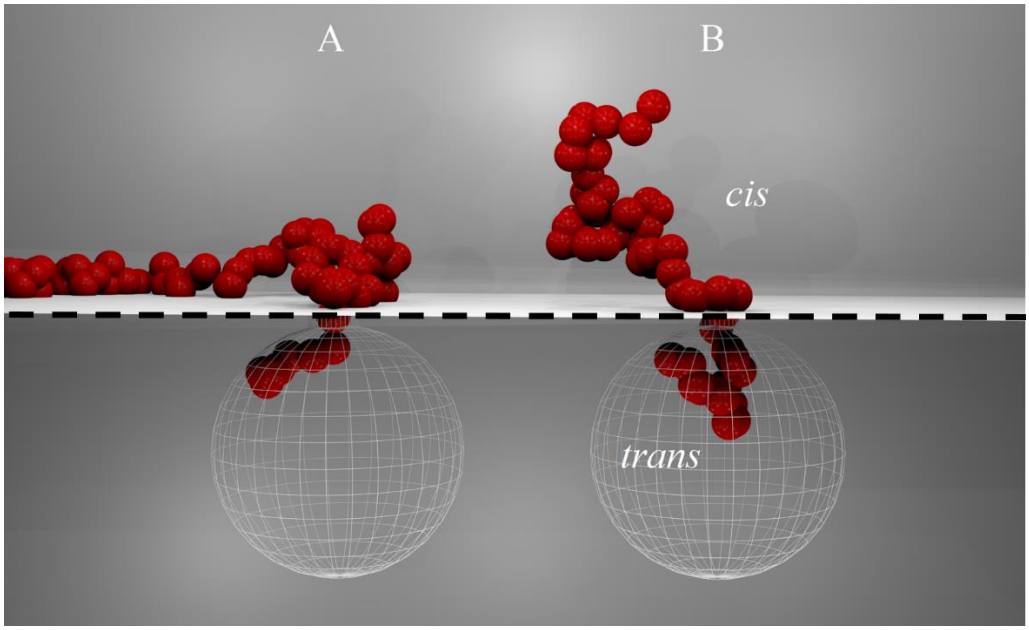

Fig. 6.6. Partially confined chains in two conformations: (A) strong adsorption ($|U| > |U_C|$) and (B) weak adsorption ($|U| < |U_C|$). Dashed line represents delineation between *cis* and *trans* states.

The free energy of partially confined chains was a subject of detailed studies related to the translocation of chain molecules into nanopores[65, 72]. The free energy of a partially confined chain of length N is presented as a function of the degree of translocation s – the number of monomers inside the pore. The free energy F (N, s) is composed of the free energies of *cis* $F^C(N\text{-}s)$ and *trans* $F^T(s)$ subchains: F (N, s) = $F^C(N\text{-}s) + F^T(s)$, where *cis* denotes beads outside the pore, and *trans* - inside the pore (See **Fig. 6.6**.B). The sub-chain free energies are themselves composed of the sum of the incremental chemical potentials for *cis* and *trans* chains of length N-s and s respectively. For details of the free energy calculations of flower conformations, see **Appendix E**.

The *cis*- and *trans*- sub-chains are simulated independently, in a manner similar to that used for externally adsorbed or completely confined chains. In each case, sub-chains are tethered by a terminal monomer with a center distanced 0.5b from the surface separating *cis* and *trans*

conformations (denoted by the dashed line in **Fig. 6.6**). Upon equilibration, the incremental chemical potentials of the *cis* and *trans* sub-chains are measured and the free energies of *cis* $F^C(N-s)$ and *trans* $F^T(s)$ subchains are calculated. The sum of sub-chain free energies gives the free energy $F(N,s)$ of the partially translocated chains with given degree of translocation.

In order to determine the free energy $F(N)$ of the ensemble of flower chains with different degrees of translocation $s = (1 \ldots N)$, one has to sum the Boltzmann-weighted free energies $F(N,s)$ of the chains with given degree of translocation[73] :

$$F(N) = -\ln\left(\sum_{s=1}^{N} exp\left(-F(N,s)\right)\right) \tag{6.4}$$

It is important to note that each state $F(N,s)$ is itself an ensemble average of the chain free energy representing the free energy of the most favorable conformations at given degree of translocation. **Fig. 6.7**.A-B below shows the incremental chemical potential and free energy difference $\Delta F = F(N) - F^0(N)$ as functions of the chain length N for chains partially confined to a small pore ($R_{pore} = 1.5b$) and exposed to different adsorption potentials.

The effect of the pore is evident from the behavior of the incremental chemical potential of the partially confined chains. For all but the smallest chain lengths, the incremental chemical potential is a constant in chain length and resembles the behavior of an end-tethered chain[197]. For strong potentials $|U| > |U_C|$, where $U_C = -0.725$ is the CPA found previously for non-porous surface, the incremental chemical potential is more negative than that of the free chain, indicating that the *cis* sub-chain is mostly adsorbed (**Fig. 6.7**.A). The incremental chemical potential for weak potentials $|U| < |U_C|$ however approaches the free chain value, indicating that most *cis* beads are not adsorbed (see **Fig. 6.7**.B). Noteworthy, at $U \sim U_C$, the incremental chemical potential equals that of an unconfined chain, fulfilling the CPA condition Eq. (6.1).

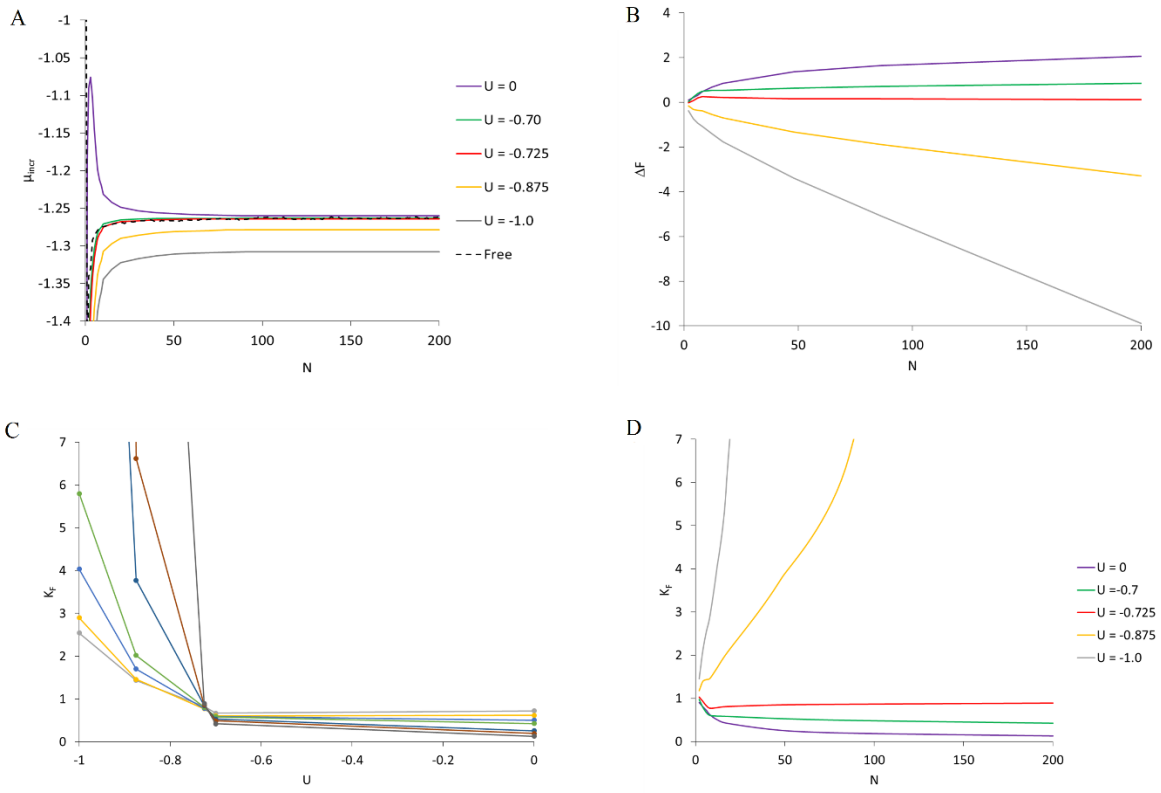

Fig. 6.7 (A) Incremental chemical potential, and (B) free energy difference as functions of chain length N for chains partially confined to a pore of radius 1.5b for several adsorption potentials U = 0 to -1. Partition coefficient K_F for chains partially confined to a pore of radius R_{pore} = 1.5b as (C) a function of adsorption potential U for several N and (D) for N = 1-200 for several U.

The difference in free energy (**Fig. 6.7**.B) as a function of the chain length is a clear indicator of the existence of critical conditions for partially confined chains. For adsorption potentials stronger than U_C, ΔF decreases with chain length, indicating that longer chains are more likely to be adsorbed than shorter ones. For potentials weaker than U_C, ΔF increases with chain length, meaning short chains are more likely to be adsorbed. At the critical conditions, the free energy difference becomes constant, and notably, this critical condition U_C = -0.725 is the same as for the externally adsorbed chains.

In a manner similar to completely confined chains, we define the partition coefficient for flower conformations as the exponent of the difference in free energy between a confined and unconfined chain: $K_F = \exp[-\Delta F]$. The partition coefficient for chains partially confined to a pore

of size R_{pore} = 1.5b is given in **Fig. 6.7**.C-D as a function of adsorption potential U and chain length N, respectively. The partition coefficient of partially confined chains demonstrates several key features, which differentiate it from the case of complete confinement. First, for potentials stronger than the critical conditions $|U| > |U_C|$, the partition coefficient is monotonically increasing in chain length. (**Fig. 6.7**.C, |U| > 0.725; **6.7**.D, yellow, gray lines). These potentials ($|U| > |U_C|$) indicate enhanced adsorption of longer molecules (LAC conditions). Second, there exists a characteristic potential (the critical point, U_C = -0.725), where the partition coefficient switches from a decreasing function of N to an increasing one (**Fig. 6.7**.C interstection point, **6.7.D** red line). At the critical potential U_C, the partition coefficient does not depend on N. This potential is identical to the critical potential of chains adsorbed at a non-porous surface, which was described above. For potentials weaker than that corresponding to the critical condition $|U| < |U_C|$, K_F decreases with chain length, indicating enhanced partition of small molecules (SEC conditions) (**Fig. 6.7**.C, |U| < 0.725, **6.7**.D, green, purple lines). The transition from SEC to LAC through the CPA is very sharp – adsorption is greatly enhanced (relative to the weak adsorption case) for all molecules beyond the critical conditions at $|U| > |U_C|$.

The ability of partially confined chains to experience critical adsorption conditions illustrates the importance of accounting for the mechanisms which include external surface adsorption in the case of porous substrates. Indeed, the mechanism of partial confinement offers an explanation for experimental observations of critical conditions. In the final section below, we explore the application of external surface adsorption and in particular, the contribution of partial confinement to chain retention in polymer chromatography on porous substrates.

6.7. Chain Retention on Porous Substrates

Assuming the thermodynamic equilibrium between unretained and retained analyte (chains), the retention volume V_R is defined as the ratio of the total quantity N_{tot} of analyte in the

column to the bulk concentration c_0 of the unretained analyte in the interstitial volume, $V_R = N_{tot}/c_0$. Accounting for all three possible mechanisms of retention, N_{tot} can be expressed as

$$N_{tot} = c_0[V_I + K_H S_{ext} + K_P V_P + K_F V_O] \tag{6.5}$$

Equation 6.5 states that the total amount of analyte in the column is divided into four contributions from chains located: (1) in the interstitial volume V_I (unretained), (2) on the external surface of the stationary phase particles of area S_{ext}, (3) completely within the pores of accessible volume V_P, and (4) at the external surface of stationary phase particles in flower conformations, where V_O is the volume of surface pore openings. Normalizing Eq. (6.5) by the bulk concentration c_0, one arrives at the equation of the retention volume

$$V_R = V_I + K_H S_{ext} + K_P V_P + K_F V_O \tag{6.6}$$

In the spirit of the Gibbs adsorption theory [143] the sum of the last three terms in the right-hand side of Eq.6.5 represents the excess adsorption $N_{ex} = c_0[K_H S_{ext} + K_P V_P + K_F V_O]$ of analyte in the column, as compared to the amount of analyte in the interstitial volume at the bulk concentration, $N_0 = c_0 V_I$. Provided the excess adsorption is attributed to the retained analyte, the overall partition coefficient K can be defined as the ratio of the *excess adsorption* concentration, $c_{ex} = N_{ex}/V_S$, per unit volume of the porous solid particles of volume $V_S = V_{col} - V_I$ and the bulk concentration c_0 in the solvent, $K = c_{ex}/c_0$ [221]. Note that the volume V_S includes the volume of pores inside the particles. As such, the retention expression (6.6) may be rewritten as $V_R = V_I + KV_S$, with the overall partition coefficient

$$K = K_H \hat{S}_{ext} + K_P \varepsilon_P + K_F \varepsilon_S \tag{6.7}$$

Here, $\hat{S}_{ext} = S_{ext}/V_S$ is the specific external surface area per unit volume of solid phase, $\varepsilon_P = V_P/V_S$ is the accessible porosity of the substrate, and ε_S is the surface porosity. The surface porosity is defined as $\varepsilon_S = n_S v_O \hat{S}_{ext}$; n_S is the number of pore openings per unit of external surface area and v_O

– the volume of one pore opening. These parameters are determined by the column packing geometry and particle structure. Eq. (6.7) represents the extension of the definition of the partition coefficient for a nonporous surface [221] to a porous substrate.

The chain model employed is described in **Section 6.3** with the monomer size scaled to represent the Kuhn segment of polystyrene at good solvent conditions (molar mass 832 Da, b=2nm)[62]. The chain length in the simulations varies from N = 2 to 200 that corresponds to the variation of molecular mass M of polystyrene fractions from 1,664– 166,400 Da. In **Fig. 6.9**, chain length N is converted to molecular mass M via the Kuhn segment mass.

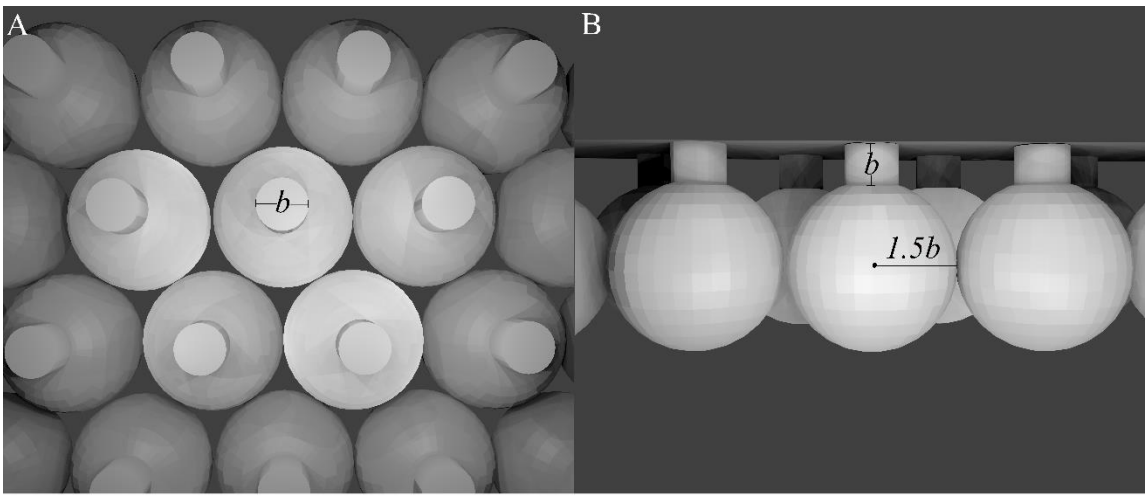

Fig. 6.8. Model porous substrate:.plane surface perforated by ink-bottle pores with spherical bodies and cylindrical openings. (A) Top-view (B) Side-view.

As a structural model of porous substrate, we use the surface perforated by ink-bottle pores with cylindrical pore openings and spherical pore bodies, **Fig. 6.8**. The diameter and length of the pore opening are set equal to the bead diameter b, so that $v_O = \pi b^3/4$. The size of pore bodies is set to $R_{pore} = 1.5b$, reflecting the nominal pore width of 6nm of NovaPak® C_{18} substrate from Waters Tech. (Milford, MA), used in[213]. Assuming a dense packing of spherical pores, the surface pore density is set to $n_S = 0.13/b^2 = 3.2\text{x}10^{12}/\text{cm}^2$. The fixed density n_S corresponds to a surface porosity of $\varepsilon_S = 0.1$ and an accessible volume porosity of $\varepsilon_P = 0.09$. This model implies that the retention

volume (6.6) depends only on two column parameters, the packing porosity $\varepsilon_C = V_I/V_{col}$, where V_{col} is the total column volume, and substrate external surface area S_{ext}:

$$V_R = \varepsilon_C V_{col} + S_{ext}[K_H + 1.8bK_P + 0.1bK_F] \quad (6.8)$$

Equation (6.8) is used directly to calculate the theoretical retention plotted in **Fig. 6.9**.B. To illustrate the influence of multiple retention mechanisms – and in particular the role of partial confinement (flower conformations) – on chain adsorption and partitioning, we have applied our model to a well-characterized example of isocratic elution of polystyrene (PS) fractions in binary mixtures of THF and ACN on a chromatographic column packed with porous particles [213].

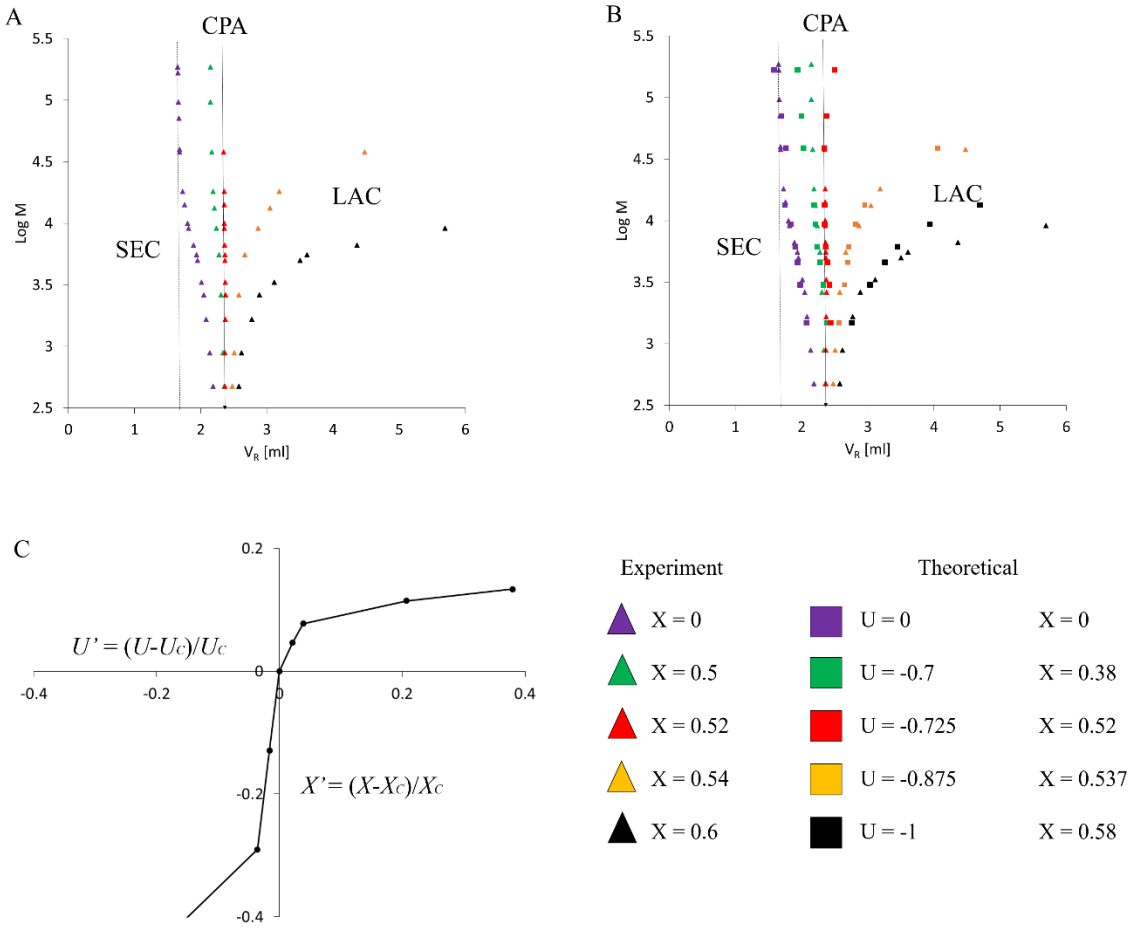

Fig 6.9. (A) Molecular mass *M* elution profiles for the isocratic separation of polystyrene [213]. The solvent composition *X* of the experimental data is given in terms of the volume fraction of

acetonitrile, X = 0 to 0.6. Three chromatographic modes, SEC, LCCC (elution at CPA) and LAC are clearly distinguished by the shape of elution profiles. (B) The same experimental data (triangle symbols) alongside theoretical retention volumes (square symbols) calculated using the retention equation (8) in conjunction with the partition coefficients derived from simulations. In both graphs, solid vertical line denotes CPA retention volume, V_{CPA} = 2.35 ml, dashed line – retention volume of largest chains, N = 200 in SEC mode (X = 0), fitted by adjusting the column porosity to ε_C = *0.53*, corresponding to interstitial volume V_I= 1.9 ml. (C) Correlation between effective adsorption potential U and solvent composition X in terms of dimensionless deviation U', X' from the critical values, U_C and X_C, for a nonporous column.

The diagram in **Fig 6.9**.A shows the experimental correlation between the chain molecular weight and the retention volume for a range of solvent compositions in terms of volume fraction X of ACN recalculated from the data presented in [213]. As clearly seen, the composition of X_C =0.52 corresponds to the critical conditions of molecular weight independent elution with the CPA retention volume V_{CPA}=2.35 ml. Compositions $X < X_C$ correspond to the SEC order of elution with larger chains eluted first, most prominent for the limiting case of pure THF (X = 0). At this mobile phase composition, (X = 0) the chain retention exhibits a characteristic shape that points toward different states of polymer chains depending on molecular weight. Larger chains are excluded from the surface and it is less probable for them to enter the pores of the substrate than for smaller chains. Conversely, it is possible for smaller chains to penetrate into the pores of the substrate and the retention of these chains may be influenced by the presence of partially confined (flower) conformations. Above the CPA (X > 0.52), the elution volume increases with the molecular weight that implies the LAC regime, with chains strongly attracted to the substrate and the reverse sequence of elution. Larger chains have a higher probability to interact with the substrate than smaller ones, and therefore are more strongly retained. When chains are strongly adsorbed, the enthalpic effects favor the chains to penetrate into the pores and therefore one may expect a larger contribution of flower conformations for chains of all molecular weights than is present in the SEC regime.

To describe the chain retention in this system, we made the following assumptions. First, we associated the SEC conditions observed in pure THF (X=0) with the negligible adsorption

potential, $U = 0$, and the CPA conditions at $X_C = 0.52$ with the critical adsorption potential $U = U_C = -0.725$. Next, we determined the packing porosity ε_C, and the external surface area, S_{ext}, which are the only two adjustable parameters in our model. The packing porosity $\varepsilon_C = 0.53$ (corresponding to $V_I = 1.9$ cm^3, for a column of volume $V_{col} = 3.58$ cm^3) was adjusted to fit the theoretical retention volume of chains of length $N = 200$ (V_R =1.6 ml, **Fig. 6.9**.B, dashed line) for the case of zero adsorption potential ($U = 0$) to the experimental retention of the largest (166,400 Da) chains in pure THF ($X = 0$). $S_{ext} = 4\text{x}10^5$ cm^2 was chosen to best reproduce the critical retention volume $V_{CPA} = 2.35$ ml (**Fig. 6.9**.A, B solid line). The value of S_{ext} is larger than the estimate made by assuming smooth, spherical particles of nominal radius $R_P = 2\mu$m[213], which may imply a significant degree of surface roughness and particle size heterogeneity. With these parameters, we predicted the retention behavior at different molecular weights and selected adsorption potentials (U=0, -0.7, -0.725, -0.875, and -1).

The experimental and theoretical retention are overlaid in **Fig. 6.9**.B. The square symbols correspond to the theoretical retention of chains exposed to a range of adsorption potentials $U = 0$ to -1. The experimental and theoretical retention volumes at SEC (X=0, U=0) and CPA (X=0.52, $U = U_C = -0.725$) conditions are in good agreement, since the selected points at these conditions were chosen for the fitting of model parameters. For potentials weaker than U_C, retention is a decreasing function of molecular weight. For potentials stronger than the critical value, the theoretical retention mimics qualitatively the behavior of chain retention in the LAC regime. Note that the shown experimental and theoretical dependences deviate because the chosen values of the adsorption potential do not match the experimental compositions.

In order to match the effective adsorption potential U employed in simulations and the solvent composition X, we employ the correlation derived in **Chapter 5** of this dissertation [221] for chain separation on a non-porous column, **Fig. 6.9**.C. This correlation relates the dimensionless deviations of the potential $U' = (U-U_C)/U_C$ and composition $X' = (X-X_C)/X_C$, both reduced to their

respective critical values. Using this correlation, the potentials employed in calculations U = (0,-0.7, -0.725, -0.875, and -1) correspond respectively to the solvent compositions X = (0, 0.38, 0.52, 0.537, 0.58). (See legend in **Fig. 6.9**). This correlation leads to logical results: theoretical and experimental retention volumes are properly ordered and theoretical data for X=0.38, 0.537, and 0.58 are located to the left of experimental data at X=0.5, 0.54, and 0.6, respectively. Noteworthy, the quantitative agreement found with the correlation derived for a non-porous column confirms the robustness of our model and transferability of obtained parameters.

In **Fig. 6.10**, we present the calculated contributions of different adsorption mechanisms in retention of polymer chains of different length at three different adsorption potentials U = 0, -0.725 and -1, which have been shown to correspond to the SEC, LCCC and LAC conditions from the experiments. We quantify the contribution of each mechanism to theoretical retention using the components of **Eq. 6.8** attributed to external surface, complete confinement to pores, and flower conformations, respectively:

$$V_{R,ext} = K_H S_{ext};\ V_{R,pore} = K_P 1.8 b S_{ext};\ V_{R,fl} = K_F 0.1 b S_{ext} \tag{6.9}$$

The contributions (6.9) in cm^3 are plotted as functions of the chain length. For the SEC regime (U = 0), the (exclusion) contribution from the external surface $V_{R,ext}$ dominates (**Fig. 6.10**.A); it is negative due to the excluded volume effects prominent in the absence of adsorption potential. The complete confinement contribution is negligible and the flower conformations contribute only into the retention of smaller chains. At the critical conditions ($U = U_C$), the contributions of external adsorption and flower conformations are comparable and constant for larger chains (**Fig. 6.10**.B). The contribution from the complete adsorption is notable only for the smallest chains and rapidly decreases with the chain length. Even at strong adsorption ($U = -1$), external adsorption and flower conformations dominate for all but the smallest chains (**Fig. 6.10**, C). Noteworthy, the contribution from complete adsorption progressively vanishes with the increase of the chain length and the decrease of adsorption potential, see **Fig. 6.10**.D.

This analysis indicates that adsorption on the external surface and partial confinement in pores represent the major factors determining chain partition. The mechanism of partial confinement (flower conformations) helps one explain the presence of critical conditions observed in polymer chromatography with porous substrates and resolve the controversy between the experimental observations and prior molecular simulations [50, 57] which focused entirely on the behavior of chains completely confined in pores neglecting the external surface effects.

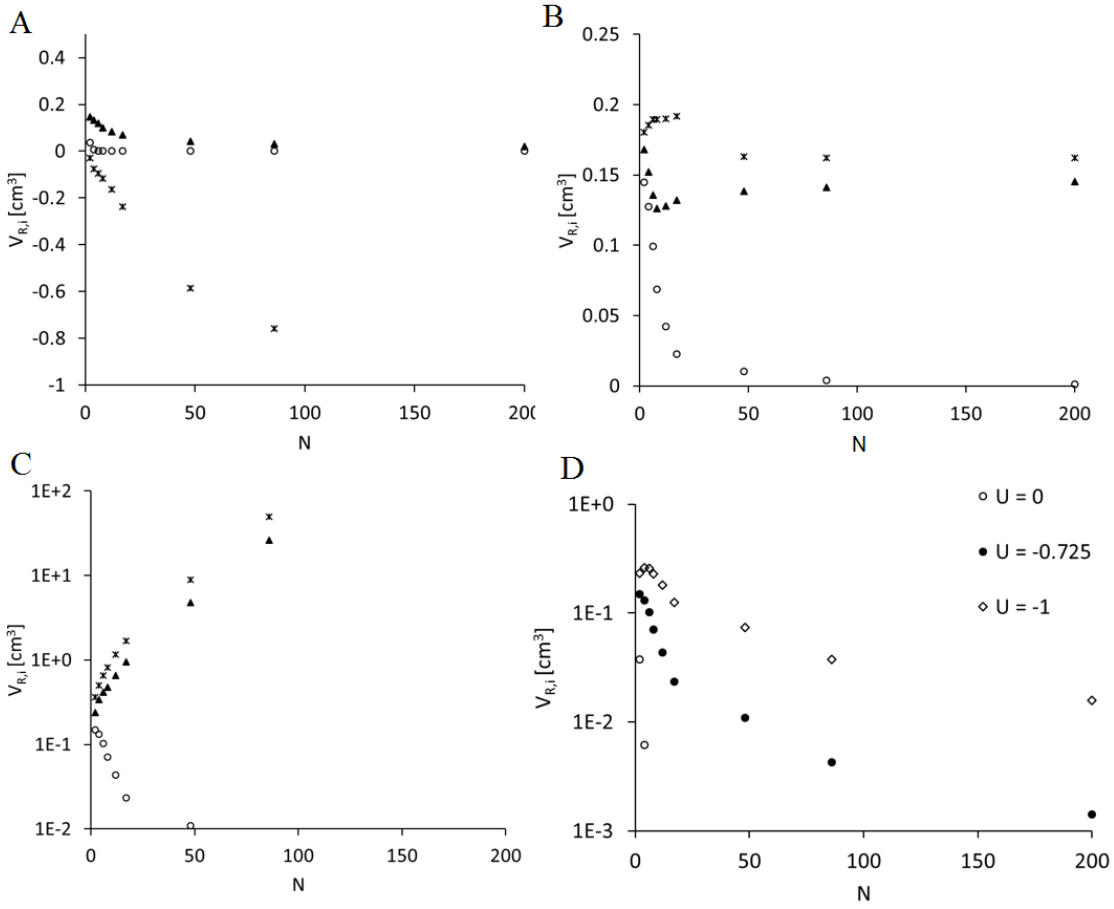

Fig. 6.10. Contributions of adsorption mechanisms in SEC, LCCC, and LAC regimes: A. $U = 0$, B. $U = U_C$, and C. $U = -1$. Symbols for A-C: Stars–external adsorption. Open circles – complete confinement. Filled triangles –flower conformations. D. Comparison of contribution of complete confinement across adsorption potentials – rapidly diminishes with the decrease of adsorption potential and increase of the chain length.

6.8. Summary

Using a simple excluded volume chain model and MC simulations of thermodynamic equilibrium between adsorbed and free chains, we examine mechanisms of chain adsorption on a model porous substrate searching for conditions of the critical point of adsorption (CPA), at which the partition coefficient in the process of chromatographic separation is chain length independent. We distinguish three adsorption mechanisms depending on the chain location: on external surface, completely confined in pores, and also partially confined in pores in so-called "flower" conformations. The chain adsorption is treated in terms of the Gibbs excess adsorption theory developed in **Chapter 5** for non-porous surfaces[143]. The thermodynamic condition of the CPA is defined from the equality of the incremental chemical potentials of adsorbed and free chains[197]. The free energies of different conformations of adsorbed chains are calculated by the incremental gauge cell MC method[198] that allows one to determine the partition coefficient as a function of the adsorption potential, pore size, and chain length. We confirm the existence of the CPA for the chain length independent separation on porous substrates, which is explained by the dominant contributions of the chain adsorption at the external surface, in particular in flower conformations. The CPA, known in chromatography as the LCCC regime, separates the regime of weak adsorption with SEC sequence of elution, with longer chains spending shorter time in the column, and the LAC regime of strong adsorption with the reverse sequence of elution. We show that as the magnitude of adsorption potential becomes stronger and approaches the CPA, the chains completely confined in pores are expelled to the external surface forming flower conformations. This mechanism was neglected in previous studies of excluded volume chains in pores, which questioned the very existence of the CPA for porous substrates. Moreover, we show that the critical conditions for porous and nonporous substrates are identical and depend only on the surface chemistry.

It is hypothesized that the experimentally observed critical adsorption on porous substrates may be explained by the presence of external adsorption and partially confined or 'flower

conformation' chains, and it was shown that flower conformations exhibit the same critical point as externally adsorbed chains.

The theoretical results are confirmed by comparison with experimental data on chromatographic separation of a series of linear polystyrenes with variable solvent composition[213]. The overall partition coefficient, which included contributions from all three adsorption mechanisms, was calculated for chains adsorbing to a model porous substrate perforated by ink-bottled pores. Although this model does not imitate the pore structure of real chromatographic substrates, it captures the major physical mechanisms in a coherent fashion. The advantage of this model is a minimal number of adjustable parameters, the column packing porosity and packing external area, which were determined to get the best fit to the experimental data on the retention volumes at the non-adsorption surface (SEC regime) and at CPA. The presence of molecular weight independent elution at CPA and SEC-, LAC-like behavior was confirmed by varying the adsorption potential. The retention volume contributions of each adsorption mode were calculated and compared at characteristic adsorption potentials, corresponding to SEC, LCCC, and LAC conditions. It was found that external adsorption and flower conformations dominate over the mechanism of complete confinement, providing an explanation for the disagreement between the results of previous simulations and experimental observations. Finally, using a correlation between the effective adsorption potential in our model and the solvent compositions previously determined for separations on nonporous substrate[221], the adsorption potentials in the porous substrate model were related to the expected solvent compositions that led to a quantitative agreement with the experimental observations.

In conclusion, we developed a thermodynamic framework for modeling chain adsorption on porous substrates that is based on the Gibbs excess adsorption theory and the establishment of the equilibrium conditions from the equality of excess free energies of the adsorbed and free chains. The critical conditions of chain length independent separation are defined by the additional

condition of equality of the incremental chemical potentials of the adsorbed and free chains. Using a simple yet instructive model of porous substrate, we show the existence of the CPA for excluded volume chains and describe the SEC, LCCC, and LAC regimes observed for separation of linear polystyrenes on non-porous and porous chromatographic columns in a unified fashion. A quantitative agreement was achieved with transferring the adsorption potential – solvent composition correlation determined for the non-porous column to the porous column. This confirms the robustness of the proposed methodology and its potential applicability, with proper extensions to more complex systems including block-copolymers, star polymers, end-functionalized chains, as well as to the challenging problem of separation of polymer grafted nanoparticles.

APPENDICES

Appendix A

Supplementary Information for Chapter 2

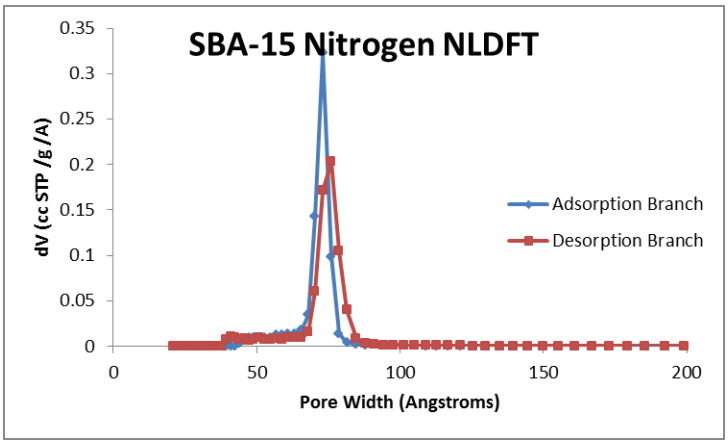

Fig. A.1. Volumetric differential pore size distributions calculated with the NLDFT model of independent cylindrical pores from adsorption (blue) and desorption (red) isotherms of N2 on SBA-15 shown in Fig. 2.2 (left). The two distributions agree within reasonable accuracy of the pore size characterization method.

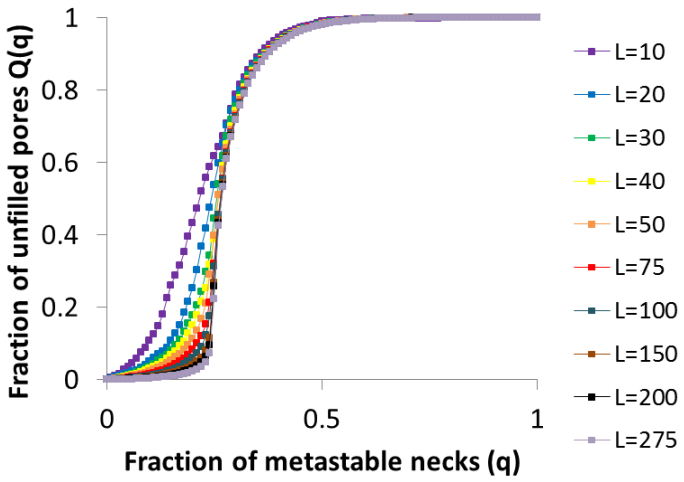

Fig. A.2. – A plot of the dependence of $Q_{-}(q)$ on the lattice size L, for $Q_{+}(\chi_a) = 0$ (boundary desorption). The lattice of size 200 is nearly indistinguishable from that of 275.

A. Fitting surface area parameter S_{FIT}

As discussed in section 2.3.1, the surface area parameter S_{FIT} in our modeling scheme is fitted to the adsorption isotherm, and is always found to be well within 15% of the BET surface area of the material. As an example, below we present a sample calculation of the BET surface and the corresponding S_{FIT} for SBA-15.

Procedure: The pressure points on the adsorption curve, from relative pressures of 0.0499863 to 0.349993, and corresponding to volumes of 258.681 cc/g STP to 429.5579 cc/g STP were plugged into the BET formula:

$$f\left(\frac{P_o}{P}\right) = \frac{1}{v * \left(\frac{P_o}{P} - 1\right)}$$

and plotted as a function of the relative pressure, P/P_o. The result was linear curve from which the slope and intercept were calculated. The monolayer capacity v_m was then determined by the following formula:

$$v_m[\frac{cc}{g}] = \frac{1}{slope + intercept}$$

The monolayer capacity in this case was found to be 285.06 cc/g, which was then used to compute the BET area as follows:

$$S_{BET}[\frac{m^2}{g}] = \frac{v_m\left[\frac{cc}{g}\right] * \sigma_{N_2}\left[\frac{nm^2}{molecule}\right] * N_A\left[\frac{molecules}{mol}\right]}{V_{STP}\left[\frac{cc}{mol}\right]} * \left(\frac{10^{-18}m^2}{nm^2}\right)$$

where V_{STP} = 22400, and σ_{N2} = 0.162. The resulting area is 1241.52 m^2.

$V_S(\chi)$ & $V_C(\chi)$: The theoretical boundary curves, corresponding to the nonporous adsorption (Vs) and the condensed fluid adsorption (Vc) were next computed using the newly fitted data. using the FHH equation for layer thickness, multiplied by a parameter representing the surface area:

$$V_s(\chi)\left[\frac{mmol}{g}\right] = \frac{S_{FIT}\left[\frac{m^2}{g}\right]\left(\frac{K}{-\ln(\chi)}\right)^{\frac{1}{m}}[\text{Å}]}{10 * V_{liq}\left[\frac{cc}{mol}\right]}$$

where V_{liq} is the liquid molar volume of Nitrogen at its boiling point 34.67(77K, 0.808 cc/g). K and m are FHH parameters with values 44.54 and 2.241, such that the layer thickness is in Angstroms. The fitting parameter S_{FIT} is then used to fine tune the equation and should be comparable (to within around 15%) of the BET surface area. In the case of SBA-15, S_{FIT} was chosen to be 1265, making the error negligible.

B. Expert choice of the limits of hysteresis

The limits of the hysteresis loop must be chosen such that there are well-defined limits of relative pressure χ, corresponding to the four major hysteresis loop points (A, B, C and E) (**See Fig. 2.6**). The procedure for choice of these four points can be broken down into two parts: choice of the departure points B and E, and choice of the closure points A and C.

Closure points: Closure points A and C are chosen by the experimental overlap of adsorption and desorption boundary curves.

Departure points: the points at which the boundary curves depart from V_C & V_S are similarly defined, as the experimental points at which the boundary curves no longer overlap the reference curves.

Thus we are limited by the uncertainty inherent to experimental measurement when defining these points, which is estimated as less than ~2% for our instrumentation.

C. Bond Percolation Algorithm

The following short C++ program can be used to generate the function $Q_{-}(q)$ for any $0 \leq Q_{+}(\chi_a) \leq 1$. The only line which must be altered is the value in parentheses for the integer 'empties', which corresponds to the fraction of unfilled pores at the beginning of scanning desorption.

```
/*Scanning Bond Percolation Program for 3D Cubic Lattice
 Richard Cimino, Rutgers University
 July 2012

 Based on the work of M.E.J. Newman and R.M. Ziff, 2001
 */

//Calculates the number of sites connected to the external
surface of a 3D Cubic Lattice over the complete
//range of metastable necks.

//Update Aug 1 2012 - fixed Q+(Xa) and measurement offset error.
Only interior sites may now become scanning sites
//Update Aug 2 2012 - Changed back to both interior and edge site
choosing. Enhanced site picking speed by changing temp
//                    to a vector and removing chosen sites.
Fixed an error creating a floating point exception.
```

```
/*-----------------------------------------------------------------
--------------------------------*/
//Preprocessor Directives and namespace declarations
# include <stdlib.h> //for compatibility with Linux machines
# include <iostream>
# include <vector>
# include <fstream>
# include <time.h>

using namespace std;

/*-----------------------------------------------------------------
--------------------------------*/
//Percolation Simulation Global Variables

const int L=200; //side length - maximum this program can utilize
const int N = L*L*L; //number of sites, total
const int S = (L-2)*(L-2)*(L-2); //total number of interior sites
const int N_Ext = N-S;//total number of exterior (boundary) sites
const int NS = L*L; //number of sites per slice
const int z = 6; //connectivity of the lattice
const int M =(1./2.)*N*z+N_Ext;//number of bonds - (Interior
Periodic) + Exterior Sites
const int empties = (0.85)*N; //number of internal sites empty at
beginning of simulation
int bond_list[M][2];//list of bonds: index:[site1][site2]
int ptr[N+1]; //pointer to sites; double duty: root: -cluster
size; nonroot: points to root; Nth = External Surface
int nn[N][z]; //array of nearest neighbors; used for filling
bond_list; [D U B F R L]
int order[M]; //order in which bonds are sequentially filled
int Ext[N_Ext]; //External surface sites
vector< vector < vector <int> > > temp;//temp array to hold site
numbers
int empty_pores[empties];//array to hold site numbers of empty
pores
double Qm[M]; //holds microcanonical measurements
double btr[M]; //holds binomial distribuition
//----------------------------------Main Program----------------
--------------------------------

void boundaries()
{    //set up nearest neigbor sites array with periodic
boundaries
    int i,j,k;
    int n = 0;

    //set up size of temp
    temp.resize(L);
    for (i = 0; i < L; ++i) {
        temp[i].resize(L);
    }
```

```
for (i = 0; i < L; ++i) {
    for (j = 0; j<L; j++) {
        temp[i][j].resize(L);
    }

}
for (i=0; i<L; i++) {
    for (j=0; j<L; j++) {
        for (k=0; k<L; k++) {
            temp[i][j][k] = n;
            //increment
            n++;
        }
    }
}

n=0; //set up nearest neighbor sites
for (i=0; i<L; i++) {
    for (j=0; j<L; j++) {
        for (k=0; k<L; k++) {
            if(j<L-1){nn[n][0] = temp[i][j+1][k];}
            if(j==L-1){nn[n][0] = temp[i][0][k];}
            if(j>0){nn[n][1] = temp[i][j-1][k];}
            if (j==0) {nn[n][1] = temp[i][L-1][k];}
            if(i<L-1) {nn[n][2] = temp[i+1][j][k];}
            if(i==L-1) nn[n][2] = temp[0][j][k];
            if(i>0){nn[n][3] = temp[i-1][j][k];}
            if(i==0) nn[n][3] = temp[L-1][j][k];
            if(k<L-1){nn[n][4] = temp[i][j][k+1];}
            if(k==L-1) nn[n][4] = temp[i][j][0];
            if(k>0){nn[n][5] = temp[i][j][k-1];}
            if(k==0) nn[n][5] = temp[i][j][L-1];
            n++;
        }
    }
}

//make a list of the exterior sites for use in bond_list
n = 0;
//k=0 surface
for (i=0; i<L; i++) {
    for (j=0; j<L; j++) {
        Ext[n] = (temp[i][j][0]);
        n++;
    }
}
//k=L-1 surface
for (i=0; i<L; i++) {
    for (j=0; j<L; j++) {
        Ext[n] = (temp[i][j][L-1]);
        n++;
    }
```

```
    }
    //i=0 surface
    for (j=0; j<L; j++) {
        for (k=1; k<L-1; k++) {
            Ext[n] = (temp[0][j][k]);
            n++;
        }
    }
    //i=L-1 surface
    for (j=0; j<L; j++) {
        for (k=1; k<L-1; k++) {
            Ext[n] = (temp[L-1][j][k]);
            n++;
        }
    }
    //j=0 surface
    for (i=1; i<L-1; i++) {
        for (k=1; k<L-1; k++) {
            Ext[n] = (temp[i][0][k]);
            n++;
        }
    }
    //j=L-1 surface
    for (i=1; i<L-1; i++) {
        for (k=1; k<L-1; k++) {
            Ext[n] = (temp[i][L-1][k]);
            n++;
        }
    }

    //set up empty_pores[] - edge sites are allowed - for now
   int col,row,dep;
   int ind;
   int counter = 0;

   while (counter<empties) {
       col = rand() % L; //from 0 to L-1
       row = rand() % L;
       if(temp[col][row].size() > 0){
           ind = rand () % temp[col][row].size(); //choose a
random site from temp[col][row] 0 to size-1
           empty_pores[counter] = temp[col][row][ind]; //allocate
this sitenumber to empty_pores
           temp[col][row].erase(temp[col][row].begin()+ind);
//remove this entry from the vector to prevent doubling
           cout<<"Empty Site ["<<counter<<"]:
"<<empty_pores[counter]<<endl;
           counter++;
       }
    }

}
```

```
void makelist(){
    //make a list of the bonds
    int i,j,n;
    n = 0;

    //interior bonds
    for (i=0; i<N; i++) {
        for (j=0; j<z; j++) {
            if(nn[i][j]>i){
                bond_list[n][0] = i;
                bond_list[n][1] = nn[i][j];
                n=n++;
            }
        }
    }

    //exterior bonds
    for (i=0; i<N_Ext; i++) {
        bond_list[n][0] = Ext[i];
        bond_list[n][1] = N;
        n=n++;
    }

}

void permutation(){
    //create a permutation of the bond numbers
    int i,j;
    int temp;

    for (i=0; i<M; i++) order[i] = i;
    for (i=0; i<M; i++) {
        j = i + (M-i)*drand48();
        temp = order[i];
        order[i] = order[j];
        order[j] = temp;
    }
}

int findroot(int i)
{ // recursive rootfinding algorithm
    if (ptr[i]<0) return i;
    return ptr[i] = findroot(ptr[i]);
}

void percolate(){
    int i,j;
    int s1,s2;
    int r1,r2;
    int big=0;
```

```
    for (i=0; i<N; i++) ptr[i] = -1; //set all interior sites to
cluster of size 1
    ptr[N] = -N-1; //set external surface site to -(N+1)

    for (i=0; i<empties; i++) { //create bonds between interior
empties and ext.
        s1 = empty_pores[i];//empty pore
        s2 = N;//exterior surface
        r1 = findroot(s1); //find the root of site 1
        r2 = findroot(s2); //find the root of site 2

        //update cluster information
        if (r1 != r2) {
            if (ptr[r1]>ptr[r2]) {
                ptr[r2] += ptr[r1];
                ptr[r1] = r2;
                r1=r2;
            }
            else{
                ptr[r1] += ptr[r2];
                ptr[r2] = r1;
            }
        }

    }

    for (i=0; i<M; i++) { //do bond percolation

        //site finding
        s1 = bond_list[order[i]][0]; //find site 1
        s2 = bond_list[order[i]][1]; //find site 2
        r1 = findroot(s1); //find the root of site 1
        r2 = findroot(s2); //find the root of site 2

        //update cluster information
        if (r1 != r2) {
            if (ptr[r1]>ptr[r2]) {
                ptr[r2] += ptr[r1];
                ptr[r1] = r2;
                r1=r2;
            }
            else{
                ptr[r1] += ptr[r2];
                ptr[r2] = r1;
            }
        }
        Qm[i] = (-ptr[N]-(N+1)); //microcanonical measurement
        cout<<"Sites connected to External Surface:
"<<Qm[i]<<endl;
    }

}
```

```
void binomial(double p){
    double C=0; //normalization
    int nmax = p*M; //set nmax

    btr[nmax] = 1;

    //range n < nmax
    for (int i = nmax-1; i>0; i--) {
        double num = (double)i + 1.0;
        double denom = (double)M-(double)i;
        double fract = num/denom;
        btr[i] = btr[i+1]*fract*((1.0-p)/p);
    }
    //range n > nmax
    for (int i = nmax+1; i<M; i++) {
        double num = (double)M -(double)i + 1.0;
        double denom = (double)i;
        double fract = num/denom;
        btr[i] = btr[i-1]*fract*(p/(1.0-p));
    }

    //normalization
    for (int i=0; i<M; i++) {
        C=C+btr[i];
    }
    for (int i=0; i<M; i++) {
        btr[i] = btr[i]/C;
    }

}

double calculate(double q){
    //calculate the value of the canonical ensemble
    int i;
    double Qp = 0;

    binomial(q);//call binomial calculator

    //take ensemble average
    for (i=0; i<M; i++) {
        Qp = Qp + btr[i]*Qm[i];
    }
    return Qp;
}

int main(){

    srand(time(NULL));
    srand48(time(NULL));

    boundaries();
```

```
    makelist();
    permutation();
    percolate();

    ofstream results;
    results.open("SimulationResults.txt");

    int Mesh = 100;
    for (int i=0 ; i<=Mesh; i++) {
        results<<((double)i/(double)Mesh)<<":
"<<calculate((double)i/(double)Mesh)<<endl;
    }
    results.close();

    return 0;
}
```

Appendix B

Supplementary Information for Chapter 3

A. CO_2-DFT liquid and vapor densities and CO_2 model surface tension

The VLE for CO_2 @ 273K was fitted by varying the fluid-fluid interaction energy parameter ε_{ff} to reproduce the theoretical VLE data gathered from NIST.gov's chemistry webbook (accessible online via http://webbook.nist.gov/chemistry/). A plot of the VLE (temperature-density) curve for CO_2 is presented below in **Fig B.1**. Notably, it is (not) possible for a 1-center LJ representation of CO_2 to reproduce the entire VLE curve using constant parameterization across temperatures. However, for our purposes, fitting to 273K is sufficient.

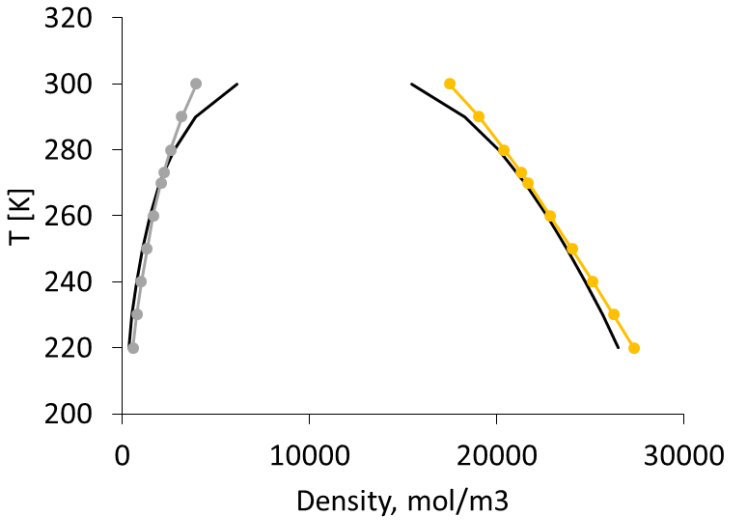

Figure B.1. Comparison of vapor (left branch) and liquid (right branch) densities as predicted with DFT (points) to NIST's empirical VLE data (line) for a range of temperatures.

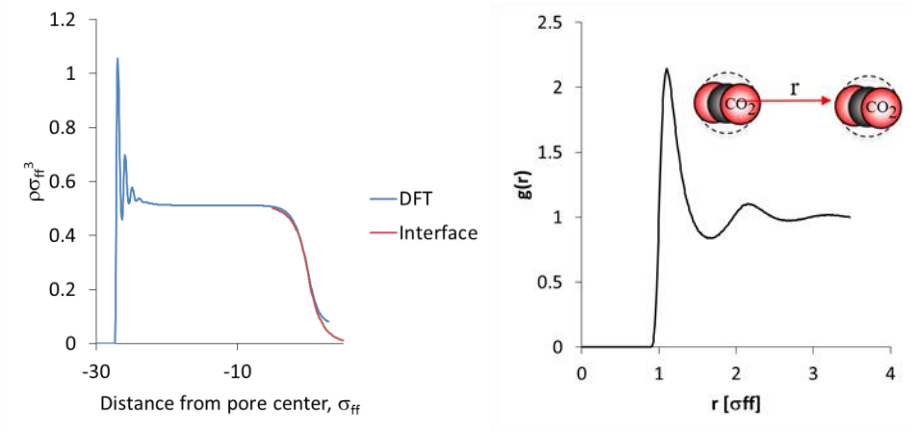

Figure B 2. (Left) QSDFT CO_2 density profile in $60\sigma_{ff}$ pore, used to fit the model (red line) vapor-liquid interface. The red-line is input to the surface tension equation. **(Right)** Radial distribution function $g(r_2\text{-}r_1)$ for Lennard-Jones CO_2, calculated by NVT MC simulation.

Accurately reproducing the liquid-vapor surface tension of the target fluid is considered a key property of fluid models for adsorption purposes. In this work, we estimate the surface tension of the CO_2 model using an approach devised by Berry, Durrans, and Evans [ref B1] in the early 1970s, which is easily applied to Lennard Jones molecules and DFT/Monte Carlo simulations. This method is based on the Kirkwood Buff theory and assumes a smooth transition from liquid to vapor phases across a well-defined interface. The model has the additional simplification that the radial distribution function is approximated by its liquid value over the entire interfacial (transition) region[ref B1].

The surface tension γ is presented in integral form over the interfacial region and takes into account the two particle distribution function n_2 and the interaction potential ϕ:

$$\gamma = \left(\frac{1}{2}\right)\int_{-\infty}^{\infty} dz_1 \iiint dr\, n_2(z_1, r)\left(\frac{d\phi}{dr}\right)(x^2 - z^2)/r \qquad \text{(B.A1)}$$

In this case, the interaction potential is the Lennard Jones potential, and its derivative is:

$$\left(\frac{d\phi}{dr}\right) = -\frac{48\epsilon_{ff}}{r}\left(\left(\frac{\sigma_{ff}}{r}\right)^{12} - \left(\frac{1}{2}\right)\left(\frac{\sigma_{ff}}{r}\right)^{6}\right) \qquad \text{(B.A2)}$$

The two particle distribution function n_2 is assumed to be directly related to the one particle distributions and the radial distribution function as:

$$n_2(r_1, r_2) \cong n(r_1)n(r_2)g(|r_2 - r_1|) \tag{B.A3}$$

The one particle distribution at the interface is modeled by a piecewise exponential function $n(z)$:

$$n(z) = \begin{cases} n_0\left(1 - \frac{e^{\frac{z}{L}}}{2}\right) & z < 0 \\ \frac{n_0}{2}e^{-\frac{z}{L}} & z > 0 \end{cases} \tag{B.A4}$$

Where n_0 is the bulk liquid density and L is the interface width. After some intricate integration, the surface tension can be rewritten in terms of the interface width and interparticle distance r as:

$$\gamma = \frac{\pi n_0^2 L^4}{8}\int_0^\infty dR_g(r)\left(\frac{d\phi}{dr}\right)\left\{\left(\frac{r}{L}\right)^4 - 8\left(\frac{r}{L}\right)^2 + 72 - e^{-\left(\frac{r}{L}\right)}\left(4\left(\frac{r}{L}\right)^3 + 28\left(\frac{r}{L}\right)^2 + 72\left(\frac{r}{L}\right) + 72\right)\right\} \tag{B.A5}$$

Application of Eq. B.A5 to estimate the surface tension of model CO_2 is straightforward. First, a single DFT calculation is performed in a large slit pore ($60\sigma_{ff}$) at $p \sim 0.9p_0$ and Eq. (B.A4) is fitted to the resulting liquid-vapor density profile (see **Fig. B.2**, (left). Use of a large pore ensures that 1.) there is a substantial liquid film along the pore wall 2.) that the liquid film is minimally affected by the solid-liquid interactions and 3.) that there is a well-defined liquid-vapor transition region in the density profile. A single NVT MC simulation is next run to determine the radial distribution function of the CO_2 molecules, given the DFT density and temperature. These functions are then plugged into Eq. B.A5 and integrated until the LJ cutoff (in this case, $5\sigma_{ff}$). The resulting surface tension for CO_2 at 273K is: 4.56 dyn/cm, which is in excellent agreement with experimentally determined surface tension estimates (4.57-4.62 dyn/cm) [refs B2, B3].

B. CO_2 Model Saturation Pressure

While the saturation densities and the vapor-liquid surface tension of the CO_2 model are in excellent agreement with empirical models and experimental data, the saturation pressure of CO_2 is not accurately predicted by DFT (shown below in **Fig. B. 3**, left). As such, the saturation pressure must be taken as an additional parameter of the model, in order to shift the condensation pressure of isotherms to the appropriate relative pressure. To determine the appropriate shifting satuation pressure, the CO_2 condensation pressures of the three experimental samples were mapped to their N_2 pore size. The plot of condensation pressure vs. pore size was then compared to the CO2 prediction, and the saturation pressure was fitted to minimize the least-square error between the experimental and DFT-calculated pore sizes/pressures. The fitting process is shown in Fig. B.3 (right). This work, the saturation pressure of CO_2 predicted by DFT is 38.9 bar and the fitted pressure is 36.5 bar.

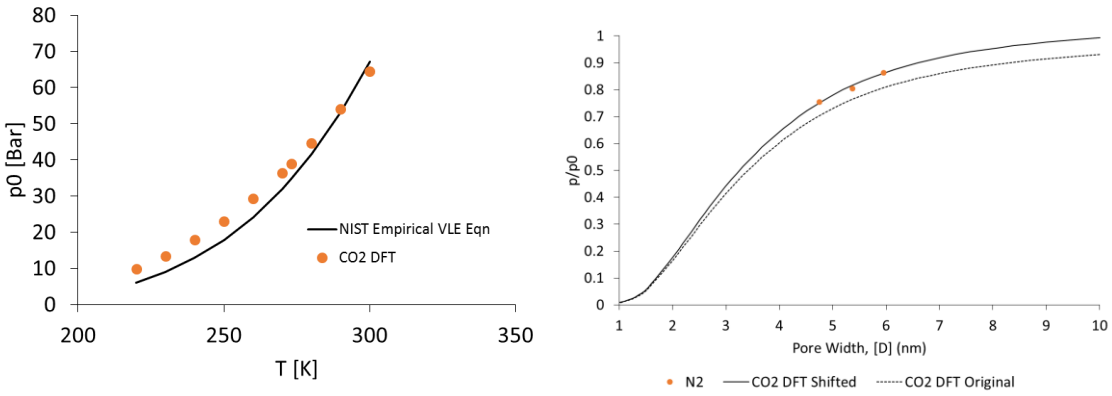

Fig. B. 3 (Left) Saturation pressure as a function of temperature for DFT (points) and empirical equation from NIST.gov. **(Right)** Fitting of the CO_2 saturation pressure by choosing p_0 to coincide with the N_2 pore size. (Points – N_2; solid line – CO_2 p_0 shifted to 36.5 bar; dotted line – CO_2 p_0 = 38.9 bar).

C. Fitting Comparison

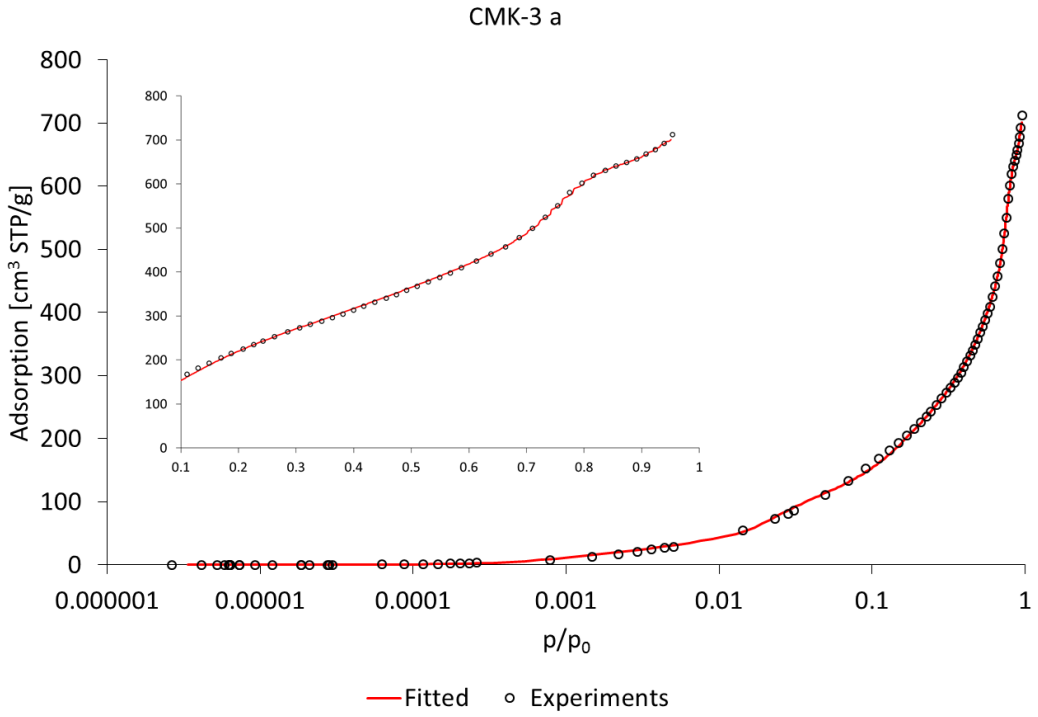

Fig. B.4 CMK-3 a experimental data (circles) alongside fits from slit/cylindrical kernel (line).

To determine the pore size distribution each isotherm in the applied kernel is are given a weight, which is then convoluted to produce a "best fit" composite isotherm. **Fig. B.4** illustrates one such best-fit isotherm (red line) for the CMK-3 sample a using the slit/cylindrical kernel (K3) for CO_2. With an appropriate pore model, the best fit isotherm should be well-fitted to the experimental isotherm over the entire range of relative pressures. The fit is excellent for this example, shown in log and linear scales to illustrate good fitting over multiple decades in relative pressure. In the inset of **Fig. B. 4**, a detail of the capillary condensation region is shown. The general fit of this kernel to the isotherm indicates that the assumption of slit shaped micropores and cylindrical mesopores is a decent assumption for this material.

D. Excess vs. Absolute Adsorption of CO_2

In the context of an adsorption experiment, the adsorption measurement provides the amount adsorbed n as a function of externally imposed pressure p. Due to the nature of volumetric adsorption experiments, this amount adsorbed n reflects not the total amount adsorbed (n^a) but the *excess adsorption*, $n = n^s$. The excess adsorption is defined in accordance with the Gibbs adsorption theory as the amount of adsorbed fluid which is in excess of the amount that would be present in the same volume, in the absence of an adsorbent. Use of the excess adsorption definition allows one to forego any definitions of adsorption which explicitly differentiate between "adsorbed" or "unadsorbed" molecules. The term *amount adsorbed* in adsorption literature most often to refers to the excess, as this is the quantity which is determined during volumetric adsorption experiments. For the more conventionally used analysis gases N_2 and Ar, where the adsorbate is far below the critical point, the excess adsorbed amount is essentially identical to the total amount adsorbed. This fact has enabled the direct correlation of theoretical DFT isotherms - which are always measured in absolute adsorption – to experimental isotherms, producing both accurate PSDs and total volume/surface area calculations. However, it is well known that CO_2 excess adsorption at pressures approaching 35 bar is significantly less than the absolute amount adsorbed.

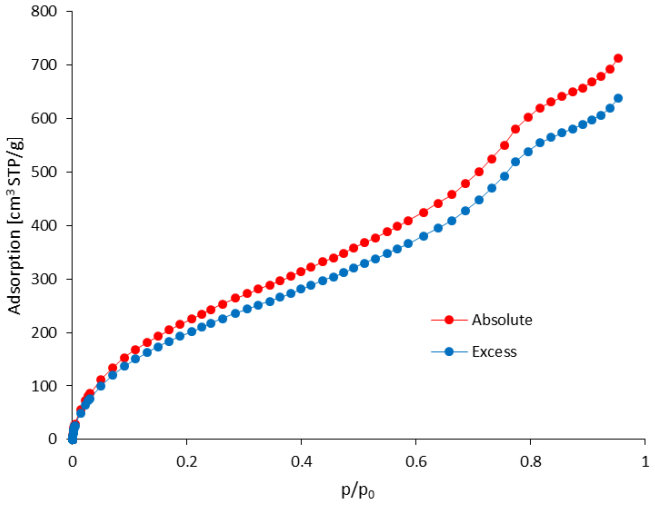

Fig. B. 5. Experimental adsorption isotherm of CO2 @ 273K on CMK-3 carbon. Blue – surface excess adsorption. Red – absolute adsorption, calculated using Eq. B.D1

The discrepancy between excess and absolute amount adsorbed for CO_2 has immediate consequences when characterizing experimental isotherms. As mentioned above, experiments do not record the absolute adsorbed amount – only the excess is measureable. For this reason, it is necessary to estimate the absolute adsorbed amount. In this work, conversion between excess and absolute adsorption is estimated using the following general equation:

$$n^a = n^s/(1 - \rho_v/\rho_l\,) \tag{B.D1}$$

Where ρ_v and ρ_l are the bulk vapor and liquid densities of CO_2 @ 273K, respectively. An example of the application of Eq. B.D1 is shown in **Fig.D. 5** above, which compares the surface excess adsorption of CO_2 @ 273 K on CMK-3 a carbon to the absolute amount adsorbed, as estimated by Eq. B.D1. In this example, the amount adsorbed in the primary mesopore plateau region (p/p_0 ~ 0.85) differs by approximately 20% between absolute and surface excess. In this case, application of standard methods such as the Gurvich rule that rely on the adsorbed amount would significantly underestimate the total pore volume if excess were used in place of the absolute adsorbed amount. In all of the main paper discussion, Eq. B.D1 has been applied to each experimental excess isotherm of CO_2, to arrive at an accurate estimate of the absolute adsorption. These absolute adsorption isotherms were in turn used to calculate the PSD and pore volumes of each sample.

E. Library of QSDFT Kernels for Ar adsorption on MMC

In addition to the CO_2 kernels developed for this work, several argon @ 87K kernels were developed with models identical to N_2 kernels previously published for analysis of micro-mesoporous (MMC) carbons in various geometries. A brief description of each Ar kernel is presented here for general information purposes. These kernels (along with the CO_2 kernels

described in **Chapter 3**) have been incorporated into the latest release of the Autosorb iQ software for data reduction analysis and are available to the public.

Ar @ 87K Cylindrical-Equilibrium

Kernel consisting of cylindrical geometry, equilibrium isotherms in the pore size range 0.5175 –-50.2 nm. This kernel is suitable to analyze the desorption branches of argon isotherms on hierarchically structured carbons.

Ar @ 87K Cylindrical-Adsorption

Kernel consisting of cylindrical geometry isotherms with 67 equilibrium isotherms in the pore size range 0.5175 –-4.84 nm and metastable adsorption isotherms in the range 5.0-50.2 nm. This kernel is suitable to analyze the adsorption branches of argon isotherms on hierarchically structured carbons.

Ar @ 87K Slit-Cylindrical-Equilibrium

Kernel consisting of slit geometry, equilibrium isotherms in the pore size range 0.325 – 2nm plus cylindrical equilibrium isotherms from 2.1-50.2 nm. This kernel is suitable to analyze the desorption branches of argon isotherms on hierarchically structured carbons with substantial activation.

Ar @ 87K Slit-Cylindrical-Adsorption

Kernel of slit equilibrium isotherms in the pore size range 0.325 – 2 nm plus cylindrical equilibrium isotherms in the pore size range 2.1 – 5.0nm plus cylindrical metastable adsorption isotherms from 5.2- 50.2 nm. This kernel is suitable to analyze the adsorption branches of argon isotherms on hierarchically structured carbons with substantial activation.

Ar @ 87K Cylindrical-Spherical Adsorption

Kernel of cylindrical equilibrium isotherms in the pore size range 0.5175 – 4.84 nm plus spherical metastable adsorption isotherms from 5.0- 50.2 nm. This kernel is suitable to analyze the adsorption branches of argon isotherms on hierarchically structured carbons with large cagelike pores connected by smaller windows.

Appendix B References

B1. Berry, M. V., Durrans, R. F., Evans, R. The calculation of surface tension for simple liquids. J. Phys. A. Gen. Phys. 1972 5(1) 166-170.

B2. Quinn, E. L. The surface tension of liquid carbon dioxide. JACS. 1927 49(11) 2704-2711.

B3. Skripov, V. P., Muratov, G. N. Data about surface tension of liquids and their analysis using thermodynamic similarity. Zh. Fiz. Khim. 1977 51(6) 1369-1372.

Appendix C

Supplementary Information for Chapter 4

A. Corroboration of IGCM results by the MDGC method and Chain Free Energy

The incremental chemical potential was calculated by both Ideal Gas (IG) and Mean Density (MD) methods. In the MD method, the incremental chemical potential for a chain of length *N* is calculated from a simple average of sampled incremental chemical potentials over the course of a simulation. The MD method assumes the 'mean density' of monomers in the gauge cell reflects the simulation's equilibrium state. The function $\mu_{incr}(N)$ is then 'built up' by averaging over many iterations of the same simulation for each value of *N* desired. In the IG method, a histogram (series of μ_{incr} values for N_i near *N*) of the incremental chemical potential is collected. Histograms for different chain lengths are then combined to create a 'smooth' function $\mu_{incr}(N)$. The latter method requires a relatively fine grid of *N*, to ensure that the histogram peaks overlap sufficiently to render a statistically sound average. The penalty of utilizing a fine grid however is more than compensated for when compared to the MD method, which takes anywhere from 20 to 100 simulations (per *N*) to render statistically sound results. In order to test the applicability of both of these methods, two sets of IGCM simulations were performed, one with MD and one with IG. The MD simulations consisted of 20 to 100 simulations at each value of *N* = 25, 50, 100, 150 and 200 for each value of *U* = 0, -3, -5, -6…-10. The IG simulations consisted of one simulation at each value of *N* = 3, 5, 10, 15…200, for the same range of *U* values. Each set consisted of 400 equilibration and 500 production sets of between 850,000 and 1 million Monte Carlo moves per set.

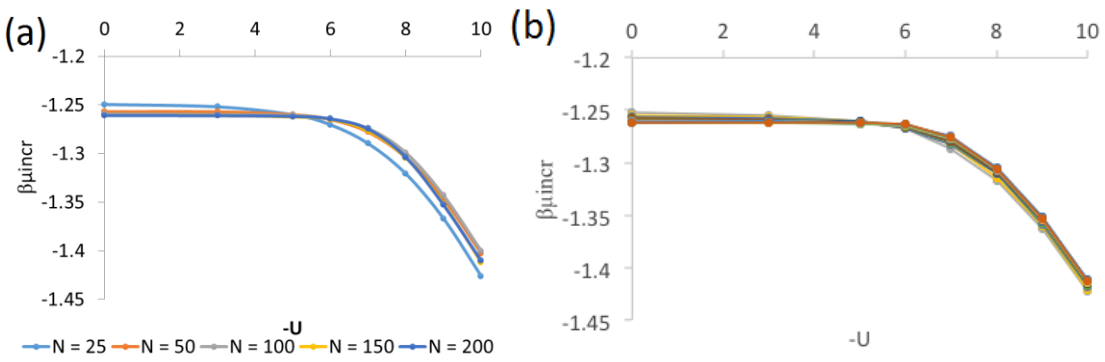

Fig. C.A.1. Dependence of the incremental chemical potential on the adsorption energy *U* for tethered chains of different length *N* from 25 to 200. The intersection point corresponds to the CPA at *U*=*Uc*=-5.4 +/- 0.05. Free jointed LJ chain model. Calculations with the incremental gauge cell MC method; (a) – MD, (b) – IG.. For the MD, *N* = 25, 50, 100, 150, 200. For the IG, results are presented for *N* = 30, 40, …, 200. In both cases, there is clear intersection at the point *Uc* = -5.4 +/- 0.05.

The chain incremental chemical potential for sufficiently large chains ($N > 30$) is shown to be a constant in our work. It follows that chain free energy, which is the sum of the chain incremental chemical potentials, should be linear in *N* for the same range of *N*. The linearity of the chain free energy dependence on *N* is illustrated in **Fig. C.A.2** below.

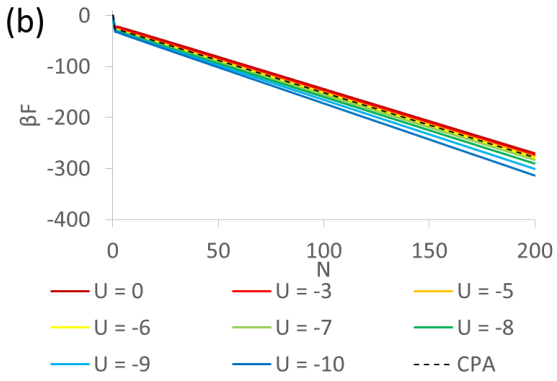

Fig. C.A.2. The chain free energy as a function of *N*. These calculations support the chain increment ansatz: for sufficiently large *N* the incremental chemical potential is constant and the chain free energy in a linear function of *N*.

B. Geometrical method for determination of the CPA

As noted in **Chapter 4**, DeGennes defined the CPA from the criterion that below the CPA, the probability P_a of adsorption for a monomer distanced from the tethered end by *n* monomers

decreases to 0 as *n* increases. Above the CPA, this probability approaches a finite limit as $n \to \infty$. The respective graph is shown in **Fig. C.B.1**. (a). Likewise, utilizing the ansatz (2), the CPA may be found from the extrapolation of the linear region of a plot relating the fraction of adsorbed monomers to the adsorption energy **Fig. C.B.1** (b).

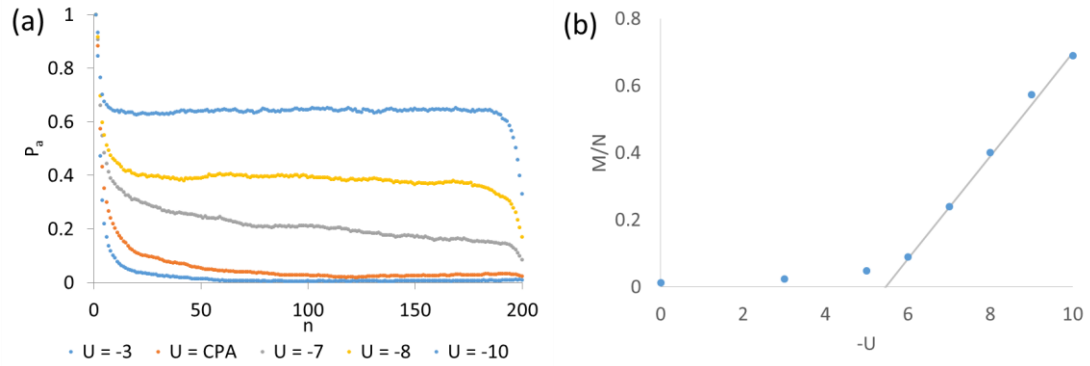

Fig. C.B.1. (a) Probability of adsorption for a monomer distanced from the tethered end by *n* monomers, P_a; Adsorption energies U = -3, -5.4 (CPA), -7, -8, and -10. Results averaged for 40 chains. (b) Fraction of adsorbed monomers M/N as a function of adsorption energy $-U$; N = 200.

Futhermore, in the geometrical framework several important scaling relationships for large chains have been developed. We are concerned here only with those governing the radii of gyration Rx^2, Ry^2 and Rz^2, from which are derived the radii of gyration normal and parallel to the surface of the adsorbent:

$$R_{g\perp}^2 = R_z^2 \tag{C.B.1}$$

$$R_{g\parallel}^2 = \frac{R_x^2 + R_y^2}{2} \tag{C.B.2}$$

These scaling relationships make use of the crossover exponent ϕ, and assume the following forms:

$$\frac{R_{g\perp}^2}{N^{\nu}} = h_{\perp}(x) = \begin{cases} c_{\perp 1} & x \to \infty \\ c_{\perp 2} & x = 0 \\ |x|^{-\frac{\nu_3}{\phi}} & x \to -\infty \end{cases} \qquad \frac{R_{g\parallel}^2}{N^{\nu}} = h_{\parallel}(x) = \begin{cases} c_{\parallel 1} & x \to \infty \\ c_{\parallel 2} & x = 0 \\ |x|^{\frac{\nu_2 - \nu_3}{\phi}} & x \to -\infty \end{cases} \tag{C.B.3a-b}$$

In (C.B3.a-b) $\nu_3 = 0.588$ and $\nu_2 = ¾$ are the 3d and 2d Flory exponents for polymer chains and $x = \tau N^{\phi}$. It is worth noting that these scaling equations are plausible qualitative approximations, which

reflect the asymptotic behavior at large *N*. Equations (C.B3.a-b) imply that the ratio of these primary radii of gyration gives rise to a function that is invariant in *N* at the critical point. Therefore, a plot of the ratio of the radii of gyration as a function of *U* for several values of *N* should intersect at the critical point, U_c. This property is used to estimate the critical point in the geometrical method. However, since it holds only with the provision of large enough *N*, the geometrical method applied for finite length chains may overestimate the critical point, as shown below in **Fig. C.B.2**.

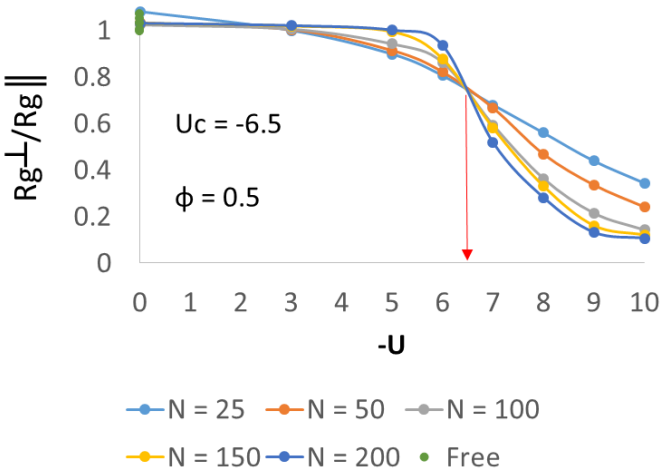

Fig. C.B.2. Ratio of the radii of gyration of a tethered chain as a function of adsorption energy. Clear intersection occurs at around *U* = -6.5, somewhat more negative in value than the IG/MD results.

For a long chain free in solution, the radii of gyration in each coordinate should approach the same value, and thus the polymer should approach a sphere-like shape. The ratio of these radii should therefore be unity, as is shown within experimental error in **Fig. C.B.2**. For a tethered chain, this ratio will necessarily be slightly skewed, due to anisotropy of the chain and the limitation of conformations thus imposed upon it. However, as the chain becomes large, this anisotropy should decrease. Indeed, we see in **Fig. C.B.2** that for chains beyond 50 monomers, this effect is about the same. In the presence of an adsorption field, the tethered chains undergo a geometrical transition, from the three-dimensional solvated chain, to one which is mostly adsorbed and two-dimensional. As implied by (C.B3.a-b), at the CPA, these curves should intersect for all values of *N*. **Fig. C.B.2**. shows that this transition does indeed occur, though at a value of *U* slightly more

negative than found by the adsorption method. The geometrical CPA occurs at approximately Uc_{GM} = -6.5 +/- 0.1.

In the repulsion limit at $x = \tau N^{\phi} \to \infty$, both $R_{\perp}$ and $R_{\parallel}$ scale as N^{ν_3}, and respectively $R_{\perp}/R_{\parallel}$~1. At the very CPA in the limit of $|\tau| \ll N^{-1/2}$, $h_{\perp}$ and $h_{\parallel}$ approach certain constants, $h_{\perp}(0)$ and $h_{\parallel}(0)$. Thus, the scaling *ansatz* (3) implies that $R_{\perp}/R_{\parallel}$ is independent of *N* at $\tau \to 0$. This conclusion was previously used by others (see **Chapter 4**) for the practical calculation of the CPA from the point of intersection of $R_{\perp}/R_{\parallel}$ versus *U* plots for the chains of different length *N*. However, since the scaling *ansatz* holds only with the provision of large *N*, such a geometrical method applied for finite length chains may overestimate the critical point. In addition it is worth mentioning, that from the asymptotes (4) it follows that $(R_{\perp}/R_{\parallel})N^{\nu_2} \propto |\tau|^{\frac{-\nu_2}{\phi}} = |\tau|^{-3/2}$ at $x \to -\infty$. As such, the CPA can be estimated by plotting $(R_{\perp}/R_{\parallel})N^{\nu_2}$ versus *U* and fitting to the asymptote $|\tau|^{-3/2}$. However, it does not seem to be practical for the relatively short chains *N*<200, as seen from **Fig. C.B.3**.

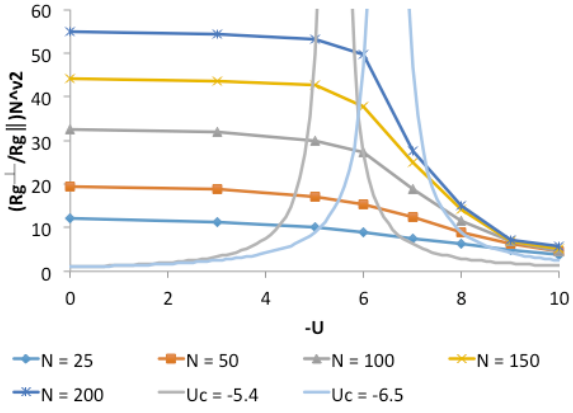

Fig. C.B.3. Plot of ratio of radii of gyration times N^{ν_2} versus adsorption energy. Asymptotic lines for $|\tau|^{-\frac{3}{2}}$ versus *U* also included for U_c = -5.4 and -6.5.

C. Alternative consideration of the scaling at CPA.

$R_\perp$ is determined by the characteristic length l of the loops formed by non-adsorbed monomers, as $R_\perp \propto l^{\nu_3}$. The loop length $l \propto \frac{N}{M} \propto N^{1-\phi}$, and, as such, $R_\perp \propto N^{(1-\phi)\nu_3}$. $R_\parallel$ is determined by the distribution of M=N^ϕ adsorbed monomers; this distribution can be viewed as resulting from a 2d random walk with the characteristic step equal to the characteristic loop extension in the parallel direction, which should be of the order of $R_\perp$. Thus, $(R_\perp/R_\parallel) \propto N^{-\phi\tilde{\nu}_2}$, where $\tilde{\nu}_2$ is the respective 2d random walk exponent. It is debatable whether this 2d random walk should be treated as ideal or as a self-avoiding trajectory; in the former case $\tilde{\nu}_2$=1/2 and $(R_\perp/R_\parallel) \propto N^{-1/4}$, while in the latter case $\tilde{\nu}_2$=3/4 and $(R_\perp/R_\parallel) \propto N^{-3/8}$. This consideration negates the above conclusion that that $R_\perp/R_\parallel$ is independent of N at $\tau \to 0$, which is worth additional verification.

Appendix D

Supplementary Information for Chapter 5

A. Glossary

a_{ex}	Excess adsorption
b	Polymer chain model unit size (Kuhn segment)
c	Concentration of chains near a surface
c_0	Bulk concentration of chains
D_{col}	Column diameter
D_M	Diffusion coefficient
d_p	Particle diameter
F	Excess free energy of a chain molecule
F^{ads}	Excess free energy of an adsorbed chain molecule
F^0	Excess free energy of a free chain molecule
K	Thermodynamic partition (distribution) coefficient of polymer chromatography
K_H	Henry adsorption coefficient
K_{LAC}	Partition coefficient of liquid adsorption chromatography
K_{LCCC}	Partition coefficient of liquid chromatography at critical conditions
K_{SEC}	Partition coefficient of size exclusion chromatography
k_B	Boltzmann constant
k’	Retention factor
l	Characteristic length scale (for Péclet number)
N	Chain length (number of segments)
N*	Characteristic chain length
N_{tot}	Total amount of analyte in column
Pe	Péclet Number
R_C	Capillary radius
Re	Reynolds Number
R_{eff}	Effective hydrodynamic radius of chain
R_G	Radius of gyration
R_P	Average particle radius
S	Surface area of stationary phase
T	Kelvin Temperature
T*	Reduced temperature
t_m	Retention time of a solvent molecule
t_R	Retention time
U	Adsorption potential of solid wall
U’	Reduced, normalized adsorption potential
U_{CPA}	Critical adsorption potential
V_{col}	Total column volume
V_I	Interstitial volume
V_L	Liquid volume
V_M	Mobile phase volume
V_P	Particle pore volume
V_R	Retention volume
V_{ST}	Stationary phase volume
V_S	Volume of solid particles
v_0	Superficial column velocity
$\dot{v}_0$	Volumetric flow rate
X	Mobile phase composition

X' Reduced, normalized mobile phase composition
z Perpendicular distance from a flat adsorbing surface

Greek Symbols

ΔF Difference between chain excess free energy in the adsorbed and free states
δ_{film} Stagnant zone thickness
ϵ Column packing porosity

Greek Symbols (cont'd)

λ Ratio of chain radius of gyration to capillary radius
ρ Fluid density
η Fluid viscosity
μ_{incr} Incremental chemical potential
μ_{incr}^{0} Incremental chemical potential of free chain

Abbreviations

ACN Acetonitrile
CPA Critical point of adsorption
HDC Hydrodynamic Chromatography
HPLC High performance liquid chromatography
ICP Incremental chemical potential
LAC Liquid adsorption chromatography
LCCC Liquid chromatography at critical conditions
MC Monte Carlo
SEC Size exclusion chromatography
THF Tetrahydrofuran
UV Ultraviolet

B. MC Simulations and Derivation of Henry Coefficient

The Henry coefficient is a thermodynamic variable comprised of the statistical sum of chain configurations within an arbitrary volume $V = S \cdot L$ that encompasses the adsorption interface and some part of the bulk volume. The Henry coefficient is also a function of the chain length and excess free energy (see Eq. (5.5) in the main text and (**Fig. D.1**). Assuming that the adsorbent is planar and homogeneous in the directions parallel to the adsorption surface, only variation in the chain configurations perpendicular to the surface will affect the chain free energy. Therefore, free energy of the chain is characterized as a function of the chain length and the perpendicular distance from the adsorbing surface, *z* as *F(N,z)*.

The MC simulations sample the volume *V* near the adsorbing surface and measure the incremental chemical potential of chains in order to ultimately determine the Henry coefficient. In each set of simulations, a chain is anchored by a terminal monomer (gray beads in **Fig. D.1**, below) at a distance z and is grown from 1 to *N* beads. The incremental chemical potential of the chain μ_{incr} is determined for each chain length 1 to *N* and the free energy of the chain of length *N* is calculated using $F(N,z) = \sum_{i=0}^{N-1} \mu_{incr}(i,z)$.

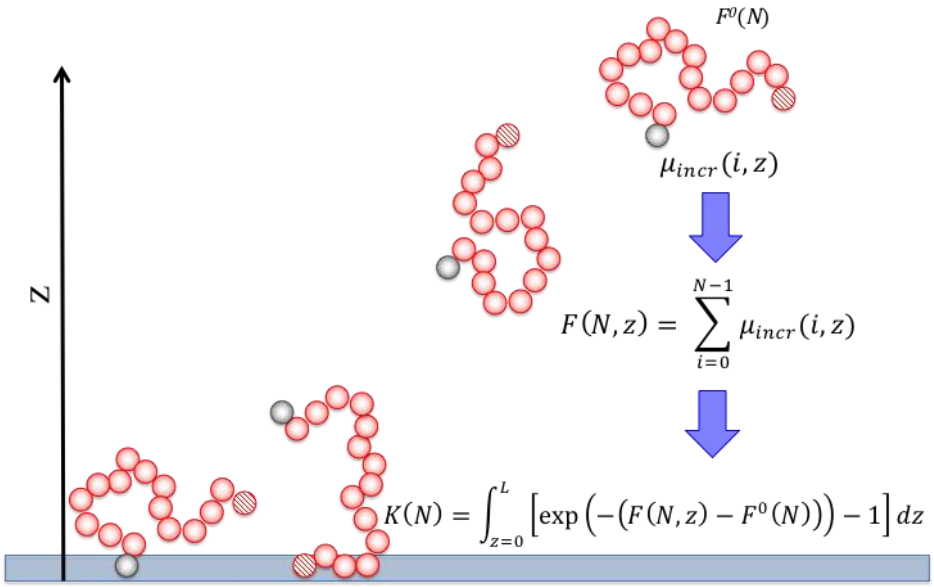

Figure D.1. Schematic of calculation of the Henry coefficient of chains interacting with the surface. Chains are distinguished by the position z of the end segment. By using MC simulation, we compute the incremental chemical potentials and excess free energies of chains anchored at distance *z* from the surface. The Henry coefficient is determined by the integrating along z the ratio of Boltzmann factors of anchored and free chains.

The free energy of the chain is then used to relate the concentration of chains of length *N* at any point z = {0,…,L}within the volume *V* to the bulk chain concentration via the Boltzmann weight of the chain free energy: $c(N,z)/c_0 = \exp[-(F(N,z)-F_0(N))]$. The *excess adsorption* a_{ex} is the amount of *N*-chains present in *V* in excess of the bulk concentration, $c_0(N)$.

$$a_{ex}(N) = \int_{z=0}^{\infty} [c(N,z) - c_0(N)]\, dz$$

The Henry coefficient K_H and excess adsorption a_{ex} are directly related through the definition: $a_{ex}(N) = K_H(N) \cdot c_0(N)$. Rearranging the $a_{ex}(N)$ expression for K_H, we obtain:

$$K_H(N) = \frac{\int_{z=0}^{\infty}[c(N,z) - c_0(N)]\, dz}{c_0(N)}$$

The bulk concentration is assumed to be constant and as such may be rearranged in the integral:

$$K_H(N) = \int_{z=0}^{\infty} \left(\frac{c(N,z)}{c_0(N)} - 1\right) dz$$

Using the equality $c(N,z)/c_0 = \exp[-(F(N,z)-F^0(N))]$, we arrive at Eq. 5.5 in the main text:

$$K_H(N) = \int_{z=0}^{\infty} [\exp[-F(N,z) - F^0(N)] - 1] dz$$

C. Hydrodynamic effects in the absence of adsorption.

The prediction of retention volume for the case of non-porous particles is dependent on the geometry/topology of the stationary phase and velocity of the fluid flowing through the column. Chains eluting in these columns are subject to different separation mechanisms (SEC, HDC, or a combination thereof) depending on the column properties [ref D1]. The discussion below compares the predictions of the standard hydrodynamic chromatography (HDC) model for the separation in

the column considered in this study in non-adsorption mode (left most data points in **Fig. 5.4** in the main text).

The Reynolds number Re of a fluid is a dimensionless grouping which is used to determine the flow regime. A laminar flow (Re < 100) is necessary to apply the hydrodynamic equations to a packed bed [ref D1]. Assuming roughly spherical stationary phase particles, the Re is given by:

$$Re = \frac{d_P v_0 \rho}{\eta}$$

The particle diameter d_p in this work is 2 microns and the average column velocity v_0 is 0.06 cm/s. The density and dynamic viscosity of THF are ~ 0.88 g/cm3 and 0.48cP at the column temperature (35 °C) [ref D2] . At these conditions, the Re is ~ 0.002, indicating laminar flow. For a column under laminar flow, we may invoke standard theory of hydrodynamic chromatography under Poisseulle flow to describe the separation of particles by their hydrodynamic radii. The retention time t_R of small particles in laminar flow in a packed bed is given by [ref D1]:

$$t_R(\lambda) = t_m(1 + 2\lambda - C\lambda^2)^{-1} \quad \text{(D.1)}$$

where t_m is the residence time of a very short chain (here, 4.37 min) and C = 2.698 for dilute solutions in thermodynamically good solvent . The aspect ratio $\lambda = R_{eff}/R_C$ is the ratio of the effective chain radius R_{eff} to the capillary radius R_C. The effective chain radius may be estimated as $R_{eff} \approx R_G\sqrt{\pi}/2$, where R_G is the chain radius of gyration. The radius of gyration for linear polystyrenes is proportional to the molecular weight [ref D3]: $Rg = 0.0118Mw^{0.6}$. Using the experimental range of chain lengths in this paper, R_{eff} ranges between 1.4-26.9nm. The capillary radius is defined by the particle diameter (2 micron) and column porosity $\epsilon = 0.44$: $R_C = \left(\frac{d_P}{3}\right)\left(\frac{\epsilon}{1-\epsilon}\right) = 5.2\ \mu m.$

The retention volume is then easy to calculate: $V_R = t_R \dot{v}$. The plot of the results obtained from hydrodynamic equation (D.1) vs. the experimental and simulation retention volumes is shown in **Fig. D.2** below:

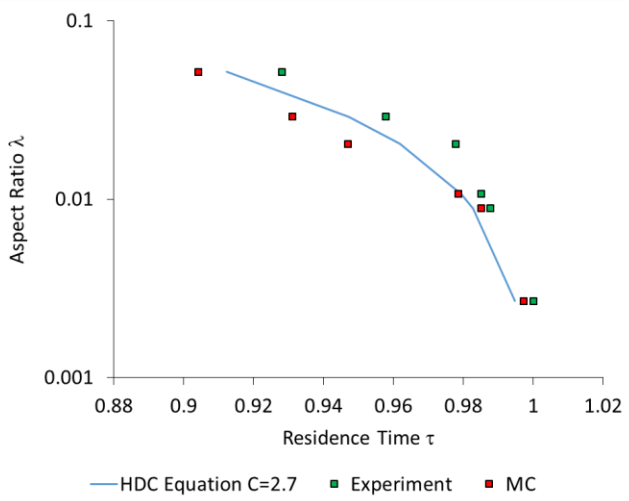

Figure D.2. Comparison of the retention volume predictions for the SEC mode (no adsorption potential) from hydrodynamic equation (blue line) and Monte-Carlo simulations (red triangles) as compared to the experimental data (green circles).

Comparison of the experimental elution (green circles) with the entropic repulsion predictions from simulations (red triangles) and hydrodynamic separation (blue line) reveals that the hydrodynamic mechanism described by the standard model of the Poiseulle flow in cylindrical capillary is reasonably suited to explain the separation of all chains on this nonporous column in the absence of adsorption; it only moderately underestimates the elution volume as the chain size increases.

Another approach to account for the flow inhomogeneity, which may explain a discrepancy between HDC equation and the simulation results, is based in the division of liquid volume into the flow and stagnant zones [ref D4]. This model is implied in our work. For the system in this study all chains are orders of magnitude smaller than the column hydrodynamic radius R_C. Our simulations and the corresponding retention volumes do not take into account the real distribution of the flow velocities. It is assumed that the flow may be separated into two regimes: a constant plug flow of velocity v_0 and stagnant zones of velocity ~ 0. We further assume the stagnant zones

present in the column are wide enough to encompass all polymer interactions near the stationary phase and are significantly wider than the radii of gyration for the largest chains considered.

To show the feasibility of this argument let's estimate of the stagnant zone thickness. The group of Ulrich Tallarek [ref D4] has shown that the Péclet number can be used to determine the effective width of the stagnation zone δ_{film} in a chromatographic column using the following relationship:

$$\delta_{film} \propto \frac{R_C}{\mathrm{Pe}^{\frac{1}{3}}}$$

The Péclet number for the nonporous column is proportionate to the characteristic length l (in this case R_C), superficial velocity and inverse diffusion coefficient [ref D5]: $Pe \propto l \cdot v_0/D_M$. Estimation of the Pe by order of magnitude gives:

$$Pe \propto \frac{10^{-4}[cm] \cdot 10^{-1}\left[\frac{cm}{s}\right]}{10^{-5}\left[\frac{cm^2}{s}\right]} \sim \mathcal{O}(1)$$

It is worth noting that the δ_{film} relationship above was implemented for systems with particle sizes an order of magnitude larger than our experimental system. However, it is reasonable to assume the behavior of the fluid scales similarly for smaller sized particles, given the laminar nature of the flow. With a Pe number of $\mathcal{O}(1)$ and R_C of $\mathcal{O}(10^{-6})$ m, it is evident that the stagnant zones are much larger than the average radii of gyration of the largest chains $\mathcal{O}(10^{-9})m$. As such, the assumption of wide stagnant zones is feasible.

Appendix D References

D1. Striegel, A., Brewer, A. Hydrodynamic Chromatography. Annu. Rev. Anal. Chem. 5 (2012) 15–34.
D2. Metz, D., Glines, A., Density, viscosity, and dielectric constant of tetrahydrofuran between -78 and 30.degree. J. Phys. Chem. 71 (1967) 1158-1158.
D3. Edam, R., Eeltink, S., Vanhoutte, D. J.D., Kok, W. Th., Schoenmakers, P. J. Hydrodynamic chromatography of macromolecules using polymer monolithic columns. Journal of Chromatography A. 1218 (2011) 8638-8645.

D4.Tallarek, U., Vergeldt, F. J., Van As, H. Stagnant Mobile Phase Mass Transfer in Chromatographic Media: Intraparticle Diffusion and Exchange Kinetics. J. Phys. Chem. B 103 (1999) 7654-7664.
D5. von Meerwall, E. D., Amis, E. J., Ferry, J. D. Self-Diffusion in Solutions of Polystyrene in Tetrahydrofuran: Comparison of Concentration Dependences of the Diffusion Coefficients of Polymer, Solvent, and a Ternary Probe Component. Macromolecules. 18 (1985) 260-266.

Appendix E

Supplemental Information for Chapter 6

A. Glossary

b	Bead diameter in the chain model
c_S	Surface concentration of chains
c_0	Bulk concentration of chains
D_{col}	Column diameter
F	Helmholtz free energy
F^0	Helmholtz free energy of an unconfined chain
F^C	Helmholtz free energy of a *cis* chain
F^T	Helmholtz free energy of a *trans* chain
K	Overall partition coefficient
K_H	Henry adsorption coefficient
K_P	Partition coefficient for complete confinement to pores
K_F	Partition coefficient for partial confinement to pores
k	Harmonic spring constant
k_B	Boltzmann's constant
L	Characteristic distance away from surface ($200b$)
M	Molecular weight
N	Number of chain segments
N^*	Critical number of chain segments
N_{ex}	Excess adsorption of chains
N_M	Number of chain segments at which a free energy minimum occurs
N_0	Bulk number of chains
N_{tot}	Total number of chains
n_S	Number of surface pores
R_G	Radius of gyration of a chain
R_G^*	Critical gyration radius
R_P	Particle radius
R_{pore}	Pore radius
r_{12}	Center-to-center distance of neighboring beads
S_{ext}	External surface area of solid particles
$\hat{S}_{ext}$	Specific external surface area
s	Number of translocated chain segments
s^*	Characteristic degree of translocation
T	Kelvin temperature
T^*	Reduced temperature $T^* = k_BT/\varepsilon$
U	Adsorption potential
Ub	Harmonic bond potential
U_C	Adsorption potential at critical conditions
V_{col}	Column volume
V_R	Retention volume
$V_{R,ext}$	Contribution to retention from external surface
$V_{R,pore}$	Contribution to retention from pores
$V_{R,fl}$	Contribution to retention from flower conformations
V_S	Solid volume

V_I Interstitial volume

V_P Accessible pore volume

V_O Volume of surface pores

v_O Volume of one surface pore

z vertical distance away from external surface of stationary phase

Greek Symbols

ΔF Difference in Helmholtz free energy between adsorbed and free chains

ε Bead-bead LJ energy parameter

ε_P Particle accessible 'chain exploratory' porosity

ε_S Surface porosity

μ_{incr} Incremental chemical potential

μ_{incr}^0 Incremental chemical potential of free chain

$\Delta\mu$ Difference in chemical potential of adsorbed and free chains

Abbreviations

CPA Critical point of adsorption

LAC Liquid adsorption chromatography

LCCC Liquid chromatography at critical conditions

MC Monte Carlo

PS Polystyrene

SEC Size exclusion chromatography

S-G Skvortsov & Gorbunov

SCFT Self-Consistent field theory

Latin Terminology

cis on external surface (not translocated)

trans within pores (translocated)

B. Derivation of the Critical Conditions of Adsorption: General Case

The definition of critical conditions from the equality of the incremental chemical potentials of adsorbed and free chains is shown below to be a natural consequence of the chain length independence of the partition coefficient for both internally and externally adsorbed chains.

Internally / partially translocated chains

The partition coefficient for case of chains adsorbing in pores is simply the exponent of the difference in free energy: $K(N) = \exp[-(F(N)-F^0(N))]$. At the critical conditions, the partition coefficient is chain length independent or:

$$at\ CPA \rightarrow \frac{dK}{dN} = 0 \tag{E.B1}$$

The derivative of the partition coefficient is:

$$\frac{d}{dN}\exp\left[-\left(F(N) - F^0(N)\right)\right] = 0$$

$$\exp\left[-\left(F(N) - F^0(N)\right)\right]\frac{d}{dN}\left(-\left(F(N) - F^0(N)\right)\right) = 0$$

The exponent of a function cannot become zero, therefore the equation reduces to:

$$\frac{d}{dN}\left(-\left(F(N) - F^0(N)\right)\right) = 0 \tag{E.B2}$$

Rearranging the terms, the equality of incremental chemical potentials is the direct consequence of Eq. (E.B2):

$$\frac{dF(N)}{dN} = \frac{dF^0(N)}{dN} \rightarrow \mu_{incr} = \mu^0_{incr}$$

Externally adsorbed chains

The case of externally adsorbed chains follows similar logic as that of internally adsorbed chains. At critical conditions,

$$\frac{dK_H}{dN} = 0 \tag{E.B3}$$

Where the Henry constant K_H is:

$$K_H(N) = \int_{z=0}^{L} (\exp[-(F(N,z) - F^0(N))] - 1)dz$$

Taking the N-derivative of Eq. (E. B3) and setting equal to zero:

$$\frac{dK_H}{dN} = \int_{z=0}^{L} \frac{d}{dN}(\exp[-(F(N,z) - F^0(N))] - 1)dz = 0$$

$$\frac{dK_H}{dN} = \int_{z=0}^{L} (\exp[-(F(N,z) - F^0(N))]) \frac{d}{dN}(-(\mathrm{F(N,z)} - \mathrm{F^0(N)})dz = 0$$

$(\exp[-(F(N,z) - F^0(N))])$ is never 0 regardless of the limit, therefore it can be removed from the equation:

$$\int_{z=0}^{L} \frac{d}{dN}(-(\mathrm{F(N,z)} - \mathrm{F^0(N)})\mathrm{d}z = 0$$

$$\int_{z=0}^{L} (-\mu_{incr}(N,z) + \mu_{incr}^0)\,\mathrm{d}z = 0$$

$$\int_{z=0}^{L} (\mu_{incr}(N,z))\,\mathrm{d}z = \int_{z=0}^{L} (\mu_{incr}^0)\,\mathrm{d}z$$

Imposing a detailed balance $\mu_{incr} = \mu_{incr}^0$ is one solution to this equation.

C. Calculation of Free Energy of Partially Confined Chains

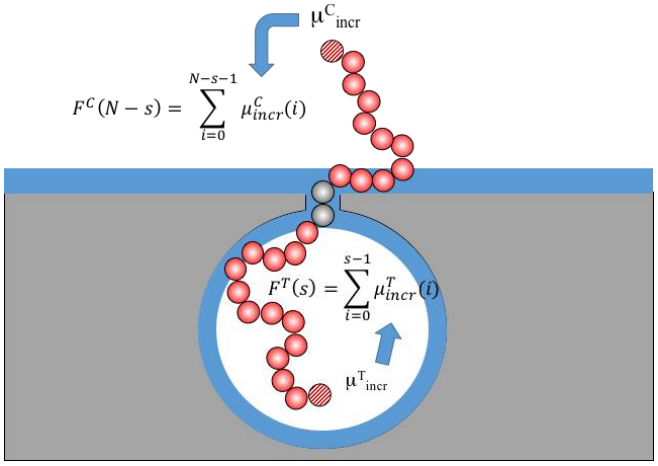

Fig. E.1 Calculation of free energies of partially confined chains in our model. Gray beads are tethered within the adsorption well. *Cis* chain is outside the pore, *trans* – inside the pore.

The free energy *F(N,s)* of a chain of *N* beads with *s* beads confined to a spherical pore such as the one shown above in **Fig. E.1** is calculated from the sum of the free energies of the *cis* (outside pore) and *trans* (inside pore) sub-chains of lengths N-s and s, respectively. The free energy of the *cis* and *trans* sub-chains is calculated based on summing the incremental chemical potentials of the independent chains:

$$F^C(N-s) = \sum_{i=0}^{N-s-1} \mu_{incr}^C \quad \text{(E.C. 1c)}$$

$$F^T(s) = \sum_{i=0}^{s-1} \mu_{incr}^T \quad \text{(E.C.1t)}$$

$$F(N,s) = F^C(N-s) + F^T(s) \quad \text{(E.C2)}$$

The incremental chemical potential of the cis and trans chains are assessed using the incremental gauge cell method (see refs. in **Chapter 6**) applied to *cis* and *trans* chains grown from 1 to *N-s* and 1 to *s* beads tethered to the external surface or tethered inside a pore by the terminal bead (gray beads in Fig. E.1) inside the adsorption well.

The free energy *F(N)* of a partially confined chain is the Boltzmann-weighted average of the free energies of chains over all degrees of translocation *F(N,s)*:

$$F(N) = -\ln\left(\sum_{s=1}^{N} exp[-F(N,s)]\right) \quad \text{(E.C3)}$$

This free energy is compared to that of a bulk chain $F^0(N)$ to calculate the partition coefficient of partially translocated chains $K_F = \exp[-(F(N)-F^0(N))]$.

ACKNOWLEDGEMENT OF PREVIOUS PUBLICATIONS

This thesis is the compilation of several published papers and papers in preparation. My contributions are specified as follows:

Chapter 1

This introduction contains material that is part of the following publication in preparation for submission: R. Cimino, C. Rasmussen, Y. Brun, A. V. Neimark. Monte Carlo Simulation of Polymer Adsorption: A Review

Chapter 2

Publication: R. Cimino, K. Cychosz, M. Thommes and A. V. Neimark, Experimental and theoretical studies of scanning adsorption–desorption isotherms, Colloids Surf. A: Physicochem. Eng. Aspects, **437** (SI) p.76-89 (2013)

Contribution: I performed all calculations in this chapter and helped to derive the equations of the Direct and Partial Correlation Models (PCM). The percolation model is based on the early work of AVN. The computer program is a modified version of one published by Mark Newmann (bibl).

Chapter 3

Publication in preparation for submission: R. Cimino, K. Cychosz, M. Thommes and A. V. Neimark, Characterization of Micro-Mesoporous Carbons by High-Pressure CO_2 Adsorption with Hybrid QSDFT Methods

Contribution: I performed all calculations and developed all CO_2 and Ar kernels mentioned in this work, using programs written by Peter Ravikovitch and Yangzheng Lin.

This chapter, Chapter 1, and Appendix B of the dissertation also contain references to additional work of mine, which was featured in the following publication: K. Cychosz, X. Guo, W. Fan, R.

Cimino, G. Gor, M. Tsapatsis, A. V. Neimark, and M. Thommes, Characterization of the Pore Structure of Three-Dimensionally Ordered Mesoporous Carbons Using High Resolution Gas Sorption, Langmuir, **28** (34) p.12647-12654 (2012)

Contribution: I developed all of the Ar kernels mentioned in this publication and performed the QSDFT adsorption isotherm analysis.

Chapter 4

Publication: R. Cimino, C. Rasmussen and A. V. Neimark, Communication: Thermodynamic analysis of critical conditions of polymer adsorption, J. Chem. Phys., **139** (20) p.201101-1-4 (2013)

Contribution: I performed all calculations and simulations mentioned in this work, using a program written by Christopher Rasmussen and modified by myself.

Chapter 5

Publication: R. Cimino, C. Rasmussen, Y. Brun, A. V. Neimark. Critical conditions of polymer adsorption and chromatography on nonporous substrates, Journal of Colloid and Interface Science **474** p. 25-33 (2016)

Contribution: I performed all calculations and simulations mentioned in this work, using a program written by Christopher Rasmussen and modified by myself.

Chapter 6

Publication: R. Cimino, C. Rasmussen, Y. Brun, A. V. Neimark. Mechanisms of Chain Adsorption on Porous Substrates and Critical Conditions of Polymer Chromatography. Journal of Colloid and Interface Science **481** p. 181-193 (2016)

Contribution: I performed all calculations and simulations mentioned in this work, using a program written by Christopher Rasmussen and modified by myself.

LIST OF PUBLICATIONS AND PRESENTATIONS

Peer-Reviewed Journal Articles

R. Cimino, C. Rasmussen, Y. Brun, A. V. Neimark. Mechanisms of Chain Adsorption on Porous Substrates and Critical Conditions of Polymer Chromatography. Journal of Colloid and Interface Science **481** p. 181-193 (2016)

C. Balzer, R. Cimino, G. Yu. Gor, A. V. Neimark, G. Reichenauer. Deformation of Microporous Carbons during N_2, Ar, and CO_2 Adsorption: Insight from the Density Functional Theory, Langmuir **32** p.8265-8274 (2016)

R. Cimino, C. Rasmussen, Y. Brun, A. V. Neimark. Critical conditions of polymer adsorption and chromatography on nonporous substrates, Journal of Colloid and Interface Science **474** p. 25-33 (2016)

R. Cimino, C. Rasmussen and A. V. Neimark, Communication: Thermodynamic analysis of critical conditions of polymer adsorption, J. Chem. Phys., **139** (20) p.201101-1-4 (2013)

R. Cimino, K. Cychosz, M. Thommes and A. V. Neimark, Experimental and theoretical studies of scanning adsorption–desorption isotherms, Colloids Surf. A: Physicochem. Eng. Aspects, **437** (SI) p.76-89 (2013)

K. Cychosz, X. Guo, W. Fan, R. Cimino, G. Gor, M. Tsapatsis, A. V. Neimark, and M. Thommes, Characterization of the Pore Structure of Three-Dimensionally Ordered Mesoporous Carbons Using High Resolution Gas Sorption, Langmuir, **28** (34) p.12647-12654 (2012)

Publications in Preparation for Submission at the Time of Writing

R. Cimino, K. Cychosz, M. Thommes and A. V. Neimark, Characterization of Micro-Mesoporous Carbons by High-Pressure CO_2 Adsorption with Hybrid QSDFT Methods

R. Cimino, P. Kowalczyk, P. Ravikovitch, A. V. Neimark. Calculation of the Isosteric Heat from the of Adsorption Isotherm Measured at One Temperature

R. Cimino, C. Rasmussen, Y. Brun, A. V. Neimark. Simulation of Polymer Interaction Chromatography: A Review

Podium Presentations at National and International Conferences

R.Cimino, P. Kowalczyk and A. V. Neimark, "Calculation of the Isosteric Heat of Adsorption using Quenched Solid Density Functional Theory," at AICHE Annual Meeting, San Francisco, CA 2016

R. Cimino, K. Cychosz, M. Thommes and A.V. Neimark, "Characterization of Micro-Mesoporous Carbons By High-Pressure CO2 Adsorption with Hybrid QSDFT Methods," at AICHE Annual Meeting, Salt Lake City, UT 2015

R. Cimino, C. J. Rasmussen, Y. Brun and A. V. Neimark, "Critical conditions of Polymer Adsorption on Porous Substrates," at AICHE Annual Meeting, Atlanta, GA 2014

R. Cimino, C. J. Rasmussen and A. V. Neimark, "Investigation of the Critical Point of Adsorption of Polymers on Porous Materials," at AICHE Annual Meeting, San Francisco 2013

R. Cimino, K. Cychosz, M. Thommes and A.V. Neimark, "Characterization of Novel Ordered Mesoporous Carbons," at AICHE Annual Meeting, Pittsburgh 2012

Poster Presentations at National and International Conferences

R. Cimino, "Predictive Tools for Modeling Adsorption Phenomena" at Faculty Candidate Poster Session, AICHE Annual Meeting, San Francisco 2016

R. Cimino, K. Cychosz, M. Thommes and A.V. Neimark, "Characterization of Micro-Mesoporous Carbons by High-Pressure N_2, Ar, and CO_2 Adsorption with Hybrid QSDFT Methods" Fundamentals of Adsorption (FOA)12, May 2016

R. Cimino, K. Cychosz, M. Thommes and A.V. Neimark, “Novel Hybrid NL-QSDFT Kernels for High Pressure CO2 Adsorption on Carbons” Characterization of Porous Materials 7(CPM-7), May 2015

R. Cimino, C. J. Rasmussen, Y. Brun and A. V. Neimark, “Simulation of the Critical Conditions of Polymer Adsorption on (non) Porous Substrates” Characterization of Porous Materials 7(CPM-7), May 2015

R. Cimino, K. Cychosz, M. Thommes and A.V. Neimark, “Theoretical and Experimental Studies of Scanning Isotherms” Characterization of Porous Materials 6 (CPM-6), May 2012

GENERAL CONCLUSIONS AND OUTLOOK

My dissertation encompasses a diverse field of physical interactions between fluids and nanoporous materials, which collectively may be labeled “adsorption phenomena”. Gas and polymer adsorption and adsorption characterization are mature fields, each with a rich history of theoretical and experimental work. In the last two decades these fields have experienced a renaissance brought about by the advent of advanced computational techniques and facilities, as well as new experimental materials – such as templated carbons, MOFS, etc…and new technologies, such as gradient elution chromatography, scanning and high pressure gas adsorption. As such, there is a need to develop tools and methods capable of predicting the physics of these systems and to characterize these new materials and processes. In my work, I have focused on the development of novel analytical and computational models to describe the adsorption of simple and complex fluids on micro-mesoporous materials for the purpose of porous materials characterization. During the course of my dissertation I have striven to provide tools and methods which are both theoretically sound and above all else, practically useful for experimentalists and theoreticians alike.

My contributions to the field of gas adsorption are twofold. The first and most prominent of my contributions is the development of the QSDFT adsorption isotherm kernels for porous materials characterization. These kernels encompass Ar and CO_2 adsorption which are both increasingly being used to assess the pore size and surface area/volume of micro- and mesoporous carbon materials. The kernels encompass a wide range of carbon pore geometries, as a means to accommodate the diverse number of templated carbon materials for energy and catalysis applications. Of particular import are the CO_2 kernels, which are the only ones of their kind for analysis of high pressure adsorption isotherms on carbons with rough surfaces. These kernels have (Ar) or are planned to be (CO_2) implemented in analytical gas adsorption software developed by the Quantachrome Instruments Company, and as such, this work has reached a broad audience.

The work on Ar adsorption in carbons is summarized in a peer-reviewed publication which is my most highly cited paper – with over thirty citations to date (Langmuir). The other, concerning CO_2 is in the final preparation for submission.

Second, I developed a unified methodology by which the pore structure of micro-mesoporous materials may be discerned based upon information from scanning adsorption isotherms. Using this method, one may differentiate between uncorrelated, partially correlated, and disordered materials. Perhaps the most novel practical results of this work are 1) capability to distinguish pore network topologies from scanning isotherms (i.e. in the absence of XRD or other costly methods) and 2) possibility to determine the neck size distribution and connectivity of disordered pore networks from the same information. These methods were summarized in my first first-author publication "Theoretical and Experimental Studies of Scanning Adsorption-Desorption Isotherms", in 2013 in the Journal of Colloids and Interfaces A: Physicochemical and Engineering Aspects. The relevance of this study is illustrated by the fact that in the short time since its publication, this paper has been cited over 15 times to date.

The other major area to which I have contributed is to the field of polymer adsorption and chromatography. From the theoretical standpoint, the most fundamental of my contributions is the description of the adsorption transition in polymer chains and the critical conditions of polymer adsorption (CPA) based upon a new thermodynamic criterion – the equality of incremental chemical potentials. This method, which is demonstrated for the case of chains tethered to a surface, is analogous to the geometrical and scaling methods utilized by previous authors. This work was published in a communication to the Journal of Chemical Physics in 2013.

The advantage of the incremental chemical potential method is that the incremental chemical potential (and hence the free energy of the chain) can be directly related to the partition of chains in polymer chromatography. To this affect, I first studied the adsorption of chains on nonporous surfaces with a simple Monte Carlo model and showed that critical conditions of

polymer adsorption may be linked to the incremental chemical potential. I developed a simple retention model based upon adsorption theory, which is capable of distinguishing the retention behavior of chains in three modes of chromatography: SEC, LAC, and LCCC. These methods were also illustrated for the first time by dedicated experiments performed by our collaborators. I next extended this work to the case of polymers adsorbing on porous substrates, where for a long time there has been a controversy over the existence of critical conditions for real chains. Introducing three mechanisms of polymer adsorption, I was able to illustrate that the critical conditions of real chains do exist for porous substrates and are the same as those found on nonporous columns. The retention was shown to be modeled accurately with retention expressions based upon the overall partition coefficient (derived from simulations) and geometrical parameters of the experimental column. Another important practical result of this work is the mapping of the experimental solvent composition – namely the fraction of poor solvent (acetonitrile) - to the effective adsorption potential. This mapping allows one to predict the "real-life" retention behavior of chains in an experimental column based on the simulated retention model, which can save experimentalists time and resources that would otherwise be expended on determining the appropriate solvent conditions needed to affect a particular separation. This work was summarized in two peer-reviewed journal articles, which have been published this year in the Journal of Colloid and Interface Science.

Future prospects

While this work has produced practical and useful results which scientists may use within the fields of adsorption and characterization, there are still plenty of avenues for future research. Of particular interest for both gas and polymer adsorption is the study of molecularly rough and heterogeneous surfaces. For example – it is known that most micro-mesoporous carbons are molecularly rough (i.e. heterogeneous) and may contain many surface defects. Such surfaces cannot be modeled easily with mean field methods such as DFT. Instead, Monte Carlo simulations

provide a more suitable framework in which to study adsorption on such surfaces. Analogously, the accurate modeling of the adsorption of polar molecules such as water within porous materials is another prime (albeit elusive) candidate for characterization of heterogeneous surfaces. Recent experimental work has shown that water adsorption is able to differentiate between topologically similar surfaces of different chemistry.

Likewise, the adsorption and separation of telechelic polymers (polymers with functionalized end-groups) on chromatographic columns remains largely open. It is proposed that these polymers can be separated by elution through columns with surfaces of different (heterogeneous) surface functionality. It is of great interest to be able to accurately predict the retention of such chains on heterogeneous surfaces and these methods could be expanded to describe the elution of star, branched, and brush polymers as well.

BIBLIOGRAPHY

1. Ravikovitch, P.I. and A.V. Neimark, *Density functional theory model of adsorption on amorphous and*

microporous solids in *Studies in Surface Science and Catalysis*, P.L. Llywellyn, et al., Editors. 2007, Elsevier. p. 9-16.

2. Ravikovitch, P.I. and A.V. Neimark, *Density functional theory model of adsorption on amorphous and microporous silica materials.* Langmuir, 2006. **22**(26): p. 11171-11179.
3. van Bemmelen, J.M., *Die Absorption das Wasser in den Kolloiden, besonders in dem Gel der Kieselsäure.* Z. Anorg. Allg. Chem., 1897. **13**: p. 233-356.
4. Zsigmondy, R., *Über die Struktur des Gels der Kieselsäure. Theorie der Entwässerung.* Z. Anorg. Allgem. Chemie, 1911. **71**: p. 356-377.
5. Thommes, M., et al., *Physisorption of gases, with special reference to the evaluation of surface area and pore size distriution (IUPAC Technical Report)*, in *Pure and Applied Chemistry*. 2015, IUPAC & De Gruyter.
6. McBain, J.W., *An explanation of hysteresis in the hydration and dehydration of gels.* Journal of the American Chemical Society, 1935. **57**: p. 699-700.
7. Cohan, L.H., *Sorption hysteresis and the vapor pressure of concave surfaces.* Journal of the American Chemical Society, 1938. **60**: p. 433-435.
8. Rao, K.S., *Hysteresis in sorption I - IV.* Journal of Physical Chemistry, 1941. **46**: p. 500-518.
9. Cohan, L.H., *Hysteresis and the capillary theory of adsorption of vapors.* Journal of the American Chemical Society, 1944. **66**: p. 98-105.
10. Burgess, C.G.V., D.H. Everett, and S. Nuttall, *ADSORPTION HYSTERESIS IN POROUS MATERIALS.* Pure and Applied Chemistry, 1989. **61**(11): p. 1845-1852.
11. Roquerol, F., J. Roquerol, and K.S.W. Sing, *Adsorption by powders & porous solids*. 1999, New York: Academic Press. 467.
12. Roquerol, F., et al., *Characterization of porous solids*, ed. S.J. Gregg, K.S.W. Sing, and H.F. Stoeckli. 1979, London: Society of Chemical Industry.
13. Barrett, E.P., L.G. Joyner, and P.P. Halenda, *The Determination of pore volume and area distributions in porous substances. I.*

computations from nitrogen isotherms. Journal of the American Chemical Society, 1951. **73**(1): p. 373-380.

14. Derjaguin, B.V., Acta Physichochim. URSS, 1940. **12**(1).
15. Broekhoff, J.C.P. and J.H. DeBoer, Journal of Catalysis, 1967. **9**(1): p. 8.
16. Neimark, A.V., et al., *Quenched solid density functional theory and pore size analysis of micro-mesoporous carbons.* Carbon, 2009. **47**(7): p. 1617-1628.
17. Rasmussen, C.J., et al., *Cavitation in metastable liquid nitrogen confined to nanoscale pores.* Langmuir, 2010. **26**(12): p. 10147-10157.
18. Thommes, M., *Physical Adsorption Characterization of Nanoporous Materials.* Chemie Ingenieur Technik, 2010. **82**(7): p. 1059-1073.
19. Thommes, M., et al., *Assessing surface chemistry and pore structure of active carbons by a combination of physisorption (H2O, Ar, N2, CO2), XPS and TPD-MS.* Adsorption, 2011. **17**(3): p. 653-661.
20. Thommes, M., et al., *Assessing surface chemistry and pore structure of active carbons by a combination of physisorption (H2O, Ar, N-2, CO2), XPS and TPD-MS.* Adsorption-Journal of the International Adsorption Society, 2011. **17**(3): p. 653-661.

21. Cychosz, K.A., et al., *Characterization of the Pore Structure of Three-Dimensionally Ordered Mesoporous Carbons Using High Resolution Gas Sorption.* Langmuir, 2012. **28**(34): p. 12647-12654.
22. Thommes, M., S. Mitchell, and J. Perez-Ramirez, *Surface and pore structure assessment of hierarchichal MFI zeolites by advanced water and argon sorption studies.* Journal of Physical Chemistry C, 2012. **116**(35): p. 18816-18823.
23. Cimino, R., et al., *Experimental and theoretical studies of scanning adsorption-desorption isotherms.* Colloids and Surfaces a-Physicochemical and Engineering Aspects, 2013. **437**: p. 76-89.
24. Thommes, M., et al., *Combining Nitrogen, Argon, and Water Adsorption for Advanced Characterization of Ordered Mesoporous Carbons (CMKs) and Periodic Mesoporous Organosilicas (PMOs).* Langmuir, 2013. **29**(48): p. 14893-14902.
25. Langer, R. and D.A. Tirell, *Designing materials for biology and medicine.* Nature, 2004. **428**: p. 487-492.
26. Brun, Y. and C.J. Rasmussen, *Chromatography, HPLC*, in *Encylcopedia of Polymer Science and Technology*. 2015, John Wiley & Sons, Inc.
27. Flory, P.F., *Statistical mechanics of chain molecules*. 1969, New York: Interscience.
28. Teraoka, I., *Polymer solutions : An introduction to physical properties*. 2002: John Wiley & Sons. 360.
29. Simha, R., H.L. Frisch, and F.R. Eirich, *The adsorption of flexible macromolecules.* Journal of Physical Chemistry, 1953. **57**(6): p. 584-589.
30. Broda, E. and H. Mark, *Zur Adsorption von Kettenmolekülen.* Zeitschrift für Physikalische Chemie: Abteilung A, 1937. **180**: p. 392.
31. Silberberg, A., *The adsorption of flexible macromolecules. Part I. The isolated macromolecule at a plane interface.* Journal of Physical Chemistry, 1962. **66**(10): p. 1872-1883.
32. Forsman, W.C. and R.E. Hughes, *Adsorption theory for flexible linear polymer molecules.* J. Chem. Phys., 1963. **38**(9): p. 2130-2135.
33. Rubin, R.J., *Random walk model of chain polymer adsorption at a surface.* J. Chem. Phys., 1965. **43**(7): p. 2392-2407.
34. DiMarzio, E.A. and F.L. McCrackin, *One dimensional model of polymer adsorption.* J. Chem. Phys., 1965. **43**(2): p. 539-547.
35. Birshtein, T.M., *Theory of adsorption of macromolecules. I. The desorption-adsorption transition point.* Macromolecules, 1979. **12**(4): p. 715-721.
36. Eisenriegler, E., K. Kremer, and K. Binder, *Adsorption of polymer chains at surfaces: scaling and monte-carlo analyses.* J. Chem. Phys., 1982. **77**(12): p. 6296-6320.
37. Kuhn, W., *Ueber die Gestalt fadenfoermiger Molekuele in Loesungen.* Kolloid-Zeitschrift, 1934. **68**(1): p. 2-15.
38. Huggins, M.L., *The viscosity of dilute solutions of long-chain molecules. III. The Staudinger viscosity law.* Journal of Applied Physics, 1939. **10**(10): p. 700-704.
39. Simha, R., *Note on volume effect in coiling molecules.* Journal of polymer science, 1948. **3**(2): p. 227-230.
40. Flory, P.J., *The configuration of real polymer chains.* The Journal of Chemical Physics, 1949. **17**(3): p. 303-310.
41. Montroll, E.W., *Markoff chains and excluded volume effects in polymer chains.* The Journal of Chemical Physics, 1950. **18**(5): p. 734-743.
42. Debye, P. and R.J. Rubin, Phys Rev, 1952. **87**(1): p. 214.

43. Zimm, B.H., W.H. Stockmayer, and M. Fixman, *Excluded volume in polymer chains.* The Journal of Chemical Physics, 1953. **21**(10): p. 1716-1723.
44. Siepmann, J.I. and D. Frenkel, *Configurational Bias Monte-Carlo - a New Sampling Scheme for Flexible Chains.* Molecular Physics, 1992. **75**(1): p. 59-70.
45. Metzger, S., et al., *Adsorption transition of a polymer chain at a weakly attractive surface: monte carlo simulation of off-lattice models.* Macromolecular Theory and Simulations, 2002. **11**(9): p. 985-995.
46. Descas, R., J.U. Sommer, and A. Blumen, *Static and dynamic properties of tethered chains at adsorbing surfaces: a monte carlo study.* J. Chem. Phys., 2004. **120**(18): p. 8831-8840.
47. Grassberger, P., *Simulations of grafted polymers in a good solvent.* J. Phys. A: Math. Gen., 2005. **38**(2): p. 323-331.
48. DeGennes, P.G., *Some conformation problems for long macromolecules.* Reports on Progress in Physics, 1969. **32**(1): p. 187-205.
49. Meirovitch, H. and S. Livne, *Computer simulation of long polymers adsorbed on a surface. II. Critical behavior of a single self-avoiding walk.* J. Chem. Phys., 1987. **88**(7): p. 4507-4515.
50. Gong, Y.C. and Y.M. Wang, *Partitioning of polymers into pores near the critical adsorption point.* Macromolecules, 2002. **35**(19): p. 7492-7498.
51. Casassa, E.F., *Equilibrium distribution of flexible polymer chains between a macroscopic solution phase and small voids.* Journal of Polymer Science Part B: Polymer Letters, 1967. **5**(9): p. 773-778.
52. Gorbunov, A.A. and A.M. Skvortsov, *Statistical Properties of Confined Macromolecules.* Advances in Colloid and Interface Science, 1995. **62**(1): p. 31-108.
53. Cifra, P., T. Bleha, and A. Romanov, *Simulation of concentration-dependence of the partition-coefficient for macromolecules in porous-media.* Makromolekulare Chemie - Rapid Communications, 1988. **9**(5): p. 355-359.
54. Teraoka, I., *Polymer Solutions in Confining Geometry.* Progress in Polymer Science, 1996. **21**: p. 89-149.
55. Davidson, M.G., U.W. Suter, and W.M. Deen, *Equilibrium partitioning of flexible macromolecules between bulk solution and cylindrical pores.* Macromolecules, 1987. **20**: p. 1141-1146.
56. Bleha, T., P. Cifra, and F.E. Karasz, *The effects of concentration on partitioning of flexible chains into pores.* Polymer, 1990. **31**(7): p. 1321-1327.
57. Cifra, P. and T. Bleha, *Steric exclusion/adsorption compensation in partitioning of polymers into micropores in good solvents.* Polymer, 2000. **41**(3): p. 1003-1009.
58. Yethiraj, A. and C.K. Hall, *Monte-Carlo simulation of the equilibrium partitioning of chain fluids between a bulk and a pore.* Molecular Physics, 1991. **73**: p. 503-515.
59. Pasch, H., Y. Gallot, and B. Trathnigg, *Chromatographic Investigations of Macromolecules in the Critical Range of Liquid-Chromatography .7. Analysis of the Poly(Methyl Methacrylate) Block in Poly(Styrene-Block-Methyl Methacrylate).* Polymer, 1993. **34**(23): p. 4986-4989.
60. Pasch, H. and B. Trathnigg, *Multidimensional HPLC of Polymers*. 1 ed. Springer Laboratory: Manuals in Polymer Science, ed. I. Alig and H. Pasch. 2013, Berlin: Springer-Verlag Berlin Heidelberg. xiv, 280.
61. Pasch, H. and B. Trathnigg, *Multidimensional HPLC of Polymers*. 2013 edition ed. 2013, New York: Springer. 280.

62. Pedersen, J.S. and P. Schurtenberger, *Static properties of polystyrene in semidilute solutions: A comparison of Monte Carlo simulation and small-angle neutron scattering results.* Europhysics Letters, 1999. **45**(6): p. 666-672.
63. Philipsen, H.J.A., et al., *Critical retention behaviour of polymers - A study on the influence of some practical parameters.* Journal of Chromatography A, 1996. **727**(1): p. 13-25.
64. Zhu, Y.T., J.D. Ziebarth, and Y.M. Wang, *Dependence of critical condition in liquid chromatography on the pore size of column substrates.* Polymer, 2011. **52**(14): p. 3219-3225.
65. Muthukumar, M., *Polymer Translocation*. illustrated ed. 2011: CRC Press. 372.
66. Striolo, A., et al., *Adsorption of comb copolymers on weakly attractive solid surfaces.* The Journal of Chemical Physics, 2005. **123**: p. 064710.
67. Elli, S., et al., *Surface adsorption of comb polymers by Monte Carlo simulations.* Polymer, 2008. **49**: p. 1716-1724.
68. Adamczyk, P., P. Romiszowski, and A. Sikorski, *Adsorption of homopolymer chains on a strip-patterned surface: a monte carlo study.* Catalysis Letters, 2009. **129**: p. 130-134.
69. Angelescu, D.G., et al., *Adsorption of branched-linear polyethyleneimine-ethylene oxide conjugage on hydrophilic silica investigated by ellipsometry and mone carlo simulations.* Langmuir, 2011. **27**: p. 9961-9971.
70. Hermsen, G.F., et al., *Monte Carlo simulation of partially confined flexible polymers.* Macromolecules, 2002. **35**(13): p. 5267-5272.
71. Hermsen, G.F., N.F.A. van der Vegt, and M. Wessling, *Monte Carlo calculations of polymer adsorption at the entrace of cylindrical pores in flat adsorbing surfaces.* Soft Materials, 2003. **1**(3): p. 295-312.
72. Rasmussen, C.J., A. Vishnyakov, and A.V. Neimark, *Translocation dynamics of freely jointed Lennard-Jones chains into adsorbing pores.* Journal of Chemical Physics, 2012. **137**(14).
73. Yang, S. and A.V. Neimark, *Critical conditions of polymer chromatography: An insight from SCFT modeling.* Journal of Chemical Physics, 2013. **138**(24).
74. Everett, D.H., *Adsorption hysteresis*, in *The Solid-Gas Interface*, E.A. Flood, Editor. 1967, Decker: New York. p. 1055-1113.
75. Roquerol, J., F. Roquerol, and K.S.W. Sing, *Adsorption by Powders and Porous Solids: Principles, Methodology and Applications*. 1998: Academic Press.
76. Horikawa, T., D.D. Do, and D. Nicholson, *Capillary condensation of adsorbates in porous materials.* Advances in Colloid and Interface Science, 2011. **169**(1): p. 40-58.
77. Monson, P.A., *Understanding adsorption/desorption hysteresis for fluids in mesoporous materials using simple molecular models and classical density functional theory.* Microporous and Mesoporous Materials, 2012. **160**: p. 47-66.
78. Rouquerol, J., D. Avnir, C. W. Fairbridge, D. H. Everett, J. M. Haynes, N. Pernicone, J. D. F. Ramsay, K. S. W. Sing and K. K. Unger, *Recommendations for the characterization of porous solids.* IUPAC Recommendations, 1994. **66**: p. 1739-1758.
79. S. Lowell, J.S., M.A. Thomas & M. Thommes, *Surface Area, Porosity and Density*. 2004: Springer.
80. Kraemer, E.O., *Treatise on Physical Chemistry*. 1931, New York: Van Nostrand.
81. Schofield, R.K., *General Discussion.* Faraday Discussions, 1948. **3**: p. 105.
82. DeBoer, J.H., *in Structure and Properties of Porous Materials.* Colston Papers, 1958. **10**: p. pp. 68.
83. Dubinin, M.M., et al., *Surface Phenomena in Chemistry and Biology*, J.F. Danielli, K.G.A. Pankhurst, and A.C. Riddiford, Editors. 1958, Pergamon: New York. p. 172.

84. Brown, A.J., *PhD Thesis.* 1963: p. 14-107.
85. Neimark, A.V., *Percolation theory of capillary hysteresis phenomena and its applications for characterization of porous solids.* Studies in Surface Science & Catalysis, 1991. **62**: p. 67-74.
86. Wall, G.C., Brown, R.J.C., *The determination of pore-size distributions from sorption isotherms and mercury penetration in interconnected pores: The application of percolation theory.* Journal of Colloid and Interface Science, 1981. **82**: p. 141-149.
87. Neimark, A.V., *Theory of capillary phenomena in porous-media and its application.* Khimicheskaya Promyshlennost (Sov. Chem. Ind.), 1981(11): p. 656-659.
88. Neimark, A.V., *Development of theory of capillary condensation and desorption in mesopores of adsorbents, on the basis of lattice models of pore structure.* Doklady Akademii Nauk Sssr, 1983. **273**(2): p. 384-388.
89. Kheifets, L.I. and A.V. Neimark, *Multiphase Processes in Porous Media*. 1982, Moscow: Khimia. 320.
90. Mason, G., *The effect of pore space connectivity on the hysteresis of capillary condensation in adsorption—desorption isotherms* Journal of Colloid and Interface Science, 1982. **88**: p. 36-46.
91. Mason, G., *A model of adsorption-desorption hysteresis in which hysteresis is primarily developed by the interconnections in a network of pores.* Proc R Soc Lond A, Math Phys Sci, 1983. **390**(1798): p. 47-72.
92. Neimark, A.V., *Theory of the calculation of scanning adsorption and desorption isotherms in mesophorous adsorbents.* Colloid Journal of the Ussr, 1984. **46**(6): p. 1004-1010.
93. Mason, G., *Determination of the pore-size distributions and pore-space interconnectivity of Vycor porous glass from adsorption desorption hysteresis capillary condensation isotherms.* Proc R Soc Lond A, Math Phys Sci, 1988. **415**(1849): p. 453-486.
94. Parlar, M. and Y.C. Yortsos, *Percolation theory of vapor adsorption desorption processes in porous materials.* Journal of Colloid and Interface Science, 1988. **124**(1): p. 162-176.
95. Parlar, M. and Y.C. Yortsos, *Nucleation and pore geometry effects on capillary desorption in porous media.* J. Colloid Interface Sci, 1989. **132** p. 425-443.
96. Wilkinson, D. and J.F. Willemsen, *Invasion percolation: A new form of percolation theory.* J. Phys. A., 1983. **16**: p. 3365-3376.
97. Neimark, A.V., *Application of lattice models of porous structure for investigation of mercury porosimetry.* Colloid J. of the USSR, 1984. **46**(4): p. 727-734.
98. Neimark, A.V., *Application of lattice models of adsorbents and catalysts in studies of their capillary properties. Analysis of scanning curves for mercury intrusion and extraction.* Colloid J. of the USSR, 1985. **47**(1): p. 86-92.
99. Seaton, N.A., *Determination of the connectivity of porous solids from nitrogen sorption measurements.* Chem. Eng. Sci, 1991. **46**: p. 1895-1909.
100. Liu, H.L., L. Zhang, and N.A. Seaton, *Analysis of sorption hysteresis in mesoporous solids using a pore network model.* Journal of Colloid and Interface Science, 1993. **156**(2): p. 285-293.
101. Lilly, M.P., P.T. Finley, and R.B. Hallock, *Memory, congruence and avalanche events in hysteretic capillary condensation.* Phys. Rev. Lett., 1993. **71**: p. 4186-4189.
102. Rajniak, P. and R.T. Yang, *A simple-model and experiments for adsorption-desorption hysteresis - water-vapor on silica-gel.* Aiche Journal, 1993. **39**(5): p. 774-786.
103. Rajniak, P. and R.T. Yang, *Hysteresis-dependent adsorption-desorption cycles - generalization for isothermal conditions.* AIChE Journal, 1994. **40**(6): p. 913-924.

104. Mayagoitia, V., F. Rojas, and I. Kornhauser, *Pore network interactions in ascending processes relative to capillary condensation.* J. Chem. Soc. Faraday Trans I, 1985. **81**: p. 2931-2940.
105. Cordero, S., et al., *Pore-blocking and pore-assisting factors during capillary condensation and evaporation* Applied Surface Science, 2002. **196**: p. 224-238.
106. Rojas, F., et al., *Capillary condensation in heterogeneous mesoporous networks consisting of variable connectivity and pore-size correlation* Phys. Chem. Chem. Phys., 2002. **4**: p. 2346-2355.
107. Neimark, A.V., *Percolation method of calculation of pore dimension distribution in mesoporous materials based on adsorption and desorption isotherms in the hysteresis loop.* Zhurnal Fizicheskoi Khimii, 1986. **60**(7): p. 1745-1750.
108. Cychosz, K.A., et al., *Characterization of the pore structure of three-dimensionally ordered mesoporous carbons using high resolution gas sorption.* Langmuir 2012. **28**(34): p. 12647-12654.
109. Kanellopoulos, N.K., *Nanoporous Materials : Advanced Techniques for Characterization, Modeling and Processing*. 2011, Boca Raton , Florida: CRC Press Taylor & Francis Distributor.
110. Lu, G.Q. and X.S. Zhao, *Nanoporous Materials : Science and Engineering*. Series on chemical engineering. 2004, London: Imperial College Press. p. xi, 897
111. Tascon, J., *Novel Carbon Adsorbents*. 1st ed, ed. J. Tascón. 2012: Elsevier.
112. Zhao, D.Y., et al., *Triblock copolymer syntheses of mesoporous silica with periodic 50 to 300 angstrom pores.* Science, 1998. **279**(5350): p. 548-552.
113. Tompsett, G.A., et al., *Hysteresis and scanning behavior of mesoporous molecular sieves.* Langmuir, 2005. **21**(18): p. 8214-8225.
114. Grosman, A. and C. Ortega, *Nature of capillary condensation and evaporation processes in ordered porous materials* Langmuir, 2005. **21**(23): p. 10515-10521.
115. Kim, T.W., et al., *MCM-48-like large mesoporous silicas with tailored pore structure: Facile synthesis domain in a ternary triblock copolymer-butanol-water system.* Journal of the American Chemical Society, 2005. **127**(20): p. 7601-7610.
116. Kleitz, F., T.W. Kim, and R. Ryoo, *Design of mesoporous silica at low acid concentrations in triblock copolymer-butanol-water systems.* Bulletin of the Korean Chemical Society, 2005. **26**(11): p. 1653-1668.
117. Kleitz, F., et al., *Probing adsorption, pore condensation, and hysteresis behavior of pure fluids in three-dimensional cubic mesoporous KIT-6 silica.* Journal of Physical Chemistry C, 2010. **114**(20): p. 9344-9355
118. Fan, W., et al., *Hierarchical nanofabrication of microporous crystals with ordered mesoporosity.* Nature Materials, 2008. **7**(12): p. 984-991.
119. Elmer, T.H., *Porous and Reconstructed Glasses*, in *Engineered Materials Handbook*, S.J. Schneider, Editor. 1990, ASM International: Materials Park, OH. p. 427-32.
120. Gelb, L.D. and K.E. Gubbins, *Characterization of porous glasses: Simulation models, adsorption isotherms, and the Brunauer-Emmett-Teller analysis method.* Langmuir, 1998. **14**(8): p. 2097-2111.
121. Kierlik, E., et al., *Binary vapor mixtures adsorbed on a graphite surface - A comparison of mean field density functional theory with results from monte-carlo simulations.* Molecular Physics, 1992. **75**(6): p. 1435-1454.
122. Everett, D.H., *A general approach to hysteresis. Part 3.—A formal treatment of the independent domain model of hysteresis.* Trans. Faraday Soc., 1954. **50**: p. 1077-1096.

123. Everett, D.H. and F.W. Smith, *A general approach to hysteresis. Part 2 - Development of the domain theory.* Trans. Faraday Soc., 1954. **50**: p. 187-197.
124. Ravikovitch, P. and A.V. Neimark, *Characterization of micro- and mesoporosity in SBA-15 materials from adsorption data by the NLDFT method.* Journal of Physical Chemistry B, 2001. **105**(29): p. 6817-6823.
125. Thommes, M., et al., *Adsorption hysteresis of nitrogen and argon in pore networks and characterization of novel micro- and mesoporous silicas.* Langmuir, 2006. **22**(2): p. 756-764.
126. Rasmussen, C., et al., *Cavitation in metastable liquid nitrogen confined to nanoscale pores.* Langmuir, 2010. **26**: p. 10147-10157.
127. Sahimi, M., *Applications of Percolation Theory*. 1994, London: Taylor & Francis.
128. Newman, M.E.J. and R.M. Ziff, *Fast Monte Carlo algorithm for site or bond percolation.* Physical Review E, 2001. **64**(1): p. 1-12.
129. Neimark, A.V. and P.I. Ravikovitch, *Capillary condensation in mesoporous molecular sieves and pore structure characterization.* Microporous and Mesoporous Materials, 2001. **44-45**: p. 697-707.
130. De Silva, P.N.K., P.G. Ranjith, and S.K. Choi, *A study of methodologies for CO2 storage capacity estimation of coal.* Fuel, 2012. **91**(1): p. 1-15.
131. Stoquart, C., et al., *Hybrid Membrane Processes using activated carbon treatment for drinking water: A review.* Journal of Membrane Science, 2012. **411-412**: p. 1-12.
132. Meng, X.J., F. Nawaz, and F.-S. Xiao, *Templating route for synthesizing mesoporous zeolites with improved catalytic properties.* Nano Today, 2009. **4**(4): p. 292-301.
133. Zhu, K.K., et al., *Carbon as a hard template for nano material catalysts.* Journal of Natural Gas Chemistry, 2012. **21**(3): p. 215-232.
134. Fang, B.Z., et al., *Hierarchical Nanostructured Carbons with Meso-Macroporosity: Design, Characterization, and Applications.* Accounts of Chemical Research, 2013. **46**(7): p. 1397-1406.
135. Qiu, S., et al., *Synthesis and Application of Three-Dimensionally Ordered Macroporous Carbon with Designed Pore Architecture.* Progress in Chemistry, 2014. **26**(5): p. 772-783.
136. Fyfe, C.A. and G.Y. Fu, *Structure Organization of Silicate Polyanions with Surfactants: A New Approach to the Syntheses, Structure Transformations, and Formation Mechanisms of Mesostructural Materials.* Journal of the American Chemical Society, 1995. **117**(38): p. 9709-9714.
137. Hu, X., et al., *CO2-Filling Capacity and Selectivity of Carbon Nanopores: Synthesis, Texture, and Pore-Size Distribution from Quenched-Solid Density Functional Theory (QSDFT).* Environmental Science & Technology, 2011. **45**(16): p. 7068-7074.
138. Silvestre-Albero, J., et al., *Physical characterization of activated carbons with narrow microporosity by nitrogen (77.4 K), carbon dioxide (273 K) and argon (87.3 K) adsorption in combination with immersion calorimetry.* Carbon, 2012. **50**(9): p. 3128-3133.
139. Garrido, J., A. Linaressolano, and J.M. Martinmartinez, *Use of N2 vs CO2 in the characterization of activated carbons.* Langmuir, 1987. **3**(1): p. 76-81.
140. Cazorla-Amoros, D., et al., *CO2 as an adsorptive to characterize carbon molecular sieves and activated carbons.* Langmuir, 1998. **14**(16): p. 4589-4596.
141. Thommes, M., et al., *Physisorption of gases, with special reference to the evaluation of surface area and pore size distribution (IUPAC Technical Report)*, in *Pure and Applied Chemistry*. 2015. p. 1-19.
142. Zhu, Y., et al., *Carbon-based supercapacitors produced by activation of graphene.* Science, 2011. **332**(6037): p. 1537-1541.

143. Roquerol, F., J. Roquerol, and K. Sing, *Adsorption by Powders and Porous Solids: Principles, Methodology and Applications*. 1999, London: Academic Press.
144. Seaton, Walton, and N. Quirke, *A new analysis method for the determination of the pore size distribution of porous carbons from nitrogen adsorption measurements.* Carbon, 1989. **27**(6): p. 853-861.
145. Vishnyakov, A., P.I. Ravikovitch, and A.V. Neimark, *Molecular level models for CO2 sorption in nanopores.* Langmuir, 1999. **15**(25): p. 8736-8742.
146. Lastoskie, C., K.E. Gubbins, and N. Quirke, *Pore-size distribution analysis of microporous carbons - a density functional theory approach.* Journal of Physical Chemistry, 1993. **97**(18): p. 4786-4796.
147. Maddox, M.W., J.P. Olivier, and K.E. Gubbins, *Characterization of MCM-41 using molecular simulation: heterogeneity effects.* Langmuir, 1997. **13**(6): p. 1737-1745.
148. Ustinov, E.A., D.D. Do, and V.B. Fenelonov, *Pore size distribution analysis of activated carbons: application of density functional theory using nongraphitized carbon clack as a reference system.* Carbon, 2006. **44**(4): p. 653-663.
149. Neimark, A.V., et al., *Quenched solid density functional theory and pore size analysis of micro-mesoporous carbons.* Carbon, 2009. **47**(7): p. 1617-1628.
150. Landers, J., G.Y. Gor, and A.V. Neimark, *Density functional theory methods for characterization of porous materials* Colloids and Surfaces A-Physicochemical and Engineering Aspects, 2013. **437**(SI): p. 3-32.
151. Gor, G.Y., et al., *Quenched solid density functional theory method for characterization of mesoporous carbons by nitrogen adsorption.* Carbon, 2012. **50**(4): p. 1583-1590.
152. Ryoo, R., S.H. Joo, and S. Jun, *Synthesis of Highly Ordered Carbon Molecular Sieves via Template-Mediated Structural Transformation.* Journal of Physical Chemistry B, 1999. **103**(37): p. 7743-7746.
153. Huwe, H. and M. Froeba, *Iron (III) oxide nanoparticles within the pore system of mesoporosu carbon CMK-1: Intra-pore synthesis and characterization.* Microporous and Mesoporous Materials, 2003. **60**(1-3): p. 151-158.
154. Ravikovitch, P.I., et al., *Unified Approach to Pore Size Characterization of Microporous Carbonaceous Materials from N2, Ar, and CO2 Adsorption Isotherms.* Langmuir, 2000. **16**(5): p. 2311-2320.
155. Yang, K., et al., *Effects of coal deformation upon CO2 adsorption and sequestration.* Journal of Geophysical Research - Solid Earth, 2011. **116**(b8).
156. Ravikovitch, P.I., et al., *Capillary hysteresis in nanopores: theoretical and experimental studies of nitrogen adsorption on MCM-41.* Langmuir, 1995. **11**(12): p. 4765-4772.
157. Olivier, J.P., *Improving the models used for calculating the size distribution of micropore volume of activated carbons from adsorption data.* Carbon, 1998. **36**(10): p. 1469-1472.
158. Rosenfeld, Y., *Free-energy model for the inhomogeneous hard-sphere fluid mixture and density-functional theroy of freezing.* Physical Review Letters, 1989. **63**(9): p. 980-983.
159. Rosenfeld, Y., et al., *Fundamental-measure free-energy density functional for hard spheres: dimensional crossover and freezing.* Physical Review E, 1997. **55**(4): p. 4245-4263.
160. Skripov, V.P. and G.N. Muratov, *Data about surface tension of liquids and their analysis using thermodynamic similarity.* Zhurnal Fizicheskoi Khimii, 1977. **51**(6): p. 1369-1372.
161. Quinn, E.L., *The surface tension of liquid carbon dioxide.* Journal of the American Chemical Society, 1927. **49**(11): p. 2704-2711.
162. Berry, M.V., R.F. Durrans, and R. Evans, *The calculation of surface tension for simple liquids.* Journal of Physics A: General Physics, 1972. **5**(1): p. 166-170.

163. Steele, W.A., *The interaction of rare gas atoms with graphitized carbon black.* Journal of Physical Chemistry, 1978. **82**(7): p. 817-821.
164. Ravikovitch, P.I., *Characterization of nanoporous materials by gas adsorption and density functional theory*, in *Chemical Engineering*. 1998, Yale: Hartford, CT.
165. Lawson, C.L. and R.J. Hanson, *Solving least squares problems*. SIAM. 1995, Philadelphia.
166. Thommes, M., et al., *Assessing surface chemistry and pore structure of active carbons by a combination of physisorption (H2O, Ar, N-2, CO2), XPS and TPD-MS* Adsorption - Journal of the International Adsorption Society, 2011. **17**(3): p. 653-661.
167. Everett, D.H., *Adsorption Hysteresis*. The Solid-Gas Interface. 1967, New York: Dekker.
168. Harris, J.G. and K.H. Yung, *Carbon Dioxides Liquid-Vapor Coexistence Curve and Critical Properties as Predicted by a Simple Molecular-Model.* Journal of Physical Chemistry, 1995. **99**(31): p. 12021-12024.
169. Potoff, J.J., J.R. Errington, and A.Z. Panagiotopoulos, *Molecular simualtion of phase equilibria for mixtures of polar and non-polar components.* Molecular Physics, 1999. **97**(10): p. 1073-1083.
170. DeGennes, P., *Some conformational problems for long macromolecules.* Rep. Prog. Phys., 1969. **32**(1): p. 187-205.
171. Broda, E. and H. Mark, *Zur Adsorption von Kettenmolekülen.* Zeitschrift fuer Physikaliche Chemie: Abteilung A, 1937. **180**: p. 392.
172. Higuchi, W.I., *Effects of short range surface-segment forces on the configuration of an adsorbed flexible chain polymer.* J. Phys. Chem., 1961. **65**(3): p. 487-491.
173. Edwards, S.F., *The statistical mechanics of polymers with excluded volume.* Proc. Phys. Soc., 1965. **85**(4): p. 613-624.
174. Hoeve, C.A.J., E.A. DiMarzio, and P. Peyser, *Adsorption of polymer molecules at low surface coverage.* J. Chem. Phys., 1965. **42**(7): p. 2558-2563.
175. Roe, R.J., *Conformation of an isolated polymer molecule at an interface.* Proceedings of the National Academy of Science, 1965. **53**(1): p. 50-57.
176. Mark, P. and S. Windwer, *Polymer adsorption on a surface by exact enumeration study.* Macromolecules, 1974. **7**(5): p. 690-697.
177. Torrie, G.M., et al., *Self avoiding walks interacting with an interface.* J. Chem. Phys., 1976. **65**(5): p. 1867-1871.
178. Lepine, Y. and A. Caille, *the configuration of a polymer chain interacting with a plane interface.* Canadian Journal of Physics, 1978. **56**(4): p. 403-308.
179. Birshtein, T.M., *Theory of adsorption of macromolecules. 2. Phase transitions in adsorption: general approach.* Macromolecules, 1983. **16**(1): p. 45-50.
180. De'Bell, K. and T. Lookman, *Surface phase transitions in polymer systems.* Reviews of Modern Physics, 1993. **65**(1): p. 87-113.
181. Eisenriegler, E., *Polymers Near Surfaces*. 1993, Singapore: World Scientific.
182. Klushin, L.I., et al., *Adsorption of a single polymer chain on a surface: effects of the potential range.* Phys. Rev. E: Stat., Nonlinear, Soft Matter Phys., 2013. **87**: p. 022604-1-022604-16.
183. Metzger, S., et al., *Adsorption transition of a polymer chain at a weakly attractive surface: monte carlo simulation of off-lattice models.* Macromolecular Theory and Simulations, 2002. **11**(9): p. 985-995.
184. Skvortsov, A.M. and A.A. Gorbunov, *Adsorption effects in the chromatography of polymers.* J. Chromatogr. A, 1986. **358**(1): p. 77-83.
185. Philipsen, H.J., et al., *Critical retention behaviour of polymers - A study on the influence of some practical parameters.* Journal of Chromatography, A, 1996. **727**(1): p. 13-25.

186. Brun, Y., *The mechanism of copolymer retention in interactive polymer chromatography. I. Critical point of adsorption for statistial copolymers.* Journal of Liquid Chromatography & Related Technologies, 1999. **22**(20): p. 3027-3065.
187. Macko, T. and D. Hunkeler, *Liquid Chromatography under critical and limiting conditions: A survey of experimental systems for synthetic polymers.*, in *Liquid Chromatography/FTIR Microscopy/Microwave Assisted Synthesis*, R. Bhargava, Editor. 2003, Springer: Berlin. p. 61-136.
188. Rasmussen, C.J., A. Vishnyakov, and A.V. Neimark, *Calculation of chemical potentials of chain molecules by the incremental gauge cell method.* J. Chem. Phys., 2011. **135**(21): p. 214109-1 - 214109-14.
189. Rasmussen, C.J., A. Vishnyakov, and A.V. Neimark, *Monte carlo simulation of polymer adsorption.* Adsorption, 2011. **17**(1): p. 265-271.
190. Siepmann, J.I. and D. Frenkel, *Configurational-bias Monte Carlo - A new sampling scheme for flexible chains.* Molecular Physics, 1992. **75**: p. 59-70.
191. Neimark, A.V. and A. Vishnyakov, *Gauge cell method for simulation studies of phase transitions in confined systems.* Phys. Rev. E: Stat., Nonlinear, Soft Matter Phys., 2000. **62**(4): p. 4611-4622.
192. Neimark, A.V. and A. Vishnyakov, *A simulation method for the calculation of chemical potentials in small, inhomogeneous, and dense systems.* J. Chem. Phys., 2005. **122**(23): p. 234108-1-234108-11.
193. Hegger, R. and P. Grassberger, J. Phys. A: Math. Gen., 1994. **27**(12): p. 4069-4082.
194. Janse van Rensburg, E.J. and A.R. Rechnitzer, J. Phys. A: Math. Gen., 2004. **37**(27): p. 6875-6898.
195. Klushin, L.I. and A.M. Skvortsov, *Unconventional phase transitions in a constrained single polymer chain.* Journal of Physics A-Mathematical and Theoretical, 2011. **44**(47).
196. Berek, D., *Molecular Characterization of Complex Polymers by Coupled Liquid Chromatographic Procedures*, in *Chromatography of Polymers*. 1999, American Chemical Society. p. 178-189.
197. Cimino, R., C.J. Rasmussen, and A.V. Neimark, *Communication: Thermodynamic analysis of critical conditions of polymer adsorption.* Journal of Chemical Physics, 2013. **139**(20).
198. Rasmussen, C.J., A. Vishnyakov, and A.V. Neimark, *Calculation of chemical potentials of chain molecules by the incremental gauge cell method.* Journal of Chemical Physics, 2011. **135**(21).
199. Snyder, L.R., *Classification of the solvent properties of common liquids.* Journal of Chromatographic Science, 1978. **16**(6): p. 223-234.
200. Kazakevich, Y.V. and H.M. McNair, *Thermodynamic Definition of HPLC Dead Volume.* Journal of Chromatographic Science, 1993. **31**: p. 317-322.
201. Striegel, A., et al., *Retention*, in *Modern Size-Exclusion Liquid Chromatography: Practice of Gel Permeation and Gel Filtration Chromatography, 2nd Edition*. 2009, Wiley. p. 18-47.
202. Kazakevich, Y.V., *High-performance liquid chromatography retention mechanisms and their mathematical descriptions.* Journal of Chromatography A, 2006. **1126**(1-2): p. 232-243.
203. Snyder, L.R., J.J. Kirkland, and J.W. Dolan, *Introduction to Modern Liquid Chromatography*. 3rd ed. 2010: Wiley.
204. Synder, L.R., J.J. Kirkland, and J.W. Dolan, *Introduction to Modern Liquid Chromatography*. 3rd ed. 2009, Hoboken, N.J: Wiley. 960.
205. Cassasa, E.F. and Y. Tatami, *An equilibrium theory for exclusion chromatography of branched and linear polymer chains.* Macromolecules, 1969. **2**(1): p. 14-26.

206. Kazakevich, Y.V. and R. LoBrutto, *HPLC for Pharmaceutical Scientists*. 2007: Wiley.
207. Rouquerol, F., J. Rouquerol, and K. Sing, *Adsorption by powders and porous solids*. 1998: Academic Press.
208. Riedo, F. and E. Kovats, *Adsorption from liquid mixtures and liquid chromatography.* Journal of Chromatography, 1982. **239**: p. 1-28.
209. Yun, K.S., C. Zhu, and J.F. Parcher, *Theoretical Relationships between the Void Volume, Mobile Phase Volume, Retention Volume, Adsorption, and Gibbs Free Energy in Chromatographic Processes.* Analytical Chemistry, 1995. **67**: p. 613-619.
210. Kumar, S.K., I. Szleifer, and A.Z. Panagiotopoulos, *Determination of the chemical potentials of polymeric systems from Monte Carlo simulations.* Phys. Rev. Lett. , 1991. **66**(22): p. 2935-2938.
211. Skvortsov, A.M. and A.A. Gorbunov, *Adsorption effects in the chromatography of polymers* Journal of Chromatography 1986. **358**(1): p. 77-83.
212. Grassberger, P. and R. Hegger, *Monte Carlo simulations of off-lattice polymers.* Journal of Physics: Condensed Matter, 1995. **7**(16): p. 3089-3097.
213. Brun, Y. and P. Alden, *Gradient separation of polymers at critical point of adsorption.* Journal of Chromatography A, 2002. **966**(1-2): p. 25-40.
214. Striegel, A.M. and A.K. Brewer, *Hydrodynamic Chromatography.* Annual Review of Analytical Chemistry, 2012. **5**: p. 15-34.
215. DiMarzio, E.A. and C.M. Guttman, *Separation by Flow.* Macromolecules, 1970. **3**: p. 131-146.
216. Tallarek, U., F.J. Vergeldt, and H. Van As, *Stagnant mobile phase mass transfer in chromatograhic media: Interparticle diffusion and exchange kinetics.* Journal of Physical Chemistry B, 1999. **103**(36): p. 7654-7664.
217. Horvath, C. and H.-J. Lin, *Movement an band spreading of unsorbed solutes in liquid chromatography.* Journal of Chromatography 1976. **126**(1): p. 401-420.
218. Macko, T., D. Hunkeler, and D. Berek, *Liquid chromatography of synthetic polymers under critical conditions. The case of single eluents and the role of Theta conditions.* Macromolecules, 2002. **35**(5): p. 1797-1804.
219. Hunkeler, D., T. Macko, and D. Berek, *Critical Conditions in the Liquid-Chromatography of Polymers.* Acs Symposium Series, 1993. **521**: p. 90-102.
220. Entelis, S.G., V.V. Evreinov, and A.V. Gorshkov, *Functionality and molecular weight distribution of telechelic polymers*, in *Pharmacy/Thermomechanics/Elastomers/Telechelics*, K. Dušek, Editor. 1986, Springer Berlin Heidelberg. p. 129-175.
221. Cimino, R., et al., *Critical conditions of polymer adsorption and chromatography on non-porous substrates.* Journal of Colloid and Interface Science, 2016. **474**: p. 25-33.
222. Skvortsov, A.M., et al., *First-order coil-to-flower transition of a polymer chain pinned near a stepwise external potential: Numerical, analytical, and scaling analysis* Journal of Chemical Physics, 2001. **115**(3): p. 1586-1595.
223. Skvortsov, A.M., J. van Male, and F.A.M. Leermakers, *Exactly solvable model with an unusual phase transition: the rolling transition of a pinned Gaussian chain* Physica A, 2001. **290**(3-4): p. 445-452.